

Molybdenum Oxide and Tin Oxide/Sulfide Nanostructured Materials for Anodes in Lithium Ion Batteries

Akkisetty Bhaskar

**A Dissertation Submitted to
Indian Institute of Technology Hyderabad
In Partial Fulfillment of the Requirements for
The Degree of Doctor of Philosophy**



भारतीय प्रौद्योगिकी संस्थान हैदराबाद
Indian Institute of Technology Hyderabad

Department of Materials Science and Metallurgical Engineering

September, 2014

Declaration

I declare that this written submission represents my ideas in my own words, and where others' ideas or words have been included, I have adequately cited and referenced the original sources. I also declare that I have adhered to all principles of academic honesty and integrity and have not misrepresented or fabricated or falsified any idea/data/fact/source in my submission. I understand that any violation of the above will be a cause for disciplinary action by the Institute and can also evoke penal action from the sources that have thus not been properly cited, or from whom proper permission has not been taken when needed.



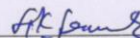
(Signature)

(Akkisetty Bhaskar)

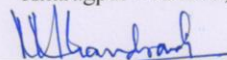
(MS10P007)

Approval Sheet

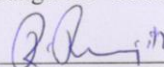
This thesis entitled “Molybdenum Oxide and Tin Oxide/Sulfide Nanostructured Materials for Anodes in Lithium Ion Batteries” by Akkisetty Bhaskar is approved for the degree of Doctor of Philosophy from the Indian Institute of Technology Hyderabad.



External Examiner
Prof. Suneel K. Srivastava
Department of Chemistry
Indian Institute of Technology Kharagpur
Kharagpur - 721302, India



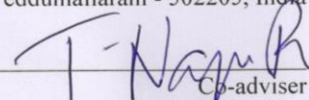
External Examiner
Prof. N. Munichandraiah
Department of Inorganic and Physical Chemistry
Indian Institute of Science
Bangalore - 560012, India



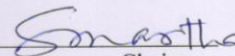
Internal Examiner
Dr. Ranjith Ramadurai
Department of Materials Science and Metallurgical Engineering
Indian Institute of Technology Hyderabad
Yeddumailaram - 502205, India



Adviser
Dr. M. Deepa
Assistant Professor
Department of Chemistry
Indian Institute of Technology Hyderabad
Yeddumailaram - 502205, India



Co-adviser
Dr. Tata Narasinga Rao
Scientist F
International Advanced Research Centre for
Powder Metallurgy & New Materials (ARCI)
Balapur P.O., Hyderabad-500005, India



Chairman
Dr. Surendra K. Martha
Department of Chemistry
Indian Institute of Technology Hyderabad
Yeddumailaram - 502205, India

Acknowledgements

I would like to express my sincere thanks to my supervisor Dr. Melepurath Deepa for her constant support and guidance throughout my research work. Her enthusiasm, ardor to work, remarks and comments helped me a lot in shaping my research work. Her confidence in me always encourages me to do better. I also thank my external mentor Dr. T. Narsinga Rao for his support for performing SEM, TEM and XPS characterization at ARCI. I would like to thank Prof. U. V. Varadaraju for providing excellent instrumentation facilities and also for helping me in the beginning of my work. His invaluable suggestions and comments during my initial research stage helped me to understand the subject well.

My sincere thanks to Dr. Pinaki Prasad Bhattacharjee, Head, Department of Materials Science and Metallurgical Engineering, to Prof. Faiz Ahmed Khan, Head, Department of Chemistry and to Prof. U.B. Desai, Director, IIT Hyderabad, for the excellent work culture and infrastructure.

I wish to thank to all my Doctoral committee members, Dr. Suhash Ranjan Dey, Dr. Ranjith Ramadurai and Dr. Vinod Janardhanan for their useful suggestions and comments, which aided me a lot in improving my research work. I would also like to express my sincere thanks to all other faculty members of the Department of MSME. My special thanks to Dr. Surendra Kumar Martha, an expert in battery research, for fruitful discussions on the subject and for the presentation of my research work.

I am deeply grateful to Ms. Revathi Janardhanan and Dr. S. Anandan for helping me with various characterization experiments at ARCI. I would like to thank all my lab mates: N. Remya, B. Narsimha Reddy, S. Rambabu and my juniors: P. Naresh, Radha, S. Krishna Kumar, and V. Naresh for their kind help during the experiments and presentations. I wish to thank my friends: T. Karthik, P. Srinivas, Jaggarao, and Pankaj Kumar Jha for the kind help and encouragement.

I thank International Advanced Research Centre for Powder Metallurgy and New Materials (ARCI) for PhD research fellowship for four years of my PhD work and the Indo-French Centre for the Promotion of Advanced Research (CEFIPRA) for financial support to purchase chemicals. I thank the Council of Scientific and Industrial Research (CSIR) and the Department of Science and Technology (DST) for support of travel grant and registration fee which enabled me to participate in international conferences.

Finally, I thank my family members for their whole-hearted support, for without their support, this work would not have been possible.

.

Dedicated to
My Beloved Parents & Teachers

Abstract

The ever-increasing global warming due to gaseous emissions, the burgeoning fuel costs and their limited availability have escalated the search for viable energy efficient alternatives. During the last two decades, most of the portable electronic devices such as cellular phones, laptops, camcorders and notebooks etc., have been using the Li-ion battery (LIB) technology. Li-ion batteries (LIBs) are considered promising for even powering electric and hybrid electric vehicles (EVs). However, the current electrode materials are too costly to penetrate into the EV industry, for not only, does it need high performance materials, but at the same time, the materials should be environmentally benign. In terms of performance, nanostructured materials offer many advantages; the large contact area between the electrode and the electrolyte and the short diffusion path lengths due to small sized crystallites, lead to higher charge storage capacity and increased power rate compared to their bulk counterparts. In commercially available LIBs, the anode is, typically, graphite, which, is characterized by a rather low theoretical specific capacity of 374 mAh g^{-1} . The low capacity of the anode material limits the performance of battery. Benefiting from nanotechnology, metal oxides (e.g. MoO_2) through conversion and tin based oxides and sulfides through alloy/dealloy mechanisms can offer a large lithium storage capacity i.e., almost two times more than the current graphite anodes. However, despite delivering high energy densities, these materials experience substantial volume variation during Li^+ insertion/extraction process, which manifests in the pulverization of the electrode material and rapid decline of capacity. To counter the aforementioned issues, oxides/sulfides in nanostructured forms and their composites with carbonaceous materials such as graphene, multiwalled carbon nanotubes or MWCNTs and conducting polymers are used. Nanostructured materials, compared to bulk, provide shorter diffusion path lengths for Li-ions, during ingress/egress phenomena. Moreover, carbonaceous materials can enhance electronic conductivity and buffer the large volume expansion and contraction incurred by oxides during charge/discharge processes, which result in increased cycling stability and specific capacity. In this thesis, various methods were employed to synthesize the MoO_2 ,

SnX₂ (X = O, S) nanostructured anodes and their composites with graphene oxide, MWCNTs and poly(3,4-ethylenedioxythiophene) or PEDOT. The materials were characterized by X-ray diffraction (XRD), Raman spectroscopy, X-ray photoelectron spectroscopy (XPS), UV-Vis spectroscopy and electron microscopy. The Li-ion charge storage mechanisms and cycling behavior of different composites have been elucidated by measuring electrochemical properties (cyclic voltammograms and galvanostatic charge-discharge response at different current densities), *ex-situ* XRD and impedance spectra. Overall, in this thesis, how the microstructure of different metal oxides and how the incorporation of carbon nanostructures/conducting polymer in the oxide controls the specific capacity, rate capability and durability of the electrode when used as an anode in a LIB is explained.

Nomenclature

EV	Electric vehicle
MWCNT	Multi walled carbon nanotubes
GO	Graphene oxide
PEG	Polyethylene glycol
PEDOT	Poly(3,4-ethylenedioxythiophene)
EDOT	3,4-ethylenedioxythiophene
AOT	Bis(2-ethylhexyl) sulfosuccinate sodium salt
CTAB	Hexadecyltrimethylammonium bromide
MPA	Mercapto propionic acid
AcAc	Acetylacetone
AHM	Ammonium heptamolybdate tetrahydrate
EC	Ethylene carbonate
DMC	Dimethyl carbonate
NMP	N-methyl-2-pyrrolidone
PVdF	Polyvinylidene fluoride
CV	Cyclic voltammetry
EIS	Electrochemical impedance spectroscopy
XRD	X-ray diffraction
EDX	Energy-dispersive X-ray spectroscopy
FE-SEM	Field emission scanning electron microscopy

HRTEM	High resolution transmission electron microscopy
TEM	Transmission electron microscopy
TGA	Thermo gravimetric analysis
DTA	Differential thermal analysis
XPS	X-ray photoelectron spectroscopy
CAFM	Conductive atomic force microscopy

Contents

Declaration.....	ii
Approval Sheet	Error! Bookmark not defined.
Acknowledgements.....	iv
Abstract.....	vii
Nomenclature.....	ix
Chapter 1 Introduction.....	1
1.1. Importance of energy storage.....	1
1.2. Classification of batteries.....	2
1.3. Lithium-ion battery (LIB).....	2
1.3.1. Operating principle.....	4
1.3.2. Open circuit potential.....	5
1.3.3. Cathodes.....	7
1.3.3.1. Layered transition metal oxide structures (LiMO ₂ where M = Co, Ni, Mn etc.).....	8
1.3.3.2. Polyanion-based cathodes.....	14
1.3.4. Anode materials.....	19
1.3.4.1. Intercalation based anodes.....	22
1.3.4.2. Alloying-dealloying mechanism based anode materials.....	26
1.3.4.3. Conversion mechanism based materials.....	32
1.3.5. Electrolytes.....	35
1.3.5.1. Electrolytes containing organic solvent.....	35
1.3.5.2. Ionic liquid electrolytes.....	36
1.3.5.3. Solid polymer electrolytes.....	37
1.3.6. Objectives of current thesis.....	38
Chapter 2 Experimental and Characterization Techniques.....	46
2.1. Synthesis techniques.....	46
2.2. Preparation of electrodes and cell fabrication.....	46
2.3. Characterization techniques.....	47
2.3.1. Powder X-ray diffraction technique.....	47
2.3.2. Raman spectroscopy.....	48
2.3.3. Scanning electron microscope (SEM).....	50

2.3.4. Transmission electron microscopy (TEM).....	51
2.3.5. X-ray photoelectron spectroscopy (XPS).....	53
2.3.6. Thermogravimetric analysis (TGA).....	55
2.4. Calculation of theoretical specific capacity and C-rate.....	55
2.5. Electrochemical property measurement.....	56
2.6. Cyclic voltammetry (CV).....	57
2.7. Electrochemical Impedance spectroscopy (EIS).....	59
2.8. Other instruments.....	60
Chapter 3 Structure-Electrochemical Activity Correlation in a MoO₂/Multiwalled Carbon Nanotubes (MWCNTs) Hybrid.....	62
3.1. Abstract.....	62
3.2. Introduction.....	62
3.3. Experimental.....	64
3.3.1. Materials.....	64
3.3.2. Synthesis of the MoO ₂ /MWCNT hybrid.....	64
3.4. Results and discussion.....	65
3.4.1. Structural characterization.....	65
3.4.2. Growth mechanism of MoO ₂ flowers.....	71
3.5. Electrochemical characteristics.....	77
3.6. Ex-situ XRD analyses and impedance spectra.....	85
3.7. Summary.....	91
Chapter 4 Influence of Graphene on Li - ion Storage in a MoO₂/Graphene Composite.....	94
4.1. Abstract.....	94
4.2. Introduction.....	94
4.3. Experimental.....	96
4.3.1 Chemicals.....	96
4.3.2. Preparation of Graphene oxide and MoO ₂ /Graphene.....	96
4.3.3. Preparation of Graphene.....	97
4.3.4. Preparation of MoO ₂	98
4.3.5. Preparation of MoO ₂ /Graphene oxide.....	98
4.4. Results and discussion.....	98
4.4.1. X-ray diffraction and Raman spectra.....	98
4.4.2. Electron microscopy.....	100

4.4.3. XPS and C-AFM.....	104
4.5. Electrochemical charge-discharge studies.....	108
4.6. Ex-situ XRD analyses and impedance spectra.....	114
4.7. Summary.....	119
Chapter 5 Effect of Graphene Oxide and Poly(3,4-ethylenedioxythiophene) on the Electrochemical Performance of SnO₂ Hollow Spheres/GO/PEDOT Hybrid.....	123
5.1. Abstract.....	123
5.2. Introduction.....	123
5.3. Experimental.....	125
5.3.1. SnO ₂ hollow spheres (HS) and nanostructures.....	125
5.3.2. SnO ₂ HS/GO hybrid.....	126
5.3.3. SnO ₂ HS/GO/PEDOT hybrid.....	127
5.4. Results and discussion.....	127
5.4.1. Growth mechanism by structure evolution analysis.....	127
5.4.2. Structure and composition of the hybrid.....	134
5.4.3. Electrical conduction response.....	140
5.5. Electrochemical response.....	142
5.6. Summary.....	150
Chapter 6 Size Control of SnO₂ Hollow Spheres and How Size Governs Li-ion Storage Behavior.....	153
6.1. Abstract.....	153
6.2. Introduction.....	153
6.3. Experimental.....	154
6.3.1. Synthesis of SnO ₂ HS and nanostructures.....	154
6.4. Results and discussion.....	155
6.4.1. Structural aspects.....	155
6.4.2. Optical characteristics.....	156
6.4.3. Electron microscopy analyses.....	158
6.4.4. Growth mechanism.....	160
6.4.5. Surface area determination.....	169
6.5. Electrochemical Li storage behavior.....	171
6.6. Summary.....	175

Chapter 7	Electrochemical Performance of SnS₂-Nanosheets and Nanoflowers Grown by Precursor Modification	177
7.1.	Abstract	177
7.2.	Introduction	177
7.3.	Experimental	180
7.4.	Results and Discussion	180
7.4.1.	Powder X-ray diffraction patterns	180
7.4.2.	Morphology studies	182
7.4.3.	Growth mechanism	186
7.4.4.	Optical properties	193
7.5.	Electrochemical property	194
7.5.1.	Li-ion storage for half-cell	194
7.5.2.	Full cell demonstration	198
7.6.	Summary	200
Chapter 8	Summary and Conclusions	203

Chapter 1

1. Lithium Ion Batteries: An Overview

1.1. Importance of energy storage

Due to a limited availability of energy resources, combined with the greenhouse gaseous emissions from the burning of fossil fuels and biomass, there is a quest for other alternative renewable energy sources. Some important alternative energy sources are solar, wind, wave and thermal energy. These energy sources are not always available, especially at night time, and the technology needs to be improved in order to store these energy sources and utilize them efficiently. Nuclear reactors can produce continuous energy but radioactive disposals have harmful effects on living organisms. The other form of energy storage is chemical energy. Batteries, fuel cells and capacitors are the devices which are used to store chemical energy and convert it into electrical energy. Among these options of energy storage technologies, batteries are considered to be most useful for portable energy storage devices. A battery consists of a group of interconnected cells. Each cell comprises of two dissimilar electrodes which are mixed (both electronic and ionic) conductors immersed in an electrolyte which is an ionic conductor. At the anode or the negative electrode, an oxidative chemical reaction occurs, which releases electrons into the external circuit and at the cathode or the positive electrode, a reductive chemical reaction occurs by gaining of electrons from the external circuit. In between the anode and the cathode, is a separator which is soaked with the electrolyte. The electrolyte is a pure ionic conductor and the separator serves as a physical barrier that prevents electrical shorting. The separator can be a gelled electrolyte or a micro porous plastic film or any other porous inert ion conductor.

1.2. Classification of batteries:

Batteries are classified as primary and secondary batteries.

Primary Batteries

Primary batteries are non-rechargeable, since electrochemical reactions are not reversible (e.g. alkaline battery, aluminium battery, zinc-carbon and zinc-manganese dioxide).

Secondary Batteries

Secondary batteries are rechargeable batteries. They have the advantage of being more cost-efficient over the long term. The chemical reactions are reversible and electrical energy is converted into chemical energy during the charging process (e.g. lead - acid, lithium - ion batteries, nickel - metal hydride batteries, nickel-cadmium batteries etc.).

1.3. Lithium-ion battery (LIB)

For the first time in 1976, Stanley Wittingham demonstrated the concept of a rechargeable lithium battery, using TiS_2 as cathode, metallic lithium as anode by using non-aqueous electrolyte[1]. During discharge, lithium ions are inserted into the van der Waals gap of TiS_2 , which is accompanied by reduction of Ti^{4+} to Ti^{3+} . During charge, lithium is extracted from the van der Waals gap. But the cell failed in commercial applications due to serious safety problems associated with lithium metal, primarily due to dendrite formation. To circumvent the safety issues associated with the use of Li metal, another material capable of Li-ion intercalation was employed as the anode. The replacement was “graphite”. In this case, the reversible intercalation of Li-ion into graphitic carbon, at an open circuit voltage (V_{oc}) = 0.2 V *versus* Li^+/Li , was found to deliver a theoretical capacity of 372 mAh

g^{-1} . It was found that, with slow discharge and charge rates, the material did not form any dendrites, and later in 1991, Sony commercialized the first LIBs composed of $\text{Li}_{1-x}\text{CoO}_2$ as the cathode and graphite as the anode. This announcement was preceded by several separate inventions that included the works of Goodenough's group, Yazami and others[2-4]. Since the advent of notebook computers, digital cameras, and many other portable electronic devices and electric vehicles, the demand for LIBs is on the rise. Consequently, the research in this field has witnessed meteoric rise worldwide, and these LIBs are considered to be frontrunners as power sources in most of the contemporary applications, mostly due to high volumetric and specific energy densities. A comparison of energy densities of some of the conventional batteries is presented in Figure 1.1.

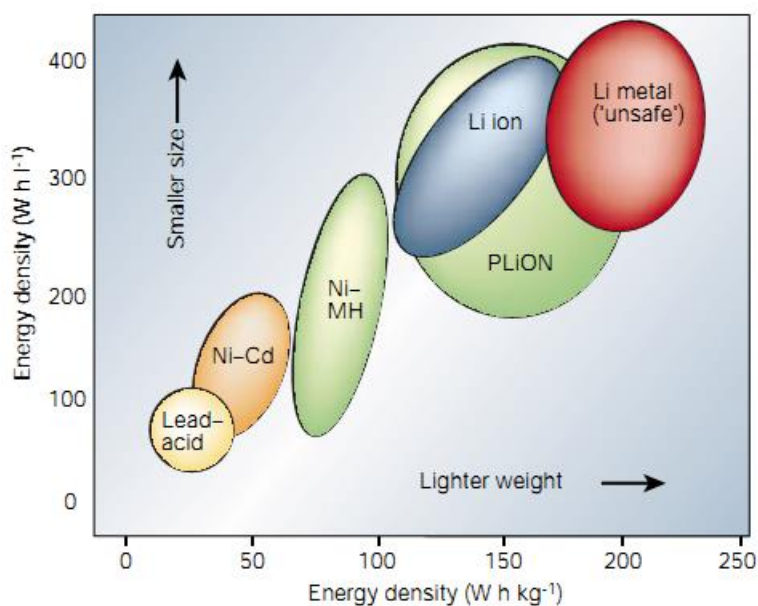


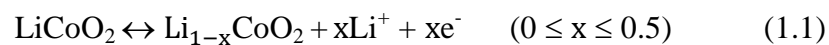
Figure 1.1. Comparison of different batteries in terms of their volumetric and gravimetric energy densities [Adapted from J. M. Tarascon, M. Armand, Nature, 414 (2011) 359-367, Copyright Nature publications (2014)].

1.3.1. Operating principle

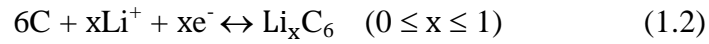
In general, a LIB consists of a cathode and an anode, which are separated by separator soaked with an electrolyte. In the LIB, either graphite, lithium titanium oxide ($\text{Li}_4\text{Ti}_5\text{O}_{12}$) etc. are used as anode materials whereas lithium transition metal oxides such as LiMO_2 ($\text{M} = \text{Co}, \text{Ni}, \text{Mn}$ etc.), spinel LiMn_2O_4 or lithium transition metal phosphates LiMPO_4 ($\text{M} = \text{Fe}, \text{Mn}$, etc.), are used as cathode materials. LiClO_4 , LiBF_4 or LiPF_6 (lithium salts) dissolved in non-aqueous solvents such as alkyl carbonates like ethylene carbonate, propylene carbonate, ethyl methyl carbonates etc. are used as electrolytes. The illustration of charge-discharge mechanism of a lithium-ion cell with a graphite anode and LiCoO_2 positive electrode is shown in Figure 1.2. The cell is constructed in the discharged state, and upon charging, Li-ions deintercalate from the LiCoO_2 cathode (positive electrode), diffuse through the electrolyte and intercalate into the graphite anode (negative electrode) while the same number of electrons pass through the external circuit from the cathode to the anode. During discharge, the same process is reversed, wherein Li-ions from graphite anode intercalate into the $\text{Li}_{1-x}\text{CoO}_2$ positive electrode, forming the original composition. Here, only the Li-ions are involved during the charge-discharge phenomenon and the cell delivered a specific capacity of ~ 150 mAh g^{-1} and a potential of ~ 3.5 V.

The electrochemical reactions at the electrodes in a LIB (LiCoO_2 : cathode and Graphite: anode) are shown below.

At the positive electrode:



At the negative electrode:



Overall cell reaction:

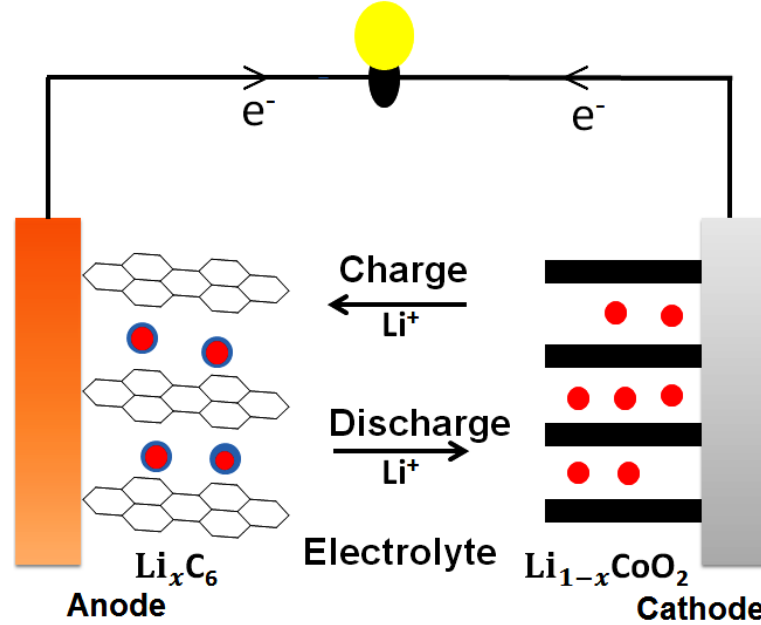
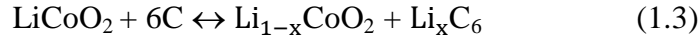


Figure 1.2. Schematic representation of the charge/discharge mechanism of a rechargeable Li-ion cell consisting of graphite as the anode and a layered LiCoO₂ as the cathode.

1.3.2. Open circuit potential (V_{OC})

The V_{OC} of a Li-ion cell can be determined based on the thermodynamic chemical potentials of cathode and anode materials, as shown in equation 1.4.

$$V_{OC} = \frac{\mu_a^{Li} - \mu_c^{Li}}{F} \quad (1.4)$$

In the above equation, μ_a^{Li} and μ_c^{Li} are the chemical potentials of the anode and cathode, respectively, and F is the Faraday's constant. The V_{OC} of a cell constrained by the voltage window or Fermi energy (E_g) of electrolyte. For a cell to be

thermodynamically stable, the electrode chemical potentials should lie within the electrolyte window, as shown in Figure 1.3.

$$V_{oc} = \frac{\mu_a^{Li} - \mu_c^{Li}}{F} \leq E_g \quad (1.5)$$

In the schematic of a Li-ion cell, the energy separation of lowest unoccupied molecular orbital (LUMO) and the highest occupied molecular orbital (HOMO) is the window of the electrolyte, the anode is the reducing agent and the cathode is the oxidizing agent. If the anodic chemical potential (μ_a^{Li}) lies above the LUMO level of electrolyte, it will transfer electrons to the electrolyte to form a stable passivation layer of the solid electrolyte interface (SEI), which can further prevent the electron transfer from the anode to electrolyte. Similarly, if the cathodic chemical potential (μ_c^{Li}) lies below the HOMO level of electrolyte, the electrode will take an electron from the electrolyte to form a SEI layer and thus block electron transfer from the electrolyte to the cathode. Thus, a stable SEI layer formation between the electrode and electrolyte can give a kinetic stability to a larger V_{oc} of the cell, provided that the difference ($V_{oc} - E_g$) is not too large.

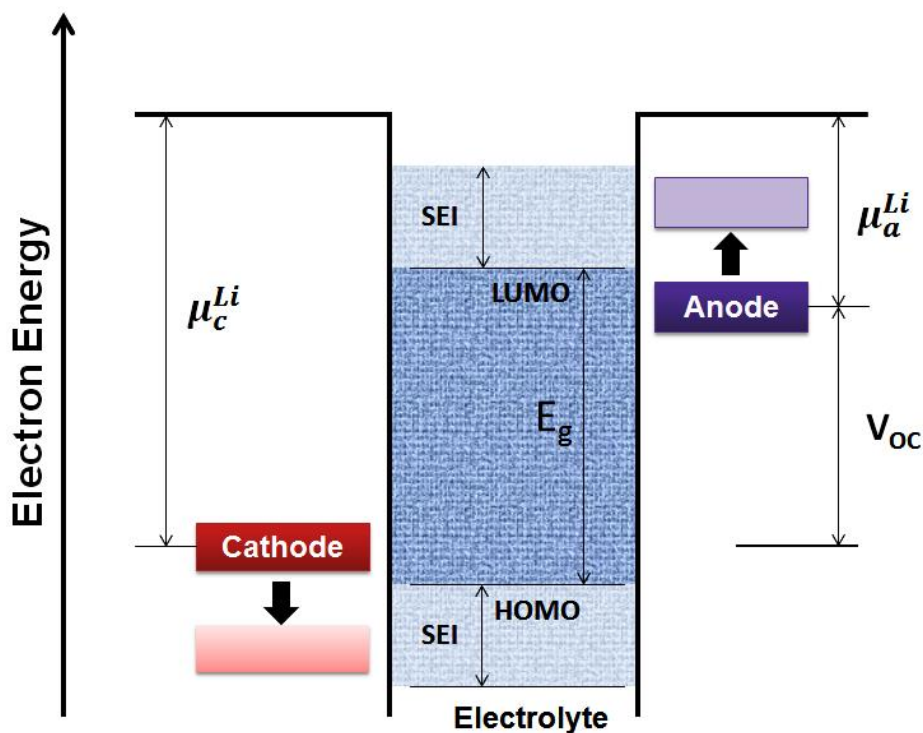


Figure 1.3. Energy diagram of a Li-ion cell at open circuit. μ_a^{Li} and μ_c^{Li} represent the lithium chemical potentials in the anode and cathode. E_g is the measure of the thermodynamic stability of the electrolyte. A $\mu_a^{\text{Li}} > \text{LUMO}$ and/or a $\mu_c^{\text{Li}} < \text{HOMO}$ are required for the formation of a stable SEI layer [Modified from J. B. Goodenough, Y. Kim, Chem. Mater., 22 (2010) 587-603].

1.3.3. Cathodes in LIBs

The key requirements for a material to be successfully used as a cathode in a rechargeable LIB are summarized below.

- The material must contain a readily reducible/oxidizable ion, for example a transition metal ion.
- The ideal cathode must react with lithium in a reversible manner without undergoing any degradation.
- An ideal cathode should not react or dissolve in the electrolyte.
- An ideal cathode must react with lithium which can result in a high free energy of reaction.
- An ideal cathode should contain or react with at least one lithium per transition metal ion that can result in high capacity.

- An ideal cathode must be a high voltage material, preferably around 4 V (as limited by the stability of electrolyte).
- The material must be capable of storing a large amount of energy.
- An ideal cathode material must be a mixed conductor, i.e., both electronic as well as ionic conduction should be possible.
- An ideal cathode material must be stable, i.e., not undergo structural changes or degradation, upon over-discharge and over-charge.
- An ideal cathode material must be of low cost and should be environmentally benign.

A brief literature survey on conventional and some of the latest cathode materials is provided below.

1.3.3.1. Layered transition metal oxide structures (LiMO₂ where M = Co, Ni, Mn etc.)

Transition metal oxide compounds such as LiCoO₂, LiVO₂, LiCrO₂, LiFeO₂ and LiNiO₂ are isostructural and their crystal structure is shown in Figure 1.4. LiMO₂ has a two dimensional (2D) layered structure similar to α -NaFeO₂, where the anions occupy the cubic close packed lattice and the lithium and transition metal ions ordering in the octahedral voids is such that the MO₂ layers are formed, consisting of edge-sharing [MO₆] octahedra. In between these layers, Li-ion resides in the octahedral [LiO₆] coordination, leading to alternating (111) planes with a cubic rock salt structure. This (111) ordering induces a slight distortion of the lattice to the hexagonal symmetry. Complete deinsertion of lithium ions results in the layered CdCl₂ type structure. Among the above mentioned isostructural compounds, particularly LiCoO₂, LiNiO₂ and solid solutions of Li[CoNi]O₂ have been used in industrial applications. These materials are thermodynamically unstable when complete deinsertion of lithium occurs from the lattice. The reason for this, is the high electronegativity of oxygen, which leads to a higher ionic character of the

metal-oxygen bonds. The resulting negative charge of the transition metal-oxygen layers causes repulsive interactions between adjacent layers, which have to be compensated for by the positively charged ions between the adjacent oxygen layers[5,6]. Hence, for these kinds of materials, the deinsertion of one mole of lithium per LiMO_2 formula unit leads to structural transitions during charging.

LiCoO_2

Goodenough's group first introduced Li_xCoO_2 as a cathode for LIB applications using lithium metal as anode, in 1980[2]. The theoretical specific capacity of LiCoO_2 is 274 mAh g^{-1} based on one mole of lithium per formula unit. But practically, it is only possible to deinsert/insert in Li_xCoO_2 , about ($0.5 < x < 1$) moles of Li-ions for many charge-discharge cycles without any capacity decay, which limits the specific capacity to about 130 to 140 mAh g^{-1} at the V_{OC} of $\sim 4 \text{ V}$. During lithium extraction (charge), the material experiences phase transitions, and when $x \geq 0.5$, then the material shows an expansion of interlayer c-axis without any phase (hexagonal) change. When $x \approx 0.5$, a hexagonal to monoclinic i.e., order to disorder transition was observed. Finally, when $x \approx 0.05$, the O3 structure of LiCoO_2 (close-packed oxygen layers with an ABCABC stacking sequence) transform into the O1 Li_xCoO_2 phase (ABAB stacking sequence). The letter "O" represents the octahedral site coordination of Li^+ and the number represents the number of CoO_2 sheets in the unit cell. This transformation proceeds via an intermediate phase, $\text{Li}_{0.12}\text{CoO}_2$, (H1 - 3)[7]. The capacity of this material can be improved by coating a metal oxide (Al_2O_3 , MgO and SnO_2 etc.) or phosphate (AlPO_4 etc.), on the surface of the Li_xCoO_2 particles[6,7]. In this way, the capacity could be increased to 170 mAh g^{-1} when cycled between 2.75 and 4.4 V, without capacity fade, over 70 cycles.

The mechanism of protection is related to minimizing the reactivity of Co^{4+} on charge, with HF in the electrolyte formed from the interaction of the electrolyte with trace amounts of moisture. Replacing the LiPF_6 salt by Lithium bis(oxalate)borate (LiBOB) or by completely drying LiCoO_2 , by heating to over $550\text{ }^\circ\text{C}$, improved the capacity retention to 180 mAh g^{-1} at a 4.5 V cutoff[8]. The limited availability and toxic nature of cobalt heralded the search for alternative cathodes.

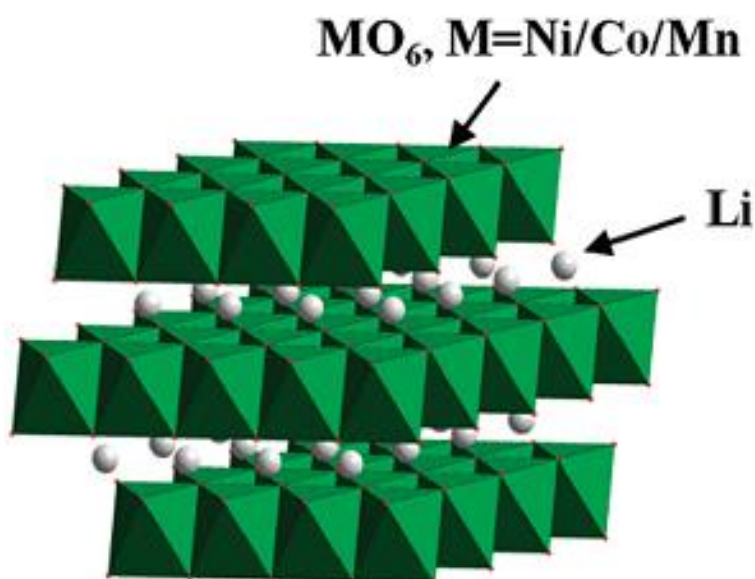


Figure 1.4. Layered structure of LiMO_2 ($\text{M} = \text{V}, \text{Co}, \text{Ni}, \text{Fe}$ and Cr etc.), showing the lithium ions between the transition metal oxide. The actual stacking of the metal oxide sheets depends on the transition metal and the anion [Adapted from Z. Yang, J. Zhang, M. C. W. Kintner-Meyer, X. Lu, D. Choi, J. P. Lemmon, J. Liu, Chem. Rev., 111 (2011) 3577-3613 Copyright RSC Publications (2014)].

LiNiO_2

When compared to Co , Ni is nontoxic, more abundant and cheaper. LiNiO_2 is considered to be an attractive alternative to LiCoO_2 . During charge/discharge, $\text{Li}_{1-x}\text{NiO}_2$ undergoes structural transformation in a manner, exactly similar to LiCoO_2 . At the initial extraction of Li -ions, $\text{Li}_{1-x}\text{NiO}_2$ maintains its rhombohedral phase ($x < 0.25$) and, in the range of $0.25 < x < 0.55$, $\text{Li}_{1-x}\text{NiO}_2$ transforms into the

monoclinic phase. The rhombohedral phase re-appears upon further extraction of Li-ions from $\text{Li}_{1-x}\text{NiO}_2$ in the region $0.55 < x < 0.75$. Finally, $\text{Li}_{1-x}\text{NiO}_2$ experiences a rhombohedral two-phase reaction in the range of $0.75 < x < 1$, which changes the interlayer distance significantly, leading to poor capacity retention. Therefore, the use of $\text{Li}_{1-x}\text{NiO}_2$ in LIBs is recommended in the range $0 < x < 0.75$. One can expect a very high practical reversible capacity $\sim 200 \text{ mAh g}^{-1}$, when this material is used for LIBs. However, there are certain issues with LiNiO_2 such as synthesis of stoichiometric LiNiO_2 , cation site disorder, caused by size similarity of Ni^{2+} and Li^+ , and evolution of O_2 during charge leads to an irreversible capacity loss. Therefore, partial substitution of (Ni^{3+} by Co^{3+}) or solid solution of Ni^{3+} by Co^{3+} was examined to stabilize the oxidation state of Ni^{3+} and formation of Ni^{2+} . A wide range of $\text{Li}[\text{Ni}_{1-x}\text{Co}_x]\text{O}_2$ materials were examined and these material show a lower irreversible capacity losses[9-11].

LiMnO₂

Lithium manganese oxides are cheap, abundant, environment friendly and even upon overcharge, these materials are safe to use. But the layered LiMnO_2 , is thermodynamically unstable at higher temperatures and cannot be easily prepared by the solid state method[12]. However, the metastable phase of layered LiMnO_2 can be prepared from the stable phase of NaMnO_2 by ion exchange of Na^+ with Li^+ [13,14]. Because of the Jahn-Teller distortion of Mn^{3+} upon cycling, $\text{Li}_{0.5}\text{MnO}_2$ converts into the LiMn_2O_4 spinel, resulting in a poor cycling performance[15,16]. To inhibit phase transformation, a series of solid solutions of LiMO_2 ($\text{M} = \text{Mn, Co, Ni}$ etc.) were attempted. Dhan et al., and Ohzuku et al., in 2001 demonstrated a greatly improved electrochemical property for a $\text{Li}[\text{Mn}_{0.5}\text{Ni}_{0.5}]\text{O}_2$ system synthesized

at a higher temperature ($> 800\text{ }^{\circ}\text{C}$)[17,18]. In a report by Makimura et al., on $\text{Li}[\text{Ni}_{0.5}\text{Mn}_{0.5}]\text{O}_2$ by reacting LiOH and nickel manganese double hydroxides at $1000\text{ }^{\circ}\text{C}$ in air, the material showed reversible capacities of 200 mAh g^{-1} ($2.5 - 4.5\text{ V}$ window *versus* Li/Li^+) with little capacity fading [19]. Kang et al., reduced the cation site disorder to 4-5% by synthesizing the $\text{Li}[\text{Mn}_{0.5}\text{Ni}_{0.5}]\text{O}_2$ using ion exchange of Na^+ from $\text{Na}[\text{Mn}_{0.5}\text{Ni}_{0.5}]\text{O}_2$ by Li^+ [20]. This material exhibited vastly improved rate capability, delivering 183 mAh g^{-1} at a current rate of 6C (1C rate: 280 mA g^{-1}). By substituting Co in $\text{Li}[\text{Mn}_{0.5}\text{Ni}_{0.5}]\text{O}_2$, $\text{Li}[\text{Mn}_{1/3}\text{Ni}_{1/3}\text{Co}_{1/3}]\text{O}_2$ was prepared, wherein, the cation site disorder was further minimized to 1-6%[21-23]. Further, $\text{Li}[\text{Mn}_{1/3}\text{Ni}_{1/3}\text{Co}_{1/3}]\text{O}_2$ is safe to use and undergoes minimum volume change of 1-2% during cycling thus rendering it to be suitable for commercial applications.

$x\text{Li}_2\text{MnO}_3 \cdot (1 - x)\text{LiMO}_2$

Another set of promising cathode materials are the lithium excess layered oxides $\text{Li}[\text{Li},\text{Mn},\text{Ni},\text{Co}]\text{O}_2$, which are solid solutions of layered $\text{Li}[\text{Li}_{1/3}\text{Mn}_{2/3}]\text{O}_2$ (commonly designated as Li_2MnO_3) and LiMO_2 ($\text{M} = \text{Ni}, \text{Co}, \text{Mn}$)[24]. The composite, $x\text{Li}_2\text{MnO}_3 \cdot (1 - x)\text{LiMO}_2$ material was originally designed to structurally stabilize the LiMO_2 with Li_2MnO_3 phases, since the latter part is electrochemically inactive between 3 and 4 V *versus* Li/Li^+ . However, Li_2MnO_3 can transform into an active phase, $\text{Li}_{2-x}\text{MnO}_{3-(\frac{x}{2})}$ (MnO_2 at $x = 2$) by the leaching of Li_2O via chemical and electrochemical means (at high voltage $\sim 4.5\text{ V}$). Thackeray et al., showed that Li_2MnO_3 (C2/m) decomposes into $\text{Li}_{0.27}[\text{Mn}_{0.91}\text{Li}_{0.09}]\text{O}_2$ by acid treatment and $\text{Li}[\text{Mn}_{0.91}\text{Li}_{0.09}]\text{O}_2$ (R3m) is then formed by re-lithiation[25,26]. After the activation process, these composite materials offer very a high capacity of about 200 - 300 mAh g^{-1} . However, these high capacity composite materials suffer from irreversible

capacity loss of about 40-100 mAh g⁻¹ in the first few cycles due to loss of Li₂O during charging, electrolyte decomposition and formation of SEI layer.

Spinel

Spinel LiMn₂O₄, which has a theoretical charge storage capacity of 148 mAh g⁻¹, is another attractive cathode material for next generation LIBs due to low cost, low toxicity, and ease of manufacture. The anion lattice again contains cubic close-packed oxygen ions and is closely related to the R-NaFeO₂ layer structure, differing only in the distribution of the cations among the available octahedral and tetrahedral sites [27-30]. In LiMn₂O₄, the Li-ion occupies the tetrahedral 8d site in the cubic close packed oxygen array and the Mn³⁺ and Mn⁴⁺ reside in the octahedral 16c site. MnO₆ are edge shared to form a 3D framework with interconnected empty tetrahedral and octahedral sites which lead to a very high Li-ion mobility (Figure 1.5). In LiMn₂O₄, the charge-discharge proceeds in two steps, one around 4 V and the other around 3 V. The plateau at ~4 V, corresponds to Li⁺ insertion into the tetrahedral sites whereas at ~3 V, Li⁺ removal from octahedral site occurs. Usually the 4 V plateau is used, so that the cell is constructed in the discharged state and should be charged before use, just as for LiCoO₂. Spinel LiMn₂O₄ suffers from severe capacity fading, particularly, at elevated temperatures (> 50 °C). Several factors that contribute to the degradation are: Jahn-Teller distortion of Mn³⁺, Mn dissolution into the electrolyte, loss of crystallinity, development of microstrain due to lattice mismatch between the two distinct cubic phases formed on cycling; and an increase in oxygen deficiencies or oxygen loss upon cycling[31-35]. Among all, Mn dissolution in electrolyte is considered as a major cause for capacity degradation. The dissolution is due to the presence of a small amount of HF in the electrolyte,

which causes a disproportionation reaction of Mn^{3+} to Mn^{2+} and Mn^{4+} , where Mn^{2+} dissolves in the electrolyte very easily. It has been demonstrated that doping Li^+ in the octahedral voids of LiMn_2O_4 minimized the dissolution. Some other strategies to mitigate Mn dissolution are: substitution of dopants in spinel structure by fluorine instead of oxygen, use of metal oxide surface coatings, and electrolyte additives. Recent attempts on synthesis of nanostructured materials such as ordered mesoporous, nanorods structures of pristine material and/or composites of LiMn_2O_4 with graphene, CNTs and other carbonaceous materials showed improved rate capability and cycling stability[36-40].

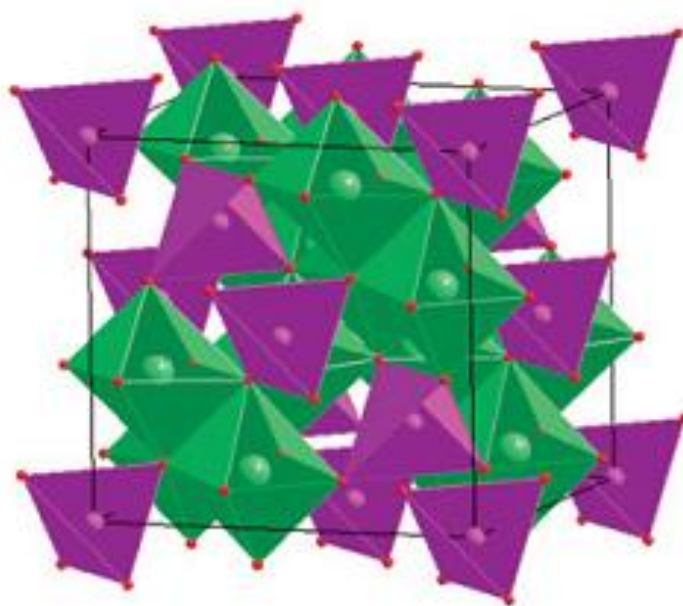


Figure 1.5. Spinel structure of LiMn_2O_4 [Adapted from A. Manthiram, A. Vadivel Murugan, A. Sarkar, T. Muraliganth, *Energy Environ. Sci.*, 1 (2008) 621-638, Copyright RSC publications (2014)].

1.3.3.2. Polyanion-based cathodes

Phosphates with olivine structure LiMPO_4 (M = Fe, Mn, Co and Ni)

The layered metal oxides LiMO_2 (M = Co, Ni and Mn), upon charging to very high voltages, tend to behave as strong oxidizers (for instance, $\text{Co}^{3+}/\text{Co}^{4+}$ and

Mn³⁺/Mn⁴⁺) and release oxygen from the crystal lattice to the electrolyte solution, which manifests in thermal runaway reactions. As a consequence, these materials are unsafe for large-scale applications such as electric vehicles. Therefore, the search for alternates intensified; polyanions such as tetrahedral (XO₄)^{y-} groups (X = P, Mo, W, S, Si, As) as potential replacements for close packed oxygen atoms in the lattice, were considered. Inductive effect in (PO₄)³⁻ and (SO₄)²⁻ ions raises the redox energy compared to that in oxides and increases the structural stability[41]. The presence of inductive effect in the polyanion (XO₄)^{y-} groups with strong X-O covalent bonds lowers the covalency of the M-O bond and as a result, potential will increase. Padhi et al., first introduced LiMPO₄ (M = Fe, Mn, Co and Ni) based cathodes in 1997[42]. Among them, iron based compounds were advantageous, these were naturally abundant and inexpensive, less toxic than V, Co, Mn and Ni based compounds. LiFePO₄, naturally available in the triphylite form, exhibits a very high theoretical capacity of 170 mAh g⁻¹ with a V_{OC} ~ 3.5 V *versus* Li/Li⁺. The crystal structure of LiFePO₄ is shown in Figure 1.6. LiFePO₄ shows an olivine crystal structure consisting of a distorted hexagonal close packed oxygen framework with 1/8 of the tetrahedral sites occupied by P, and 1/2 of octahedral sites occupied by Li⁺ and Fe²⁺. Layers of FeO₆ octahedra are corner shared in the bc plane and linear chains of LiO₆ octahedra are edge-shared in a direction parallel to the b-axis [42]. Unlike the conductive metal oxides, an electronic conductivity of 10⁻⁹ S cm⁻¹ and 1D Li⁺ diffusion limits its electrochemical performance. The flat electrochemical profile over a large range of composition indicates two phase lithium insertion/extraction mechanism. The second phase is FePO₄ which crystallizes in the same space group as LiFePO₄ (Pnma). It was found that the

synthesis procedure plays a major role in the formation of lattice defects and lithiation and de-lithiation mechanisms.

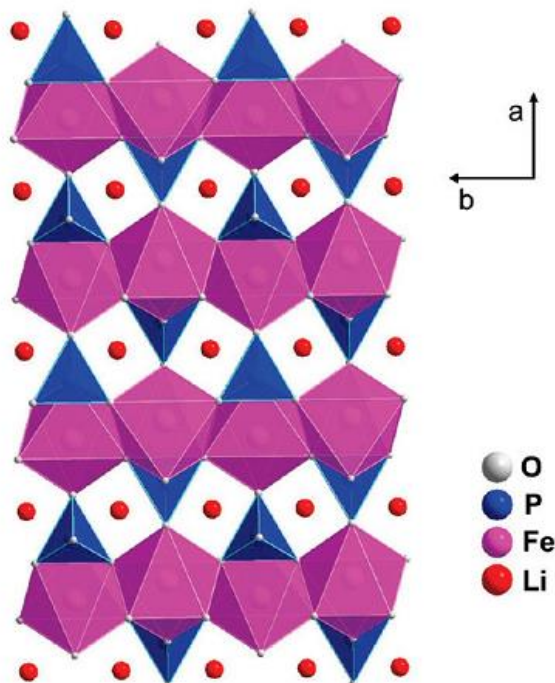


Figure 1.6. Olivine structure of LiFePO₄ showing Li⁺ in the 1D channels [Adapted from J. B. Goodenough, Y. Kim, Chem. Mater., 22 (2010) 587-603, Copyright ACS publications (2014)].

The olivine LiMnPO₄ is isostructural with LiFePO₄ and has a similar theoretical capacity (~ 170 mAh g⁻¹). The flat charge-discharge plateau at V_{OC} of about ~ 4.1 V results in a very high energy density and makes it an attractive candidate for EV applications. Bulk LiMnPO₄ exhibits a very low electrical conductivity and structural distortion upon oxidation to MnPO₄ hinder ionic transport. This problem was mitigated by reducing the particle size to improve the diffusion process and coating the particles with carbon to improve surface conduction. It was shown that by substitution of small amounts of Fe in place of Mn in LiMn_{1-x}Fe_xPO₄, improves capacity and cycle life, significantly[43].

LiCoPO_4 and LiNiPO_4 have very high electrode potentials (4.8 and 5.1 V *versus* Li/Li^+ , respectively), but their electrochemical performances are poor due to electrolyte decomposition at such high voltages.

Silicates

The LiMPO_4 based materials suffer from a major shortcoming, as their theoretical specific capacity is limited to 170 mAh g^{-1} , which corresponds to one electron (1 Li^+) reaction per formula unit. Contrasting this, lithium orthosilicates such as Li_2MSiO_4 ($\text{M} = \text{Mn, Fe, Co}$) are safe and their theoretical specific capacity of $\sim 330 \text{ mAh g}^{-1}$ corresponds to 2 Li^+ and 166 mAh g^{-1} for 1 Li^+ per formula unit. These silicates are quasi layered structures and crystallize in various polymorphs, all of which are structurally similar to $\beta\text{-Li}_3\text{PO}_4$ or $\gamma\text{-Li}_3\text{PO}_4$, where all the cations occupy the tetrahedral sites. The transition metal and the silicate tetrahedral with corner sharing form a layered structure in which a 2-D zigzagging diffusion pathway is available for Li-ion to intercalate and diffuse (Figure 1.7)[44]. Synthesis of phase pure form of silicate based materials is very difficult and moreover these materials are intrinsically poor conductors and the Li^+ diffusion is also slower than LiMPO_4 . It was hypothesized that with a carbon coating and by confining its particle size to nano-dimensional, the intrinsic low conductivity of silicate materials could be overcome. Nyten et al., first synthesized the pure phase of $\text{Li}_2\text{FeSiO}_4$ in 2005[45]. The author observed that after carbon coating with a resorcinol-formaldehyde gel, it delivered a reversible capacity of 165 mAh g^{-1} [45].

$\text{Li}_2\text{MnSiO}_4$ is viewed as an attractive cathode material, in terms of energy density and the possibility of expanding a >1 -electron redox process since the higher manganese oxidation state Mn^{4+} is more accessible than Fe^{4+} . Domniko et al., first

synthesized $\text{Li}_2\text{MnSiO}_4$ by modified Pechini sol-gel synthesis route in 2005 and obtained a V_{OC} of ~ 4.1 V *versus* Li/Li^+ for this material[46]. $\text{Li}_2\text{MnSiO}_4$ shows an orthorhombic crystal structure that exists in three different polymorphs. Many of the electrochemical studies on $\text{Li}_2\text{MnSiO}_4$, showed a gradual fade in capacity with increase in cycle number. Amorphization of the silicate material and Jahn-Teller distortion of Mn^{3+} are the main causes for gradual capacity fading with cycling. By preparing solid solutions of $\text{Li}_2[\text{MnFe}]\text{SiO}_4$ in order to stabilize the Mn^{3+} in the tetrahedral site, good reversibility could be obtained[47].

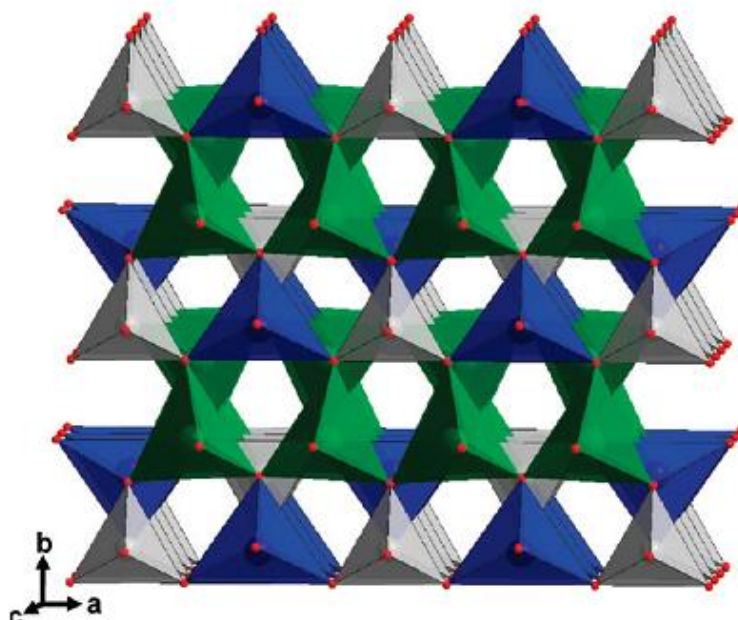


Figure 1.7. Structural representation of $\text{Li}_2\text{FeSiO}_4$. The irons in tetrahedral sites are shown in blue, the lithium tetrahedra in green, and the silicate tetrahedra in gray [Adapted from B. L. Ellis, K. T. Lee, L. F. Nazar, *Chem. Mater.*, 22 (2010) 691-714, Copyright ACS publications (2014)].

1.3.4. Anode materials

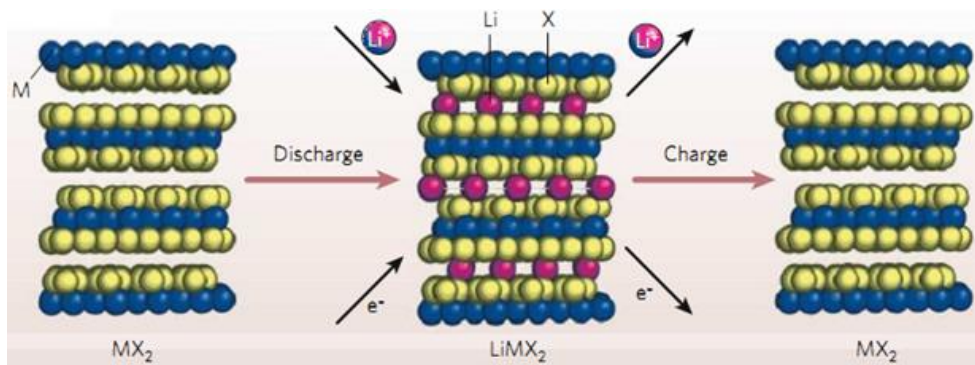
Before Sony Co. introduced LIBs, using graphite as the anode and LiCoO_2 as the cathode, Li metal was used as an anode. Pure Li metal, due to a very high reduction potential and light weight, can exhibit a very high specific capacity and specific energy. The use of Li metal however, posed serious safety issues. The high activity of Li causes the formation of dendrites, which in turn, leads to internal short circuit. Another limitation of Li, is that at very low voltages, the electrolyte undergoes decomposition, to form a SEI layer, on the surface of lithium electrode which leads an irreversible capacity loss during the first few cycles. For safety reasons, graphite is used as an anode, for commercial applications. In graphite, Li can undergo intercalation up to LiC_6 with a reversible capacity of 372 mAh g^{-1} [5]. The main advantage of the graphite is that the V_{OC} is $\sim 0.25 \text{ V}$ versus Li/Li^+ , which is very low and when a cell is fabricated with a suitable cathode, can deliver a high cell voltage. There have been many reports on the carbon based anodes such as hard, soft carbons, carbon nanotubes (CNTs) and graphene. The low theoretical specific capacity of graphite (370 mAh g^{-1}) and the low V_{OC} , limit its use in large scale applications like EVs. The intercalation potential of Li^+ in graphite is very close to lithium metal deposition, during charging, at very high current density or current rate. Lithium metal deposits on the graphite electrode in the form of dendrites and as a result, cell will short. Other drawback is that solvent co-intercalation along with lithium during charging results in exfoliation of graphite layers which manifest in rapid capacity fading with cycle number. Other alternates to graphite are intermetallic compounds, metal-oxides and chalcogenides.

The key requirements for anode materials to be successfully used in LiB applications are summarized here.

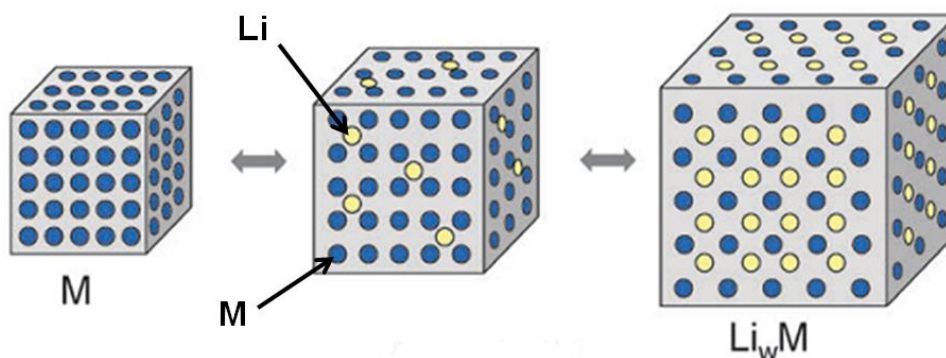
- An ideal anode must contain elements or compounds with low atomic or formula weights, have low density, accommodate fairly large amounts of Li^+ per formula unit, be cyclable, to yield large, stable, and reversible gravimetric (mAh g^{-1}) and volumetric (mAh cm^{-3}) capacities.
- An ideal anode material must show a potential as close to that of Li metal as possible and must not show large variations in the potential with changes in the Li^+ content.
- It must not be soluble in the solvents of the electrolyte and must not chemically react with the salt or solvents of the electrolyte.
- An ideal anode must possess good electronic and Li^+ ionic conductivity (mixed conduction) so that the electrode will offer small impedance for current pick-up and for the movement of the Li-ions within the active material.
- It must be cheap and environmentally benign.

Most of the research work on anode materials in LIBs is based on three different mechanisms (shown in Figure 1.8.). These are: (i) Intercalation/deintercalation, (ii) alloy/dealloy and (iii) conversion-based mechanisms. Some of the conventional and latest anode materials are briefly discussed in the sections below.

Intercalation/deintercalation mechanism:



Alloying/dealloying mechanism:



Conversion mechanism:

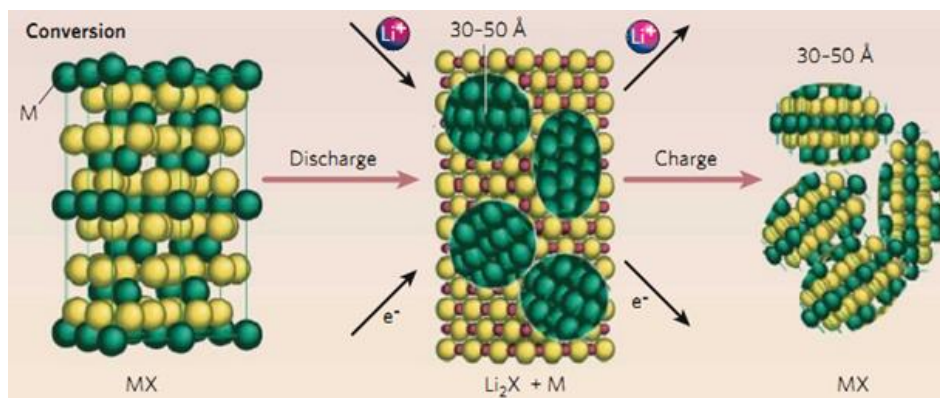


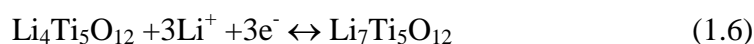
Figure 1.8. Schematic representation of different reaction mechanisms observed during charge-discharge in Li-ion battery anodes [Adapted from M. Armand and J.M. Tarascon, *Nature*, 45 (2008) 652-657. M. Rosa Palacin, *Chem. Soc. Rev.*, 38 (2009) 2565-2575, Copyright RSC publications (2014)]

1.3.4.1. Intercalation/deintercalation mechanism based anodes

Titanium based oxides

$\text{Li}_4\text{Ti}_5\text{O}_{12}$

Titanium oxide based materials are considered as promising alternative to graphite because of the low cost, abundance and eco-friendly nature. Through intercalation mechanism, these materials operate at a very high potential (about 1.3 to 1.8 V *versus* Li/Li⁺) and moreover the minimal SEI layer formation can offer a safe and a long life battery. In early 1990s, Dahn, Thackeray and Ohzuki et al., studied the semiconducting Lithium titanium oxide (LTO) with a cubic spinel structure $\text{Li}_4\text{Ti}_5\text{O}_{12}$ [48-50]. The formula of $\text{Li}_4\text{Ti}_5\text{O}_{12}$ can also be expressed as $\text{Li}_{4/3}\text{Ti}_{5/3}\text{O}_4$ or in the spinel form (Li[Li_{1/3}Ti_{5/3}]O₄). The crystal structure consists of a cubic close packed oxygen array in which Li-ion occupy both the tetrahedral (8a) and octahedral (16c, 16d) voids, while Ti ions occupy a part of the Li-ion sites in the octahedral voids of a cubic unit cell with space group Fd3m. Each LTO can accommodate a maximum of 3 lithiums, which limit the theoretical specific capacity to about 170 mAh g⁻¹ at an insertion potential of ~ 1.55 V *versus* Li/Li⁺. The lithium ion insertion into the 3D network of [Li_{1/3}Ti_{5/3}]O₂ is very fast and it is a biphasic reaction which results a flat voltage plateau. The lithium intercalation reaction into the LTO is based on the following equation.

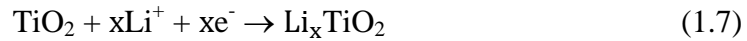


A negligible volume change ~ 0.2 % was observed between the two end members of $\text{Li}_4\text{Ti}_5\text{O}_{12}$ and $\text{Li}_7\text{Ti}_5\text{O}_{12}$, which indicated that it is a zero strain material and as a result, the material could perform an excellent cycling stability. However, the $\text{Li}_4\text{Ti}_5\text{O}_{12}$ material is inherently insulating due to the empty Ti 3d states with a band

energy of about 2 eV, which adversely affects its high rate performance[51,52]. There have been several reports on this material, by making nano size particles or a variety of nanostructured forms and carbon coating to achieve improved rate capability[53].

TiO₂ polymorphs

TiO₂ exists in different polymorphs such as anatase, rutile, brookite, TiO₂-B (bronze), TiO₂-R (ramsdellite), TiO₂-H (hollandite), TiO₂-II (columbite), and TiO₂-III (baddeleyite). Among all, the electrochemical performance for anatase, rutile and TiO₂-B, have been reported thoroughly[54]. The lithium insertion in these materials can be expressed shown in following equation



All the TiO₂ polymorphs follow the same equation and the value of x varies, depending on the polymorph, morphology and the size of particles.

Rutile TiO₂

The thermodynamically stable form of TiO₂ is rutile TiO₂, and upon heating or mechanical milling the anatase form, it can be converted into the rutile phase. The rutile form has a tetragonal structure (a = b = 4.593 Å, c = 2.96 Å, cell volume V = 62.8 Å³) which is made up of TiO₆ octahedra. These octahedra share edges to form single chains, extending along the c-axis, thus resulting in a (1 × 1) tunnel structure (Figure 1.9a). The Li-ions occupy these tunnels during intercalation. In general, the bulk form of the rutile phase shows an almost negligible amount of lithium storage i.e., < 0.1 mol of lithium per FU. However, the Li⁺ storage in rutile TiO₂ was further improved by using nanostructured TiO₂, to 0.5 lithium per FU, when cycled between 1-3 V *versus* Li/Li⁺[54].

Anatase TiO₂

Among various forms of TiO₂, the anatase form is highly suitable for Li-ion intercalation. The crystal structure of anatase (Figure 1.9b) will adopt a body centered tetragonal and the Ti ions are occupied in octahedral coordination and these TiO₆ octahedra are edge shared to form a 3D network[55]. The Li-ion will undergo intercalation-deintercalation through the octahedral voids via equation 1.7 and the charge neutrality is maintained by the reduction of Ti⁴⁺ to Ti³⁺. In bulk anatase, the lithium ion insertion occurs in a biphasic reaction which results in a flat charge-discharge plateau at 1.7 V *versus* Li/Li⁺ with an extended cycle. A maximum of 0.5 Li⁺ can insert/deinsert in bulk anatase TiO₂, by decreasing the particle size to a nano-dimensions (< 100 nm) ~ 0.8 Li insertion/deinsertion has been observed. The Li-interaction with the nanostructures appears to deviate from the two phase equilibrium phenomenon in the bulk materials, but behaving more like solid solution[56]. However, these materials are inherently insulating property which seriously hinders its high rate performance. There have been several reports on this material, by making nano size particles or variety of nanostructured form and carbon coating could improve the rate capability.

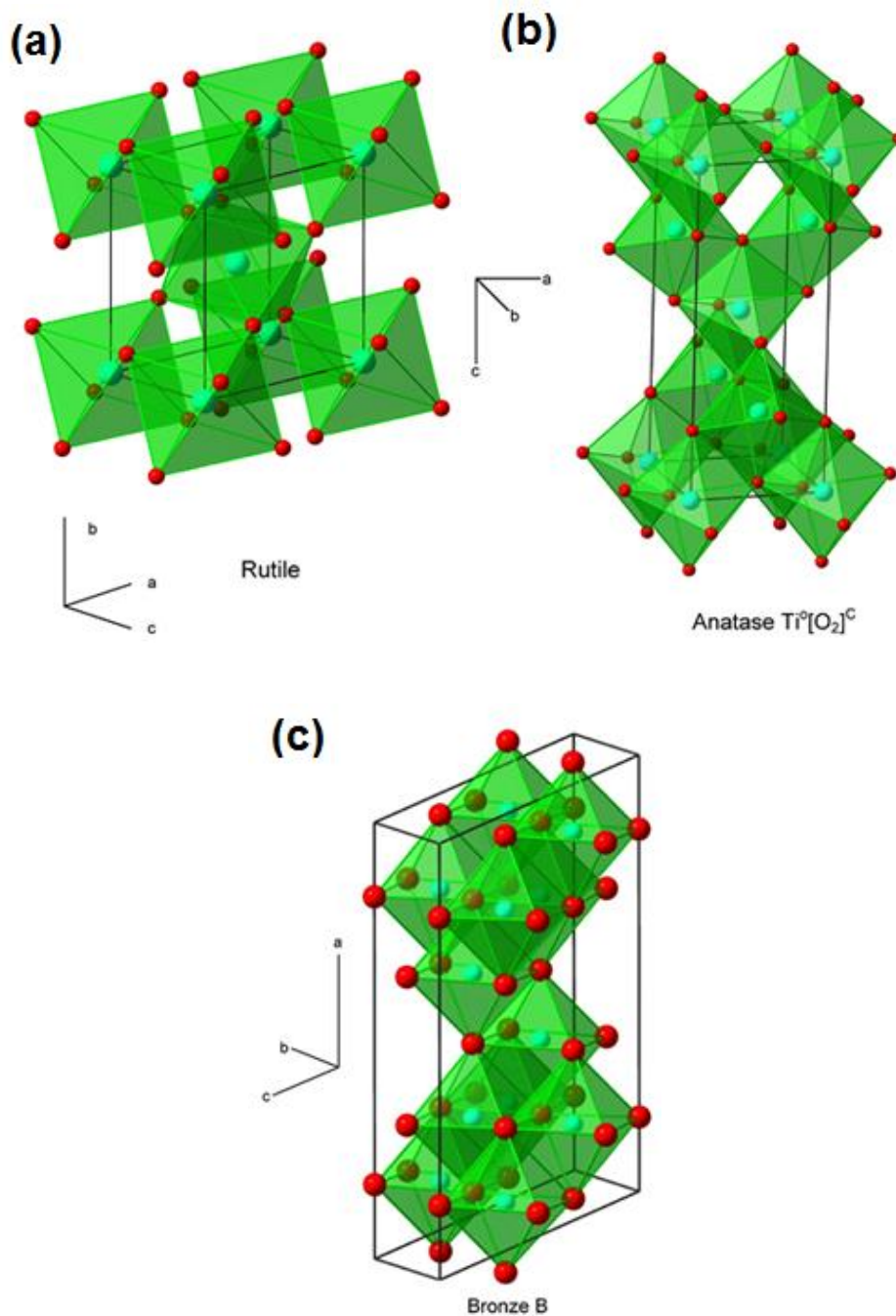


Figure 1.9. Crystallographic representation of (a) rutile, (b) anatase and, (c) bronze (B) TiO₂. Blue and red spheres are Ti and O atoms respectively. The arrangement of TiO₆ octahedra and outline of the unit cell are shown for each polymorph [Adapted from Z. Yang, D. Choi, S. Kerisit, K. M. Rosso, D. Wang, J. Zhang, G. Graff, J. Liu, *J. Power Sources* 192 (2009) 588-598, Copyright Elsevier publications (2014)]

TiO₂-B

Among all titanium based oxides, TiO₂-B (bronze), due to its very high specific capacity and low voltage has gained enormous research interest. The crystal structure of TiO₂-B is monoclinic, composed of edge and corner sharing TiO₆ octahedra (Figure 1.9c). One of its most appealing structural features is the characteristic parallel channels running along the [010] orientation. Such a unique feature has been shown to be favorable for the incorporation and diffusion of Li-ions in the channels theoretically and experimentally, which is important for its use as an anode in LIBs. DFT studies showed that the [010] orientation is the preferable direction for Li⁺-ion mobility[57]. The Li-ion storage kinetics in TiO₂-B is mainly governed by two factors i.e., (i) a pseudo-capacitive faradic process, and (ii) a diffusion-limited solid-state reaction. These two factors are further dependent on microstructures of TiO₂-B materials[58]. Therefore, in order to obtain facile Li-ion diffusion pathways and a high charge storage capacity, morphology tailoring and structural design play a key role.

1.3.4.2. Alloying-dealloying mechanism based anodes

The theoretical specific capacity of the insertion/extraction mechanism based anodes is very low and moreover, the very high voltage profiles of these Titanium based anodes minimize the overall cell voltage and as well as the specific energy. An alternate to the insertion materials are the Li-alloy based materials which can offer a very high specific energies and energy densities. Dey et al., in 1971, first demonstrated that lithium can form alloys with several metals in an organic electrolyte at room temperature and this opened up new avenues in LIBs[59]. During the last a few decades, the Li-alloying reactions with metallic or

intermetallic elements such as Si, Sn, Sb, Bi, Pb, Al and As etc. has been studied. Lithium can form alloys with these elements, and the alloys can deliver a very high specific capacity[60]. However, these alloy based materials experience a huge volume variation during cycling, and as a result, the capacities decline rapidly. The volume expansion values, theoretical specific capacity, and some other properties of some of the most widely studied alloy based materials such as Si, Sn and Sb are shown below in Table 1.1.

Table 1.1.: Capacities and volume changes of different alloy based materials.

Starting material	C	Al	Si	Sn	Sb	Bi
Lithiated phase	LiC ₆	LiAl	Li _{4.4} Si	Li _{4.4} Sn	Li ₃ Sb	Li ₃ Bi
Theoretical Specific capacity (mAh g ⁻¹)	372	993	4,200	994	660	385
Density (g cm ⁻³)	2.25	2.7	2.33	7.29	6.7	9.78
Theoretical volumetric capacity (mAh cm ⁻³)	837	2681	9786	7246	4422	3765
Volume changes (%)	12	238	400	300	200	115

Silicon based anodes

Silicon can form an alloy with lithium to yield a Li_{4.4}Si alloy, which can offer a very high theoretical specific capacity of ~ 4,200 mAh g⁻¹ which is even higher than lithium metal. Si is very cheap, readily available, ecofriendly and it's very high specific capacity and energy density makes it an attractive anode for advanced LiBs. The huge volume expansion ~ 400% during lithium insertion and extraction cause cracking and pulverization of active particles and the surrounding matrix, thus leading to the detachment of some alloy particles from the conductive carbon or current collector. This in turn, results in a rapid capacity decline with cycling. This

also accompanied by the formation of an unstable SEI layer on the electrode surface, which is also responsible for the irreversible capacity loss. According to the Li-Si phase diagram, four crystalline Li-Si phases exist: $\text{Li}_{12}\text{Si}_7$, Li_7Si_3 , $\text{Li}_{13}\text{Si}_4$, and $\text{Li}_{22}\text{Si}_5$ [61]. Peaks in the polarization curve, during lithiation of Silicon, are frequently assigned to these phases, and some evidence exists to indicate that, these phases may be formed during electrochemical cycling. In many cases, a single long voltage plateau is observed near 100 mV (*versus* Li/Li^+) during cathodic polarization, suggesting a continual lithiation of an amorphous alloy rather than sequential formation of distinct lithium silicide phases[62,63]. When silicon electrodes are charged to below 50 mV (*versus* Li/Li^+), a peak in the differential capacity curve due to the formation of a crystalline $\text{Li}_{15}\text{Si}_4$ phase was observed in previous studies[64,65].

Different strategies have been adopted in the past for increasing the cycling stability by allowing volume variation. For example, composites of Si with an inactive matrix or an active matrix showed an improved cycling performance. The primary purpose of dispersing active alloy particles within a composite matrix (filler) is to use the host matrix to buffer the large volume change of the active particles so that the electrode integrity and the electronic contact between the active particles and conductive phase can be maintained. In Si-active metal matrix composites the active metal also participates in the electrochemical response. Metals like Ag, Mg and Ca etc. also form alloys with lithium and the intermetallic compounds of Si with these metals have been explored by several research groups. Anani and Huggins reported that Li ternary silicides (Li–Metal–Si) can have a more favorable voltage profile and a higher reversible capacity than Li–Si binary alloys on

the basis of thermodynamic calculations[66,67]. Kim et al., Moriga et al., and Roberts et al., reported the electrochemical mechanisms of Mg_2Si [68-70]. In another report, a Ca_2Si alloy was also studied but this electrode material showed rapid capacity fade. On the other hand, in Si-metal-inactive matrix based composites, the matrix element does not exhibit any electrochemical response. Wang et al., examined the electrochemical properties of NiSi and FeSi[71]. In these alloys, Ni and Fe do not participate in any electrochemical reaction; instead these elements act as buffer matrices. These electrodes showed superior electrochemical response than pristine Si but capacity fading was still observed, due to large volume changes. Another type of Si-inactive matrix composites are composites of Si with metallic compounds such as TiN and TiB_2 buffer matrix. Kumta and co-workers synthesized composites of amorphous Si with crystalline TiN and TiB_2 using high energy mechanical milling. Authors obtained reversible capacities of 300–400 mAh g^{-1} , which remained stable for 15-20 charge-discharge cycles[72,73].

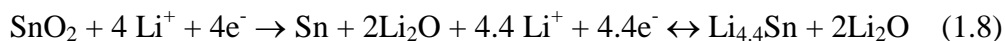
Other interesting strategy to accommodate the volume variation involves the preparation of various nanostructures or porous structures such as nanowires, rods, hollow tubes and nanosheets and their composites with carbonaceous materials such as graphite, acetylene black, CNTs, CNFs and graphene etc.[74-78]. Nanostructured materials are highly porous and can have a very high surface area; the space between each nanoparticle can accommodate the volume expansion and contraction without undergoing any mechanical failure. Moreover, by coating these nanostructures with carbonaceous materials, further improvement in electronic conductivity is achieved. Carbon materials based coating also assist in the inhibiting side reactions between electrode and electrolyte and as a result, the irreversible capacity losses can be

minimized. There are several reports on a variety of nanostructured materials wherein appreciable Li-ion storage performance were achieved.

Tin based alloys

Electrochemical lithiation of Sn at elevated temperatures, carried out by Wen and Huggins showed that Sn reacted with lithium to yield seven different Li-Sn line phases within the Li-Sn phase diagram: Li_2Sn_5 , LiSn , Li_7Sn_3 , Li_5Sn_2 , $\text{Li}_{13}\text{Sn}_5$, Li_7Sn_2 , and $\text{Li}_{22}\text{Sn}_5$ [61]. In the end member, $\text{Li}_{22}\text{Sn}_5$, each Sn can react with a maximum of 4.4 Li^+ , which yields a maximum theoretical specific capacity of 994 mAh g^{-1} with a working potential about 0.5 V *versus* Li/Li^+ . Although Sn has a lower gravimetric capacity than Si and metallic lithium, Sn is an attractive anode material due to its volumetric capacity of about 2000 mAh cm^{-3} , which is higher than that of even metallic Li and is comparable to Si. However, like other Li-alloying materials, its commercial use is limited by its comparatively poor capacity retention due to mechanical degradation such as cracking and pulverization caused by large volume changes which occur in the co-existing Li-Sn intermetallic phase region, during cycling. This behavior was observed by Dey in an early publication pertaining to Li-alloying metals in 1971[59]. *In-situ* atomic force microscopy and *in-situ* stress measurements studies on electroplated Sn film showed morphological changes due to the fact that, the Sn film underwent a stress transition during cycling and the induced stresses were released in the form of cracks in the electrode, which were accompanied by a drastic capacity fade[79,80]. In a previous report by Fuji et al., on an amorphous tin-based composite oxide, a reversible capacity of more than twice of that of graphite was obtained[81,82]. Much research in the past has been devoted to the development of high capacity Sn-based oxide materials, including

SnO₂, SnO, and Sn-based composite oxides. The reaction mechanisms of Sn-based oxide materials are shown below.



During the initial lithiation, the Sn-O bonding is irreversibly dissociated into Li₂O and metallic Sn, which is responsible for the reversible alloying/dealloying reaction. The Sn-based oxide anode showed an improved capacity retention compared to metallic Sn, which was mainly attributed to the resulting composite structure consisting of electrochemically active Sn and an inactive lithium phase such as Li₂O. Li₂O served as a matrix, wherein the reduced Sn phase was finely dispersed and thereby prevented the aggregation of Sn atoms. However, upon repeated cycles, the Sn phases surrounded by the Li₂O matrix, arising from the delithiation of the Li-Sn alloy phase, showed a tendency to aggregate and form large particles which were directly observed by HRTEM [83,84]. This coarsening of Sn particles after prolonged cycles caused a large volume change and destruction of the Li₂O matrix phase, which reduced the capacity retention capability of the Sn oxide anode. Control of the cut-off voltage for delithiation was highly effective in suppressing the coarsening of Sn particles during delithiation from a Li-Sn intermetallic phase to Sn thereby improving the cycling stability. Other strategies involve introduction of an inactive matrix in tin oxide, the use of amorphous Sn-based glass materials, and downsizing the Sn oxide particles to nanoscale and preparing various nanostructures along with carbon coatings. However, the irreversible capacity loss during the first discharge, due to Li₂O formation poses a major hurdle for the commercialization of Sn based oxides. Other approaches

include: Sn–M alloys where M can be an active phase or inactive phase. In the Sn-active metal alloys, $\text{Sn}_x\text{Sb}_{1-x}$ gained an enormous interest due to its high capacity retention for prolonged cycles[85]. The cycling stability is due to the fact that expansion of the more reactive phase in the composite can be buffered by a less active matrix. Thus, the extent of mechanical degradation in the overall electrode material is small. In the past, Sn-inactive metal matrix composites such as Cu_6Sn_5 and Sn_2Fe have been explored[86,87]. In 2005, Sony announced the commercialization of an amorphous Sn-Co-C and its composite with Ti as anode for the first time[88]. In this material, Co functioned as the inactive buffer matrix and carbon served as an inert and conductive moiety and the role of Ti was not disclosed. Despite its remarkable performance, and successful commercialization of this amorphous Sn–Co–C composite anodes, it was observed that Co was very expensive and therefore, for economic reasons, it was required to be replaced with cheaper metals. As an alternate to Co, many other composite alloys were also explored such as Sn-Mn-C, Sn-Fe-C and Sn-Co-Fe-C etc.[89].

1.3.4.3. Conversion mechanism based anodes

Poizot et al., showed that transition metal oxides can react with lithium reversibly and convert into Li_2O and metal (M), and this reaction, is called a conversion reaction[90]. The gravimetric energy density of these materials is almost more than three times that of graphite and therefore, they are considered to be promising anodes for LIBs. The conversion mechanism can be generalized, as shown below in the following reaction.



In 1.10, M = transition metal ion i.e., Co, Ni, Fe, Cu, Mo etc., X = anion i.e., O, S, N, F and P etc., and n = formal oxidation state of X.

The key to the reversibility of the conversion reaction lies in the formation, upon complete reduction of the metal oxides, of nanoparticles that, owing to the large amount of interfacial surface, are very active towards the decomposition of the matrix of the lithium binary compound (Li_nX), in which they are embedded, when a reverse polarization is applied. The nanometric character of the metal particles was shown to be maintained even after several reduction-oxidation cycles. The typical charge-discharge profiles for the conversion mechanism based reactions and various phase formations are shown in Figure 1.10[91]. The actual potential at which conversion reaction occurs depends on the covalence of the M-X bond, if the electronegativity of X is more and more will be the potential at which conversion reaction occurs. Despite a very high energy density, these conversion based materials have not been commercialized yet due to the following reasons. During the first discharge, the huge structural reorganization causes a large volume change that leads to detachment from the current collector, isolation of particles and pulverization which leads to rapid capacity fade. The large voltage hysteresis between the discharge and charge steps and the large Coulombic inefficiency during initial cycles due to electrolyte decomposition and formation of SEI layer, also contribute to the capacity fade.

The strategies to improve the cycling stability are similar to the ones employed in alloy-based electrodes. These are: modifying the electrode, by forming nanocomposites with carbon or by increasing the amount of polymeric binder. The carbon coating techniques are advantageous. Carbon is active at low voltages at

which some of the conversion reactions occur, and thus it partially compensates the decrease in capacity associated with the dilution of the active phase. There are many metal oxides, sulfides, phosphides and fluorides such as CoO, NiO, Fe₃O₄, CuS, MnO₂, Cr₃O₄, FeP, FeF₃, MoO₃, FeF₂ etc. which have been explored. An excellent review by Cabana et al., provides an exclusive overview of developments in the area of conversion based anodes[91]. Another noteworthy feature, is that some of these transition metal oxides such as CoO, NiO and MoO₂ etc. exhibit capacities in excess of the theoretical limit for many cycles. The extra capacity is due to electrolyte decomposition and interfacial storage. It was proven from IR, NMR, XPS and mass spectroscopy, that during discharge, to below 1 V, a polymeric thin film forms on the surface of the metal nanoparticles which is reversible for many cycles [92]. In the second mechanism, it was proved from theoretical calculations that the Li_nX/M interface allows the storage of additional Li⁺ on lithium compound side and electrons are localized on the metallic side, which leads to charge separation[93].

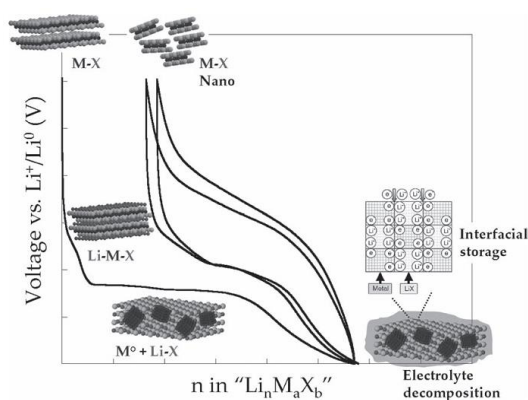


Figure 1.10. Typical voltage versus composition profile of the first two and half cycles for an electrode containing a material that reacts through a conversion reaction, measured against a lithium counter-electrode. The light grey, dark grey and black balls depict X, Li and M, respectively. The scheme of the interfacial storage mechanism [Adapted from J. Cabana, L. Monconduit, D. Larcher, M. R. Palacín, *Adv. Mater.*, 22 (2010) E170-E192, Copyright Wiley publications (2014)].

1.3.5. Electrolytes

Besides the electrodes, the electrolyte is also a key component of a battery and the electrolyte is generally a solution consisting of a salt and a solvent. There are several electrolytes comprising of inorganic salts and organic solvents, ionic liquids etc. which have been used in LIBs. The ideal electrolyte for a LIB should fulfill the following criteria.

- A high Li-ion conductivity ($\sigma_{\text{Li}^+} > 10^{-4} \text{ S cm}^{-1}$) over the battery's operational range of temperature, to minimize the cell resistance.
- Low electronic conductivity ($\sigma_e < 10^{-10} \text{ S cm}^{-1}$), so that the electrolyte is largely an ionic conductor.
- High chemical stability at ambient temperatures and at the temperature generated at high power rate.
- It should have a large electrochemical window to tolerate the high voltage difference between anode and cathode (usually $> 4 \text{ V}$).
- The electrolyte should easily retain electrode/electrolyte interphase during cycling when the electrode particles undergo large volume change.
- It should be chemically stable towards the electrodes and the electrolyte should have the ability to form a solid electrode/electrolyte interphase layer rapidly, during which the electrolyte should be kinetically stable.
- It should have a high boiling point to provide safety and prevent explosions resulting from high pressure build-up in the cell.
- It should be non-toxic and inexpensive.

A few electrolytes that are proposed for LIBs and some of the most commonly used electrolytes are shown in Table 1.2.

1.3.5.1. Electrolytes containing organic solvent

Organic carbonates such as ethylene carbonate (EC), diethyl carbonate (DEC) and dimethyl carbonates (DMC) etc. are generally used as solvents in Li-ion based electrolytes. The Li-salts can easily dissolve in these solvents. These have generally

oxidation potentials (HOMO) at ~ 4.7 V and reduction potentials at about 1 V *versus* Li/Li⁺[41]. Moreover, they are less viscous and the Li-ion can easily diffuse which results very high Li-ion conductivity. In most of the cases, EC is used as the common solvent because it can provide passivation layer or SEI layer very easily upon the decomposition of electrolyte[94]. However, the flash points of these carbonate based solvents are very low, about 30 °C, and these are highly flammable. In addition, LiPF₆, the most commonly used salt, can autocatalytically decompose into LiF and PF₅; at about 60 °C and any trace amount of water present in the electrode or solvent can cause the PF₅ to react irreversibly to form HF. (PF₅ + H₂O = PF₃O + 2HF)[95]. These side reactions lead to degradation of the battery performance and thus, can cause safety hazards. However, the autocatalytic decomposition of LiPF₆ salt can be suppressed by adding additives which lower the operating temperature.

1.3.5.2. Ionic liquid electrolytes

Room temperature ionic liquid electrolytes have several advantages when compared with organic liquids. They have a very high electrochemical voltage window, high lithium solubility, low boiling point, and they are nonflammable, nontoxic and thermally stable. Unfortunately, the Li-ion conductivity is very low due to the high viscous nature of ionic liquids. Among many ionic liquids, imidazolium-based cations are considered as most suitable candidates due to their low viscosity and a high Li-salt solubility, at room temperature. The Li-ion conductivity can be improved by adding an optimized concentration of carbonate solvents. However, below 1 V *versus* Li/Li⁺, [96] ionic liquids have a low stability additives such as EC must be added for the SEI layer formation.

1.3.5.3. Solid polymer electrolytes

There are many advantages with a solid electrolyte for it acts as separator, offers a large electrochemical potential stability window and it can also retain contact over the electrode/electrolyte interphase during modest changes of the electrode volume with the state of charge of the battery. Polymer-salt complexes such as the combination of poly(ethylene oxides) (PEOs) and lithium salt (LiPF₆ or LiAsF₆) are attractive due to good chemical stability, low-cost and nontoxic[97]. The main problem associated with these electrolytes is the poor Li-ion conductivity ($\sigma_{\text{Li}} < 10^{-5}$ S cm⁻¹) at room temperature and therefore, they are not suitable for power-battery system. The conductivity and transference number of Li-ion can be improved by the introduction of nanoparticles of ceramic oxide fillers such as Al₂O₃, TiO₂, SiO₂, or ZrO₂ in the matrix[98,99]. One of roles of the fillers is to create a more amorphous polymer matrix by inhibiting polymer chain crystallization and attracting Li-ions from its salt. The result is an enhanced σ_{Li} and Li-ion transference number, but σ_{Li} is still not comparable to that of the carbonate electrolytes.

Table 1.2.: Non-aqueous electrolytes for Li-ion batteries

Electrolytes	Examples of electrolytes	Electrochemical window (V) vs Li/Li ⁺	
		Reduction	Oxidation
Organic liquid	1M LiPF ₆ in EC:DEC (1:1)	1.3	4.5
	1M LiPF ₆ in EC:DMC (1:1)	1.37	> 5.0
Ionic liquids	1M LiTFSI in EMI-TFSI	1.0	5.3
	1M LiBF ₄ in EMI-BF ₄	0.9	5.3
Polymer	LiTFSI-P(EO/MEEGE)	< 0.0	4.7
	LiClO ₄ - PEO ₈ + 10 wt % TiO ₂	< 0.0	5

1.3.6. Objectives of current thesis

The current thesis describes about anode materials that can undergo conversion and alloy/dealloy mechanisms. These materials can offer very high capacity for example molybdenum oxide (MoO_2) and tin based oxides and sulfides (SnX_2 , $\text{X}=\text{O}$, S). With the view of unraveling the issues that are described for MoO_2 conversion and SnX_2 ($\text{X}=\text{O}$, S) alloy/dealloy based anode materials, the objectives of the current thesis are summarized as follows.

- To prepare a unique nanostructured MoO_2 /MWCNT hybrid by a hydrothermal method, assisted by an anionic surfactant and to probe Li-ion intercalation/deintercalation in the same.
- To understand the Li-ion charge storage mechanism and to study the diffusion rate of Li-ion in MoO_2 and in the MoO_2 /MWCNTs hybrid.
- To synthesize a nanocomposite of MoO_2 /Graphene using a facile single step hydrothermal process and study the Li-ion charge storage mechanism.
- To prepare SnO_2 HS hybrid nanostructures with a conducting polymer and graphene oxide (GO) for use as durable anodes in LIBs.
- To develop a template-free, one-pot hydrothermal approach for preparing SnO_2 hollow spheres (HS) with controlled HS size by using organic additives as structure directing agents.
- To prepare SnS_2 nanosheets and 3D-nanoflowers and study their electrochemical and optical properties.
- To construct a prototype full cell using SnS_2 3D nanoflowers as the anode and LiFePO_4 as the cathode and demonstrate the LIB performance.

To meet the above described objectives, various methods were employed to synthesize the MoO_2 , SnX_2 ($\text{X} = \text{O}$, S) anodes and their composites with GO, MWCNTs and poly(3,4-ethylenedioxythiophene) or PEDOT. The materials were characterized by XRD, Raman spectroscopy, XPS, UV-vis spectroscopy and electron microscopy. The Li-ion charge storage mechanisms and cycling behavior of

different composites have been elucidated by measuring electrochemical properties (cyclic voltammograms and galvanostatic charge-discharge response at different current densities), *ex-situ* XRD and impedance spectra. In **Chapter 3**, an easy single step synthesis of a MoO₂/MWCNT hybrid by a hydrothermal method is presented. AOT or sodium dioctyl sulfosuccinate was used therein: it not only served as a reducing agent for Mo salt reduction but also tailored the growth of MoO₂ nanoparticles into three-dimensional spherical shaped flower-like morphologies. In addition, AOT also aided in dispersing MWCNTs. The electrochemical characteristics of the MoO₂/MWCNT hybrid and neat MoO₂ were compared. The enhanced performance of the hybrid compared to neat MoO₂ was corroborated using *ex-situ* XRD studies on cycled electrodes. In **Chapter 4**, the influence of Graphene on Li-ion storage in a MoO₂/Graphene composite was studied. In this chapter, a non-toxic reagent, namely, citric acid along with poly(ethylene glycol) or PEG were used, respectively, to reduce GO to Graphene and the metal oxide precursor to MoO₂. In **Chapter 5**, hydrothermal synthesis of SnO₂ hollow spheres using an organic bi-functional molecule followed by formation of a hybrid electrode with GO and PEDOT is presented. While GO nanosheets served as a scaffold for entrapment of SnO₂ hollow spheres and prevented their coalescence during electrochemical cycling, the PEDOT overlayer being a robust conducting polymer, effectively inhibited the disintegration of SnO₂ HS during charge/discharge cycling and cumulatively both GO and PEDOT afforded capacity retention with cycling. In **Chapter 6**, a template-free, one-pot hydrothermal approach was developed for preparing SnO₂ HS with controlled hollow sphere size by using organic additives such as acetyl acetone or AcAc and mercaptopropionic acid or MPA as structure

directing agents. The optimization of SnO₂ HS (size and empty core dimensions) was accomplished by evaluating the Li-ion storage performance of various electrodes. In addition, the SnO₂ HS also exhibited blue light luminescence. In **Chapter 7**, a simple one-pot solvothermal route was used to synthesize SnS₂ nanosheets and hierarchical 3D flowers by using ethanol as the solvent. For the generation of SnS₂ nanosheets, urea played a significant role and when urea was replaced by TU (TU), 3D architectures of flower like shapes of SnS₂ were obtained. The role of the solvent and the proportion of urea or TU control the growth of SnS₂ nanosheets and flowers, respectively. The comparison of Li-ion storage performance of SnS₂ nanosheets and flowers electrodes as anodes were studied. In addition, the SnS₂ nanosheets and flowers were also found to be luminescent and the two architectures showed a significant difference in their luminescent properties. Overall, in this thesis, how the microstructure of different metal oxides and how the incorporation of carbon nanostructures/conducting polymer in the oxide controls the specific capacity, rate capability and durability of the electrode when used as an anode in a LIB is explained.

References

1. M. S. Whittingham, *Science*, 192 (1976) 1126-1127.
2. K. Mizushima, P. C. Jones, P. J. Wiseman, J. B. Goodenough, *Solid State Ionics*, 3-4 (1981) 171-174.
3. R. Yazami, P. Touzain, *J. Power Sources*, 9 (1983) 365-371.
4. K. Ozawa, *Solid State Ionics*, 69 (1994) 212-221.
5. M. Winter, J. O. Besenhard, M. E. Spahr, P. Novak, *Adv. Mater.*, 10 (1998) 725-763.
6. M. S. Whittingham, *Chem. Rev.*, 104 (2004) 4271-4301.
7. B. L. Ellis, K. T. Lee, L. F. Nazar, *Chem. Mater.*, 22 (2010) 691-714.

8. Z. Chen, J. R. Dahn, *Electrochim. Acta*, 49 (2004) 1079-1090.
9. I. Saadoune, C. Delmas, *J. Mater. Chem.*, 6 (1996) 193-199.
10. A. Rougier, I. Saadoune, P. Gravereau, P. Willmann, C. Delmas, *Solid State Ionics*, 90 (1996) 83-90.
11. E. Zhecheva, R. Stoyanova, *Solid State Ionics*, 66 (1993) 143-149.
12. S. K. Mishra, G. Ceder, *Phys. Rev. B*, 59 (1999) 6120-6130.
13. A. R. Armstrong, P. G. Bruce, *Nature*, 381 (1996) 499-500.
14. F. Capitaine, P. Gravereau, C. Delmas, *Solid State Ionics*, 89 (1996) 197-202.
15. G. Vitins, K. West, *J. Electrochem. Soc.*, 144 (1997) 2587-2592.
16. G. Ceder, A. Van der Ven, *Electrochim. Acta*, 45 (1999) 131-150.
17. E. Rossen, C. D. W. Jones, J. R. Dahn, *Solid State Ionics*, 57 (1992) 311-318.
18. T. Ohzuku, Y. Makimura, *Chem. Lett.*, (2001) 744-745.
19. Y. Makimura, T. Ohzuku, *J. Power Sources*, 119 (2003) 156-160.
20. K. S. Kang, Y. S. Meng, J. Breger, C. P. Grey, G. Ceder, *Science*, 311 (2006) 977-980.
21. S. C. Yin, Y. H. Rho, I. Swainson, L. F. Nazar, *Chem. Mater.*, 18 (2006) 1901-1910.
22. H. Kobayashi, Y. Arachi, S. Emura, H. Kageyama, K. Tatsumi, T. Kamiyama, *J. Power Sources*, 146 (2005) 640-644.
23. P. S. Whitfield, I. J. Davidson, L. M. D. Cranswick, I. P. Swainson, P. W. Stephens, *Solid State Ionics*, 176 (2005) 463-471.
24. M. M. Thackeray, C. S. Johnson, J. T. Vaughey, N. Li, S. A. Hackney, *J. Mater. Chem.*, 15 (2005) 2257-2267.
25. M. H. Rossouw, M. M. Thackeray, *Mater. Res. Bull.* 26 (1991) 463-473.
26. M. H. Rossouw, D. C. Liles, M. M. Thackeray, *J. Solid State Chem.*, 104 (1993) 464-466.
27. M. M. Thackeray, W. I. F. David, P. G. Bruce, J. B. Goodenough, *Mater. Res. Bull.* 18 (1983) 461-472.
28. J. M. Tarascon, D. Guyomard, *Solid State Ionics*, 69 (1994) 222-237.
29. J. M. Tarascon, W. R. McKinnon, F. Coowar, T. N. Bowmer, G. Amatucci, D. J. Guyomard, *J. Electrochem. Soc.*, 141 (1994) 1421-1431.

30. M. Yonemura, A. Yamada, H. Kobayashi, M. Tabuchi, T. Kamiyama, Y. Kawamoto, R. Kanno, *J. Mater. Chem.*, 14 (2004) 1948-1958.
31. M. M. Thackeray, Y. Shao Horn, A. J. Kahaian, K. D. Kepler, J. T. Vaughey, S. A. Hackney, *Electrochem. Solid-State Lett.*, 1 (1998) 7-9.
32. D. H. Jang, Y. J. Shin, S. M. Oh, *J. Electrochem. Soc.*, 143 (1996) 2204-2211.
33. H. Huang, C. A. Vincent, P. G. Bruce, *J. Electrochem. Soc.*, 146 (1999) 3649-3654.
34. Y. J. Shin, A. Manthiram, *J. Electrochem. Soc.*, 151 (2004) A204-A208.
35. B. H. Deng, H. Nakamura, M. Yoshio, *J. Power Sources*, 180 (2008) 864-868.
36. J. S. Gnanaraj, V. G. Pol, A. Gedanken, D. Aurbach, *Electrochem. Commun.*, 5 (2003) 940-945
37. F. Jiao, J. L. Bao, A. H. Hill, P. G. Bruce, *Angew. Chem., Int. Ed.*, 47 (2008) 9711-9716.
38. D. K. Kim, P. Muralidharan, H. W. Lee, R. Ruffo, Y. Yang, C. K. Chan, H. Peng, R. A. Huggins, Y. Cui, *Nano Lett.*, 8 (2008) 3948-3952.
39. S. M. Bak, K. W. Nam, C. W. Lee, K. H. Kim, H. C. Jung, X. Q. Yang, K. B. Kim, *J. Mater. Chem.*, 21 (2011) 17309-17315.
40. C. Arbizzani, M. Mastragostino, M. Rossi, *Electrochem. Commun.*, 4 (2002) 545-549.
41. J. B. Goodenough, Y. Kim, *Chem. Mater.*, 22 (2010) 587-603.
42. A. K. Padhi, K. S. Nanjundaswamy, J. B. Goodenough, *J. Electrochem. Soc.*, 144 (1997) 1188-1194.
43. H. Wang, Y. Yang, Y. Liang, L. F. Cui, H. S. Casalongue, Y. Li, G. Hong, Y. Cui, H. Dai, *Angew. Chem. Int. Ed.*, 50 (2011) 1-6.
44. B. Xu, D. Qian, Z. Wang, Y. S. Meng, *Materials Science and Engineering R*, 73 (2012) 51-65
45. A. Nyten, A. Abouimrane, M. Armand, T. Gustafsson, J. O. Thomas, *Electrochem. Commun.*, 7 (2005) 156-160.
46. R. Dominko, M. Bele, M. Gaberscek, A. Meden, M. Remskar, J. Jamnik, *Electrochem. Commun.*, 8 (2006) 217-222.
47. Z. L. Gong, Y. X. Li, Y. Yang, *Electrochem. Solid-State Lett.*, 9 (2006) A542-A544.

48. K. K. Colbow, J. R. Dahn, R. R. Haering, *J. Power Sources*, 26 (1989) 397-402.
49. E. Ferg, R. J. Gummov, A. de Kock, M. M. Thackeray, *J. Electrochem. Soc.*, 141 (1994) L147-L150.
50. T. Ohzuku, A. Ueda, N. Yamamoto, *J. Electrochem. Soc.*, 142 (1995) 1431-1435.
51. C. Y. Ouyang, Z. Y. Zhong, M. S. Lei, *Electrochem. Commun.*, 9 (2007) 1107-1112.
52. T. Brousse, P. Fragnaud, R. Marchand, D. M. Schleich, O. Bohnke, K. West, *J. Power Sources*, 68 (1997) 412-415.
53. G. N. Zhu, Y. G. Wang, Y. Y. Xia, *Energy Environ. Sci.*, 5 (2012) 6652-6667.
54. D. Wang, D. Choi, Z. Yang, V. V. Viswanathan, Z. Nie, C. Wang, Y. Song, J. Zhang, J. Liu, *Chem. Mater.*, 20 (2008) 3435-3442.
55. Z. Yang, D. Choi, S. Kerisit, K. M. Rosso, D. Wang, J. Zhang, G. Graff, J. Liu, *J. Power Sources*, 192 (2009) 588-598.
56. M. Wagemaker, W. J. H. Borghols, F. M. Mulder, *J. Am. Chem. Soc.*, 129 (2007) 4323-4327.
57. C. Arrouvel, S. C. Parker, M. S. Islam, *Chem. Mater.*, 21 (2009) 4778-4783.
58. G. Armstrong, A. R. Armstrong, J. Canales, P. G. Bruce, *Electrochem. Solid-State Lett.*, 9 (2006) A139-A143.
59. A. N. Dey, *J. Electrochem. Soc.*, 118 (1971) 1547-1549.
60. G. R. Goward, N. J. Taylor, D. C. S. Souza, L. F. Nazar, *J. Alloys Compd.*, 329 (2001) 82-91.
61. B. A. Boukamp, G. C. Lesh, R. A. Huggins, *J. Electrochem. Soc.*, 128 (1981) 725-728.
62. P. Limthongkul, Y. I. Jang, N. J. Dudney, Y. M. Chiang, *Acta Mater.*, 51 (2003) 1103-1113.
63. A. Netz, R. A. Huggins, W. Weppner, *J. Power Sources*, 119-121 (2003) 95-100.
64. T. D. Hatchard, J. R. Dahn, *J. Electrochem. Soc.*, 151 (2004) A838-A842.
65. J. Li, J. R. Dahn, *J. Electrochem. Soc.*, 154 (2007) A156-A161.
66. A. Anani, R. A. Huggins, *J. Power Sources*, 38 (1992) 351-362.
67. A. Anani, R. A. Huggins, *J. Power Sources*, 38 (1992) 363-372.

68. H. Kim, J. Choi, H. J. Sohn, T. Kang, *J. Electrochem. Soc.*, 146 (1999) 4401-4405.
69. T. Moriga, K. Watanabe, D. Tsuji, S. Massaki, I. Nakabayashi, *J. Solid State Chem.*, 153 (2000) 386-390.
70. G. A. Roberts, E. J. Cairns, J. A. Reimer, *J. Power Sources*, 110 (2002) 424-429.
71. G. X. Wang, L. Sun, D. H. Bradhurst, S. Zhong, S. X. Dou, H. K. Liu, *J. Power Sources*, 88 (2000) 278-281.
72. I. S. Kim, P. N. Kumta, G. E. Blomgren, *Electrochem. Solid-State Lett.*, 3 (2000) 493-496.
73. I. S. Kim, G. E. Blomgren, P. N. Kumta, *Electrochem. Solid-State Lett.*, 6 (2003) A157-A161.
74. H. Wu, G. Chan, J. W. Choi, I. Ryu, Y. Yao, M. T. McDowell, S. W. Lee, A. Jackson, Y. Yang, L. Hu, Y. Cui, *Nature Nanotechnology*, 7 (2012) 310-315.
75. H. Zhang, P. V. Braun, *Nano Lett.*, 12 (2012) 2778-2783
76. Y. Yao, N. Liu, M. T. McDowell, M. Pasta, Y. Cui, *Energy Environ. Sci.*, 5 (2012) 7927-7930
77. N. Liu, H. Wu, M. T. McDowell, Y. Yao, C. Wang, Y. Cui, *Nano Lett.*, 12 (2012) 3315-3321
78. K. Evanoff, J. Benson, M. Schauer, I. Kovalenko, D. Lashmore, W. J. Ready, G. Yushin, *ACS Nano*, 6 (2012) 9837-9845.
79. L. Y. Beaulieu, T. D. Hatchard, A. Bonakdarpour, M. D. Fleischauer, J. R. Dahn, *J. Electrochem. Soc.*, 150 (2003) A1457-A1464.
80. H. Mukaibo, T. Momma, Y. S. Diamand, T. Osaka, M. Kodaira, *Electrochem. Solid-State Lett.*, 10 (2007) A70-A73.
81. I. A. Courtney, J. R. Dahn, *J. Electrochem. Soc.*, 144 (1997) 2045-2052.
82. I. A. Courtney, J. R. Dahn, *J. Electrochem. Soc.*, 144 (1997) 2943-2948.
83. I. A. Courtney, W. R. McKinnon, J. R. Dahn, *J. Electrochem. Soc.*, 146 (1999) 59-68.
84. T. Brousse, R. Retoux, U. Herterich, D. M. Schleich, *J. Electrochem. Soc.*, 145 (1998) 1-4.
85. J. Yang, M. Wachtler, M. Winter, J. O. Besenhard, *Electrochem. Solid State Lett.*, 2 (1999) 161-163.

86. O. Mao, R. A. Dunlap, J. R. Dahn, *J. Electrochem. Soc.*, 146 (1999) 405-413.
87. L. M. L. Fransson, E. Norstrom, K. Edstrom, L. Haggstrom, J. T. Vaughey, M. M. Thackeray, *J. Electrochem. Soc.*, 149 (2002) A736-A742.
88. H. Ishihara, S. Mizutani, H. Inoue, *US Pat.*, 0 115 734 (2006).
89. P. P. Ferguson, M. L. Martine, A. E. George, J. R. Dahn, *J. Power Sources*, 194 (2009) 794-800.
90. P. Poizot, S. Laruelle, S. Grugeon, L. Dupont, J. M. Tarascon, *Nature*, 407 (2000) 496-499.
91. J. Cabana, L. Monconduit, D. Larcher, M. R. Palacín, *Adv. Mater.*, 22 (2010) E170-E192.
92. A. Debart, L. Dupont, P. Poizot, J. B. Leriche, J. M. Tarascon, *J. Electrochem. Soc.*, 148 (2001) A1266-A1274.
93. P. Balaya, H. Li, L. Kienle, J. Maier, *Adv. Funct. Mater.*, 13 (2003) 621-625.
94. R. Fong, U. V. Sacken, J. R. Dahn, *J. Electrochem. Soc.*, 137 (1990) 2009-2013.
95. S. E. Sloop, J. K. Pugh, S. Wang, J. B. Kerr, K. Kinoshita, *Electrochem. Solid-State Lett.*, 4 (2001) A42-A44.
96. J. Fuller, R. T. Carlin, R. A. Osteryoung, *J. Electrochem. Soc.*, 144 (1997) 3881-3886.
97. A. Nishimoto, M. Watanabe, Y. Ikeda, S. Kojiya, *Electrochim. Acta*, 43 (1998) 1177-1184.
98. F. Croce, G. B. Appetecchi, L. Persi, B. Scrosati, *Nature*, 394 (1998) 456-458.
99. F. Croce, L. Settini, B. Scrosati, *Electrochem. Commun.*, 8 (2006) 364-368.

Chapter 2

Experimental and Characterization Techniques

This chapter gives brief descriptions about various synthesis methods and characterization techniques that were used in the thesis.

2.1. Synthesis techniques

Different synthetic methods were used such as hydrothermal/solvothermal route, solid state method, combustion, and simple solution methods with refluxing and stirring and the details for each and every material prepared are provided in the respective chapters.

2.2. Preparation of electrodes and cell fabrication

To measure the charge-discharge characteristics of the synthesized materials (active material), a slurry was prepared by mixing with an appropriate amount of acetylene black as the conductive additive and poly(vinylidene fluoride) (PVdF) as binder and by adding N-methylpyrrolidine (NMP) as the solvent. For the preparation of slurry, 80 wt.% of active material, 10 wt.% of acetylene black and 10 wt.% of PVdF were mixed and grinded using agate mortar for about 30 min. To the resulting powder, a few drops of the solvent: NMP were added. After grinding again for 10 min., a slurry was formed. The resultant slurry was coated on 13 mm stainless steel foils using a smooth brush and dried at 80 °C for 12 h in a vacuum oven for the removal of NMP.

In the case of SnS₂, the slurry was prepared in a slightly different way. Initially, PVdF was added to an appropriate amount of the NMP solvent. After stirring for about 30 min., a transparent gel was obtained. To this gel, the active material (SnS₂), acetylene black and PVdF in a 8:1:1 weight ratio were added and stirred for about

24 h. The resulting slurry was applied on a Cu sheet using the doctor blade method and dried in a vacuum oven at 80 °C for about 12 h. After complete drying, the coated Cu foil was cut into 10 mm sized electrodes using circular disc cutter.

The above prepared electrodes were incorporated in Swagelok cells and/or coin cells for electrochemical measurements and these cells were assembled inside an Argon filled glove-box (O_2 and H_2O concentration ≤ 0.5 ppm and 0.5 ppm). A Lithium foil was used as a counter/reference electrode and a Whatman glass microfiber filter paper functioned as the separator. The electrolyte was 1 M $LiPF_6$ in EC:DMC (1:1 v/v).

2.3. Characterization techniques

2.3.1. Powder X-ray diffraction technique

Powder X-ray diffraction is one of the most powerful techniques used for the identification of the crystal structure of a material. The structural characteristics of materials prepared in this thesis, were performed on a PANalytical, X'PertPRO instrument with Cu $K\alpha$ -radiation of wavelength 1.5406 Å. The accelerated voltage and current used for this instrument were 40 kV and 30 mA, respectively. The step size used for the scan is 0.02° per step in the 2θ angle range of 10 to 70° for most of the samples in this thesis. The interatomic distance in a unit cell of the crystal is equal to the wavelength of X-ray. When an electromagnetic radiation with an X-ray wavelength having photon energies between 3 and 8 keV impinges on crystalline materials, it undergoes diffraction through constructive or destructive interference (Figure 2.1). After the synthesis of samples, they were ground for about 10 min. for XRD measurement and loaded in a zero background sample holder or sprinkled on a

glass slide. The data was collected on an X'pert data collector and the software used for XRD analysis is X'pert high score and Origin.

The crystallite sizes in the samples were calculated based on broadening of XRD peaks, using the Debye-Scherrers formulae[1].

$$D = \frac{K\lambda}{\beta_{2\theta} \cos \theta} \quad (2.1)$$

In the above equation, K is the shape factor, generally equal to 0.94, λ is the X-ray wavelength (0.15406 nm), $\beta_{2\theta}$ is the full width at half maximum of the respective peak in radians and θ is the Bragg's angle. The Scherrer's equation can only be applied to particles with size less than 1 μm .

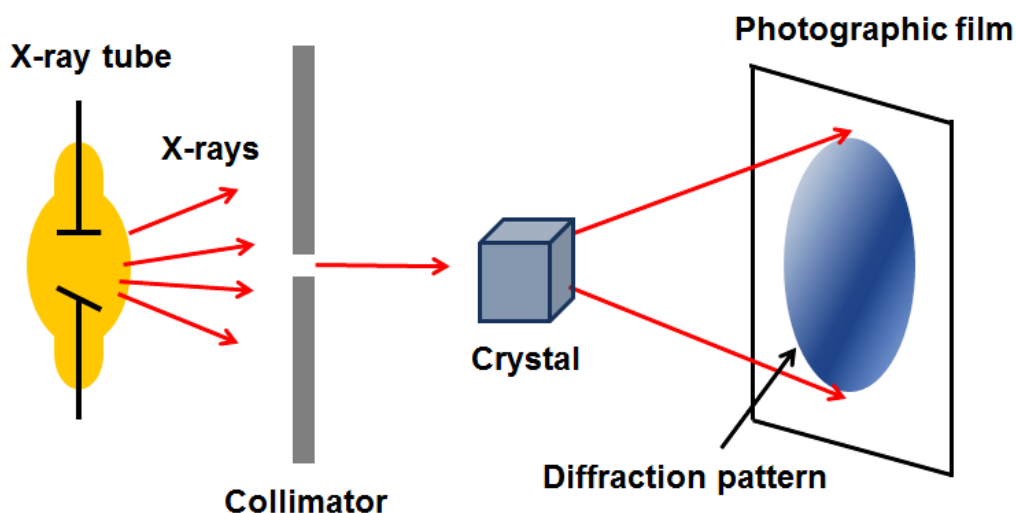


Figure 2.1. Schematic showing the principle of XRD.

2.3.2. Raman spectroscopy

Raman spectroscopy is extensively used to identify functional groups and lattice vibrations in a sample, typically, over a wavenumber range of 100-4000 cm^{-1} . Recent studies have shown that Raman spectroscopy can be used to characterize carbonaceous materials such as graphite, CNTs and graphene. Raman spectroscopy is based on scattering phenomenon, and it was first observed by Sir C. V. Raman in

1920. When a photon of light interacts with matter or a molecule, the photon is either absorbed or scattered. When the energy of incident photon, equals to the difference between the energy levels, then the molecule absorbs light undergo excitation to the next higher level. The change in energy from incident light can be measured in absorption spectroscopy. However, the photons, which are not absorbed will be scattered, and for scattering, the incident photons need not be resonant with the two energy states of the molecule. The scattered photons can be observed by collecting light at an angle perpendicular to the incident light beam, provided there is no absorption from any electronic transitions which have energies similar to that of the incident light, the efficiency increases as the fourth power of the frequency of the incident light[2]. A Raman spectrum is therefore a plot of the intensity of Raman scattered radiation as a function of its frequency difference from the incident radiation. This difference is called Raman shift. A Bruker Senterra dispersive micro Raman spectrometer with a laser source having a wavelength of 532 nm was used recording for Raman spectra for all samples, prepared in this thesis. For recording Raman spectra, the samples were mounted on a glass slide, and pressed with a pelletizer. A schematic of the Raman instrument is displayed in Figure 2.2.

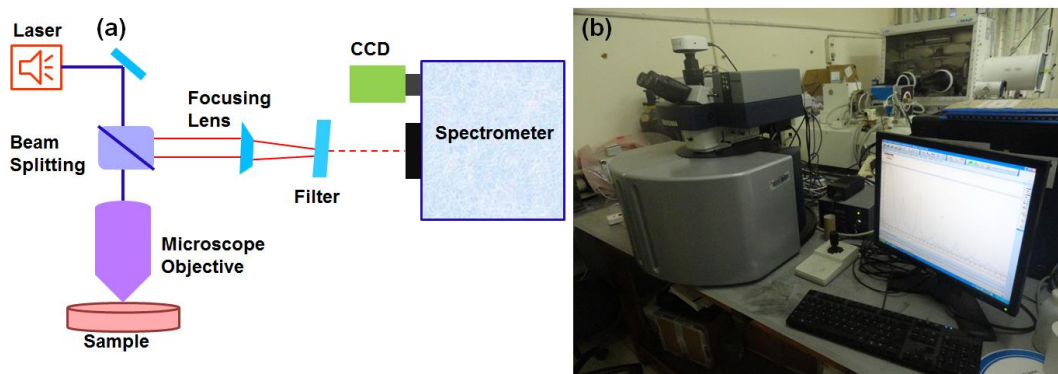


Figure 2.2. (a) Schematic of a micro-Raman spectrometer where illumination and collection are performed through a microscope objective, and (b) the digital photograph of the Raman instrument used in this thesis.

2.3.3. Scanning electron microscope (SEM)

In this thesis, morphological studies, energy dispersive spectroscopic (EDS) analysis, size of particles and elemental mapping for samples were obtained by using field emission scanning electron microscopy (FE-SEM). In SEM, a suitable electron source such as a field emission gun or a tungsten filament is used in the form of a beam to generate electrons which is accelerated towards the specimen, by using a high potential (e.g. 20 kV). The stream of electron beam is then passed through a series of apertures and electromagnetic lenses or condenser lenses to produce a thin beam of electrons which are used to scan the surface of a specimen by means of scan coils. The scanning beam can cause the specimen to emit electrons and these electrons are called secondary electrons. These ejected electrons are collected by a suitably positioned detector. Through this process, the secondary electrons are used to image the specimen and a surface morphology image is produced[3]. A schematic of a SEM is shown in Figure 2.3. The anode materials that were prepared and characterized in this thesis, were electronically conductive materials therefore they were used directly for FE-SEM. For the samples

MoO₂/Graphene, FE-SEM, Hitachi S-4300 SE/N was used whereas for other samples Carl Zeiss (Supra 40) FE-SEM was used.

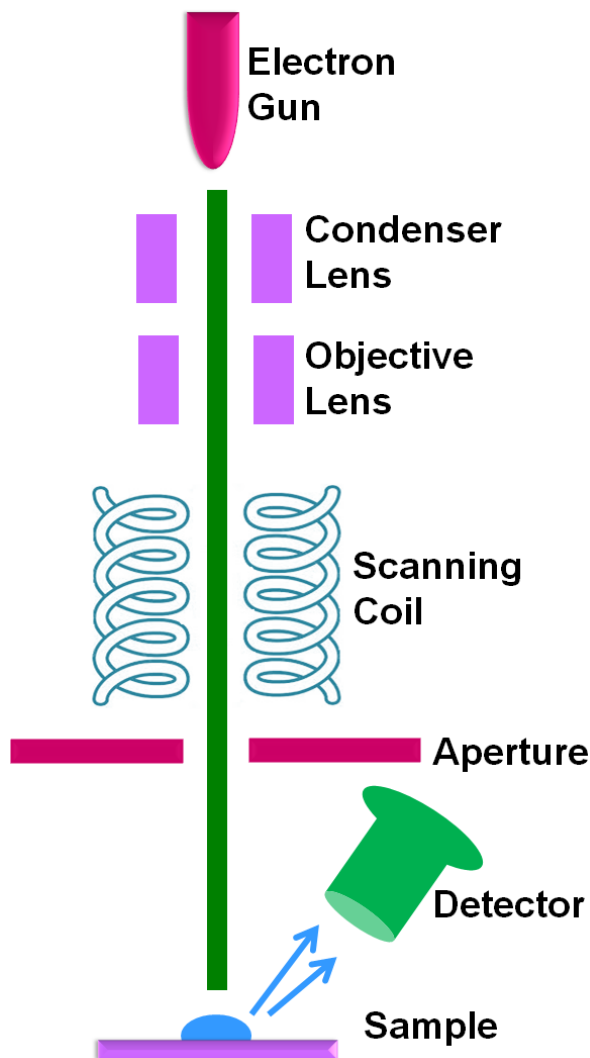


Figure 2.3. Schematic of a SEM.

2.3.4. Transmission electron microscopy (TEM)

Similar to SEM, the TEM also gives information about the internal structure and about the primary/secondary particles sizes in nanostructure. In addition, high resolution TEM (HRTEM) is an excellent technique which yields lattice fringes and diffraction patterns of crystalline materials and thus gives the crystal structural information. A TEM, typically, consists of a suitable electron source or an electron

gun which is used to produce a stream of electrons that are accelerated through a very high voltage (e.g. 100, 200 and 300 kV) towards the specimen. This stream of electrons is then passed through the metal apertures and magnetic lenses called “condenser lenses” to generate a thin, focused, monochromatic beam. The beam impinges sample and a portion of it passes through it. This part of the beam is re-focused with lenses known as “objective lenses” into an image. The image is fed through the column through the “intermediate and projector lenses”, which magnifies the image. The image then strikes a phosphor screen and light is provided and the user sees the image[3,4]. A schematic of TEM is shown in Figure 2.4. In this thesis, for MoO₂/Graphene, a TECNAI G-20, FEI with an accelerating voltage of 200 kV was used. For the remaining samples, TEM, JEOL 3010 with an accelerating voltage of 200 kV was used. Before recording TEM/HRTEM, the samples were ultrasonicated for about 30 min. in water and carefully extracted onto a carbon coated copper grid and the solvent was evaporated.

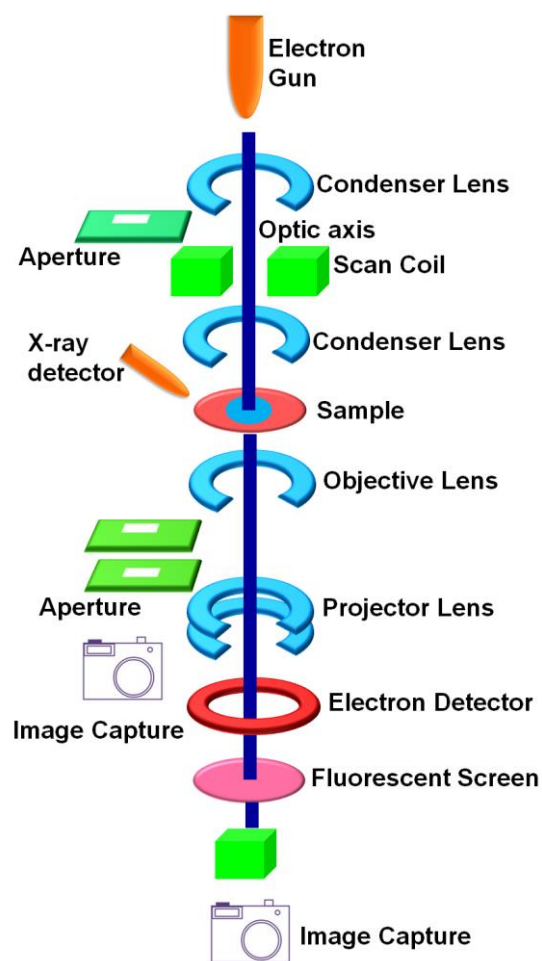


Figure 2.4. Schematic of a TEM.

2.3.5. X-ray photoelectron spectroscopy (XPS)

XPS is a powerful tool for analyzing the chemical composition of samples; the nature of bonds and oxidation states. It is a versatile technique used for studying the physical and chemical phenomena occurring at the surface. XPS is surface sensitive, probing a depth of ~ 10 nm, from the top of the surface. XPS works on the principle of photoelectric effect; an X-ray photon interacts with a core level electron transferring its energy to the electron and causing emitting of the electron in the form of kinetic energy. Based on this, the binding energy of the electron can be calculated by using Einstein's photoelectric effect equation.

$$E_b = h\nu - E_k - \phi_s \quad (2.2)$$

In (2.2), E_b is the binding energy of the electron, E_k is the kinetic energy of the electron, $h\nu$ is the incident X-ray photon energy and ϕ_s is the spectrometer work function. A schematic of an XPS system is shown in Figure 2.5.

XPS gives the spectral intensity of the emitted electron from the core level *versus* the binding energy of the electron. The binding energy of the core electrons are essentially dependent on the species to which it is bonded and the resulting charge transfer determines the magnitude of the “chemical shift”. Thus, information about the bonding environment (chemical state) can be determined[5]. Chemical shifts can arise in several ways including differences in formal oxidation states, electronegativity, molecular environment, lattice sites, etc. XPS spectra for the samples prepared herein, were recorded on an Omicron UK ESCA+ instrument with an AlK α monochromatic X-ray radiation with an energy of 1486.6 eV.

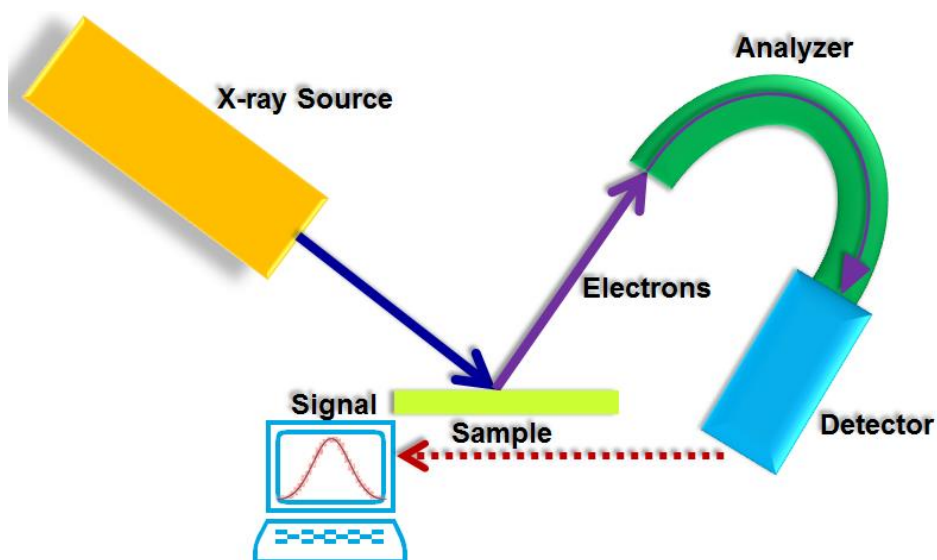


Figure 2.5. Schematic of an XPS.

2.3.6. Thermogravimetric analysis (TGA)

TGA measures the change in the mass of a substance as a function of temperature. The experiment is normally performed in O₂, N₂ or in any inert atmosphere. TGA can be combined with other analysis instruments, such as mass spectrometry (MS). With TGA-MS, it is easy to monitor the weight change as well as the decomposition component analysis. In this thesis, TGA was carried out on a TA Instruments Q600 Thermogravimetric analyzer. The sample was heated to a desired temperature at a constant ramp and cooled at the same ramping. The method was used for the quantifying the amount of carbon content in the active anode/cathode materials containing carbon or its allotropes. Since the sample loading affects the accuracy of the results, typical sample mass, was controlled at the range of 5-10 mg, during these analyses.

2.4. Calculation of theoretical specific capacity and C-rate

The charge storage capacity of a cell can be calculated, from the amount of current that is withdrawn in a specific voltage window. The theoretical specific capacity of a cell depends only on the active materials participating in the electrochemical reaction and is based on Faraday's first law of electrolysis. Theoretically, one gram equivalent weight of a material delivers 96,487 C or 26.8 Ah of charge. Since Lithium insertion/deinsertion involves a single electron transfer, the theoretical specific capacity equals to 26.8 Ah divided by the molecular weight of the active material in grams[6].

For example, the molecular weight of LiFePO₄ is 157.75 g. The theoretical specific capacity of LiFePO₄ is $26.8/157.75 = 170 \text{ mAh g}^{-1}$. The charge-discharge characteristics can be measured at different current rates like 1C, 2C or C/5 or at

different current densities like 50, 100, 500 or 1000 mA g⁻¹. 1C – represents that the cell takes one hour to completely remove or insert one mole of Lithium, and C/5 – represents that one mole of Lithium reaction occurs in 5 h. A 100 mA g⁻¹ current density implies that, 1 g of the material can deliver 100 mA of current. Based on the active materials weight, one can calculate the amount of current that has to be supplied, for capacity measurement.

2.5. Electrochemical property measurement

Electrochemical property measurements provide information on chemical reactions occurring at cathode/anode of a battery and kinetic properties of battery constituents. These aspects help in the determination of reaction voltages and characteristic discharge-charge responses, and digression from the expected theoretical behavior. The typical electrochemical charge-discharge behavior can be measured in constant current (CC) or constant current constant voltage (CCCV) mode. In the CC mode, a constant current is applied for the duration of charging or discharging, but it is not necessary that both charging and discharging currents should be equal. In the intermittent mode, or the CCCV mode, a constant current is applied for some duration, so that the reaction proceeds to some extent. At this point, the upper or lower cut-off voltage is reached and the reaction is held for some pre-set time. The voltage hold allows the mobile species in electrodes to equilibrate. The commonly used method for presenting and analyzing the data through the use of charge and discharge curves is, by plotting the cell voltage as a function of the state of charge. The charge-discharge voltage curve can vary significantly depending on the current rate, for one particular material and it also depends on the type of material. Typical discharge curves of electrode materials are shown in Figure 2.6[6].

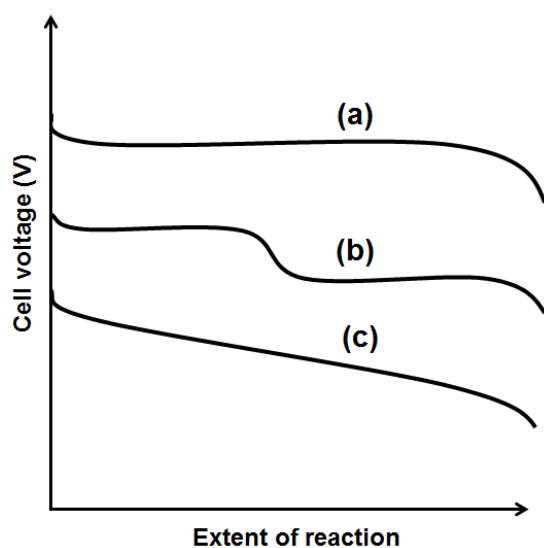


Figure 2.6. Schematic representation of different types of discharge curves. These curves are (a) flat, (b) multi-steps flat plateau and (c) sloping, respectively.

The flat curve represents multiphase reactions with potentials that are essentially independent of the state of charge of the cell. A sloping curve indicates a solid solution or undesirable reactions between two or more components of the battery, such as the electrolyte and active material, where the potential varies with the state of charge. Galvanostatic charge-discharge measurements were performed on a battery testing unit (Arbin Instruments, BT 2000) at different current densities in the various voltage ranges *versus* Li/Li^+ at room temperature.

2.6. Cyclic voltammetry (CV)

In a LIB, CV is widely used to determine the oxidation and reduction potentials of an electroactive electrode material, to determine the potentials at which the side reactions between electrode and electrolyte occur and to determine the diffusion coefficient of Li-ions in the electrodes. The basic operating principle of CV is a triangular potential wave (in relation to the reference electrode) imposed on the working electrode as a function of time. A CV scan begins at an initial potential (V_1 , Figure 2.7a). The scan, then proceeds to a final (or reverse) potential (V_2) and then

returns to the initial potential. The scan rate (v) is the change of potential as a function of time ($v = dE/dt$) and can be deduced from the gradient of the curve (Figure 2.7a). During the scan, the flowing current is recorded (Figure 2.7b). Since potential and current, are both functions of time, they can be easily interrelated and the current flow can be plotted as a function of the applied electrode voltage. Figure 2.7c shows the result of a CV experiment: a cyclic voltammetric curve, or a voltammogram, which illustrates diffusion controlled process (or mass transfer). As shown by the CV curve, when the voltage is increased from V_1 to V_2 with scan rate v , at first, almost no current flows, with the exception of the capacitive background current. From a certain potential, the current begins to increase up to a maximum value owing to an electrochemical oxidation reaction on the electrode surface, and then decreases afterwards. This maximum current is called the peak current, for the anodic oxidation process (i_{pa}). The respective potential, at which maximum current is observed, is called the peak potential, and at this point, it is called the anodic peak potential (V_{pa}). After reaching V_2 , and decreasing the potential back to V_1 , the respective reduction reaction starts to proceed and the peak cathodic current (i_{pc}) and the associated peak potential (V_{pc}) can be identified[7,8,9]. CV experiments for the as fabricated cells were performed on an Autolab PGSTAT 302N electrochemical workstation equipped with a NOVA 1.9 software at various scan rates.

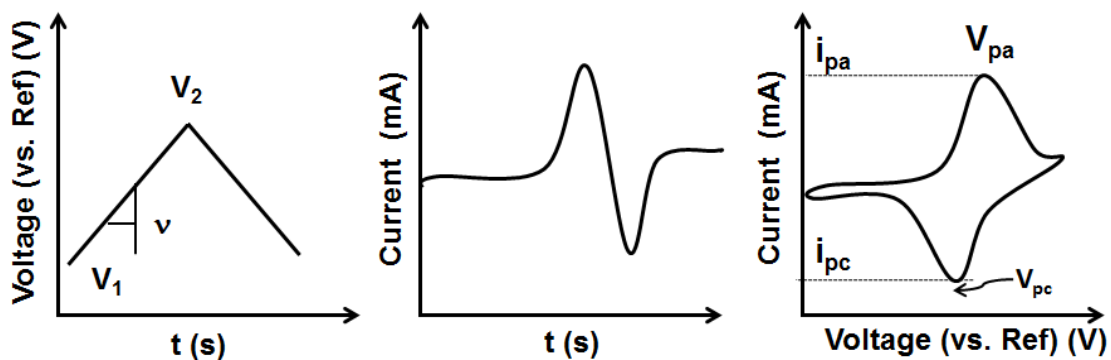


Figure 2.7. Applied potential (a) and the flowing current (b) as function of time in a CV experiment and (c) shows a derived cyclic voltammogram (CV), which shows current produced as a function of applied potential.

2.7. Electrochemical impedance spectroscopy (EIS)

EIS is a useful technique for the determination of resistances due to various components, capacitances due to their physical structures and for calculation of the diffusion coefficient of Li-ion through the bulk of the electrode in an electrochemical cell such as a LIB. Similar to dc resistance, impedance is also the measure of the resistance altered to the propagation of current, as a function of applied voltage. If the circuit is composed of pure resistive components, then both current and voltage are in phase, when an ac voltage is applied to the circuit. The phase difference between I and V is: $(\phi) = 0$, over the entire frequency range. However, when the circuit also contains capacitive and inductive components then, when an amplitude of ac voltage is applied across a cell, both current and voltage are out of phase ($\phi \neq 0$) and thus are dependent on varying frequency. In general, impedance data can be represented as Nyquist plots i.e., the imaginary part of impedance as a function of real part of impedance, as is shown in Figure 2.8[10]. EIS measurements on the cells with active material as the working electrode were carried out on an Autolab PGSTAT 302N electrochemical workstation with a

frequency response analyser over a frequency range of 10 KHz - 10 mHz, and by using ac amplitude of 0.01 V.

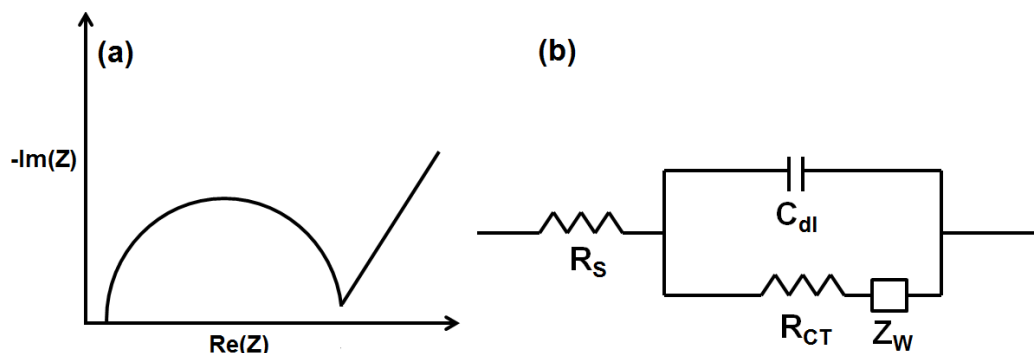


Figure 2.8. (a) Schematic of a Nyquist plot, (b) the plot can be fitted into an equivalent circuit with R_s (electrolyte resistance), C_{dl} (surface layer capacitance), R_{CT} (charge-transfer resistance) and Z_W (diffusional (Warburg) impedance).

2.8. Other instruments

Brunauer-Emmett-Teller (BET) specific surface area measurements were performed on a Micromeritics, ASAP 2020. Conductive AFM (C-AFM, Veeco, Multimode 8 with ScanAsyst and Nanoscope 8.10 software) was used for recording simultaneous topography and nanoscale current images in contact mode of electrode materials. Cantilevers made of Sb doped Si (n-doped; resistivity $\sim 0.01 - 0.025 \Omega \text{ cm}$) and coated with Pt/Ir (20 nm) on the front and backside were obtained from Veeco. Spring constant of tip was 0.2 N m^{-1} and a load force of 48 nN was maintained between the tip and the sample. UV-Vis-NIR spectra were recorded for samples on a Shimadzu, UV-3600 spectrophotometer. Room temperature photoluminescence as a function of wavelength for electrode samples were performed on a Horiba, Fluoromax-4 spectrofluorometer.

References

1. A. L. Patterson, *Phy. Rev.*, 56 (1939) 978-982.
2. R. B. Hadjean, J. P. P. Ramos, *Chem. Rev.*, 110 (2010) 1278-1319.
3. Ray F. Egerton, *Physical Principles of Electron Microscopy*, Springer Science/Business Media/Inc., publications, 2005.
4. David B. Williams, C. Barry Carter, *Transmission Electron Microscopy A Textbook for Materials Science*, Springer Science/Business Media, LLC 1996, 2009
5. P. Van Der Heide, *X-Ray Photoelectron Spectroscopy: An Introduction to Principles and Practices*, John Wiley & Sons, Inc., Publications, 2012.
6. R. A. Huggins, *Energy Storage*, Springer Science/Business Media/LLC., Publications, 2010.
7. Allen J. Bard, Larry R. Faulkner, *Electrochemical Methods Fundamentals and Applications*, John Wiley & Sons, Inc., Publications, 2004.
8. F. Harnisch, S. Freguia, *Chem. Asian J.*, 7 (2012) 466-475.
9. Gary A. Mabbail, *J. Chem. Educ.*, 60 (1983) 697-702.
10. J. Ross Macdonald, *Impedance Spectroscopy Emphasizing Solid Materials and Systems*, John Wiley & Sons, Inc., Publications, 1987.

Chapter 3

Structure-Electrochemical Activity Correlation in a MoO₂/Multiwalled Carbon Nanotubes (MWCNTs) Hybrid

3.1. Abstract

In this chapter, an easy single step synthesis of MoO₂/MWCNT hybrid by a hydrothermal method is presented. AOT was used: it not only served as a reducing agent for the Mo salt reduction but also tailored the growth of MoO₂ nanoparticles into three-dimensional spherical shaped flower-like morphologies. In addition, AOT also aided in dispersing MWCNTs. HRTEM and XRD studies provided insights to the microstructural features of MoO₂/MWCNT hybrid and the neat materials (MoO₂ and MWCNTs). The electrochemical characteristics of the MoO₂/MWCNT hybrid by incorporating it as the working electrode in a Li-ion battery configuration were evaluated and correlated the outstanding performance attributes with its unique morphology were correlated.

3.2. Introduction

Among anode materials, molybdenum oxide (MoO₂) is particularly attractive, as it offers an extremely large theoretical specific capacity of $\sim 840 \text{ mA g}^{-1}$, corresponding to an insertion of 4 lithiums. To date, there are several reports on MoO₂ with different nanostructures which include mesoporous, nanowires, nanorods, and tremella like shapes[1-4]. In addition, the performances of MoO₂/C and MoO₂/graphene composites as anodes have also been investigated[5-10]. For instance, MoO₂ nanowires prepared by Gao and co-workers showed an initial capacity of 595.7 mAh g^{-1} at a current density of 200 mA g^{-1} and at the end of 20 cycles, a capacity of $\sim 500 \text{ mAh g}^{-1}$ was retained[2]. Shi et. al's report revealed the

ability of mesoporous MoO₂ to deliver a reversible capacity of 630 mAh g⁻¹ which increased to a value of 750 mAh g⁻¹ after 30 cycles. But this capacity was achieved at a rather low C-rate of 0.05[1]. In another study on ultrafine MoO₂ nanorods, 5 nm in diameter, an initial reversible capacity of 521 mAh g⁻¹ was reported and it gradually reached a value of 830 mAh g⁻¹ after 30 cycles, but again, at a very low C-rate of 0.05[3]. Tremella-like structured MoO₂ prepared by Yang et. al, showed an initial reversible capacity of 538.0 mAh g⁻¹ at a current density of 0.5 mA cm⁻² and the capacity rose to 650 mAh g⁻¹ in the subsequent cycles[4]. For a composite of ultrafine MoO₂ nanoparticles distributed homogeneously in a carbon matrix[6], authors found that it exhibited a stable capacity of ~602 mAh g⁻¹ for ~600 cycles at a current density 100 mA g⁻¹. It is apparent that MoO₂ composites with novel nanoscale architectures that can deliver high rate capability, capacity and cyclability are desirable.

Since MWCNTs are bestowed with one-dimensional tubular structures, high electrical and thermal conductivities[11], and large surface areas[12], they are ideal for combining with MoO₂. Moreover, the synergy between the functions of the two materials, the high capacity of MoO₂ and good electronic conductivity and large surface area of MWCNTs can be exploited in the MoO₂/MWCNT hybrid to yield high performance anodes in Li-ion batteries. It is well known that CNTs are highly hydrophobic and the surface should be functionalized for dispersing in an aqueous medium. CNTs can be functionalized in two different ways, one is covalent (by use of an acid) and other is non-covalent (by adsorption of a base like poly(diallyldimethylammonium chloride). The non-covalent method is preferred over covalent method because the surface property as well as electronic conductivity

is not disturbed[13-16]. Based on previous studies, one frequently used approach for increasing the dispersability of CNTs is non-covalent modification using a surfactant. This is because of the simplicity of the procedures involved, such as ultrasonication and centrifugation or filtration, along with a capacity for preserving the nanotube structures and properties. In this context an anionic surfactant like sodium di-octyl sulfosuccinate (AOT) has been used to solubilize and de-bundle single walled carbon nanotubes (SWCNTs) in aqueous solution via non-covalent interactions[13-16]. MoO₂/MWCNT hybrid was prepared by hydrothermal method and correlated with electrochemical property.

3.3. Experimental

3.3.1. Materials

All of the reactants were of analytical grade and used without further purification. Ammonium heptamolybdate tetrahydrate (AHM) and battery electrolyte: 1 M LiPF₆ dissolved in a mixture of ethylene carbonate (EC) and dimethyl carbonate (DMC) (1:1 v/v), were purchased from Merck. AOT and MWCNTs were purchased from Sigma-Aldrich. Lithium foil was purchased from Alfa-Aesar. MWCNTs were purified by ultrasonic treatment in 6 M nitric acid for 0.5 h and then refluxing in 2.6 M HNO₃ solution for 36 h before use. Ultrapure water (resistivity~ 18.2 MΩ cm) obtained through Millipore Direct-Q3 UV system was used as solvent.

3.3.2. Synthesis of the MoO₂/MWCNT hybrid

The MoO₂/MWCNT hybrid was prepared by a hydrothermal method using AOT as the surfactant. The first step involved the preparation of surface modified MWCNTs with AOT as surfactant. Typically, 100 mg of MWCNTs were added to

20 mL of absolute ethanol and ultrasonicated for 0.5 h. To this suspension, 2 g of AOT dissolved in 15 mL of cyclohexane was added and the resulting mixture was ultrasonicated again for 0.5 h and stirred for 15 min and it formed a well-dispersed and homogeneous solution of MWCNTs. In a separate beaker, 0.5 mmol AHM was dissolved in 20 mL of ultrapure water and added to the above solution. This was followed by continuous stirring for 1 h at 25 °C. The resultant black colored solution was placed in a 100 mL teflon lined autoclave and heated in an oven at 200 °C for 36 h. A black colored precipitate was obtained and it was filtered and washed with ultrapure water followed by n-hexane. The resultant black powder was dried in a vacuum oven at 80 °C for 12 h and the dried MoO₂/MWCNT hybrid was stored in a glove box. Neat MoO₂ was also prepared by following the same steps, but without adding MWCNTs. The optimization of the amount of surfactant (AOT) for producing MoO₂ flower like nanostructures, was accomplished by preparing neat MoO₂ by varying the concentration of AOT: by using 0.3, 0.6, 1 and 3 g of AOT whilst all other experimental conditions were kept constant.

3.4. Results and discussion

3.4.1. Structural characterization

The XRD patterns of hydrothermally synthesized MoO₂ by heating at 200 °C for 36 h for various proportions of AOT (in the precursor solution) are shown in Figure 3.1. The XRD patterns of neat MoO₂ prepared with 0.3, 0.6, 1 and 2 g AOT surfactant show distinct peaks corresponding to the monoclinic structure of MoO₂ with space group of P21/c(14) (PCPDF NO: 860135).

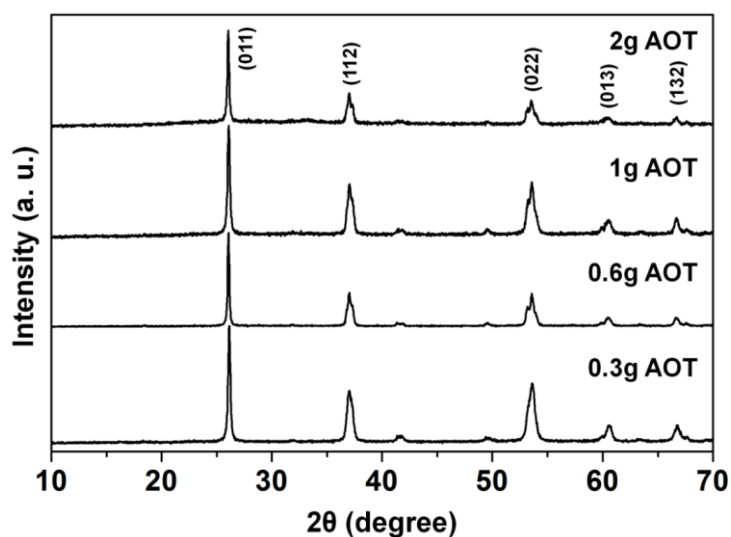


Figure 3.1. XRD patterns of neat MoO₂ prepared from solutions containing 0.3, 0.6, 1 and 2 g AOT (by heating hydrothermally at 200 °C for 36 h).

The field emission scanning electron microscopy (FE-SEM) images of these materials are shown in Figure 3.2. The morphology of MoO₂ prepared from a 0.3 g AOT formulation shows compactly packed interconnected irregular shaped particles (Figure 3.2a). On increasing the AOT proportion to 0.6 g (Figure 3.2b), the image shows MoO₂ growing into bundles of randomly oriented stubs, around 120 nm in length and 35-50 nm in diameter. At 1 g AOT content, the SEM image shows that the MoO₂ stubs evolve into MoO₂ flakes (Figure 3.2c). At 2 g of AOT, the flakes evolve into a flower like morphology, which is advantageous for ion insertion/extraction during the discharge/charge process (Figure 3.2d). The high magnification image clearly shows the sheet like-shapes (Figure 3.2e) which organize into flower like structures. Upon raising the AOT content further to 3 g (Figure 3.2f), we observed that the same nanosheet like morphology was retained, indicating that 2 g of AOT is sufficient to induce the formation of flower like shapes encompassing the flaky sheets. Therefore we used the precursor composition with 2 g AOT for preparing the hybrid with MWCNT.

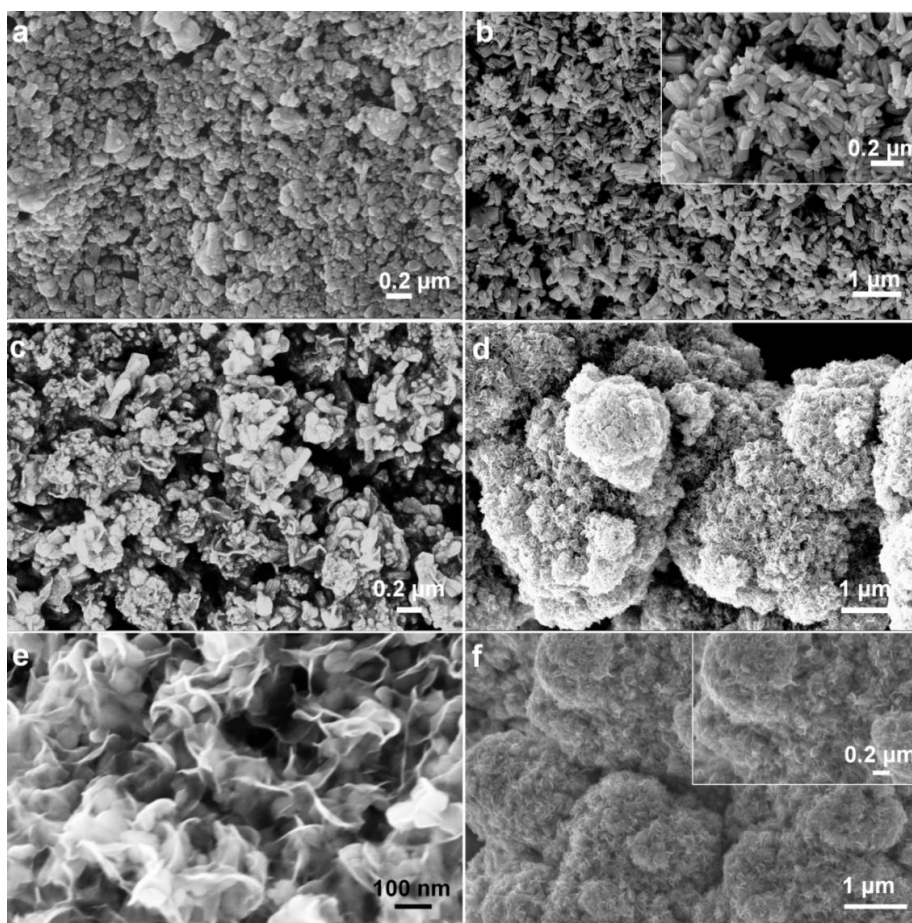


Figure 3.2. FE-SEM images of MoO₂ prepared from solutions containing (a) 0.3 (b) 0.6 (c) 1 (d, e) 2 and (f) 3 g of AOT (by hydrothermal heating at 200 °C for 36 h).

The XRD patterns of the as-synthesized MoO₂/MWCNT hybrid (based on 2 g AOT, 200 °C for 36 h) and MWCNTs are shown in Figure 3.3a. XRD patterns of the MoO₂/MWCNT hybrid can be readily indexed with monoclinic MoO₂ with a space group of P21/c(14) (PCPDF NO: 860135). The diffraction peaks at $d = 3.4256, 2.4339, 2.1797, 1.7146, 1.5322$ and 1.4017 \AA correspond to (011), (112), (212), (022), (013) and (132) reflections of monoclinic MoO₂, respectively. The XRD pattern of neat MWCNTs shows a broad peak at $d = 3.423 \text{ \AA}$ ($2\theta = 26.01^\circ$) which corresponds to (002) reflection. The Raman spectrum of neat MWCNTs and MoO₂/MWCNT hybrid are shown in Figure 3.3b. While the Raman spectrum of neat MWCNTs shows only the D and the G bands in the $1300\text{-}1600 \text{ cm}^{-1}$

wavenumber range, the Raman spectrum of the MoO₂/MWCNT hybrid shows signals, characteristic of both MoO₂ and MWCNTs. The peak at 1312 cm⁻¹ is assigned to the D mode and is attributed to the defects prevalent in the curved graphene sheets in the nanotubes[17]. The peak at 1592 cm⁻¹ corresponds to the G band that represents the crystalline structure of the nanotubes[17]. Strong intense peaks are observed at 817 and 990 cm⁻¹, attributable to $\nu(\text{Mo-O-Mo})$ and $\nu(\text{Mo=O})$ stretching modes of MoO₂, confirming the inclusion of MoO₂ in MWCNTs. The forest-like growth and entangled assembly of MWCNTs is visible from Figure 3.3c. The images of the MoO₂/MWCNT hybrid reveal the sphere shaped-flower like morphology of MoO₂ nanostructures and these nanostructures are connected by the MWCNTs (Figure 3.3d and e).

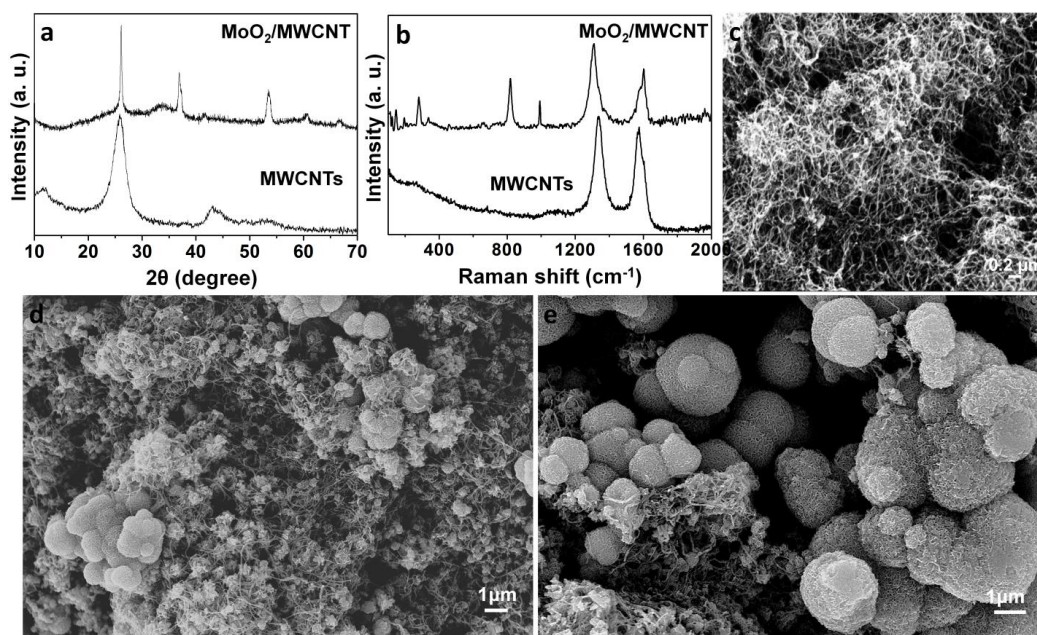


Figure 3.3. (a) XRD patterns and (b) Raman spectra of neat MWCNTs and the MoO₂/MWCNT hybrid. FE-SEM images of (c) neat MWCNTs and (d, e) MoO₂/MWCNT hybrid.

TEM and HRTEM images of the neat MWCNTs, neat MoO₂ and MoO₂/MWCNT hybrid are shown in Figure 3.4. The neat nanotubes are

characterized by curved structures and in general, they have an inner diameter of about 5-8 nm and an outer diameter of about 20 nm (Figure 3.4a and b). The high-magnification image of the tip shows that the nanotubes have open ends with circular shapes (inset of Figure 3.4a). The inset of Figure 3.4b shows the lattice scale image from an individual MWCNT, indicating the high crystallinity of the walls. The walls are composed of graphite sheets aligned parallel to the tube axis. The inter-wall spacing is about 0.31 nm which is consistent with the standard (well-reported) spacing of about 0.34 nm[18,19]. The flower-like morphology of MoO₂ is evident from Figure 3.4c, wherein one large MoO₂ particle comprising petal like shapes is seen. The low magnification image of the MoO₂/MWCNT hybrid (Figure 3.4d) reveals the spherical flower like shapes of MoO₂ to be connected by the coiled MWCNTs. The diameter of the MoO₂ spheres varies from 50 to 300 nm and in some portions the spheres tend to aggregate and form large particles. But at the nano-level, the sphere-shaped floral morphology intertwined with MWCNTs is the dominant, which is advantageous for electrochemical applications. The MWCNTs being intrinsically electron-conducting in nature, can provide conducting pathways for electron transfer and transport during charging-discharging process. The MoO₂/MWCNT hybrid is therefore expected to show an improved performance in comparison to neat MoO₂ as a Li-ion battery anode due to the presence of uniformly distributed MWCNTs in the MoO₂/MWCNT hybrid. The direct and intimate contact which is established between the MWCNTs and MoO₂ nanoparticles is perceptible from Figure 3.4e. A high magnification image of the petal like shape of MoO₂ (Figure 3.4f) shows the petals to be largely composed of elongated-strand like structures. On examining the section of one such petal (Figure 3.4g), we find that

lattice fringes of MoO₂ are oriented in a direction which is almost perpendicular to the growth axis of the MoO₂ petals. The lattice fringes of MoO₂ are not well-resolved in all regions of the MoO₂/MWCNT hybrid, owing to some degree of amorphicity in the MoO₂/MWCNT hybrid. A lattice scale image recorded from a defect-free section of the crystalline MoO₂ nanoparticles (Figure 3.4h) reveals the inter-planar spacing to be ~0.32 nm, which augurs well with a d-spacing of 3.42 Å corresponding to the (011) reflection of monoclinic MoO₂, in accordance with the PCPDF NO: 860135. The lattice scale image recorded from another region of the same MoO₂/MWCNT hybrid (Figure 3.4i) reveals the presence of crystalline particles oriented along the (020) plane of monoclinic MoO₂. Our HRTEM results are in agreement with our XRD findings.

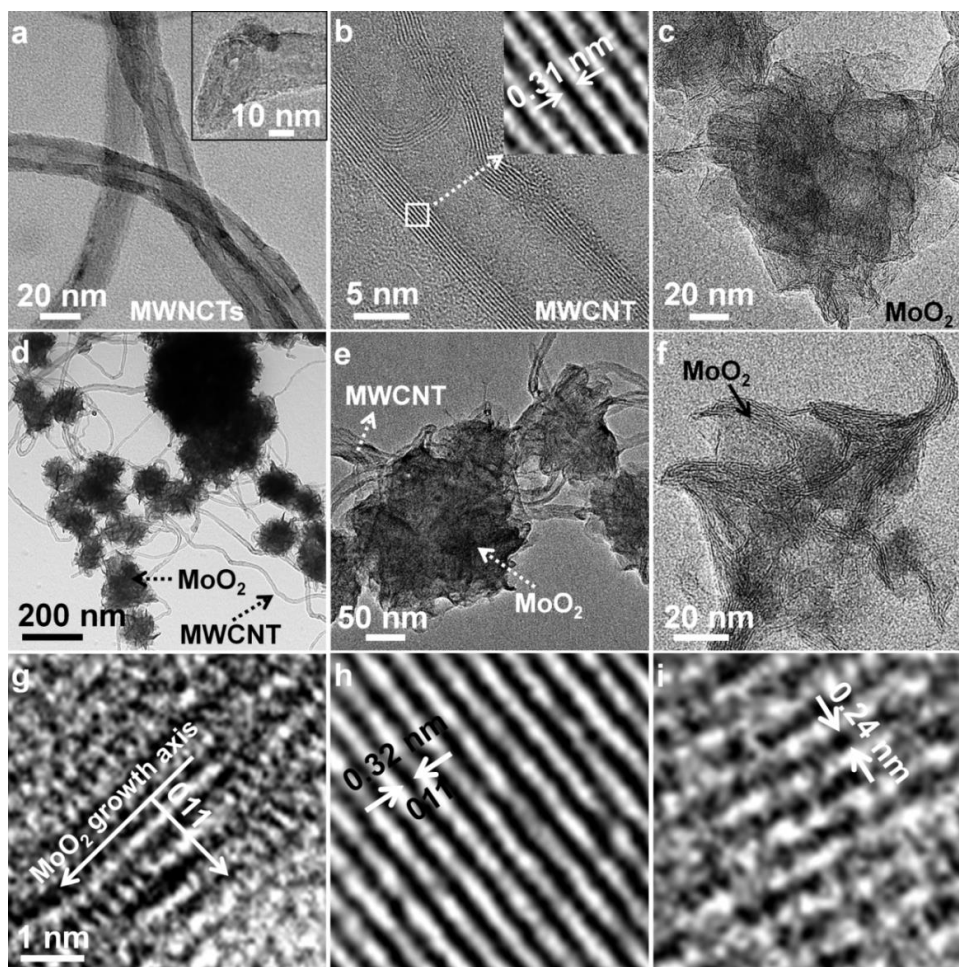
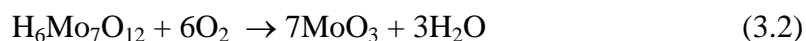


Figure 3.4. (a) TEM image of neat MWCNTs, inset shows a nanotube end, (b) HRTEM image of a single MWCNT, inset shows the corresponding lattice scale view, (c) flower-like morphology of neat MoO₂, (d) low and (e) high magnification images of MoO₂ flowers connected by MWCNTs in the MoO₂/MWCNT hybrid, (f) high magnification image illustrating the MoO₂ petals to be composed of elongated strands, (g) the growth axis of MoO₂ strands is normal to the lattice plane (011), (h) lattice scale image of MoO₂ extracted from the MoO₂/MWCNT hybrid oriented along the (011) plane and (i) a lattice scale image of a semi-crystalline MoO₂ oriented along the (020) plane.

3.4.2. Growth mechanism of MoO₂ flowers

In order to understand the growth mechanism of MoO₂ flowers, the MoO₂ precursor with fixed amount of AOT: 2 g, was heated for different durations: 6, 12 and 24 h, while keeping all other experimental parameters constant. The XRD

patterns of the products formed after 6, 12 and 24 h hydrothermal treatment correspond to monoclinic MoO₂ (Figure 3.5) and peaks from no other impurity phases and side products were observed. At the first stage, when the precursor solution of MoO₂ (AHM dissolved in H₂O) was added to AOT (dissolved in cyclohexane) solution, the MoO₂ precursor moieties are entrapped by the central polar part of the reverse micelles formed by AOT in cyclohexane. During the heat treatment under hydrothermal conditions for 6 h, the MoO₂ precursor moieties in the core of the reverse micelle nucleate and form bundles of stub-shaped particles (Figure 3.6a). The particle morphology does not alter significantly, when the heating duration was increased to 12 h (Figure 3.6b). However, when the duration of heating was increased to 24 h, the grain boundaries of the MoO₂ stub like shapes become distinct, they also flatten out and they also coalesce to form small floral shapes, with an average diameter of about 135 nm (Figure 3.6c). On further heating to 36 h, the flaky MoO₂ particles undergo Ostwald ripening and grow into spherical flower shaped nanostructures of around 1000 nm dimensions (Figure 3.6d). Under hydrothermal conditions, the heptamolybdate anions entrapped in the core of the reverse micelle undergo decomposition to form MoO₃ particles which are instantaneously reduced to MoO₂ by the carbon generated in-situ from the decomposition of AOT. We have represented these steps in equations 3.1-3.3.



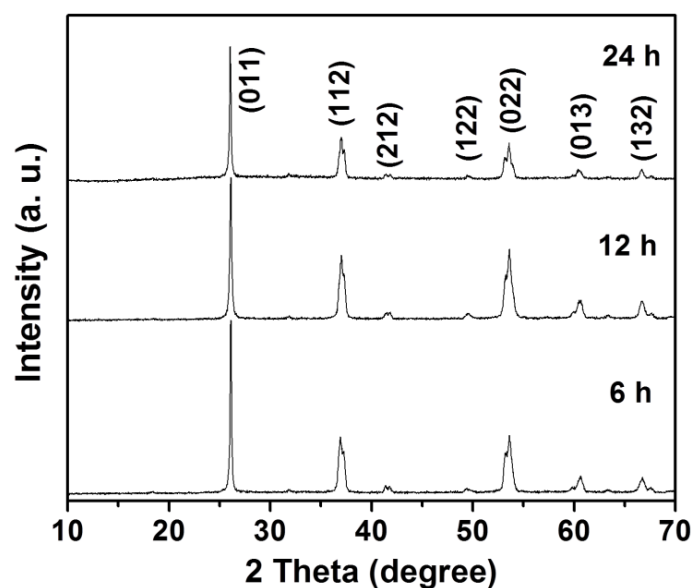


Figure 3.5. XRD patterns of neat MoO₂ prepared by heating the solution containing 2 g of AOT for different intervals of time at a constant temperature of 200 °C.

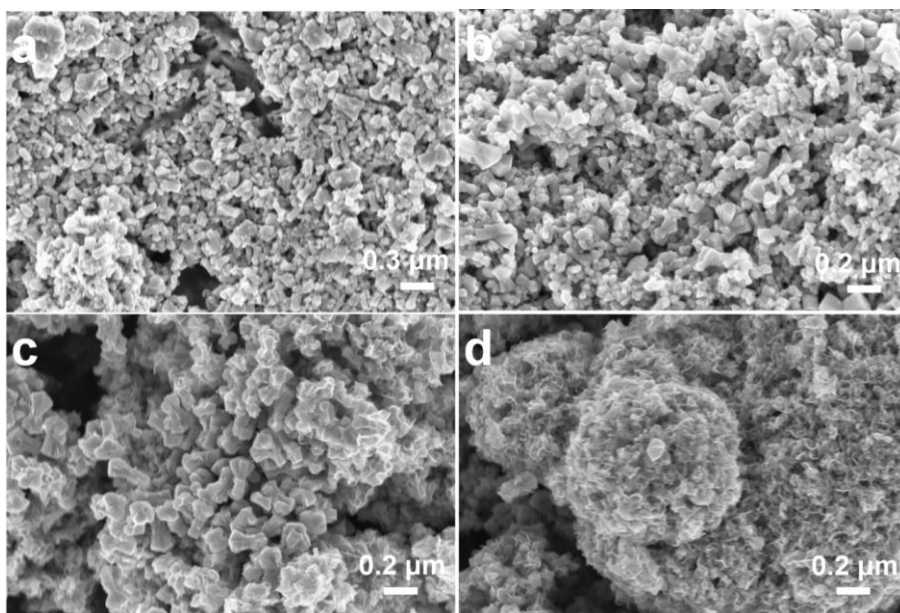
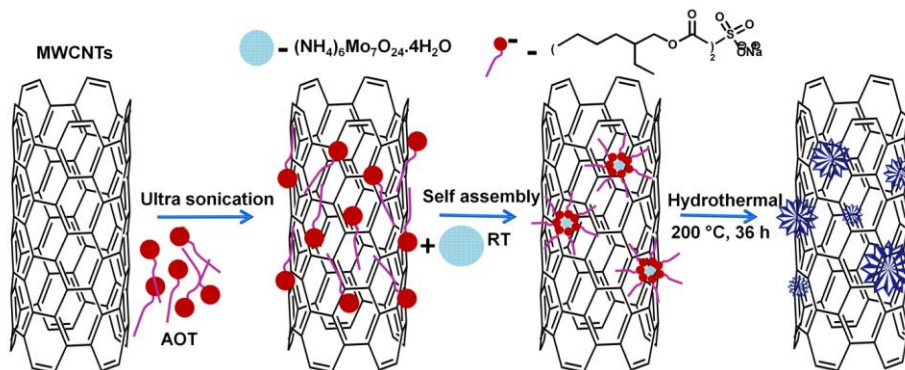


Figure 3.6. FE-SEM images neat MoO₂ prepared by hydrothermal heating of the precursor containing 2 g AOT for (a) 6 h, (b) 12 h, (c) 24 h and (d) 36 h, at a fixed temperature of 200 °C.

To further increase the electronic conductivity of MoO₂, we used MWCNTs and prepared the MoO₂/MWCNT hybrid. MWCNTs play a critical role in separating the flower-shaped nanostructures and prevent them from aggregating. The mechanism for the formation of flower kind of nanostructures is similar to the above mentioned

process but the whole process now occurs on the surface of the MWCNTs. These steps are shown in a schematic (Scheme 3.1). In the initial step, we prepared de-bundled, solubilized and well-dispersed MWCNTs in ethanol/cyclohexane solution, by addition of AOT. AOT forms reverse micelles in the medium, with the SO_4^- groups in the core of the micelle and the alkyl chains face the organic solvent molecules. These negatively charged moieties get adsorbed on the surface of MWCNTs, and prevent the MWCNTs from stacking. Upon subsequent addition of AHM/water solution to the MWCNT/AOT dispersion, the reverse micelles of AOT entrap the heptamolybdate ions via coulombic repulsion, and attach non-covalently to the surface of MWCNTs. Upon hydrothermal heating for 36 h, the floral-nanostructures of MoO_2 are flanked to the surface of MWCNTs are formed after organic burnout and they remain discrete.



Scheme 3.1.: Schematic representation for the preparation of $\text{MoO}_2/\text{MWCNT}$ hybrid.

The BET specific surface area of the $\text{MoO}_2/\text{MWCNT}$ hybrid was obtained by recording nitrogen adsorption-desorption isotherms (Figure 3.7). The as-prepared $\text{MoO}_2/\text{MWCNT}$ hybrid show a specific surface area of $117.5 \text{ m}^2 \text{ g}^{-1}$ which is higher than that observed for neat MoO_2 ($56.9 \text{ m}^2 \text{ g}^{-1}$). The larger specific surface area of $\text{MoO}_2/\text{MWCNT}$ hybrid indicates the availability of more number of electro-active

sites for Li ion storage. The pore volumes for the two samples were also calculated by using the N_2 sorption isotherm (Figure 3.7). The pore volume was found to be $0.39 \text{ cm}^3 \text{ g}^{-1}$ for the $\text{MoO}_2/\text{MWCNT}$ hybrid whereas the pore volume of neat MoO_2 was $0.24 \text{ cm}^3 \text{ g}^{-1}$. The higher specific surface area and the larger pore volume of the $\text{MoO}_2/\text{MWCNT}$ hybrid can also aid in accommodating the volume changes of MoO_2 , during charge/discharge cycles, which can lead to better cycling stability.

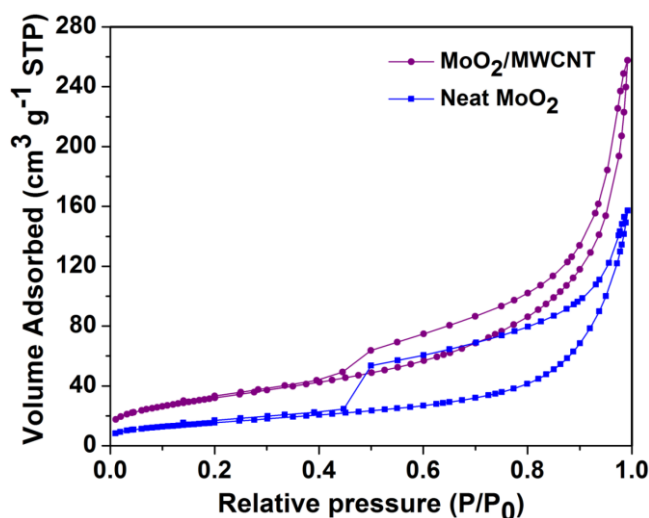


Figure 3.7. N_2 adsorption/desorption isotherms of neat MoO_2 and the $\text{MoO}_2/\text{MWCNT}$ hybrid.

To determine the chemical composition of the $\text{MoO}_2/\text{MWCNT}$ hybrid, XPS measurements were carried out and are presented in Figure 3.8. The survey spectrum (Figure 3.8a) of the $\text{MoO}_2/\text{MWCNT}$ hybrid shows distinct signals at 230.2, 284.7, 394.6, 412.1 and 530.8 eV which are assigned to the $\text{Mo}3d$, $\text{C}1s$, $\text{Mo}3p_{3/2}$, $\text{Mo}3p_{1/2}$ and $\text{O}1s$ respectively; indicating contributions from both MoO_2 and MWCNT. The $\text{C}1s$ signal (Figure 3.8b) shows an asymmetrical profile owing to the presence of different oxygen containing groups covalently linked to the carbon atoms on MWCNTs. The deconvoluted $\text{C}1s$ spectrum shows four components and these are assigned to: C-C bonds at 284.2 eV, C-O groups at 285.2 eV, C=O groups at 286.8

eV and the O-C=O moieties at 288.6 eV. The deconvoluted Mo3d core level spectrum (Figure 3.8c) shows four peaks; with the lower energy spin-spin doublet due to the +4 oxidation state of the Mo, at 231.7 and 228.4 eV due to $\text{Mo}^{\text{IV}} 3d_{3/2}$ and $\text{Mo}^{\text{IV}} 3d_{5/2}$ species, respectively. The higher energy, lower intensity peaks (in comparison to Mo^{IV} peaks) at 233 and 229 eV originate from $\text{Mo}^{\text{VI}} 3d_{3/2}$ and $\text{Mo}^{\text{VI}} 3d_{5/2}$ of MoO_3 . Our positions for Mo^{IV} and Mo^{VI} agree well with the reported values for MoO_2 [20]. MoO_3 formation occurs due to the slight surface oxidation of metastable MoO_2 in air. The broad O1s core level spectrum could be split into three deconvoluted components; two components at 533.2 and 531.8 eV are attributable to residual oxygen bonded to carbon in MWCNTs, i.e., C-O and C=O groups and the third component at 530.4 eV arises from the Mo-O bonds (Figure 3.8d).

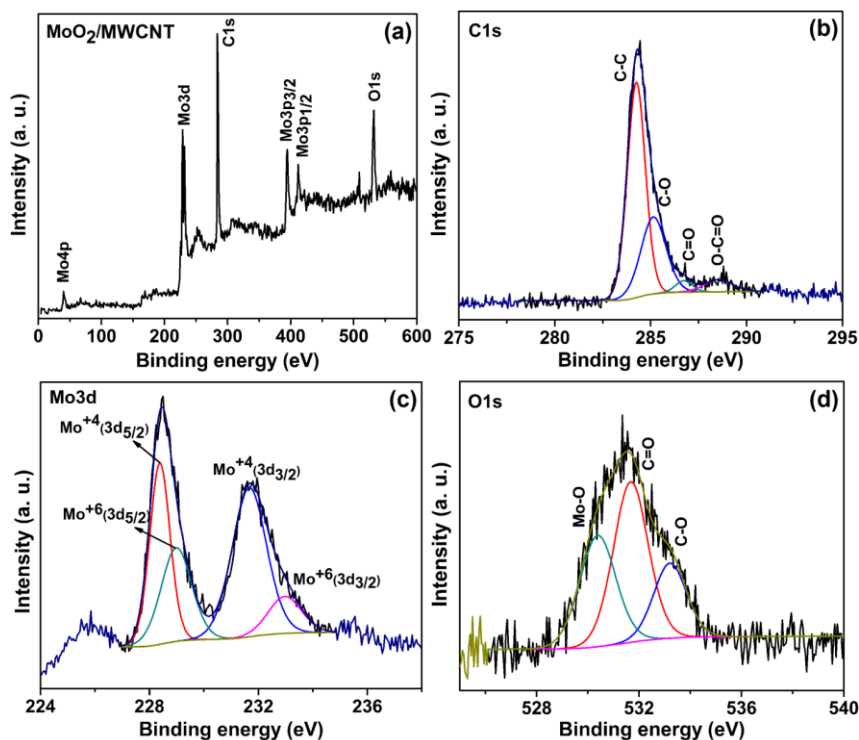


Figure 3.8. (a) XPS survey spectrum of the $\text{MoO}_2/\text{MWCNT}$ hybrid and deconvoluted core level spectra of (b) C1s, (c) Mo3d and (d) O1s of the $\text{MoO}_2/\text{MWCNT}$ hybrid.

3.5. Electrochemical characteristics

Before measuring the electrochemical performance, the amount of MWCNT in the MoO₂/MWCNT hybrid was estimated by performing thermogravimetric analysis (TGA) and differential thermal analysis (DTA) under air flow in the range of 30 to 900 °C. Figure 3.9 shows the TG/DTA curves of neat MWCNTs and the MoO₂/MWCNT hybrid. The DTA curve in Figure 3.9a shows an exothermic peak at 650 °C which corresponds to the complete combustion of MWCNTs. Figure 3.9b exhibits the TG/DTA curves for the as-synthesized MoO₂/MWCNT hybrid. From the TGA curve, a total weight loss of ~ 30% was observed for the MoO₂/MWCNT hybrid up to 700 °C. The DTA shows two broad exothermic peaks; the first peak observed in the temperature range of 200-450 °C is attributed to the oxidation of MoO₂ to MoO₃ and the second peak registered in the range of 450-600 °C is ascribed to the burn-out of MWCNTs. The theoretical value for the weight increase corresponding to the transformation of MoO₂ to MoO₃ is calculated to be 12.5%, and after taking this into consideration, the MWCNT content in the MoO₂/MWCNT hybrid was deduced to be ~17.5%.

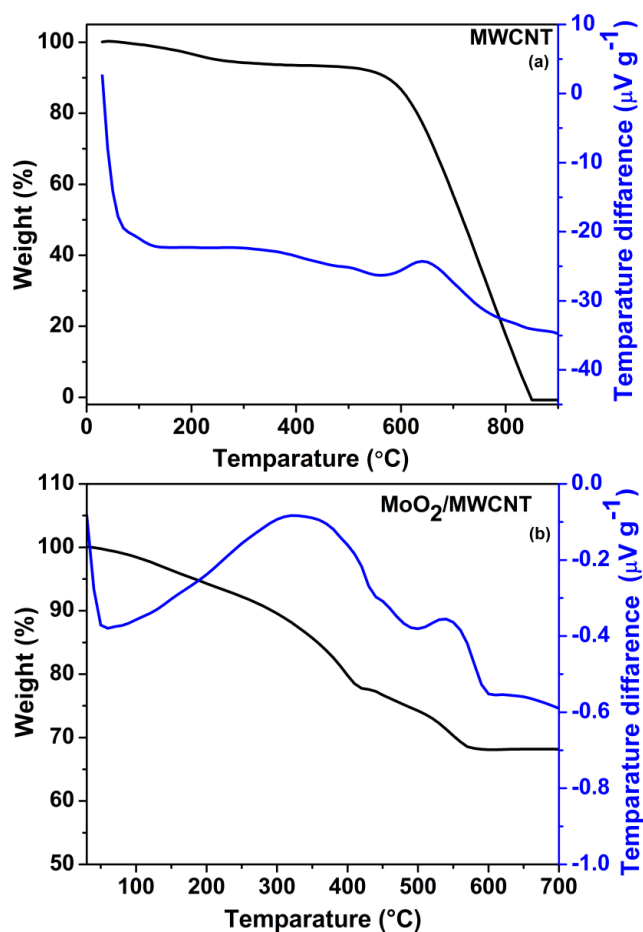


Figure 3.9. TG/DTA curves of (a) neat MWCNTs and (b) MoO₂/MWCNT hybrid.

The Li-ion storage performance of the MoO₂/MWCNT hybrid and neat MoO₂ were measured by CV and galvanostatic charge-discharge experiments. Cyclic voltammograms of the MoO₂/MWCNT hybrid recorded at scan rates of 0.05 and 0.1 mV s⁻¹, respectively, are displayed in Figure 3.10a and b. An irreversible peak observed in the first cycle at 0.45 V during the cathodic discharge, is attributed to the conversion reaction of MoO₂[21] and reduction of solution species to form a passivating film on the anode surface[2,4,22]. In the following cycles, two redox couples located around 1.74/2.37 V and 1.21/1.68 V are observed which are due to the phase transitions of the partially lithiated Li_xMoO₂ during lithium insertion and extraction[23,1-4]. The CV profiles of the MoO₂/MWCNT hybrid remain steady

with cycling whereas the area under the CV curves of neat MoO₂ (Figure 3.10c) decreased with cycling, indicating excellent cycling stability of the MoO₂/MWCNT hybrid compared to MoO₂.

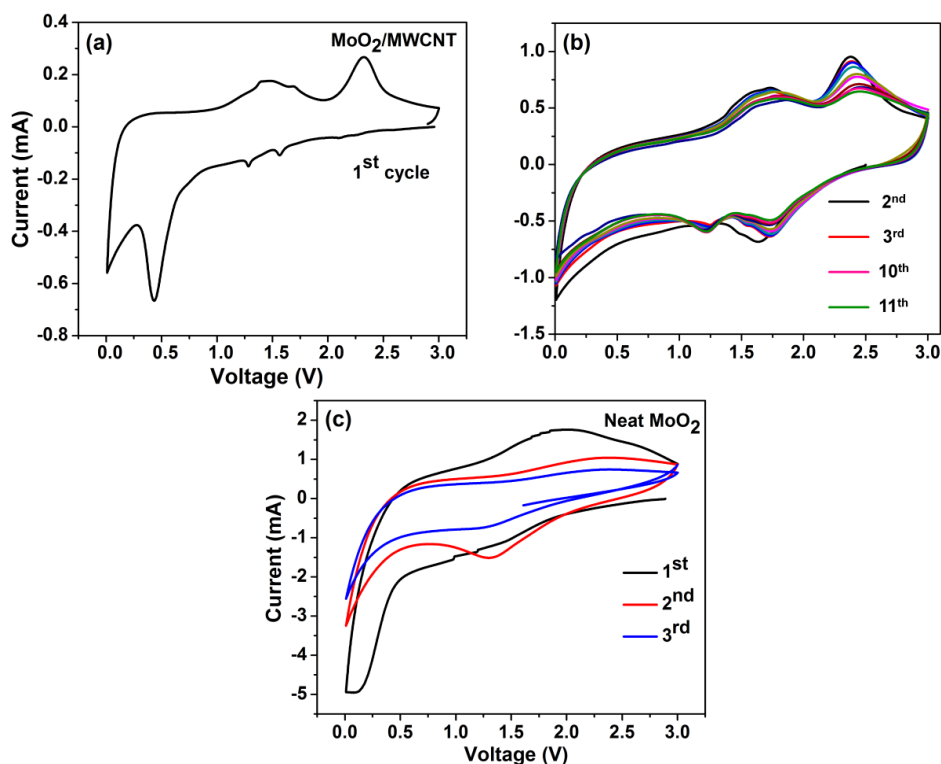


Figure 3.10. Cyclic voltammograms of the MoO₂/MWCNT hybrid at scan rates of (a) 0.05 and (b) 0.1 mV s⁻¹ in the potential range of 0 to 3 V and (c) neat MoO₂ prepared by heating the precursor at 200 °C for 36 h, recorded at a scan rate of 0.1 mV s⁻¹.

The galvanostatic charge-discharge curves of the MoO₂/MWCNT hybrid measured at a current density of 100 mA g⁻¹ and in the voltage range of 0.01 to 3 V are shown in Figure 3.11a. In the first cycle, two discharge plateaus at ~1.6/1.2 V and two charge plateaus around 1.5/2.2 V were observed; these plateaus are reversible in the subsequent cycles. These results agree well with the CV results. The first discharge and charge capacities were deduced to be 2270 and 1243 mAh g⁻¹, respectively, with 55 % coulombic efficiency. It can also be noted that during the

first cycle the irreversible capacity loss, is inevitable for most of the transition metal oxides. According to previous reports[5,6], it is due to the formation of SEI and electrolyte degradation.

Comparison of theoretical and the obtained specific capacities:

The reason for the obtained very high specific capacities than its theoretical limit is shown below. The active material weight of the electrodes was maintained about 1.2 ± 0.5 mg for both neat MoO₂ and MoO₂/MWCNT hybrid (in the latter, this weight represents the collective weight of MoO₂ and MWCNTs). The weights of acetylene black and PVDF binder were excluded. Based on these active material weights and by using a current density of 100 mA g⁻¹ we calculated the specific capacity of MoO₂/MWCNT hybrid.

The theoretical specific capacity of neat MoO₂ was calculated on the basis of 4 Li⁺ insertion/extraction, and it was found to be 838 mAh g⁻¹.

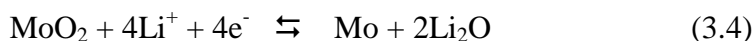
Theoretical specific capacity of MoO₂/MWCNTs hybrid

$$\begin{aligned} &= 82.5\% \text{ MoO}_2 + 17.5\% \text{ MWCNT} \\ &= 82.5\% (838) + 17.5\% (433.5) \\ &= 767.2 \text{ mAh g}^{-1} \end{aligned}$$

The MoO₂/MWCNT hybrid showed a reversible specific capacity of 1243 mAh g⁻¹ for the first cycle. The obtained specific capacity was much higher than the theoretical specific capacity of the MoO₂/MWCNTs hybrid. In earlier reports on MoO_x and other transition metal oxides[24,25], capacities much higher than the theoretical capacities were obtained. The reason for this reversible capacity is due to the reversible formation of Li₂O and Mo at the nanoscale, according to the following reaction: MoO₂ + 4Li ↔ Mo + 2Li₂O. The Mo nanoparticles formed during the first

discharge can catalytically drive the decomposition of electrolyte and formation of electrochemically active polymeric gel-like film on the surface of the electrodes. The extra capacity can also be due to the defect structure of MWCNTs and lithium ions can, in principle, intercalate into the nanoclusters, defect sites, layer sites and even the hollow core of MoO₂ nanoflowers[26].

Figure 3.11b shows the cyclability and Coulombic efficiency of MoO₂/MWCNT hybrid observed at a current density of 100 mA g⁻¹. The MoO₂/MWCNT hybrid shows excellent cycling stability for the measured 200 cycles. After 200 cycles, discharge and charge capacities are 1151.3 and 1143.7 mAh g⁻¹, respectively, with ~99% Coulombic efficiency. After 200 cycles, it retained 92% capacity of the initial cycle. Our values are comparable to those achieved in some of the earlier reports on MoO₂/C composite, MoO₃ nanobelts and MoO₃ nanorods[27-29]. For the complete reduction of Mo (IV) to Mo (0), a maximum specific capacity of 840 mAh g⁻¹ is expected, as per the following equation.



The very high capacity achieved for the MoO₂/MWCNT hybrid is due to the synergy between MoO₂ flower-like nanostructures and MWCNTs. In the MoO₂/MWCNT hybrid, the flower-like shapes of MoO₂ and the tubular structures of MWCNTs account for the high specific area, which increases the ability for Li ion uptake, and the fact that the MoO₂ flowers and the MWCNTs are directly connected, enhances the ability of the electrode to conduct electrons, as MWCNTs are intrinsic electron conductors. Furthermore, the MWCNTs prevent the MoO₂ particles from aggregating and the MoO₂ flowers also inhibit the nanotubes from bundling up.

Analyses of specific capacity variation with cycling:

The gradual decrease in capacity for the initial cycles followed by an increase in capacity with the cyclability has been previously observed for MoO_x [6,28] and for some other transition metal oxides[25,30,31] as well. From the earlier reports, one reason for the gradual increase in capacity after a few cycles is the progressive generation of electrochemically active polymeric gel-like films at the solid electrode interphase. During the discharge branch, at very low voltages, metal particles can catalytically decompose the electrolyte and form a polymeric gel-like film on the surface of the active electrode material. This polymeric gel-like film disappears during the charge process. Since this is a reversible process, it is possibly the reason for the very high capacity of the MoO_2 /MWCNTs hybrid relative to its' theoretical specific capacity. Since the MoO_2 nanosheets are aggregated during the initial discharge-charge cycles (as seen in the FE-SEM image, Figure 3.3e), all the MoO_2 sheets on MWCNTs may not be accessible for the electrolyte for the formation of polymeric gel like film. As the number of discharge-charge cycles increases (e.g., after 100 cycles) the aggregated MoO_2 sheets separate out (can be judged from the corresponding FE-SEM image in Figure 3.12) and allow a high surface contact with electrolyte, and therefore the possibility for the formation of the polymeric gel-like film at the interphase is high. Another reason for the gradual increase in capacity with cycle number is attributed to long term activation process during charge-discharge cycling. This process is associated with partial crystallinity degradation of the electrode material to a disordered or amorphous-like structure during the initial cycling. As a result, more insertion sites are made available and accessible for additional lithium storage, leading to an increase in the specific capacity.

The MoO₂/MWCNT hybrid also showed a good rate performance. The capacity was as high as 408 mAh g⁻¹ even upon increasing the current density by 10 times. At the end of 55 cycles, a capacity of ~ 935 mAh g⁻¹ at a current density of 100 mA g⁻¹ was retained even after several charge discharge cycles at various current densities (Figure 3.11c), indicating the high rate capability and good cycling stability. The effect of MWCNTs on MoO₂ was further explained by comparing the cycling behavior of neat MoO₂, neat MWCNTs and the MoO₂/MWCNT hybrid at 100 mA g⁻¹ current density (Figure 3.11d). Neat MoO₂ exhibits an initial reversible capacity of ~674.8 mAh g⁻¹ and with increasing cycles the capacity fades drastically and after 20 cycles, the capacity reduced to only 380 mAh g⁻¹. On the other hand, neat MWCNTs exhibit an initial capacity 433.5 mAh g⁻¹ and the capacity was almost stable for the measured 20 cycles.

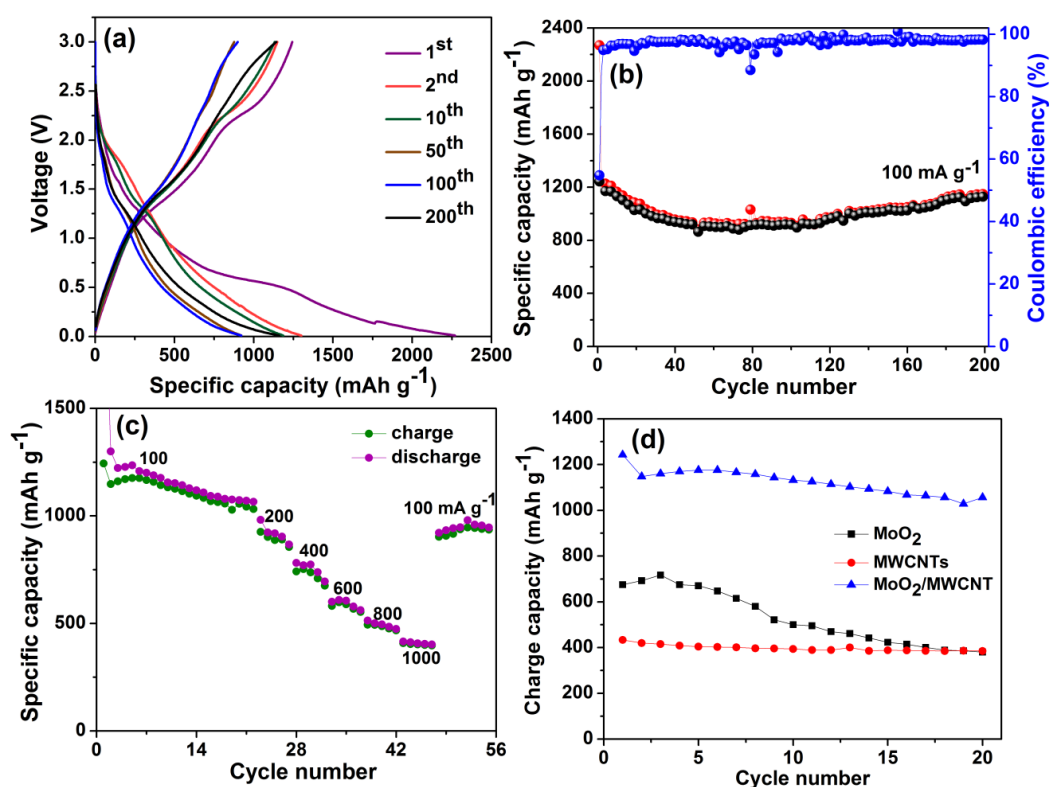


Figure 3.11. (a) Galvanostatic charge-discharge curves, (b) cyclability and coulombic efficiency of the MoO₂/MWCNT hybrid at a current density of 100 mA g⁻¹, (c) rate capability of the MoO₂/MWCNT hybrid and (d) cyclabilities of neat MoO₂, neat MWCNTs and the MoO₂/MWCNT hybrid at a current density of 100 mA g⁻¹.

The FE-SEM images of the MoO₂/MWCNT hybrid after 100 cycles measured at a current density of 100 mA g⁻¹ are shown in Figure 3.12. The FE-SEM images show that after 100 cycles, the flower-like nanostructures are retained but they seem to be composed of interconnected needle-like shapes separated by pores; the overall topology is different from that of the as-fabricated MoO₂/MWCNT hybrid, possibly due to solid electrolyte interphase formation in the cycled sample.

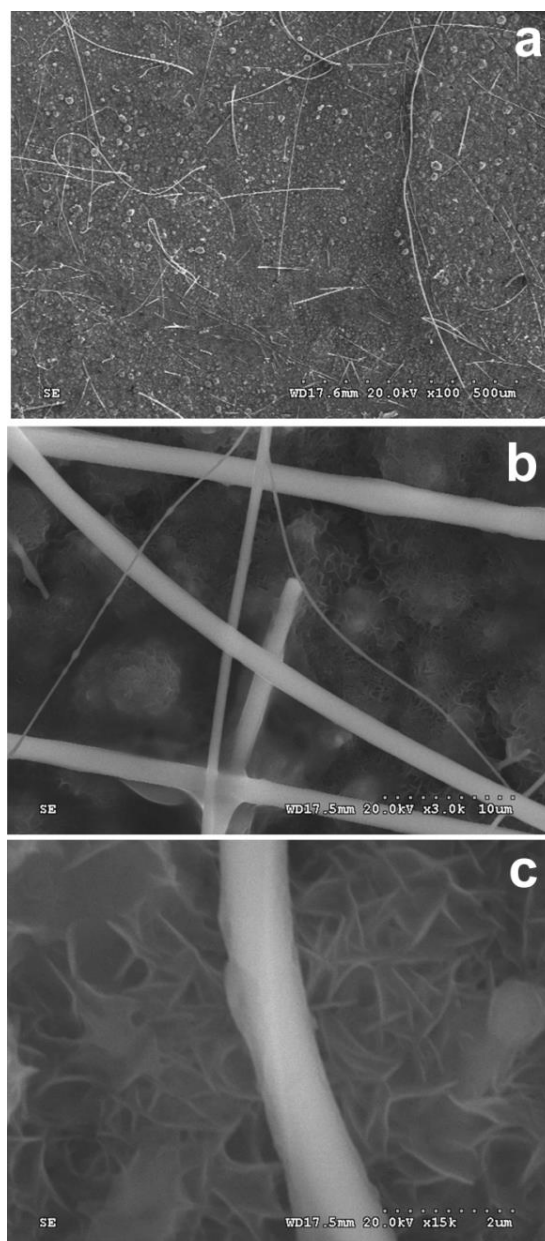


Figure 3.12. FE-SEM images of MoO₂/MWCNT hybrid recorded after 100 cycles at a current density of 100 mA g⁻¹.

3.6. *Ex-situ* XRD analyses and impedance spectra

Ex-situ XRD patterns for the neat MoO₂ and MoO₂/MWCNT hybrid in the intermittent cycles are shown in Figure 3.13. The average crystallite size of the MoO₂ particles in neat MoO₂ and MoO₂/MWCNT hybrid were calculated before and after a few charge-discharge cycles, from their *ex-situ* XRD patterns (Figure

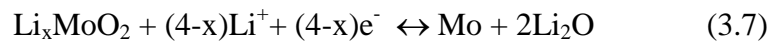
3.13a and b) recorded intermittently. The crystallite size, was calculated using Scherrer's formula:

$$D = \frac{K\lambda}{\beta_{2\theta} \cos \theta} \quad (3.5)$$

where, K is the shape factor taken as 0.94, λ is the X-ray wavelength (0.15406 nm), $\beta_{2\theta}$ is the full width at half maximum of the (011) peak in the patterns for MoO₂ and MoO₂/MWCNT hybrid, and θ is the Bragg angle. The values are summarized below in Table 3.1. The *ab-initio* value of MoO₂ particle size (prior to cycling) in neat MoO₂ is ~48 nm whereas the crystallite size of MoO₂ in MoO₂/MWCNTs hybrid is ~27 nm. The particle size is smaller for the hybrid, owing to the presence of MWCNTs.

For the calculation of particle size of MoO₂, after a few discharge-charge cycles, the *ex-situ* XRD patterns of neat MoO₂ as well as MoO₂/MWCNTs hybrid were recorded. The *ex-situ* XRD patterns were recorded for the cycled samples at a current density of 100 mA g⁻¹. Figure 3.13a shows the *ex-situ* XRD patterns of neat MoO₂. After the completion of the 1st charge-discharge cycle, the particle size of MoO₂ in neat MoO₂ was ~39 nm and after 5 cycles, the particle size reduced to ~24.5 nm. The *ex-situ* XRD patterns of MoO₂/MWCNTs hybrid are shown in Figure 3.13b. After the 1st cycle, the particle size of MoO₂ in the hybrid was ~8.5 nm and after 5 cycles the particle size reduced to ~3.5 nm. This clearly shows that while neat MoO₂ does not undergo complete conversion reaction with cycling, the MoO₂/MWCNT hybrid undergoes quasi- complete conversion reaction during discharge-charge cycles.

It is also noteworthy that after the 1st cycle, the *ex-situ* XRD pattern of neat MoO₂ retains high intensity peaks with small broadening. Even after the completion of 5 cycles, the XRD pattern continues to show distinct, but slightly broadened peaks corresponding to the monoclinic phase of MoO₂. However, after 10 cycles all the peaks shifted to lower 2θ values, which corresponds to lithiated MoO₂ (Li_xMoO₂). When MoO₂ undergoes complete conversion upon repetitive charge-discharge cycling, the electrode acquires an amorphous structure. Since neat MoO₂ remains crystalline even after 10 cycles, it is obvious that it does not undergo lithium intercalation/deintercalation via conversion. We therefore recorded *ex-situ* XRD patterns of neat MoO₂ after 1st discharge and 5th discharge. The pattern shows that the peaks arise from Li_{0.98}MoO₂. Based on the results of XRD patterns as well as in an earlier report[3], here, neat MoO₂ in all likelihood, undergoes Li-ion intercalation/de-intercalation via equation (3.6).



Initially, when neat MoO₂ is discharged to 1 V, it is converted into LiMoO₂, and upon further discharge to 0.01 V, Li_xMoO₂ does not completely convert to Mo and Li₂O, only a part of it probably converts to Mo (based on the observed capacity, shown Figure 3.11d). This could be due to the low electronic conductivity of LiMoO₂, which possibly restricts conversion to Mo. However in the case MoO₂/MWCNT hybrid, almost all of the active MoO₂ is converted into Mo, which is dispersed in the amorphous matrix of Li₂O after 1st discharge. In the hybrid, the MWCNTs provide conductive paths which enable this conversion and hence a very high capacity is achieved for the MoO₂/MWCNTs hybrid.

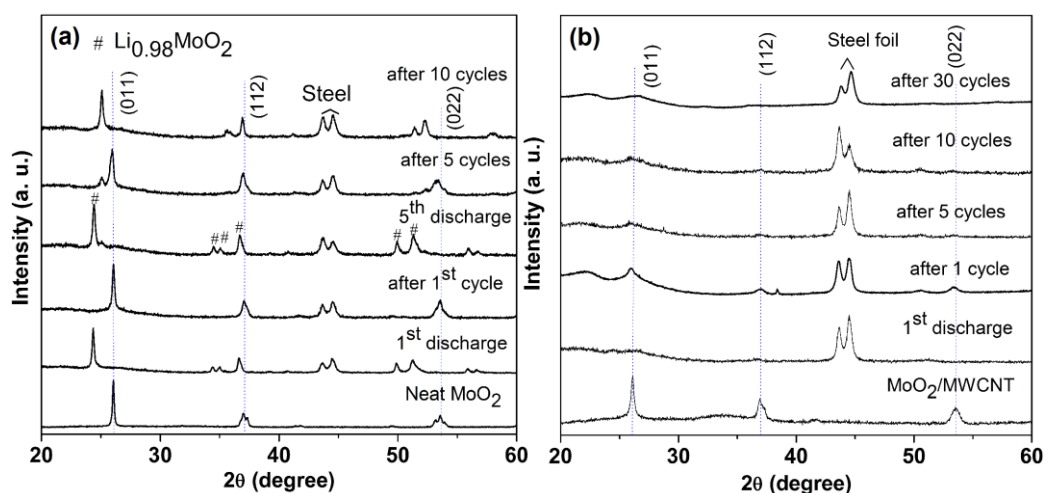


Figure 3.13. *Ex-situ* XRD patterns of (a) neat MoO₂ and (b) MoO₂/MWCNT hybrid prepared hydrothermally at 200 °C for 36 h by adding 2 g of AOT.

Table 3.1.: Crystallite size of MoO₂ determined from the *ex-situ* XRD patterns recorded intermittently during charge-discharge cycles.

Cycle number	Neat MoO ₂ (nm)	MoO ₂ /MWCNT hybrid (nm)
Before cycling	48.43	27.13
After 1 st cycle	38.89	8.50
After 5 cycles	24.50	3.50
After 10 cycles	36.25	Cannot be calculated using Scherrer's formula

EIS spectra were recorded in the initial and intermittent cycling stages and these are presented in Figure 3.14. The plots show one semicircle followed by a straight line with a slant; the latter is limited to only the low frequency region. The semicircle is attributed to a parallel combination of charge transfer resistance (R_{CT}) and electrical double layer capacitance (C_{dl}), and the straight line stems from the diffusion of charged species through the bulk of the electrode material. Nyquist plots of the MoO₂/MWCNT hybrid and neat MoO₂ are shown in Figure 3.14a. The as-fabricated cell of MoO₂/MWCNT hybrid exhibits a lower charge-transfer resistance

as compared to neat MoO₂, indicating that the MWCNTs act as efficient charge carriers and facilitate charge transfer at the interface which can lead to higher capacity as observed herein. The Z'' versus Z' curves for the MoO₂/MWCNT hybrid, recorded at intermittent stages of charge/discharge cycling are shown in Figure 3.14b. From the 1st cycle to 100th cycle, there is no observable change in charge transfer resistance, which implies that the MoO₂/MWCNT hybrid show a good cycling stability. The diffusion coefficient of lithium ion (Li⁺) was determined for the MoO₂/MWCNT hybrid during the 12th discharged state (to 1.5, 1 and 0.01 V, Figure 3.14c) by using the following equation.

$$D = \frac{R^2 T^2}{2n^4 F^4 A^2 C^2 \sigma^2} \quad (3.7)$$

In equation (3.7), R is the universal gas constant, T is the absolute temperature, n is the number of electrons involved in the oxidation/reduction per molecule, F is the faraday constant, A is the surface area of the electrode, C is the bulk concentration of lithium ions and σ is the Warburg factor. The value of σ was deduced from the slope of the linear dependence Z'' (Ω) versus $\omega^{-1/2}$ plots (Figure 3.14d) by restricting to only the low frequency region. From equation (3.7), the D_{Li^+} value after discharge to 1.5 V, for the 12th cycle, is $2.43 \times 10^{-11} \text{ cm}^2 \text{ s}^{-1}$. On further discharging the cell to 1.0 V, the MoO₂/MWCNT hybrid exhibited a D value of $3.31 \times 10^{-11} \text{ cm}^2 \text{ s}^{-1}$. Upon further discharge to 0.01 V, a D_{Li^+} of $9.2 \times 10^{-12} \text{ cm}^2 \text{ s}^{-1}$ was obtained. For neat MoO₂, for the 8th discharge to 1.0 V (Figure 3.15), a D_{Li^+} of $4.18 \times 10^{-14} \text{ cm}^2 \text{ s}^{-1}$ was observed, which is two orders of magnitude lower than that of the MoO₂/MWCNT hybrid. It is evident that the MoO₂/MWCNT hybrid has a microstructure which is

more conducive for Li-ion transport as compared to the neat oxide and is therefore a promising candidate for anodes in practical Li-ion batteries.

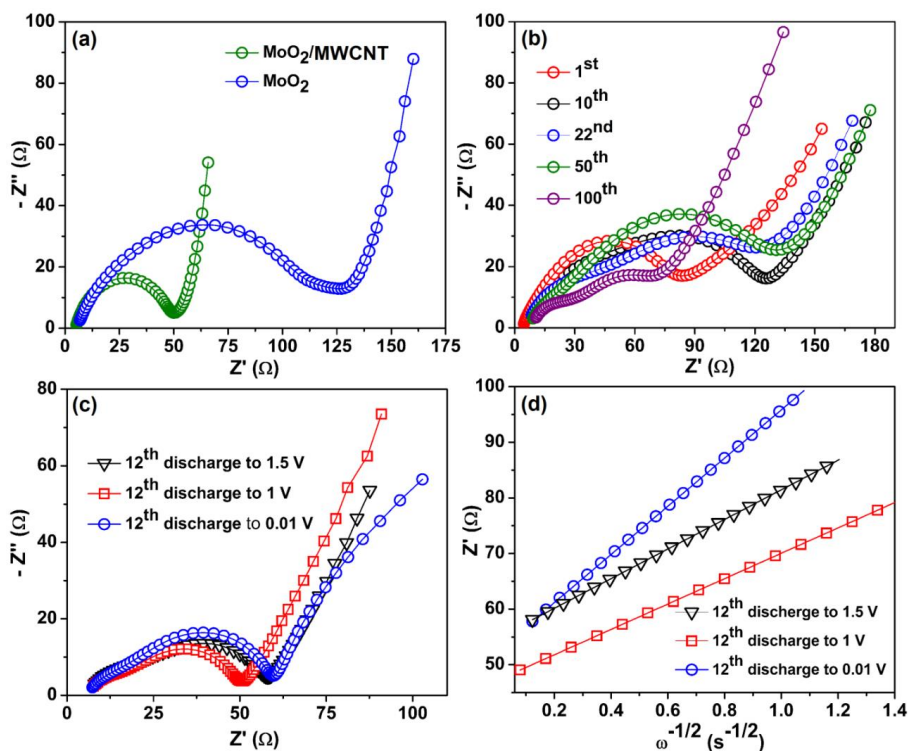


Figure 3.14. (a) Comparison of Nyquist plots of neat MoO₂ with the MoO₂/MWCNT hybrid, (b) Nyquist plots recorded intermittently during charge-discharge cycles of the MoO₂/MWCNT hybrid (c) Nyquist plots at 1.5, 1 and 0.01 V during the 12th discharge (d) Z' versus $\omega^{-1/2}$ curves in the low frequency region of the MoO₂/MWCNT hybrid.

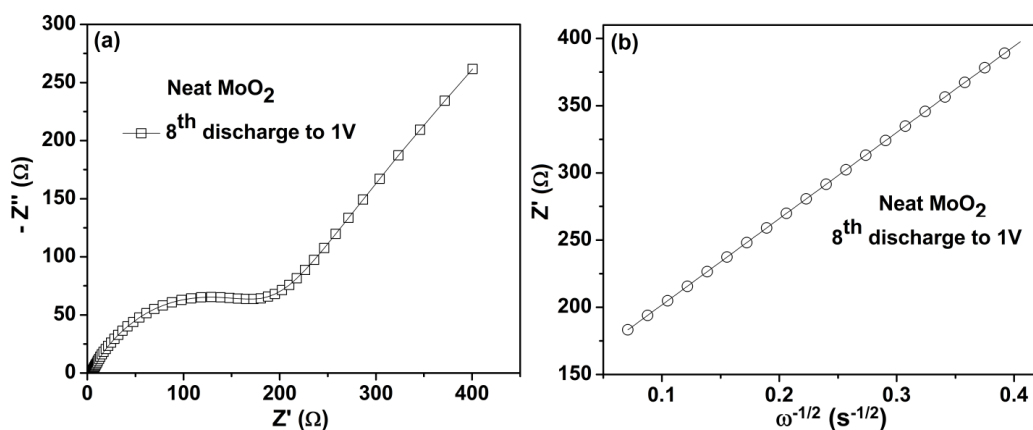


Figure 3.15. (a) Nyquist plots and (b) Z' versus $\omega^{-1/2}$ curves in the low frequency region of neat MoO₂ for the 8th discharge to 1 V.

3.7. Summary

A MoO₂/MWCNT hybrid composed of spherical floral nanostructures of MoO₂, interlinked with curved MWCNTs was synthesized by a hydrothermal route. The formation of MoO₂ flower-like shapes is dictated by the surfactant, AOT. The unique nanoscale architecture of the MoO₂/MWCNT hybrid is responsible for a large reversible electrochemical lithium storage capacity of 1025.2 mA h g⁻¹ achieved at a current density of 100 mA g⁻¹ after 160 cycles in comparison to a much lower value of 220 mA h g⁻¹ (after 20 cycles) obtained for neat MoO₂. The inherent electron conducting nature of MWCNTs enabled efficient electron transfer and transport in the MoO₂/MWCNT hybrid by the virtue of the direct interconnects formed between MoO₂ flowers and MWCNTs. The unusual topology of the MoO₂/MWCNT hybrid, the high rate capability (as it shows a capacity of 408 mAh g⁻¹ at a high current density of 1000 mA g⁻¹) and the excellent cyclability demonstrate its utilitarian value as a high performance anode in Li-ion batteries. Our simple single step approach for fabricating a MoO₂/MWCNT hybrid shows that this strategy can be applied to other oxides as well to yield unique architectures for Li-ion battery anodes.

References

1. Y. Shi, B. Guo, S. A. Corr, Q. Shi, Y. S. Hu, K. R. Heier, L. Chen, R. Seshadri, G. D. Stucky, *Nano Lett.*, 9 (2009) 4215-4220.
2. Q. Gao, L. Yang, X. Lu, J. Mao, Y. Zhang, Y. Wu, Y. Tang, *J. Mater. Chem.*, 20 (2010) 2807-2812.
3. B. Guo, X. Fang, B. Li, Y. Shi, C. Ouyang, Y. S. Hu, Z. Wang, G. D. Stucky, L. Chen, *Chem. Mater.*, 24 (2012) 457-463.
4. L. C. Yang, Q. S. Gao, Y. H. Zhang, Y. Tang, Y. P. Wu, *Electrochem. Commun.*, 10 (2008) 118-122.

5. L. Zhou, H. Bin Wu, Z. Wang, X. W. Lou, *ACS Appl. Mater. Interfaces*, 3 (2011) 4853-4857.
6. Y. Sun, X. Hu, W. Luo, Y. Huang, *J. Mater. Chem.*, 22 (2012) 425-431.
7. X. Ji, P. S. Herle, Y. Rho, L. F. Nazar, *Chem. Mater.*, 19 (2007) 374-383.
8. A. Bhaskar, M. Deepa, T. N. Rao, U. V. Varadaraju, *J. Power Sources*, 216 (2012) 169-178.
9. Y. Sun, X. Hu, W. Luo, Y. Huang, *ACS Nano*, 5 (2011) 7100-7107.
10. Y. Xu, R. Yi, B. Yuan, X. F. Wu, M. Dunwell, Q. L. Lin, L. Fei, S. G. Deng, P. Andersen, D. H. Wang, H. M. Luo, *J. Phys. Chem. Lett.*, 3 (2012) 309-314.
11. S. Iijima, *Nature*, 354 (1991) 56-58.
12. K. Balasubramanian, M. Burghard, *Small*, 1 (2005) 180-192.
13. S. C. Wang, H. Yang, S. Banerjee, I. P. Herman, D. L. Akins, *Mater. Lett.*, 62 (2008) 843-845.
14. M. F. Islam, E. Rojas, D. M. Bergey, A. T. Johnson, A. G. Yodh, *Nano Lett.*, 3 (2003) 269-273.
15. R. Rastogi, R. Kaushal, S. K. Tripathi, A. L. Sharma, I. Kaur, L. M. Bharadwaj, *J. Colloid Interface Sci.*, 328 (2008) 421-428.
16. Y. Bai, I. S. Park, S. J. Lee, P. S. Wen, T. S. Bae, M. H. Lee, *Colloids Surfaces B: Biointerfaces*, 89 (2012) 101-107.
17. C. Masarapu, V. Subramanian, H. Zhu, B. Wei, *Adv. Funct. Mater.*, 19 (2009) 1008-1014.
18. D. Baskaran, J. W. Mays, M. S. Bratcher, *Angew. Chem. Int. Ed.*, 43 (2004) 2138-2142.
19. Z. Xu, L. Wang, Q. Zheng, *Small*, 4 (2008) 733-737.
20. X. Zhao, M. Cao, B. Liu, Y. Tian, C. Hu, *J. Mater. Chem.*, 22 (2012) 13334-13340.
21. Y. S. Jung, S. Lee, D. Ahn, A. C. Dillon, S. H. Lee, *J. Power Sources*, 188 (2009) 286-291.
22. Y. Sun, X. Hu, J. C. Yu, Q. Li, W. Luo, L. Yuan, W. Zhanga, Y. Huang, *Energy Environ. Sci.*, 4 (2011) 2870-2877.
23. J. R. Dahn, W. R. McKinnon, *Solid State Ionics*, 23 (1987) 1-7.

24. C. Peng, B. Chen, Y. Qin, S. Yang, C. Li, Y. Zuo, S. Liu, J. Yang, *ACS Nano*, 6 (2012) 1074-1081.
25. S. Grugeon, S. Laruelle, L. Dupont, J. M. Tarascon, *Solid State Sci.*, 5 (2003) 895-904.
26. C. Q. Feng, J. Ma, H. Li, R. Zeng, Z. P. Guo, H. K. Liu, *Mater. Res. Bull.*, 44 (2009) 1811-1815.
27. Z. Wang, J. S. Chen, T. Zhu, S. Madhavi, X. W. Lou, *Chem. Commun.*, 46 (2010) 6906-6908.
28. J. S. Chen, Y. L. Cheah, S. Madhavi, X. W. Lou, *J. Phys. Chem. C*, 114 (2010) 8675-8678.
29. Z. Wang, S. Madhavi, X. W. Lou, *J. Phys. Chem. C*, 116 (2012) 12508-12513.
30. J. S. Do, C. H. Weng, *J. Power Sources*, 146 (2005) 482-486.
31. S. Laruelle, S. Grugeon, P. Poizot, M. Dollé, L. Dupont, J. M. Tarascon, *J. Electrochem. Soc.*, 149 (2002) A627-A634.

Chapter 4

Influence of Graphene on Li-Ion Storage in a MoO₂/Graphene Composite

4.1. Abstract

In this chapter, the use of MoO₂ for preparing high performance composites was further explored, by coupling it with Graphene. The MoO₂/Graphene composite was studied by XRD, FE-SEM, TEM, Raman spectroscopy, XPS and conducting atomic force microscopy (CAFM). The structural features of the composite and the remarkably high nanoscale current conduction capability of the composite were correlated to the outstanding capacity, rate capability and cycling performance (when employed as an anode in a Li ion battery). The performance of MoO₂/Graphene is considerably enhanced in comparison to neat Graphene, neat MoO₂ and even MoO₂/Graphene oxide (the latter three prepared herein).

4.2. Introduction

Commercial Li-ion batteries use graphite as the anode material which is characterized by a theoretical specific capacity of 372 mAh g⁻¹. Graphite by the virtue of its layered structure allows a reversible Li-insertion and extraction reaction during discharging and charging, respectively. But a low specific capacity, as six carbon atoms are required to accommodate one Li ion and abuse tolerance issues from Li plating limit its performance[1,2]. To attain higher lithium storage capacities, one exciting approach involves the synthesis of composites of oxides with carbon; the latter enhances the electronic conductivity and as a consequence the overall battery performance[3], however, the carbon coating on the metal oxide is not sufficient to buffer the volume expansion and contraction incurred by oxides

during charge/discharge processes. To address this concern, one dimensional monolayers of graphene with atomic thickness are useful as they exhibit a very high surface area ($2600 \text{ m}^2 \text{ g}^{-1}$ per sheet), large thermal and electronic conductivities, chemical resistance and mechanical flexibility[4-6]. Graphene layers prevent both volume changes and aggregation of metal oxide nanoparticles during charge/discharge processes as the oxide nanoparticles are sandwiched between the sheets and therefore cannot agglomerate. Furthermore, the attachment of metal oxide or any other inorganic moiety on graphene effectively inhibits the restacking of graphene layers. In the past, composites of graphene with Fe_3O_4 , Fe_2O_3 , Co_3O_4 , SnO_2 and TiO_2 , have been attempted and they have shown higher capacity, rate capability and cyclability as compared to their bulk oxide counterparts[7-11].

Among transition metal oxides capable of functioning as anodes, nanostructured molybdenum dioxide (MoO_2) undergoes Li^+ insertion/extraction reactions with a concurrent four electron insertion/extraction and this corresponds to a theoretical specific capacity of 838 mAh g^{-1} . Among several reports on MoO_2 and composites [12-20] as a Li-ion battery anode material, a report on a MoO_2 /Graphene composite by Sun and co-workers is noteworthy, as they achieved a reversible capacity of 342 mAh g^{-1} in the first cycle and a capacity of 598 mAh g^{-1} was acquired at the end of 70 cycles at a current density of 1000 mA g^{-1} [21]. But it must be mentioned that authors in [21] employed an elevated temperature process whereby they achieved a hierarchical assembly of MoO_2 nanoparticles and graphene layers. In this chapter, a simple one pot *in-situ* low temperature solution phase reduction method which allowed a homogeneous embedding of MoO_2 nanoparticles in reduced graphene oxide nanosheets, thus allowing an intimate and direct contact between the two

entities, is presented. Previous reports on MoO₂/Graphene or a transition metal oxide/Graphene composite have largely employed hydrazine as a reducing agent for reducing Graphene oxide to Graphene which is highly toxic[9,21].

In the present chapter, we circumvented the issue of toxicity, by using non-toxic citric acid along with Poly(ethylene glycol) or PEG to reduce Graphene oxide (GO) to Graphene, which is incidentally also a relatively inexpensive approach. By confining to a hydrothermal process for Graphene formation and conversion of the metal oxide precursor to MoO₂, the reaction was performed at a low temperature. Furthermore, the role of citric acid in controlling the reduction of Graphene oxide to Graphene by preparing samples using a protocol devoid of citric acid was studied. The MoO₂/Graphene composite structure was correlated with its electrochemical property.

4.3. Experimental

4.3.1 Chemicals

Graphite flakes (Aldrich), ammonium heptamolybdate ((NH₄)₆Mo₇O₂₄·4H₂O) (AHM) (99%, Merck), KMnO₄ (99%, Merck), Poly(ethylene glycol) 400 (PEG 400, Merck) and citric acid anhydrous (C₆H₈O₇, 99.5 %, Merck) were used as received. Reagents: H₂SO₄ (98%), H₃PO₄ (88%) and H₂O₂ (30%) of GR grade were purchased from Merck. Ultrapure water (resistivity~ 18.2 MΩ cm) obtained through Millipore Direct-Q3 UV system was used as solvent.

4.3.2. Preparation of Graphene oxide and MoO₂/Graphene

Graphene oxide (GO) was prepared by an improvised method[22,23], wherein graphite flakes (1.5 g) and KMnO₄ (9 g) was added slowly to a concentrated H₂SO₄/H₃PO₄ mixture (9:1 v/v) over a period of 30 min followed by continuous

stirring for 12 h at 50 °C. The reaction mixture was poured onto a mixture of ice water (200 mL) and 30% H₂O₂ (3 mL). The solution was centrifuged for 1 h at 4000 rpm, and the supernatant liquid was decanted away. The centrifugate was again washed with water (100 mL) followed by 30% HCl (100 mL) and ethanol (100 mL) washes. Successive washings with water and ethanol were repeated twice and the resultant suspension was dried in vacuum for 12 h at 50 °C till a dry black solid of GO was isolated, which was stored in nitrogen. To a dispersion of GO (100 mg) in water (50 mL), 0.56 mM AHM in water (20 mL), citric acid and PEG mixed in a 1:3 molar ratio were added. The solution was placed in a 100 mL Teflon lined autoclave and heated in a vacuum oven at 180 °C for 24 h. The resulting black colored MoO₂/Graphene composite was filtered and washed with water, dried and stored in inert atmosphere. Similarly, the MoO₂/Graphene composite also prepared with 70 and 130 mg of GO and the remaining all parameters maintained constant. Further, to study the effect of citric acid in inducing the reduction of Graphene oxide, a composite was prepared using the exactly same procedure, but without citric acid and the resulting product was designated as MoO₂/Graphene oxide.

4.3.3. Preparation of Graphene

To a dispersion of GO (100 mg) in water (50 mL), citric acid and PEG mixed in a 1:3 molar ratio (0.25 g citric acid, 1.56 g PEG) in 20 mL of water were added. The solution was placed in a 100 mL Teflon lined autoclave and heated in a vacuum oven at 180 °C for 26 h. The resulting Graphene was filtered and washed with water, dried and stored in an inert atmosphere. The weight of the resulting product (Neat Graphene) is 33.2 % of the total weight of the MoO₂/Graphene composite. Similarly with 70 mg and 130 mg of GO, the weight of the resulting product is, respectively

21% and 40.5% of the total weight of the MoO₂/Graphene composite. By taking 100, 70 and 130 mg of GO results a MoO₂/Graphene ratios in 2:1, 3.76:1 and 1.45:1.

4.3.4. Preparation of MoO₂

To a dispersion, 0.558 mM AHM in water (50 mL), citric acid and PEG mixed in a 1:3 molar ratio (0.25 g citric acid, 1.56 g PEG) in 20 mL were added. The solution was placed in a 100 mL Teflon lined autoclave and heated in a vacuum oven at 180 °C for 26 h. The resulting product designated as neat MoO₂ was filtered and washed with water, dried and stored in an inert atmosphere.

4.3.5. Preparation of MoO₂/Graphene oxide

To a dispersion of GO (100 mg) in water (50 mL), 0.558 mM AHM in water (20 mL) and 1.56 g of PEG were added. The solution was placed in a 100 mL Teflon lined autoclave and heated in a vacuum oven at 180 °C for 26 h. The resulting product labeled as MoO₂/Graphene oxide composite, was filtered and washed with water, dried and stored in an inert atmosphere.

4.4. Results and discussion

4.4.1. X-ray diffraction and Raman spectra

XRD patterns of the neat MoO₂, neat Graphene and MoO₂/Graphene composite are shown in Figure 4.1. The XRD pattern of the MoO₂/Graphene composite shows intense well-resolved peaks at $d = 3.42, 2.44$ and 1.71 \AA corresponding to (110), (200) and (220) planes of monoclinic MoO₂ with space group: P2₁/c(14), in concordance with JCPDF: 86-0135, thus indicating that the crystal structure of MoO₂ is preserved in the composite. The Raman spectra of GO and MoO₂/Graphene composite are shown in Figure 4.2. The Raman spectrum of neat GO shows the D band, attributable to surface defects at 1350 cm^{-1} and the G peak at 1588 cm^{-1} which

is ascribed to the in-plane vibration of sp^2 hybridized carbon atoms. The lower intensity of the D-band relative to the G-band, shows that the defect concentration in pristine GO is low, which is advantageous for improving conductive properties. In the Raman spectrum of MoO_2 /Graphene, the D and G bands are retained, albeit the relative intensities are reversed vis-a-vis neat GO. The positions of the D and G bands are also downshifted to 1309 and 1585 cm^{-1} , indicating the conversion of GO to Graphene upon composite formation. It must be recalled that this is the Raman spectrum of the product (labeled by us as MoO_2 /Graphene) formed after the hydrothermal processing of GO, molybdenum salt, citric acid and PEG. In addition, strong intense peaks are observed at 816 and 988 cm^{-1} , attributable to $\nu(Mo-O-Mo)$ and $\nu(Mo=O)$ stretching modes of MoO_2 , clearly affirming the inclusion of MoO_2 in graphene. The inset of Figure 4.2 shows the Raman spectrum of neat GO and MoO_2 /GO composite. Since the positions of D and G bands on going from the GO to the MoO_2 /GO composite show no difference, it is apparent, that citric acid is essential to bring about the reduction of GO to Graphene. For if it had been otherwise, then this product obtained after processing GO, molybdenum salt with PEG, which has been labeled by us as MoO_2 /GO, should have shown downshifted D and G bands relative to GO as observed for the product (labeled by us as MoO_2 /Graphene) obtained by using the same reactants, alongwith citric acid. It is apparent that citric acid is essential to bring about the reduction of GO to Graphene.

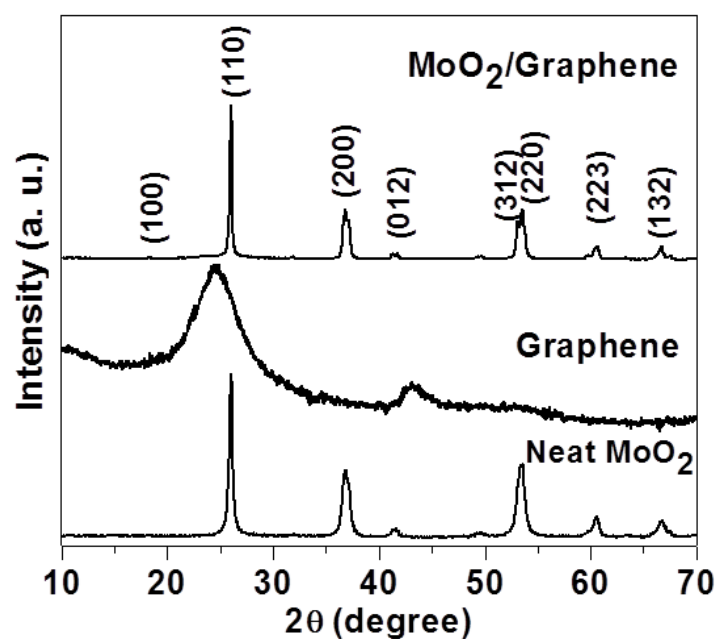


Figure 4.1. XRD patterns of neat MoO₂, neat Graphene and MoO₂/Graphene composite.

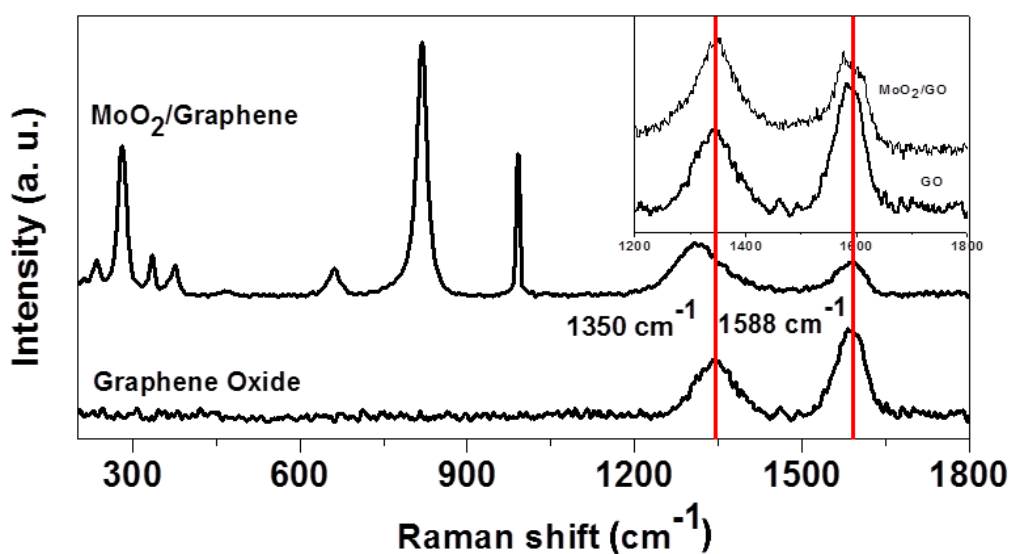


Figure 4.2. Raman spectra of MoO₂/Graphene and graphene oxide; the solid lines pass through the D and G bands in Graphene oxide. Inset shows a comparison of Raman spectra of MoO₂/Graphene oxide and Graphene oxide.

4.4.2. Electron microscopy

SEM images of neat Graphene, neat MoO₂ and MoO₂/Graphene composite are shown in Figure 4.3. Stacks of overlapping Graphene nanosheets with foldings and

wrinkles which are characteristic of Graphene, can be seen in Figure 4.3a and b[24]. The image of neat MoO₂ shows an interconnected framework of MoO₂ grains of irregular shapes (Figure 4.3c). The grains are compactly packed and they tend to form large aggregates. The low magnification image of the MoO₂/Graphene composite is representative of Graphene than of MoO₂, as it shows mingling closely packed thick flakes of Graphene with well-defined edges that seem to be protruding outwards. The wavy crumpled nature of Graphene platelets is retained in the composite and a closer inspection of the high magnification image (Figure 4.3e) shows the MoO₂ grains to be uniformly entrenched in the GO nanosheets. The low temperature hydrothermal route adopted in this report, for combining MoO₂ with Graphene allows the formation of a composite, wherein a direct contact between the two moieties could be achieved. Such an intimate connectivity between MoO₂ nanoparticles and Graphene plays a significant role in improving the electronic conduction properties of the composite, thus promoting charge transport and transfer during charge/discharge cycles. The slight difference in contrast and morphology relative to that obtained for neat Graphene is also an indicator to MoO₂/Graphene composite formation. Direct evidence for successful formation of the composite was obtained through elemental mapping and energy dispersive X-ray analysis (EDS) results which are collected in Figure 4.3f. The elemental maps of carbon, oxygen and molybdenum collected from the SEM image of the composite shown in Figure 4.3d, clearly delineate a uniform and homogeneous distribution of the three elements across the specimen, thus confirming the co-existence of Mo with C and O; the latter two being the principal constituents of GO. EDS pattern also shows prominent

signals due to C, O and Mo, again affirming the successful integration of MoO₂ with Graphene.

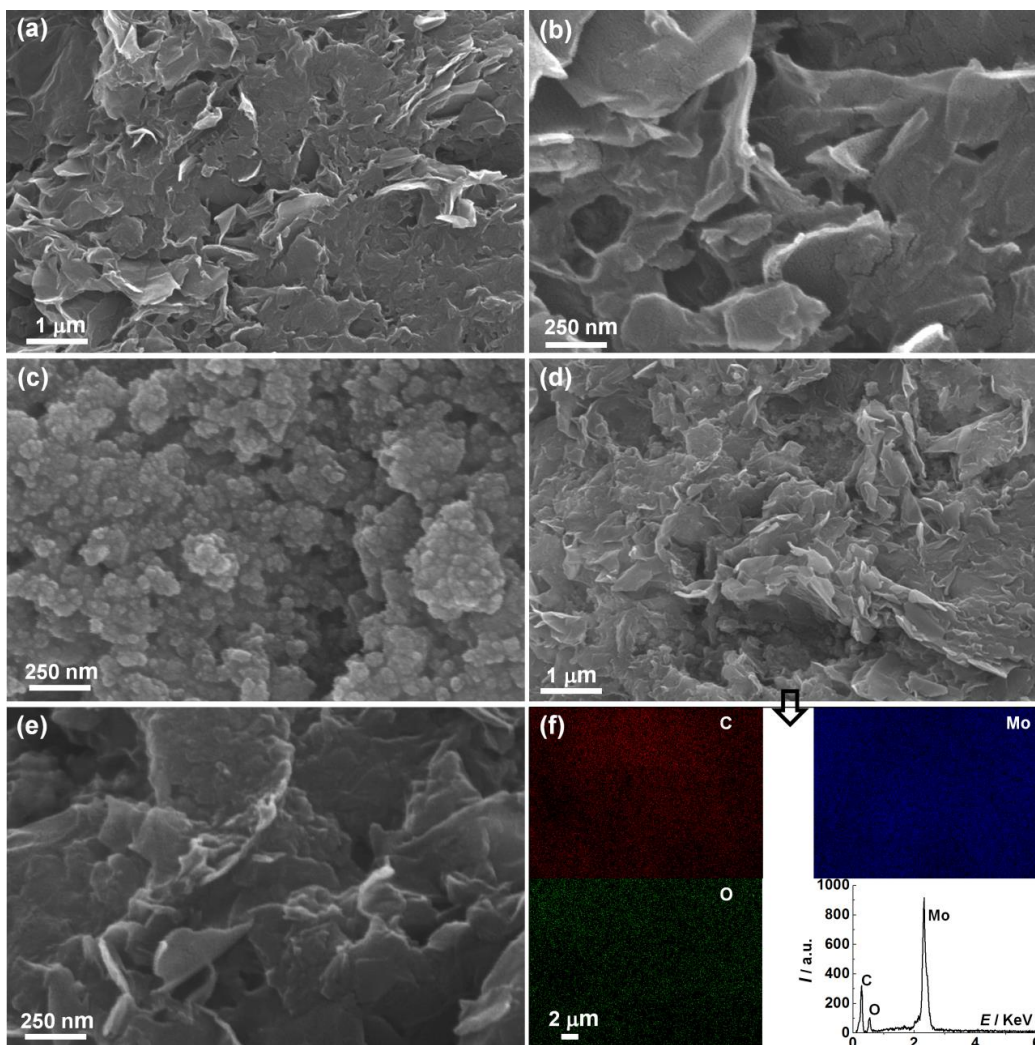


Figure 4.3. SEM images of GO at (a) low and (b) high magnifications, (c) neat MoO₂, (d) low and (e) magnification images of MoO₂/Graphene and (f) elemental maps of C, O and Mo in MoO₂/Graphene and an EDS plot of MoO₂/Graphene.

The TEM micrographs of neat Graphene, MoO₂ and MoO₂/Graphene composite are shown in Figure 4.4. The presence of few-layer graphene with well-defined edges, and the silk veil like texture of the nanosheets is also discernible from Figure 4.4a and b. The nanosheets appear to spread over a few microns in length, indicating that the exfoliated sheets even after chemical reduction, are able to retain a high

aspect ratio. The sheets are tangled, which is a signature of few-layer graphene[25]. Bright field image of neat MoO₂ (Figure 4.4c) shows densely packed agglomerates of MoO₂. The nano-platelet morphology of Graphene is best suited for forming composites with a transition metal oxide as it can easily accommodate a large quantity of the electroactive intercalant: MoO₂, which can easily slide between the nanosheets and remain entrapped therein by the virtue of electrostatic interactions between the positively charged metal ion, Mo⁴⁺ and the negatively charged carboxylate groups and the oxygens on the epoxy and hydroxyl groups, which are flanked to the graphene sheets. The TEM images of the composite (Figure 4.4d) show that the MoO₂ grains are indeed embedded in the nanosheets of graphene and the fact that these oxide grains are homogeneously implanted in the graphene oxide nanosheets is evidenced from Figure 4.4f, wherein a uniform and continuous coverage of the nanosheets by MoO₂ is attained. Well-defined plane facets of MoO₂ can also be seen in some regions of the composite (Figure 4.4e), indicating a preferred orientation for these crystallites.

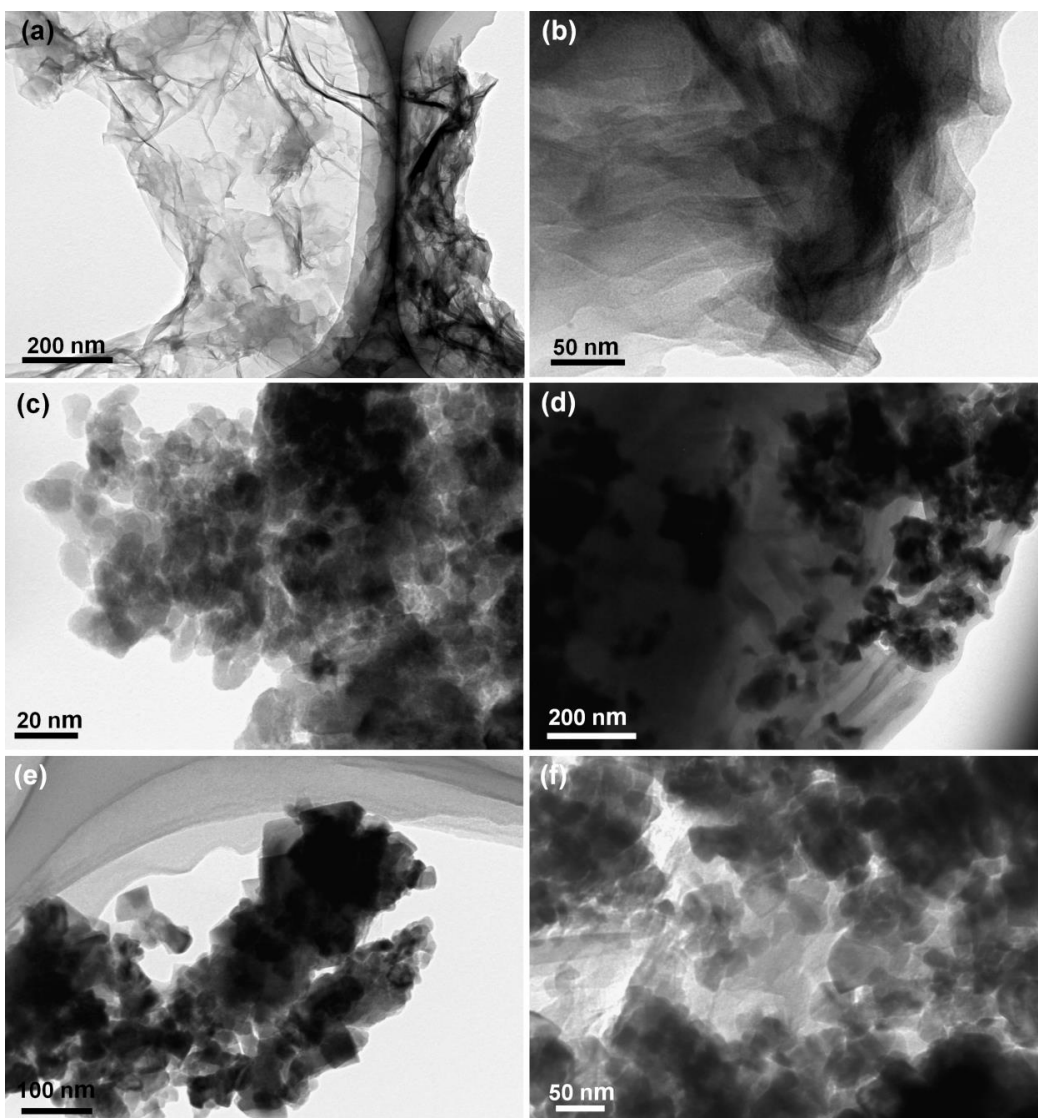


Figure 4.4. TEM micrographs of GO at (a) low and (b) high magnifications, (c) neat MoO₂, (d,e,f) MoO₂/Graphene composite at different magnifications; plane facets of MoO₂/Graphene crystallites with well-defined shapes can be seen in e and f.

4.4.3. XPS and C-AFM

XPS survey and core level spectra of MoO₂/Graphene composite are shown in Figure 4.5. The survey spectrum (Figure 4.5a) of the composite shows distinct signals at 232.9, 284.3, 397.7, 415.1 and 531.2 eV which are assigned to the Mo3d, C1s, Mo3P_{3/2}, Mo3P_{1/2} and O1s respectively; indicating the contributions from both MoO₂ and Graphene. The asymmetrical profile of the C1s signal (Figure 4.5b)

reflects different chemical environments for carbon, which obviously stems from the presence of different oxygen containing groups associated with carbon atoms on graphene. The deconvoluted C1s spectrum shows four components and these are ascribed to C-C bonds at 284.6 eV, C-O groups at 286.2 eV, C=O groups at 287.5 eV and the O-C=O moieties at 288.8 eV. The deconvoluted Mo3d core level spectrum (Figure 4.5c) shows four peaks; with the lower energy spin-spin doublet due to the +4 oxidation state of the Mo, at 232.19 and 229.06 eV due to Mo^{IV}3d_{3/2} and Mo^{IV} 3d_{5/2}. The higher energy, lower intensity peaks (in comparison to Mo^{IV} peaks) at 234 and 230 eV arise from Mo^{VI} 3d_{3/2} and Mo^{VI} 3d_{5/2} of MoO₃ resulting from the slight surface oxidation of metastable MoO₂ in air. The O1s core level spectrum shows two deconvoluted contributions at 533.6 and 531.5 eV, corresponding to residual oxygen bonded to carbon in Graphene and oxygen associated with MoO₂ respectively (Figure 4.5d). The oxygen content in reduced GO was determined by integrating the area of the curves in the XPS core level C1s spectrum of the composite (Figure 4.5b) which represents the contributions from C-O groups (C=O, C-O, O-C=O). The area thus obtained is divided by the sensitivity factor to yield the oxygen content. The oxygen content is deduced to be 25.4% which is also consistent with an oxygen content of 24% reported previously by Shen et.al., for a TiO₂/Graphene hybrid material[26]. The core level spectra again provide conclusive evidences for incorporation of MoO₂ nanoparticles in Graphene monolayers.

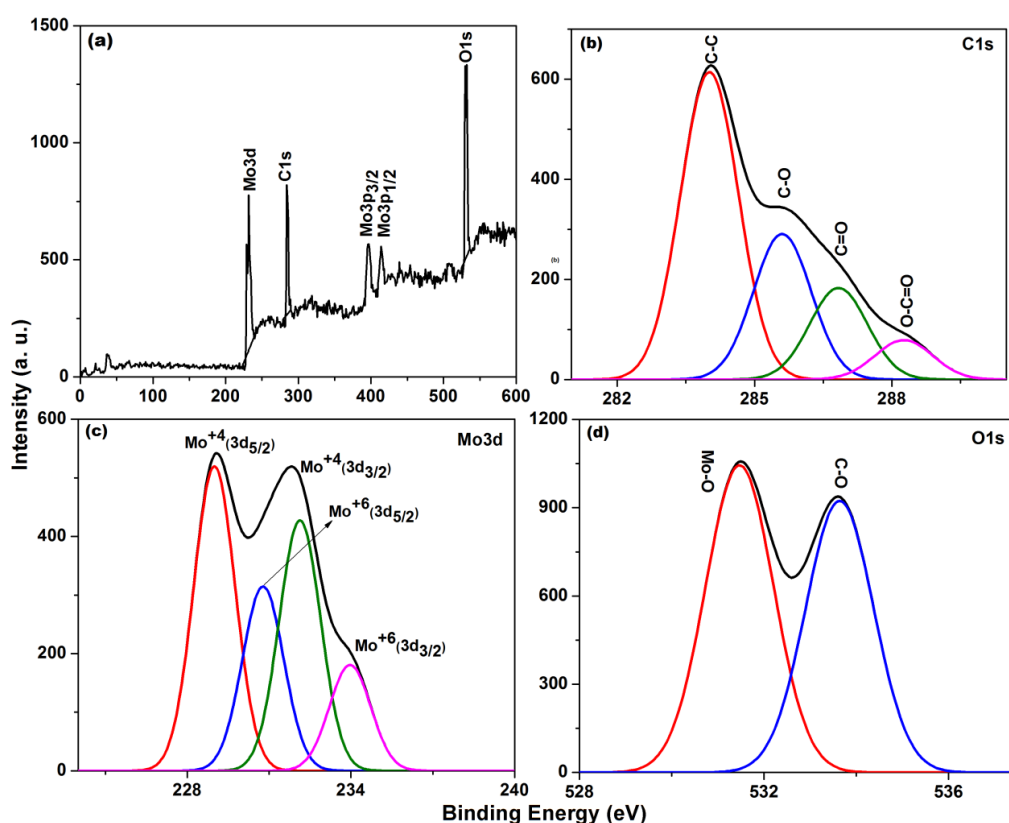


Figure 4.5. (a) survey spectrum of MoO₂/Graphene and deconvoluted core level (b) C1s, (c) Mo3d and (d) O1s of MoO₂/Graphene.

Current image of the MoO₂/Graphene composite (Figure 4.6a) obtained by C-AFM shows the presence of interconnected conducting domains spread over regions of about few micron dimensions (bright regions), and the maximum current is remarkably high ($\sim 1.2 \mu\text{A}$) contrasting against an i_{max} of only $7 \times 10^{-5} \mu\text{A}$ in neat MoO₂ (Figure 4.6b). Such an enormous differential by almost five orders of magnitude reflects the high current carrying capacity of the composite, beneficial for charge transport. The regions enclosed in circles show dull spots (corresponding to currents of $\sim 0.6 \mu\text{A}$) connecting the bright regions, are suggestive of conductive interconnects between the large conducting domains. Neat MoO₂ is almost insulating relative to MoO₂/Graphene and this is again reinforced from the representative point contact I-V curves averaged over 15 spots (Figure 4.6a' and b'),

and the nanoscale conductivity of MoO₂/Graphene deduced from the linear portion of the curve, is 3.9 S cm⁻¹ compared to a value of 2.7 × 10⁻⁸ S cm⁻¹ in neat MoO₂. It is apparent that such a massive increase in conductivity by 8 orders, upon including Graphene, can dramatically transform the electrochemical capabilities of MoO₂. Here, the use of a low temperature synthetic route for preparing the composite enabled the formation of an intimate contact between the highly conducting Graphene nanosheets and the MoO₂ nanoparticles. A direct contact between the two nanoparticles allows seamless transfer and transport of Li⁺ ions and electrodes through the bulk of the electrode. The high effective surface area of composite, due to the nano layered structure of MoO₂ which permits greater Li-ion uptake compared to neat Graphene or neat MoO₂, and a remarkably high Li-ion storage capacity results.

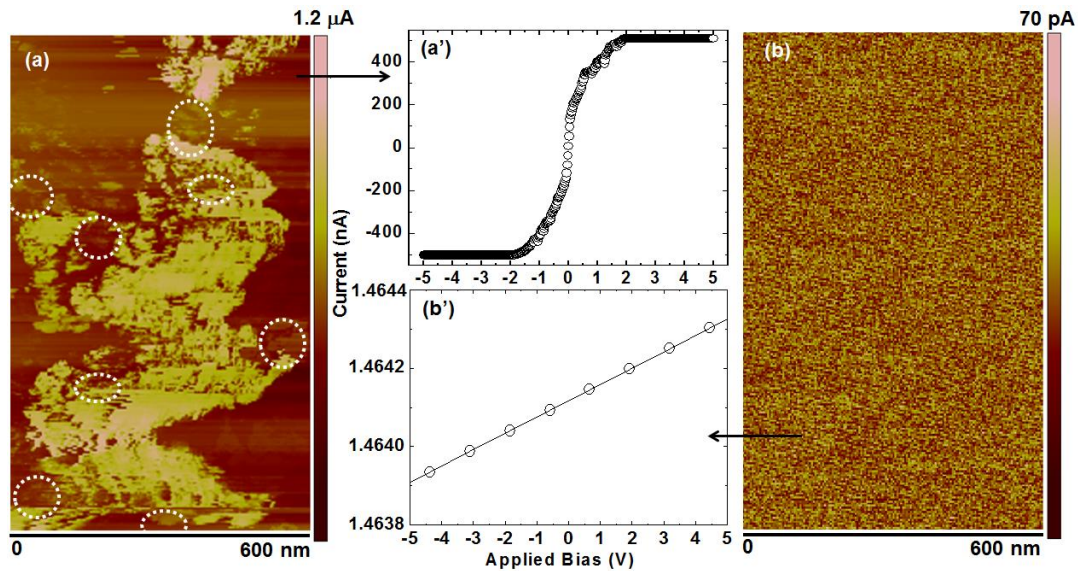


Figure 4.6. Current images of (a) MoO₂/Graphene and (b) neat MoO₂ obtained from C-AFM. Representative point contact nanoscale I-V characteristics of (a') MoO₂/Graphene and (b') neat MoO₂ obtained from the corresponding current images.

4.5. Electrochemical charge-discharge studies

The galvanostatic charge-discharge characteristics of the MoO₂/Graphene composites with MoO₂:Graphene weight ratios of 2:1, 3.76:1 and 1.45:1 are shown below in Figure 4.7. The charge-discharge curves recorded at a current density of 540 mA g⁻¹ (Figure 4.7a.) for the first cycle of MoO₂/Graphene in 2:1, 3.76:1 and 1.45:1 proportions show charge/discharge capacities, respectively, of 703/1455, 535/988 and 552/1094 mAh g⁻¹. As can be observed from Figure 4.7a, the MoO₂/Graphene composite (2:1) shows a high initial reversible capacity of 700 mAh g⁻¹ and the MoO₂/Graphene composite (3.76:1) shows an initial capacity of 535 mAh g⁻¹. The low Graphene content in the MoO₂/Graphene composite (3.76:1), renders the material less conducting which is responsible for the observed poor capacity. On the other hand, in the MoO₂/Graphene composite (1.45:1), the active material (MoO₂) concentration is low, which can cause the re-stacking of Graphene layers, and therefore a low capacity (552 mAh g⁻¹) is observed. It is obvious that the MoO₂/Graphene composite (2:1), has an optimal balance of the two components, which results in good electrochemical performance. After 50 cycles the MoO₂/Graphene composites in 2:1, 3.76:1 and 1.45:1 show reversible capacities of 760, 575 and 320 mAh g⁻¹ (Figure 4.7b).

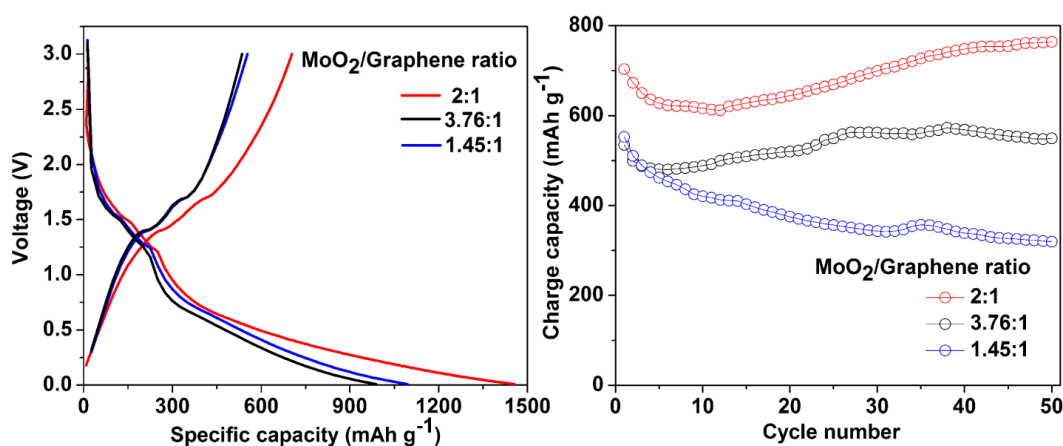


Figure 4.7. (a) Galvanostatic charge-discharge curves of MoO₂/Graphene composite with different proportions of MoO₂ and Graphene, (b) cyclability of the composites; all curves recorded at a current density of 540 mA g⁻¹.

The optimized MoO₂/Graphene composite (2:1) was studied further in terms of cyclic voltammetry, cyclability and rate capability. Cyclic voltammograms of MoO₂/Graphene composite and neat MoO₂ recorded at a scan rate of 0.1 mV s⁻¹ are displayed in Figure 4.8. For the composite (Figure 4.8a), in the first cycle, two reduction peaks in the cathodic branch are observed at 1.28 and 1.56 V which are ascribed to the phase transition of partially lithiated Li_xMoO₂ from orthorhombic to monoclinic during Li-insertion, as reported previously by Dahn and McKinnon[18]. An irreversible broad peak is also seen at 0.7 V, which can be attributed to the reduction of electrolyte solution and the formation of a passivation layer at the anode surface, as this peak disappears in the subsequent cycles. In the ensuing cycles, two redox couples located at 1.56/1.68 V and 1.28/1.39 V are observed, which are due to the phase transitions of the partially lithiated Li_xMoO₂. The CV plots for MoO₂ also show oxidation/reduction couples at 1.52/1.73 V and 1.26/1.51 V (Figure 4.8b), corresponding to phase transitions of partially lithiated Li_xMoO₂. The CV plots of the MoO₂/Graphene composite acquire stability in the 2nd cycle

itself, as in the following cycles, the curve retraces the plot obtained in the previous scan. The CV curves of the neat MoO₂ shrink with cycling, which indicates that Li⁺ intercalation and de-intercalation is not as reversible in MoO₂, as in the MoO₂/Graphene composite.

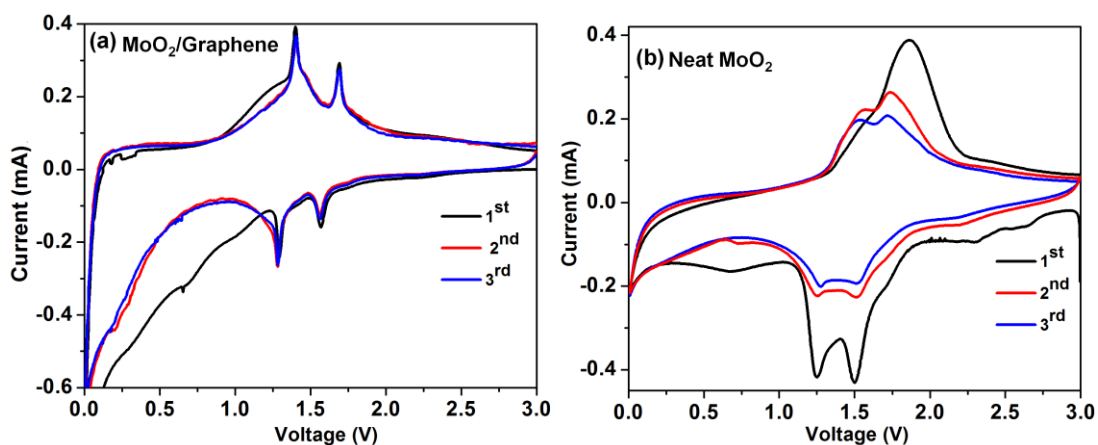


Figure 4.8. Cyclic voltammograms of (a) MoO₂/Graphene and (b) neat MoO₂ electrodes *versus* metallic Li in the 0.01 to 3.0 V potential range.

The charge-discharge curves for an as-fabricated MoO₂/Graphene electrode in the first cycle and the subsequent cycling behavior measured between 0.01 to 3.0 V *versus* Li metal at a current density of 540 mA g⁻¹ is shown in Figure 4.9a. In the first cycle, two short discharge plateaus at 1.52 and 1.25 V and two charge plateaus at 1.69 and 1.41 V were observed and these are in agreement with the CV curves.

On the basis of the composition of the as-synthesized MoO₂/Graphene electrode, which is: 66.8 % of MoO₂ and 33.2 % of Graphene, the theoretical specific capacity of the MoO₂/Graphene composite is deduced to be 766.8 mAh g⁻¹. The calculation is provided below.

Calculation of theoretical specific capacity of MoO₂/Graphene composite:

- Theoretical specific capacity of MoO₂ = 838 mAh g⁻¹ (for 4 Li⁺ insertion/deinsertion)

➤ Theoretical specific capacity of Graphene = 623 mAh g⁻¹

Theoretical specific capacity of MoO₂/Graphene

$$\begin{aligned} &= 66.8\% \text{ MoO}_2 + 33.2\% \text{ Graphene} \\ &= 66.8\% \times 838 + 33.2\% \times 623 \\ &= 766.8 \text{ mAh g}^{-1} \end{aligned}$$

For the initial cycle, MoO₂/Graphene composite electrode delivers discharge and charge specific capacities of 1450 and 703.7 mAh g⁻¹ respectively which corresponds to an irreversible capacity loss of 52%. The high irreversible capacity loss for composite electrodes is due to the following reasons: the conversion of Graphene oxide to Graphene is not absolute, even by the use of citric acid, as core level XPS spectrum of C1s reveals the presence of oxygen functionalities. These oxygen containing groups on Graphene layers can irreversibly entrap Li-ions. To support this point, the charge-discharge studies of neat Graphene were measured. The first cycle shows discharge and charge capacities of 1386.5 and 623 mAh g⁻¹ respectively, which correspond to an irreversible capacity loss of 55%. Other possible reasons include decomposition of electrolyte and formation of SEI layer[11]. The cyclability of MoO₂/Graphene composite and the Coulombic efficiency of this electrode measured at a current density of 540 mA g⁻¹ is shown in Figure 4.9b. The composite shows a gradual increase in capacity up to 83 cycles; and at this juncture, it shows a reversible capacity of 769.3 mAh g⁻¹ coupled with an excellent Coulombic efficiency of ~ 98%. From 83 cycles onwards, up to few cycles the capacity gradually decreases and thereafter it remains stable with increasing number of cycles, as at the end of 1000 charge-discharge cycles, the MoO₂/Graphene electrode still shows a reversible capacity of 530 mAh g⁻¹ with a

Coulombic efficiency almost close to 100%. The electrode retains 75.4% of its initial capacity at the end of 1000 repetitive cycles, indicating its stability for Li^+ insertion and extraction. The $\text{MoO}_2/\text{Graphene}$ electrode also shows outstanding rate capabilities (Figure 4.9c) wherein the charge-discharge capacities at different C rates of 540, 1042 and 2045 mA g^{-1} were plotted. At 1042 mA g^{-1} , after 50 cycles the composite electrode shows a reversible capacity of 497 mAh g^{-1} . At a still higher current density of 2045 mA g^{-1} the electrode shows an initial reversible capacity of 460 mAh g^{-1} which is much superior to previously reported values on $\text{MoO}_2/\text{Graphene}$ composite[21], wherein authors achieved a value of 407 mAh g^{-1} at 2000 mA g^{-1} current density after 70 cycles. At the same C-rate, after subjecting the $\text{MoO}_2/\text{Graphene}$ electrode to 50 cycles, a charge capacity of 427 mAh g^{-1} is retained. The $\text{MoO}_2/\text{Graphene}$ oxide (Figure 4.10) electrode shows a reversible capacity of 605 mAh g^{-1} in the initial cycle at current density of 540 mA g^{-1} and upon increasing the current density to 2045 mA g^{-1} the electrode shows a reversible capacity of 300 mAh g^{-1} . The high capacity and improved rate capability of $\text{MoO}_2/\text{Graphene}$ as opposed to that shown by $\text{MoO}_2/\text{Graphene}$ oxide, is a clear indicator of the fact that fewer number of oxygen containing functionalities on the Graphene layers improves the conduction capability and allow un-hindered ion and electron transport in the composite. The superior performance of $\text{MoO}_2/\text{Graphene}$ was also realized by comparing the reversible charge capacity of this electrode with that of the individual components (namely, neat Graphene and neat MoO_2) at current densities of 200, 200 and 540 mA g^{-1} and these plots recorded as function of number of cycles are displayed in Figure 4.9d. For neat Graphene the initial capacity (602 mAh g^{-1}) is close to that $\text{MoO}_2/\text{Graphene}$ electrode; however this capacity for neat

Graphene shrinks to about 300 mAh g^{-1} after enduring 50 cycles. For neat MoO_2 electrode, the reversible capacity in the first cycle is 442 mAh g^{-1} and it goes through a maximum of 495 mAh g^{-1} (in the 10th cycle) and upon further cycling, the capacity monotonically decreases to about 215 mAh g^{-1} (in the 50th cycle). For the $\text{MoO}_2/\text{Graphene}$ electrode the initial capacity (703.7 mAh g^{-1}) is higher than that of neat Graphene or neat MoO_2 even at a much higher current density of 540 mA g^{-1} .

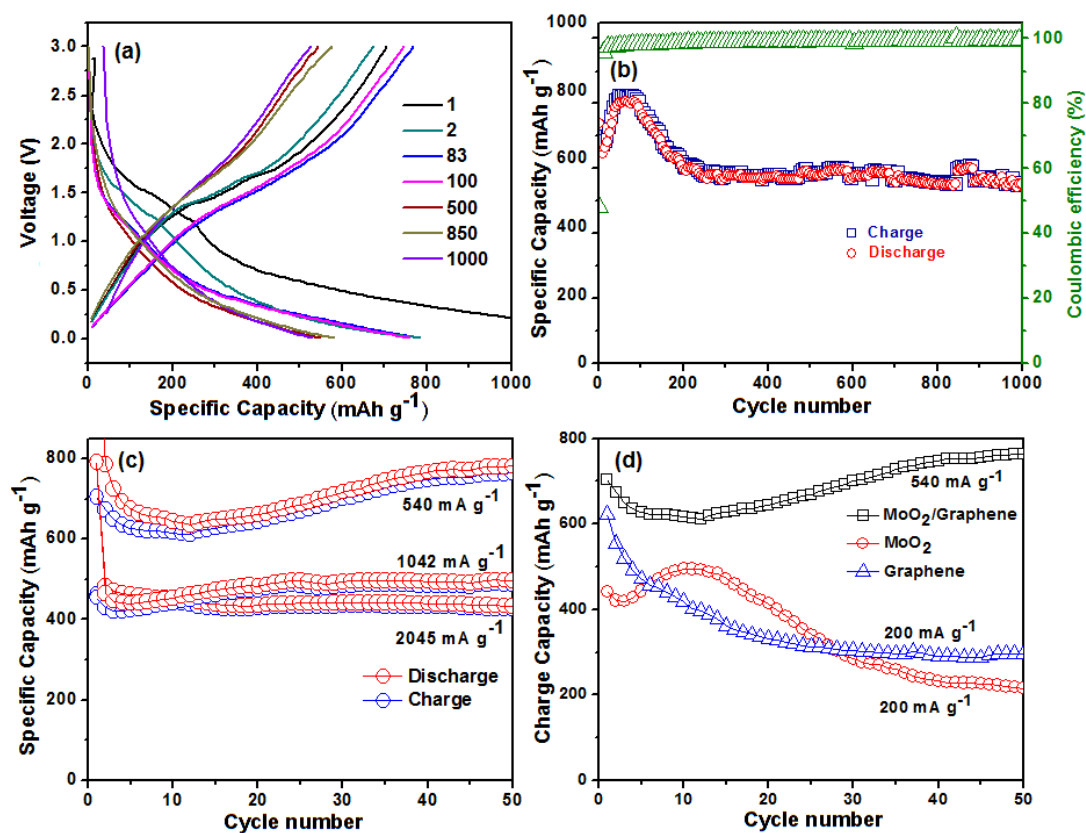


Figure 4.9. (a) Galvanostatic discharge-charge curves of the $\text{MoO}_2/\text{Graphene}$ composite electrode at a current density 540 mA g^{-1} in the voltage range of 0.01–3.0 V, (b) the cycling performance of the $\text{MoO}_2/\text{Graphene}$ at current density of 540 mA g^{-1} ; (c) rate performance of the $\text{MoO}_2/\text{Graphene}$ composite and (d) the cycling performance of $\text{MoO}_2/\text{Graphene}$, neat MoO_2 and neat Graphene electrodes at different current densities.

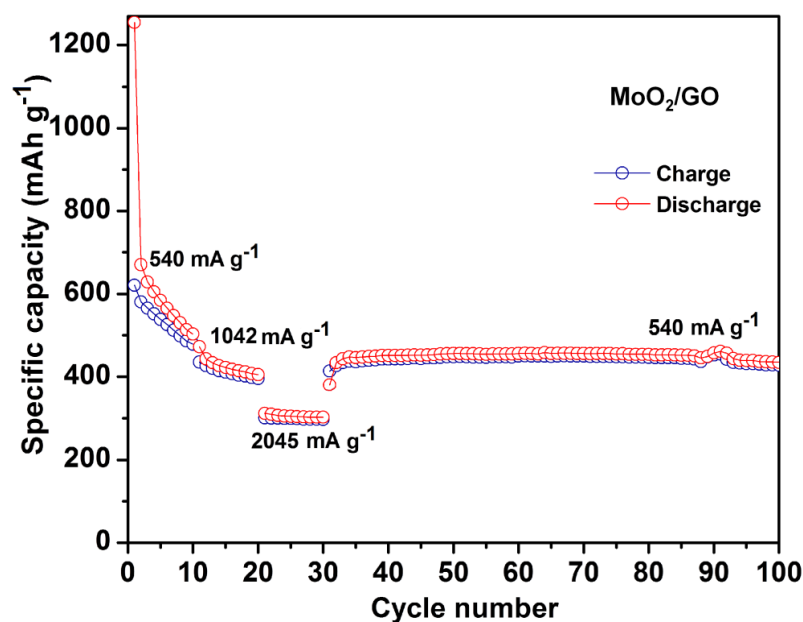


Figure 4.10. Rate capability of a MoO₂/GO composite.

4.6. *Ex-situ* XRD analyses and impedance spectra

The *ex-situ* diffractogram of the MoO₂/Graphene electrode during the 1st discharge at 1.5, 1.1 and 0.01 V was shown in Figure 4.11a. At 1.5 V, the XRD pattern is similar to that of the as-synthesized composite electrode albeit a single downshift of the peak corresponding to the (110) plane. This implies that the electrode does not undergo any phase transformation, whereas at 1.1 V, a new phase appears along with the parent monoclinic phase, at $d = 3.537$ and 1.8065 \AA , which is suggestive of a possible two phase reaction. After subjecting to complete discharge at 0.01 V, the XRD pattern is characteristic of a single phase due to Li_{0.98}MoO₂. Similar phenomena were also observed in ultrafine MoO₂ nanorods[27]. The *ex-situ* XRD patterns recorded intermittently during the cycling of the MoO₂/Graphene electrode (Figure 4.11b) shows that as the number of cycles increases, the intensity of main peaks decreases and after 70 charge-discharge cycles the crystal structure of composite electrode becomes amorphous. The amorphous structure formation could

enhance the Li^+ diffusion kinetics which in all likelihood is responsible for the retention of a high Li-ion capacity as a function of cycling[12,13,20,27]. The slight decrease in capacity with cycling (observed in Figure 4.9b, above 200 cycles) could be due to the huge volume variation and/or agglomeration of the active oxide particles and as a consequence capacity fades in a manner similar to other metal oxides. The *ex-situ* XRD pattern of the $\text{MoO}_2/\text{Graphene}$ electrode after subjecting it to 1000 cycles shows unidentified small peaks, which could be due to the formation of an unknown phase. The *ex-situ* XRD patterns recorded for the same $\text{MoO}_2/\text{Graphene}$ electrode after subjecting it to 50 charge–discharge cycles, at different C-rates of 540, 1042 and 2045 mA g^{-1} are shown in Figure 4.12. The *ex-situ* XRD pattern reveals that at a high C-rate of 2045 mA g^{-1} , and even after 50 cycles, although the electrode is pre-dominantly amorphous, but traces of the monoclinic crystal structure are seen.

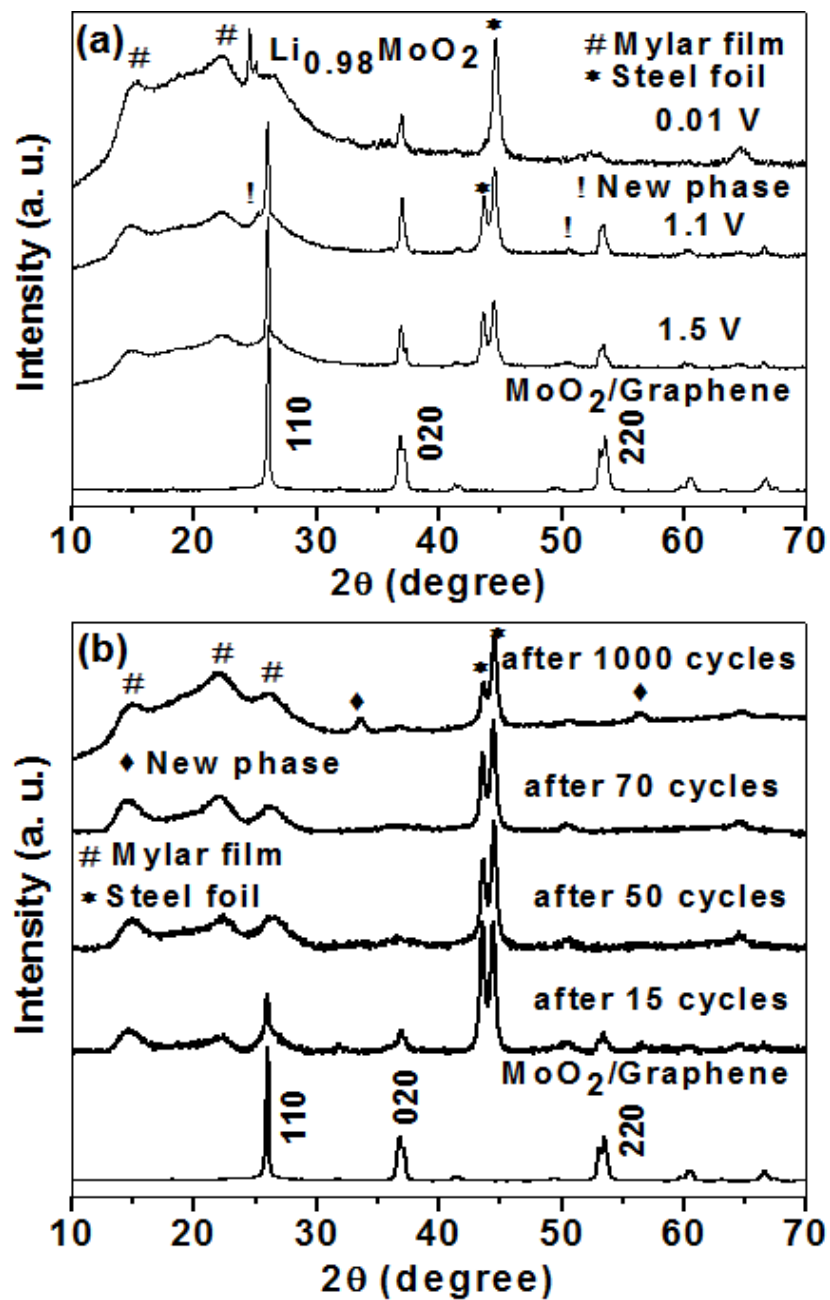


Figure 4.11. *Ex-situ* XRD patterns of (a) MoO₂/Graphene recorded intermittently during the first discharge cycle, when the cell voltage reduced to 1.5, 1.1 and 0.01 V and (b) MoO₂/Graphene before cycling and after subjecting it to 15, 50, 70 and 1000 charge-discharge cycles.

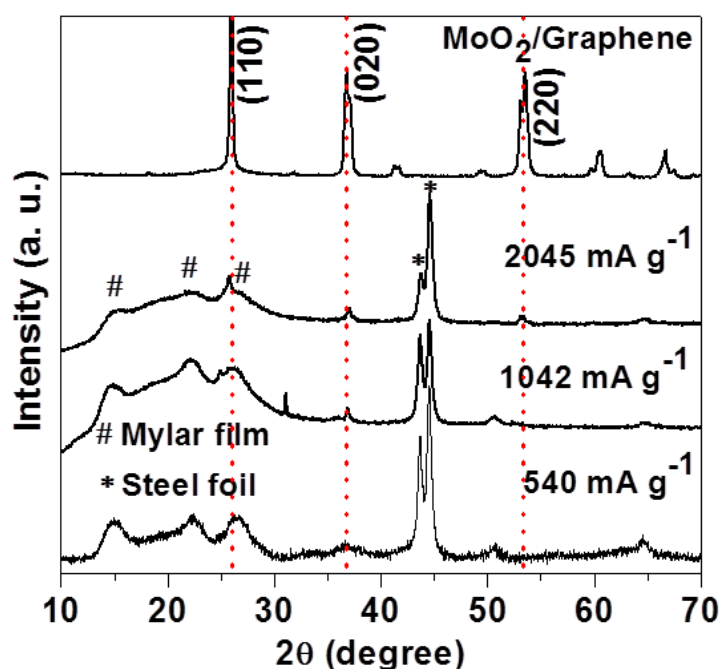


Figure 4.12. *Ex-situ* XRD patterns of MoO₂/Graphene electrode after subjecting it to 50 charge-discharge cycles, at different C-rates of 540, 1042 and 2045 mA g⁻¹.

Nyquist plots of MoO₂/Graphene composite as a function of cycling are shown in Figure 4.13a and a comparison of the Z'' versus Z' plots of neat MoO₂ and MoO₂/Graphene composite are shown in Figure 4.13b. All plots generally comprise of one depressed semicircle followed by an inclined straight line portion which appears in the low frequency range. The equivalent circuit displayed in Figure 4.13a was found to give excellent fits almost over the entire frequency range of 10 mHz to 100 KHz under consideration. The semicircle is attributed to a parallel combination of charge transfer resistance (R_{CT}) and electrical double layer capacitance (C_{dl}), while the linear portion stems from diffusion of ions/electrons through the bulk of the electrode material. The width of the semi-circle increases with cycling for the composite and this corresponds to an R_{CT} increase from 28 to 111 Ω cm⁻² ongoing from an as-fabricated electrode to the one cycled a thousand times. It is evident since the R_{CT} does not increase by orders of magnitude after 1000 cycles, the Li-ion

storage capacity does not decline steeply, and this was also observed in the cycling performance curve (Figure 4.9b). The C_{dl} also shows a change from 5 to 3 F cm⁻². The slope of straight line portion in the low frequency regime does not change significantly over 50 cycles, and since the angle which it makes with the abscissa is close to 90°, the inference that can be drawn is that the electrode remains highly capacitive for about 50 cycles. At the end of 1000 cycles, the straight line portion acquires the ideal 45° slant of the classical finite length Warburg diffusion process, which indicates a decrease in the capacitive contribution to diffusion of ions through the electrode. On comparing the response of neat MoO₂ with that of MoO₂/Graphene (Figure 4.13b), we find that the amplitude of the high frequency semicircle, is larger for neat MoO₂, corresponding to a R_{CT} of 44 Ω cm⁻² and the linear portion signifies a diffusion controlled movement of ions, through the bulk of this electrode. On the contrary, R_{CT} is only 28 Ω cm⁻² for the composite and the straight line portion shows the composite to be more capacitive. The superior capacitive character and the lower interfacial resistance of the MoO₂/Graphene composite are indirect measures of the ease of charge transfer across the electrolyte /electrode interface and the enhanced ability of this electrode to uptake charges. The nano-layered morphology of the composite allows greater charge intercalation and since graphene is an intrinsic electronic conductor, charge transfer/transport in the composite is also facilitated. These benefits cannot be realized in neat MoO₂ as it is bereft of any such electron conducting moiety or a nanostructured morphology.

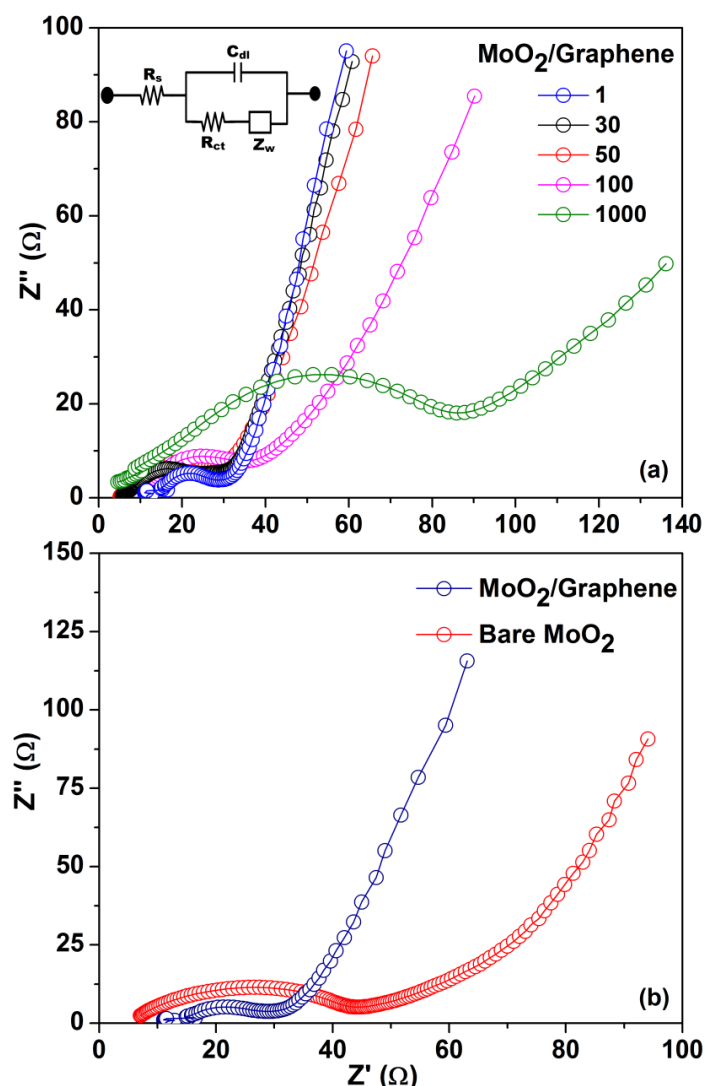


Figure 4.13. Nyquist plots recorded under an ac amplitude of 10 mV superimposed over a zero dc bias for cells based on (a) MoO₂/Graphene as the working electrode at different stages of charge-discharge cycling and (b) MoO₂ and MoO₂/Graphene as the working electrode in the as-fabricated state. Metallic Li served as counter electrode and 1 M LiPF₆ in EC/PC as electrolyte or all plots. Inset of (a) shows the Randles equivalent circuit used for fitting the experimental data.

4.7. Summary

A MoO₂/Graphene composite was synthesized by a hydrothermal route, involving the *in-situ* reduction of the molybdenum salt precursor and embedding of MoO₂ nanoparticles on graphene sheets in a single step. Electron microscopy and

XPS confirmed the homogeneous distribution of metal oxide nanoparticles in a 2D network of graphene sheets. The graphene layers prevent the aggregation of MoO₂ nanoparticles thus reducing volume expansion during cycling and the MoO₂ nanoparticles due to their confinement to graphene layers inhibit the layers from stacking. Such a concerted interplay between the two moieties, effectively manifested in a remarkably high lithium ion storage capacity, rate capability and cycling performance relative to the neat oxide or carbon nanostructure based composites prepared by other methods. Further the nanoscale current images showed a significantly amplified current carrying capability for the composite, induced by Graphene and EIS spectroscopy revealed a lower resistance to charge transfer and transport for the MoO₂/Graphene composite in comparison to neat MoO₂, which are responsible for enhanced capacity and better endurance. These results pave way for fabricating electrodes based on graphene/metal oxide composites, for realizing significant improvements in Li-ion storage performance in batteries.

References

1. N. Kambe, M. S. Dresselhaus, G. Dresselhaus, S. Basu, A. R. McGhie, J. E. Fischer, *Mater. Sci. Eng.*, 40 (1979) 1-4.
2. K. Guo, Q. Pan, S. Fang, *J. Power Sources*, 111 (2002) 350- 356.
3. L. Huiqiao, H. Zhou, *Chem. Commun.*, 48 (2012) 1201-1217
4. S. Stankovich, D. A. Dikin, R. D. Piner, K. A. Kohlhaas, A. Kleinhammes, Y. Jia, Y. Wu, S. T. Nguyen, R. S. Ruoff, *Carbon*, 45 (2007) 1558-1565.
5. A. K. Geim, K. S. Novoselov, *Nat. Mater.*, 6 (2007) 183-191.
6. A. A. Balandin, S. Ghosh, W. Bao, I. Calizo, D. Teweldebrhan, F. Miao, C. N. Lau, *Nano Lett.*, 8 (2008) 902-907.

7. B. Li, H. Cao, J. Shao, G. Li, M. Qu, G. Yin, *Inorg. Chem.*, 50 (2011) 1628-1632.
8. D. Wang, D. Choi, J. Li, Z. Yang, Z. Nie, R. Kou, D. Hu, C. Wang, L. V. Saraf, J. Zhang, I. A. Aksay, J. Liu, *ACS Nano*, 3 (2009) 907-914.
9. X. Zhu, Y. Zhu, S. Murali, M. D. Stoller, R. S. Ruoff, *ACS Nano*, 5 (2011) 3333-3338.
10. L. S. Zhang, L. Y. Jiang, H. J. Yan, W. D. Wang, W. Wang, W. G. Song, Y. G. Guo, *J. Mater. Chem.*, 20 (2010) 5462-5467.
11. G. Zhou, D. W. Wang, F. Li, L. Zhang, N. Li, Z. S. Wu, L. Wen, G. Qing (Max) Lu, H. M. Cheng, *Chem. Mater.*, 22 (2010) 5306-5313.
12. Y. Sun, X. Hu, J. C. Yu, Q. Li, W. Luo, L. Yuan, W. Zhang, Y. Huang, *Energy Environ. Sci.*, 4 (2011) 2870-2877.
13. Y. Shi, B. Guo, Serena A. Corr, Q. Shi, Y. S. Hu, K. R. Heier, L. Chen, R. Seshadri, G. D. Stucky, *Nano Lett.*, 9 (2009) 4215-4220.
14. Q. Gao, L. Yang, X. Lu, J. Mao, Y. Zhang, Y. Wu, Y. Tang, *J. Mater. Chem.*, 20 (2010) 2807-2812.
15. A. Manthiram, C. Tsang, *J. Electrochem. Soc.*, 143 (1996) L143-L145.
16. X. Ji, P. SubRamanya Herle, Y. Rho, L. F. Nazar, *Chem. Mater.*, 19 (2007) 374-383.
17. L. C. Yang, Q. S. Gao, Y. Tang, Y. P. Wu, R. Holze, *J. Power Sources*, 179 (2008) 357-360.
18. J. R. Dahn, W. R. McKinnon, *Solid State Ionics*, 23 (1987) 1-7.
19. Y. S. Jung, S. Lee, D. Ahn, Anne C. Dillon, S. H. Lee, *J. Power Sources*, 188 (2009) 286-291.
20. L. C. Yang, Q. S. Gao, Y. H. Zhang, Y. Tang, Y. P. W, *Electrochem. Commun.*, 10 (2008) 118-122.
21. Y. Sun, X. Hu, W. Luo, Y. Huang, *ACS Nano*, 5 (2011) 7100-7107.
22. D. C. Marcano, D. V. Kosynkin, Jacob M. Berlin, A. Sinitskii, Z. Sun, A. Slesarev, L. B. Alemany, W. Lu, James M. Tour, *ACS Nano*, 4 (2010) 4806-4814.
23. W. S. Hummers, R. E. Offeman, *J. Am. Chem. Soc.*, 80 (1958) 1339-1339.

24. S. J. Chae, F. Güneş, K. K. Kim, E. S. Kim, G. H. Han, S. M. Kim, H. J. Shin, S. M. Yoon, J. Y. Choi, M. H. Park, C. W. Yang, D. Pribat, Y. H. Lee, *Adv. Mater.*, 21 (2009) 2328-2333.
25. H. Kim, Ahmed A. Abdala, Christopher W. Macosko, *Macromolecules*, 43 (2010) 6515-6530.
26. J. Shen, B. Yan, M. Shi, H. Ma, N. Li, M. Ye, *J. Mater. Chem.*, 21 (2011) 3415-3421.
27. B. Guo, X. Fang, B. Li, Y. Shi, C. Ouyang, Y. S. Hu, Z. Wang, G. D. Stucky, L. Chen, *Chem. Mater.*, 24 (2012) 457-463.

Chapter 5

Effect of Graphene Oxide and Poly(3,4-ethylenedioxythiophene) on the Electrochemical Performance of SnO₂ Hollow Spheres/GO/PEDOT Hybrid

5.1. Abstract

In this chapter, mechanistic insights to the formation of high performance SnO₂ hollow spheres are furnished and a structure-property correlation is presented by linking cyclability, rate capability and capacity with structural and interfacial charge transfer and transport aspects. To the best of our knowledge this was the very first study on a SnO₂ HS/GO/PEDOT composite, wherein the conductive matrix of GO coupled with an electrochemically stable conducting polymer efficiently enhanced the capacity retention capability of SnO₂ and easily outperformed pristine SnO₂ anodes.

5.2. Introduction

In the previous two chapters, structure-electrochemical property correlation was elucidated for MoO₂ based composites. Composites of yet another transition metal oxide, namely tin oxide (SnO₂), were prepared, and Li-ion storage properties were evaluated. SnO₂ is considered to be an attractive alternative to graphite as an anode material for LIBs, because it is cheap, offers exceptionally large theoretical specific capacity (782 mA h g⁻¹) and has a low Li-ion intercalation potential. Further SnO₂, when employed as an anode in a LIB it can undergo an irreversible conversion to Sn followed by a reversible alloying with lithium metal to yield a Li_{4.4}Sn alloy, wherein each Sn can react with 4.4 Li atoms. During this reversible alloying reaction Sn undergoes a significant ~ 300% increase in volume and upon repeated cycling, the SnO₂ active electrode can undergo pulverization which causes breakdown in

electrical contact pathways between adjacent particles, leading to rapid capacity decline[1-4]. To counter the issue of fast capacity fading in SnO₂, researchers in the past have attempted SnO₂ nanostructures as electrodes; SnO₂ hollow spheres, core/shells, nanowires, nanotubes, nanosheets and mesoporous as in nanosized SnO₂ the volume change caused by the mechanical stress induced by lithium intercalation is tolerated more easily than it is in bulk SnO₂[2-13]. Other alternate approach to increase cyclability involves the preparation of hybrid electrodes of SnO₂ with carbon coating or with reduced graphene oxide or carbon nanotubes or conducting polymers. The additive (be it a carbon nanostructure or a conducting polymer) buffers the volume change incurred by the SnO₂ active phase and prevents the overall agglomeration of SnO₂ particles and also improves the electrical conductivity properties of the anode and thus reduces the capacity fading of the electrode. The second strategy has been reasonably successful in yielding anodes capable of sustained electrochemical cycling response[14-22].

Despite significant advances in SnO₂/graphene hybrids as elaborated above, hollow structures of SnO₂ are advantageous because the local empty space in the structures can partially accommodate the large volume change, delaying capacity fading, and imparting efficient catalytic activity and structural stability[5-8]. Although manipulation of SnO₂ nanostructures either by shape or size control or by inclusion of a conductive inert moiety to better battery performance had shown some promising results in the past, but much room remains for systematically engineering high capacity SnO₂ based electrodes endowed with cycling stability by use of low cost precursors and a cost effective methodology. In this chapter, we present a hydrothermal synthesis of SnO₂ hollow spheres using an organic bi-

functional molecule followed by formation of a hybrid electrode with graphene oxide and poly(3,4-ethylenedioxythiophene) (PEDOT). While graphene oxide (GO) nanosheets serve as a scaffold for entrapment of SnO₂ hollow spheres and prevent their coalescence during electrochemical cycling, the PEDOT overlayer being a robust conducting polymer, effectively inhibits the disintegration of SnO₂ HS during charge/discharge cycling and cumulatively both GO and PEDOT afford capacity retention with cycling. The conducting polymer thus offers a good trade-off between mechanical stability and electrical conductivity to the active electrode. It was observed that the performance of the binary SnO₂ HS/GO and SnO₂ HS/PEDOT electrodes was rather dismal relative to SnO₂ HS/GO/PEDOT electrode indicating that both the carbon nanostructure and PEDOT cooperatively control the electrochemical activity of electrode. The effect of the organic molecule proportion on the nanostructure and electrochemical response of pristine SnO₂ HS was studied, and using process parameters optimized for high performance SnO₂ electrode, hybrid electrodes of SnO₂ HS/GO/PEDOT were fabricated by *in-situ* polymerization of the monomer in a SnO₂ HS/GO formulation and correlated with its electrochemical property.

5.3. Experimental

5.3.1. SnO₂ hollow spheres (HS) and nanostructures

Hollow spheres of SnO₂ were prepared by a one-step hydrothermal synthesis route using water as solvent. Typically, in a 100 mL beaker, 1.1 g of 3-mercaptopropionic acid (MPA, Alfa Aesar, 98%) was dissolved in 30 mL of ultrapure water (Millipore) and stirred for 5 min. To this clear solution, 3.324 mmol of SnCl₂·2H₂O (Merck, 98%) was added and stirred for 10 min, and a solution with

$\text{SnCl}_2 \cdot 2\text{H}_2\text{O}$:MPA in a 1:3 molar ratio was obtained. To the resulting colorless clear solution 100 mg of cetyltrimoniumbromide (CTAB, Alfa Aesar, 98%) surfactant followed by 20 ml of milli-Q water was added and stirred at 1000 rpm for 2 h. The resulting solution was transferred to a 80 mL Teflon lined stainless steel autoclave. After heating at 160 °C for 12 h in oven the resulting precipitate was filtered and washed with water and dried at 80 °C for 6 h. The obtained ash colored powder was heated in an electric furnace at 500 °C for 3 h which resulted in pure SnO_2 hollow spheres or HS. Similarly solutions of (a) $\text{SnCl}_2 \cdot 2\text{H}_2\text{O}$ and MPA mixed in a 1:1 molar ratio with 100 mg of CTAB, (b) only using $\text{SnCl}_2 \cdot 2\text{H}_2\text{O}$ and MPA (1:3 molar ratio) without using CTAB and (c) only using CTAB and without MPA from an aqueous solution (50 mL) containing 100 mg of CTAB surfactant and 3.324 mmol of $\text{SnCl}_2 \cdot 2\text{H}_2\text{O}$ were also processed separately to produce SnO_2 , while maintaining all other parameters constant.

5.3.2. SnO_2 HS/GO hybrid

Graphene oxide (GO) was synthesized from graphite (Aldrich, particle size < 20 μm) by using a modified Hummers method. SnO_2 HS and GO hybrid were prepared by a simple solution method. Typically, 40 mg of GO were dispersed in 50 mL of water by ultra-sonication for one hour and 30 minutes. To the resulting well-dispersed GO solution, 100 mg of SnO_2 hollow spheres were added and stirred at 600 rpm for 6 h. The black suspension was filtered by washing with water and dried in vacuum oven for 12 h and black homogeneous solid of SnO_2 HS/GO was obtained.

5.3.3. SnO₂ HS/GO/PEDOT hybrid

In the first step, 30 mg of GO were dispersed in 40 mL of water by ultrasonication for one hour and 30 minutes. To the resulting well-dispersed GO solution, 100 mg of SnO₂ hollow spheres were added and stirred at 600 rpm for 5 min. Subsequently, 30 μ L (7 mM) of 3,4-ethylenedioxythiophene (EDOT, Aldrich, 97%) monomer was added and stirred for one hour. To the resultant suspension, 1 g of ammonium peroxodisulfate ((NH₄)₂S₂O₈, Merck) was added and stirred for 6 h. A blue colored solid precipitate of SnO₂ HS/GO/PEDOT was obtained which was washed repeatedly with water, dried in vacuum oven for 12 h at 60 °C and used.

5.4. Results and discussion

5.4.1. Growth mechanism by structure evolution analysis

The XRD patterns of SnO₂ hydrothermally synthesized by heating the precursor with the following composition: Sn salt + MPA (1:3 molar ratio) + 100 mg of CTAB at 160 °C for 12 h followed by calcination at 500 °C for 3 h are shown (Figure 5.1). The hydrothermally synthesized sample prior to calcination shows strong peaks at $d = 3.3491, 2.6434$ and 1.7636 \AA corresponding to (110), (101) and (211) planes of the tetragonal crystal structure of SnO₂ with space group P4₂/mnm in concurrence with JCPDS card no 72-1147. In addition, some impurity peaks from SnS (JCPDS card no 75-2115) are also observed. After calcining the sample at 500 °C, the XRD pattern shows peaks corresponding to only tetragonal SnO₂ and the impurity peaks were not observed anymore indicating the formation of pure phase of SnO₂.

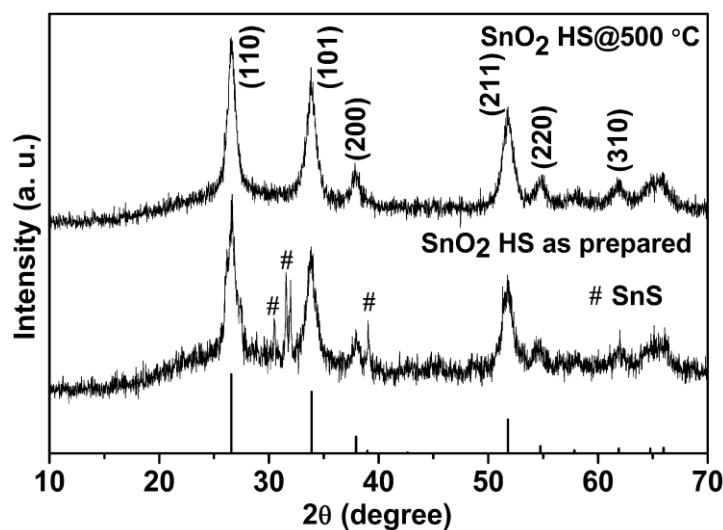


Figure 5.1. Powder XRD patterns of as-prepared SnO₂ HS and after heating at 500 °C for 3 h, each obtained from a solution of Sn salt and MPA mixed in a 1:3 molar ratio and 100 mg of CTAB and subjected to 12 h of hydrothermal heating at 160 °C. The solid lines in the bottom most part of the figure, represent the standard XRD pattern of SnO₂ (JCPDS: 72-1147).

The FE-SEM images of SnO₂ formed after calcination at 500 °C for 3 h are shown in Figure 5.2a and b. The images reveal the formation of hollow spheres of SnO₂ with an empty core and a solid shell structure. It is apparent from the contrast in the images, the core of the spheres is pre-dominantly hollow and the average size of the SnO₂ hollow sphere is in the range of 100 - 200 nm. A broken sphere could be detected in the corresponding high magnification image of the SnO₂ hollow sphere (indicated with a dashed arrow), and it is evident that the sphere does not have a solid core (Figure 5.2b). An enlarged view of a cross-section of one such hollow sphere of SnO₂ recorded by TEM is shown in Figure 5.2c. The image shows the hollow spheres to be constituted by small particles (average size of about ~8 nm) but separated by very large pores (3-5 nm in the dimensions). The packing density of particles is high at the periphery of the sphere and considerably less in the middle,

thus confirming the formation of hollow cores encapsulated by solid spherical shells.

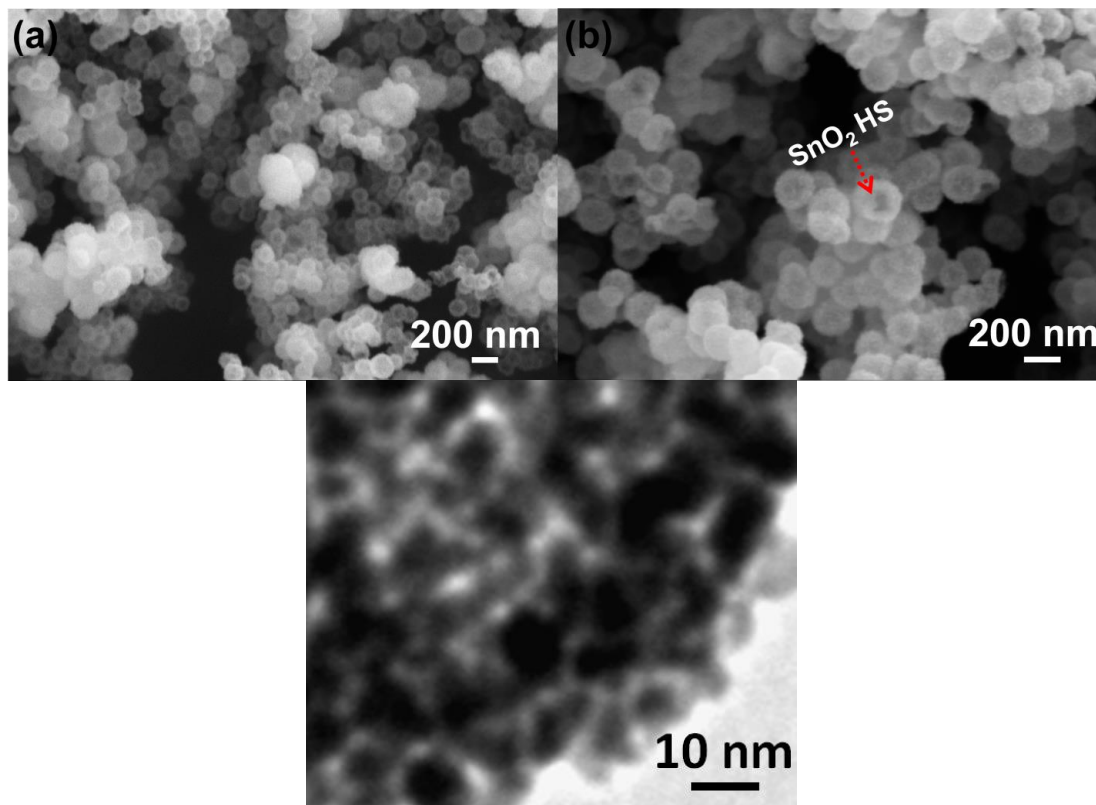


Figure 5.2. (a) Low (b) high magnification FE-SEM images, and (c) enlarged view from a TEM images of SnO₂ HS prepared by calcining at 500 °C for 3 h, the product obtained from a solution of Sn salt and MPA mixed in a 1:3 molar ratio and 100 mg of CTAB, hydrothermally heated at 160 °C for 12 h.

The growth mechanism of SnO₂ hollow spheres is unraveled by examining a time dependent change in the morphology of SnO₂. The TEM images of SnO₂ formed upon hydrothermally heating the precursor solution containing tin chloride and the optimized amounts of MPA and CTAB (Sn salt + MPA (1:3 molar ratio) + 100 mg of CTAB) for 1, 4, 8 and 12 h are shown in Figure 5.3. In each case the hydrothermally synthesized product was heated at 500 °C for 3 h. The morphology of the product obtained subsequent to 1 h of hydrothermal heat treatment comprises of aggregated spherical shapes with an average diameter of about 100 nm (Figure

5.3a). The dark contrast in the spheres indicates that the spheres are not hollow at this juncture and spheres have solid cores. Upon sequentially extending the hydrothermal heating time from 4 to 8 h, we find that the inner solid core disappears progressively (Figure 5.3b and c). After 8 h of heat treatment, spheres with thick shells are observed, and the solid core shows the presence of voids (80 - 120 nm in size) indicating that with heating the porosity of the cores increases. When the heating duration was prolonged to 12 h, the shell thickness decreased which is simultaneously accompanied by an increase in void diameters in the core thus confirming the hollow nature of the spheres. The shell is continuous and its thickness is uniform which is about 40 nm. The total diameter (shell+core) of the HS ranges between 140 to 150 nm. Based on the TEM results and previous reports on SnO₂ hollow spheres[8] we proposed an inward out Ostwald ripening mechanism which is shown in scheme 5.1. In the first step, when tin chloride was added to MPA solution it forms a Sn(O₂SC₃H₄) complex. After heating hydrothermally for 1 h, aggregated spherical particles of SnO₂ with dimensions of about 100 nm are formed. These spherical particles are composed of ultra-fine particles which are loosely packed in the interior and tightly packed at the outer surface. When the heating duration was raised to 4 h the loosely packed small crystals are dissolved in the interior because of high energy and then recrystallize on the outer surface to yield hollow spheres. When the heating duration was increased further to 8 h and 12 h more and more particles at the interior get dissolved and the diameter of the hollow core increases. The average size of the final product was around 150 nm (Figure 5.3d). Even after 2 h of ultrasonication the SnO₂ HS were not broken indicating that

the spheres were highly stable. The surface of the hollow spheres was not smooth but showed the contour of the inner SnO₂ particles.

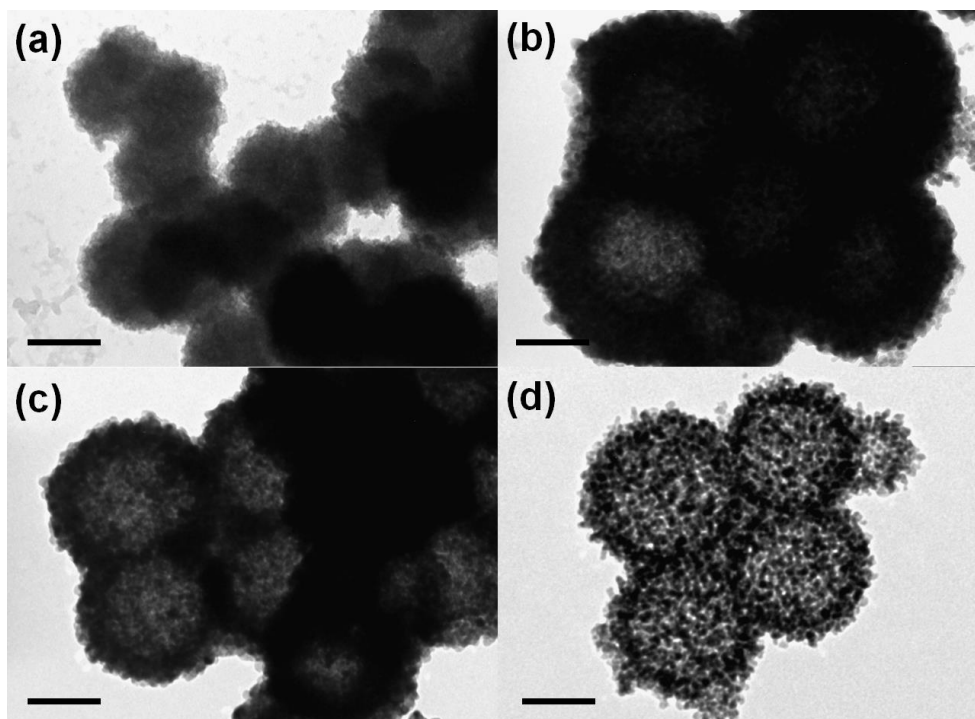
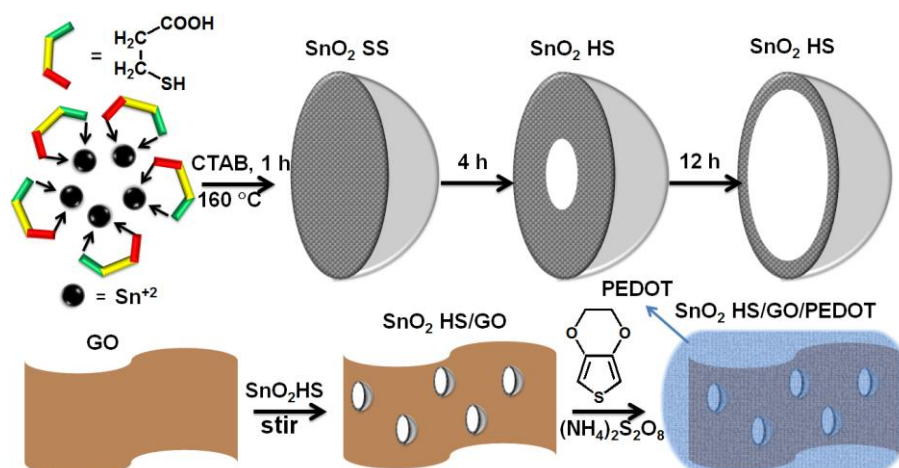


Figure 5.3. Growth mechanism study of SnO₂ HS: TEM images of SnO₂ prepared after 1 h (a) 4 h (b) 8 h (c) 12 h (d) of hydrothermal heating from a precursor containing Sn salt + MPA in a 1:3 molar ratio and 100 mg of CTAB. Each hydrothermally synthesized sample was calcined at 500 °C for 3 h prior to recording TEM micrographs. The scale bar in all TEM micrographs corresponds to 100 nm.



Scheme 5.1.: Schematic for the formation of SnO₂ HS and SnO₂ HS/GO/PEDOT hybrid.

The roles of synthetic parameters like effect of concentration of MPA, key role of MPA, solvent and CTAB for the formation of SnO₂ hollow spheres was analyzed systematically. While the optimized concentration for SnCl₂ to MPA is a 1:3 molar ratio, when a 1:1 molar ratio concentration was used while keeping all other parameters unchanged (100 mg of CTAB, 12 h hydrothermal treatment followed by 3 h at 500 °C), the morphology of SnO₂ formed was different. The FE-SEM image (Figure 5.4a) shows agglomerated particles of non-uniform size. The particles show a wide distribution in size ranging from 100 to 1000 nm. The roles of CTAB and MPA in the formation of SnO₂ hollow spheres were determined by preparing SnO₂ with only MPA (no CTAB) and with sole CTAB (no MPA). The FE-SEM image of SnO₂ prepared from an only MPA/Sn salt solution (1:3 molar ratio) shows (Figure 5.4b) aggregated spheres with thick shells whereas the micrograph of SnO₂ obtained from the CTAB/Sn salt solution (3.324 mmol of SnCl₂.2H₂O +100 mg of CTAB) reveals (Figure 5.4c) the formation of densely packed particles of irregular shapes and sizes. It is inferred that MPA is the primary structure directing agent for synthesizing SnO₂ spherical hollow spheres whereas CTAB assists as a surfactant to minimize agglomeration. The role of solvent (water) in steering SnO₂ sphere growth was followed by using a different solvent namely ethanol. SnO₂ was also prepared solvothermally by heating an optimized ethanolic solution of SnCl₂:MPA in a 1:3 molar ratio with 100 mg of CTAB at 160 °C for 12 h, followed by 3 h at 500 °C. Rotund spheres of SnO₂ with smooth exterior surfaces with diameters varying from 0.5 to 5 µm were obtained (Figure 5.4d), but the electrochemical performance was abysmal (Figure 5.5) and therefore water was preferred as the solvent. The poor Li charge storage capacity can be attributed to the unavailability of the inner core of the

sphere for ion intercalation, as opposed to the hollow sphere architecture, wherein the active sites in the core are also accessible to the electrolyte.

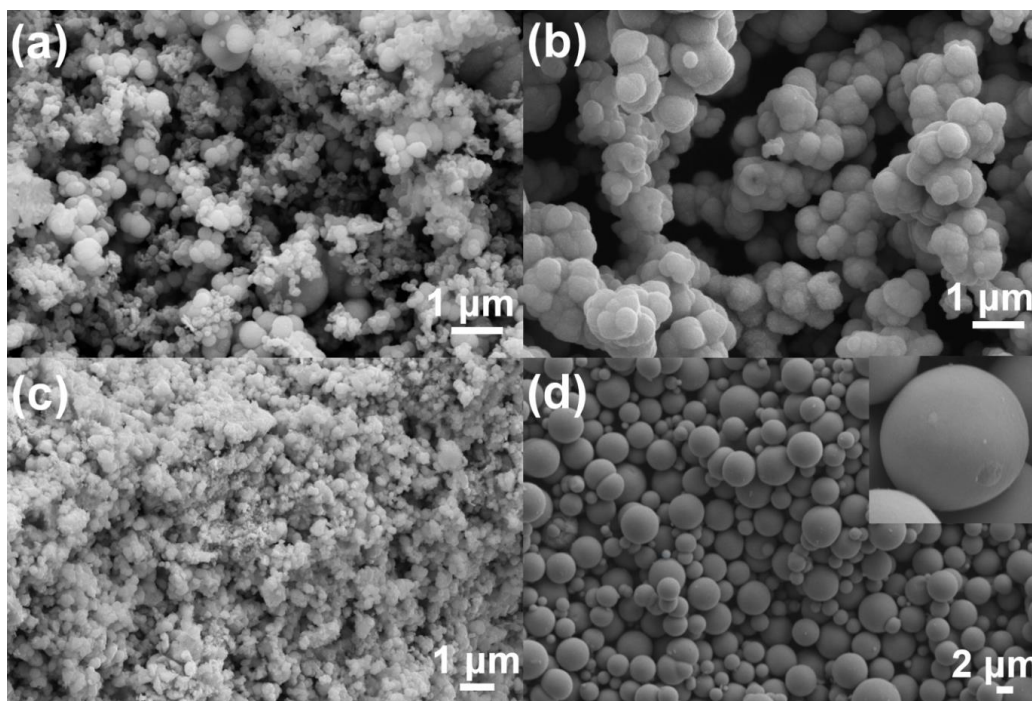


Figure 5.4. FE-SEM images of SnO_2 synthesized from solutions containing (a) 1:1 molar ratio of $\text{SnCl}_2 \cdot 2\text{H}_2\text{O}$ to MPA and 100 mg of CTAB (b) 1:3 molar ratio of $\text{SnCl}_2 \cdot 2\text{H}_2\text{O}$ to MPA (no CTAB) (c) only with CTAB (no MPA): 3.324 mmol of $\text{SnCl}_2 \cdot 2\text{H}_2\text{O}$ and 100 mg of CTAB and (d) using ethanol instead of water as solvent (from Sn salt + MPA in a 1:3 molar ratio and 100 mg of CTAB). Solvent used was water in a-c. Each of the samples was subjected to hydro- or solvo-thermal heating at 160 °C for 12 h followed by 500 °C heat treatment for 3 h.

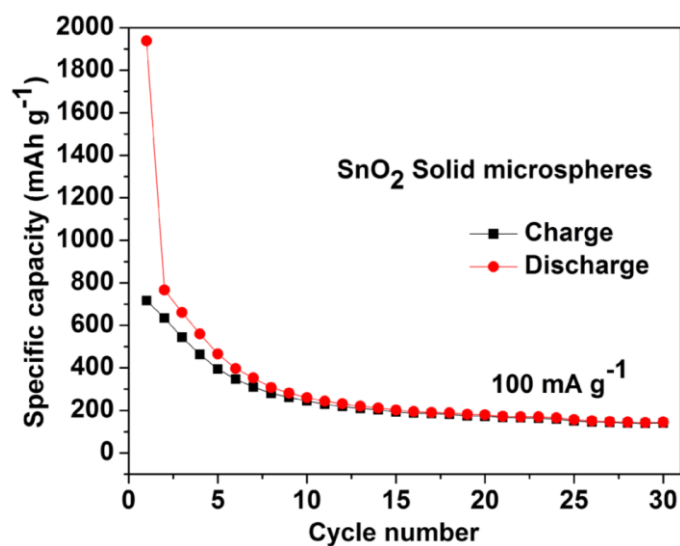


Figure 5.5. Cyclability of SnO₂ solid microspheres measured at 100 mA g⁻¹ current density in the voltage range of 0.01-2 V. SnO₂ used herein were obtained from solvothermal treatment at 160 °C for 12 h of a solution with 1:3 molar ratio of SnCl₂.2H₂O to MPA and 100 mg of CTAB, followed by calcination at 500 °C for 3 h. The solvent used was ethanol instead of water.

5.4.2. Structure and composition of the hybrid

The FE-SEM image of the SnO₂ HS/GO hybrid is shown in Figure 5.6a. It shows SnO₂ HS to be uniformly anchored onto GO nanosheets and these have been depicted with arrows. The outer diameter of the SnO₂ HS in the SnO₂ HS/GO hybrid was of the order of 190 nm which is almost same as that of pristine SnO₂ HS. The FE-SEM images of SnO₂ HS/GO/PEDOT hybrid exhibits SnO₂ HS and GO sheets to be fully coated with PEDOT polymer (Figure 5.6b and c). The polymer PEDOT tends to swamp the unique morphological characteristics of SnO₂ HS and GO. The insets of Figure 5b and 5c show that the broken SnO₂ HS that are completely coated with PEDOT. The HRTEM image of the hybrid reveals the presence of nanocrystals of SnO₂ HS in the hybrid material (Figure 5.6d). The inter-planar spacing deduced from the separation between the lattice fringes is 0.33 nm and this corresponds to the (110) orientation of the tetragonal crystal structure of SnO₂. This agrees well with

XRD results. In Figure 5.6e, it can be observed that while the lattice fringes arise from SnO_2 HS crystallites, the fuzzy contrast originates from the amorphous PEDOT polymer. To further confirm the distribution of PEDOT in the hybrid we have done elemental mapping and EDX. The elemental maps of Sn, S and O taken for the image shown in Figure 5.6c shows a uniform distribution of S and Sn across all the regions of the hybrid indicating an excellent mixing of SnO_2 and PEDOT (as the sulfur signal emanates from PEDOT). Further confirmation for inclusion of PEDOT was obtained from EDX data, as a signal from sulfur was observed which is neither present in SnO_2 nor GO. Signals from C, O and Sn from SnO_2 and GO were also obtained. Scheme 5.1 also shows how the SnO_2 HS/GO is coated with PEDOT.

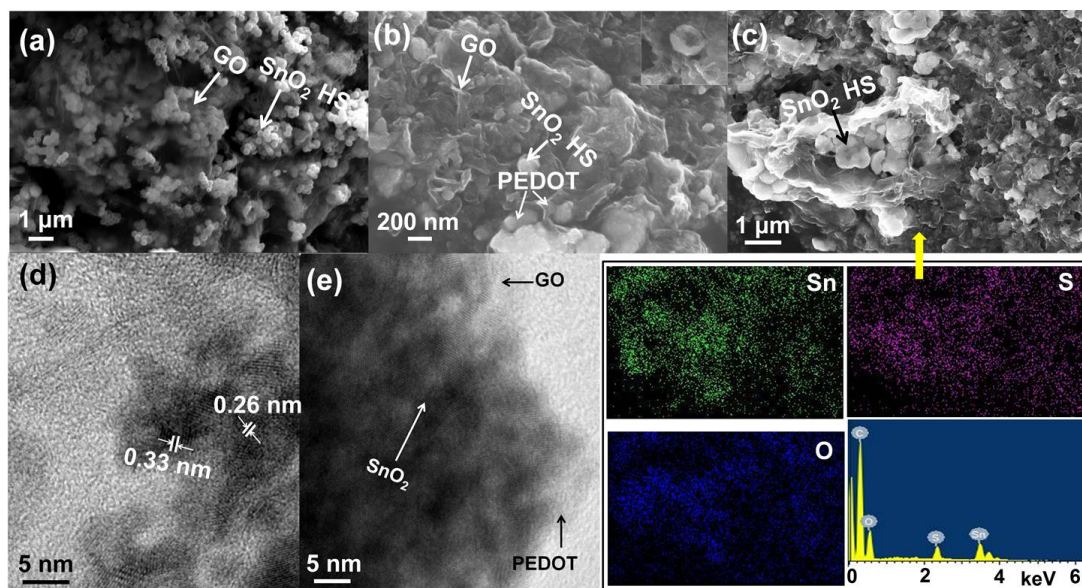


Figure 5.6. FE-SEM images of (a) SnO_2 HS/GO, (b,c) SnO_2 HS/GO/PEDOT hybrid, (d,e) HRTEM images of SnO_2 HS/GO/PEDOT hybrid, (f) Elemental mapping for Sn, S and O for the hybrid. SnO_2 HS used herein was obtained from hydrothermal treatment at 160 °C for 12 h of a solution with 1:3 molar ratio of $\text{SnCl}_2 \cdot 2\text{H}_2\text{O}$ to MPA and 100 mg of CTAB, followed by calcination at 500 °C for 3 h.

GO, SnO₂ HS/GO and SnO₂ HS/GO/PEDOT hybrid were also characterized by XRD and Raman spectroscopy. The XRD patterns of GO, SnO₂ HS/GO and SnO₂ HS/GO/PEDOT hybrid are similar to the SnO₂ HS (Figure 5.7).

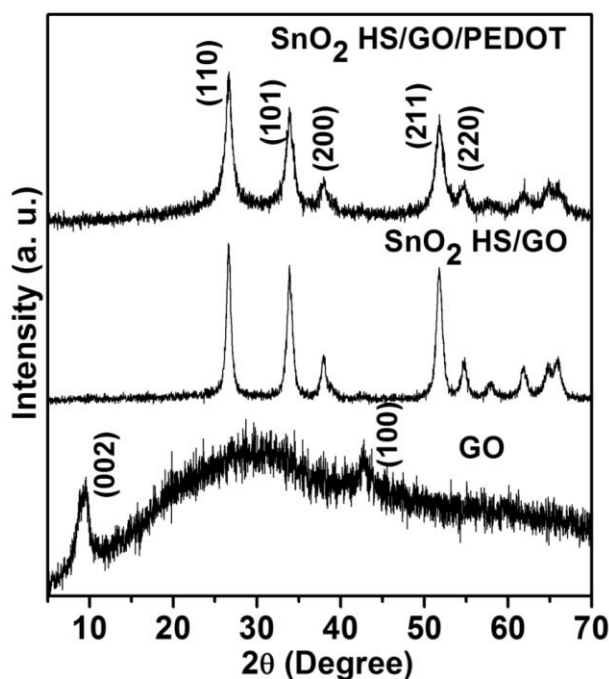


Figure 5.7. Powder XRD patterns of GO, SnO₂ HS/GO and SnO₂ HS/GO/PEDOT hybrids. SnO₂ HS used herein were obtained from hydrothermal treatment at 160 °C for 12 h of a solution with 1:3 molar ratio of SnCl₂·2H₂O to MPA and 100 mg of CTAB, followed by calcination at 500 °C for 3 h.

Raman spectra of GO, SnO₂ HS/GO and SnO₂ HS/GO/PEDOT hybrid are shown in Figure 5.8. The Raman spectrum of GO gives two prominent peaks at 1356 cm⁻¹ and 1593 cm⁻¹ corresponding to D and G bands, respectively. The G band is related to the E_{2g} mode of phonon vibrations within sp²-bonded carbon materials and the D band indicates the presence of a large number of defects in the graphene structure. The intensity ratio between D and G bands (I_D/I_G) provides information about the degree of defects that prevail in the sample. The measured I_D/I_G ratio for GO is around 1.88 which indicates a large number of defects in the as-prepared GO. When SnO₂ HS were loaded on GO to form the SnO₂ HS/GO hybrid the Raman spectrum

gives D and G bands at 1343 cm^{-1} and 1582 cm^{-1} , respectively, and the I_D/I_G ratio was around 1.4. A decreased I_D/I_G ratio indicates an increase in the ordering degree of carbon in the SnO_2 HS/GO hybrid, which is favorable to enhance electronic conductivity. The Raman spectrum of SnO_2 HS/GO/PEDOT hybrid show peaks mainly from PEDOT. The peaks at 1365 , 1428 , 1450 and 1500 cm^{-1} are attributed to $\text{C}_\beta\text{-C}_\beta$ stretching, symmetrical $\text{C}_\alpha\text{=C}_\beta$ stretching, oxidized symmetrical $\text{C}_\alpha\text{=C}_\beta$ stretching and asymmetrical $\text{C}_\alpha\text{=C}_\beta$ stretching, respectively[23]. The presence of these multiple peaks from PEDOT is indicative of a good mixing between SnO_2 HS/GO and PEDOT.

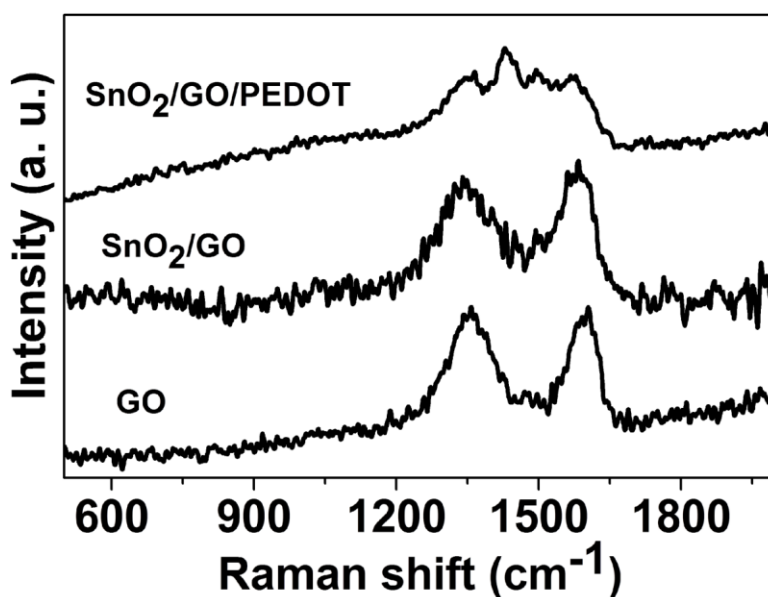


Figure 5.8. Raman spectra of GO, SnO_2 HS/GO and SnO_2 HS/GO/PEDOT hybrid. SnO_2 HS used herein was obtained from hydrothermal treatment at $160\text{ }^\circ\text{C}$ for 12 h of a solution with 1:3 molar ratio of $\text{SnCl}_2\cdot 2\text{H}_2\text{O}$ to MPA and 100 mg of CTAB, followed by calcination at $500\text{ }^\circ\text{C}$ for 3 h.

XPS was carried out to examine the surface electronic states and the composition of the SnO₂ HS and the SnO₂ HS/GO/PEDOT hybrid. The typical peaks of Sn (3p, 3d and 4d) were observed in the survey spectrum of both SnO₂ HS and hybrid (Figure 5.9a), which arise from SnO₂. In the survey spectrum of SnO₂ HS/GO/PEDOT, high intensity peaks of C1s and S2p are also observed and these stem exclusively from the thiophene rings of PEDOT. From the survey spectrum it can be concluded that PEDOT is ubiquitous in the SnO₂ HS/GO/PEDOT hybrid. The deconvoluted core-level spectrum of the Sn3d is shown in Figure 5.9b. The symmetric peaks centered at 487.0 and 495.5 eV are assigned to Sn3d_{5/2} and Sn3d_{3/2} respectively, which are characteristic of Sn⁴⁺ in SnO₂ HS[15]. Figure 5.9c shows the O1s spectrum of SnO₂ HS, deconvoluted into 2 peaks at binding energies of 530.1 and 532.1 eV corresponding to Sn-O and O-H (adsorbed water) respectively. The deconvoluted O1s spectrum of SnO₂ HS/GO/PEDOT hybrid shows Sn-O, C=O and C-O components at binding energies of 530.1, 531.6 and 533.2 eV, respectively (Figure 5.9d)[15]. The C1s core level spectrum could be deconvoluted into 5 peaks (Figure 5.9e). The assignments are as follow: 284.6 eV for graphitic carbon (C-C), 285.6 eV for C-S (solely from PEDOT), 286.4 eV for C-O, 287.4 eV for C=O and 288.9 eV for O-C=O, the latter two especially confirming the functionalization of graphene by oxygen containing moieties. The presence of oxygenated functional groups in GO and oxygens in PEDOT, can promote binding to SnO₂ HS. The S2p peak was deconvoluted into 2 peaks at 163.3 eV and 164.5 eV (Figure 5.9f) separated by 1.2 eV, and these correspond to the spin-orbit doublet of S2p_{3/2} and S2p_{1/2} components respectively, arising from the thiophene rings in PEDOT[24].

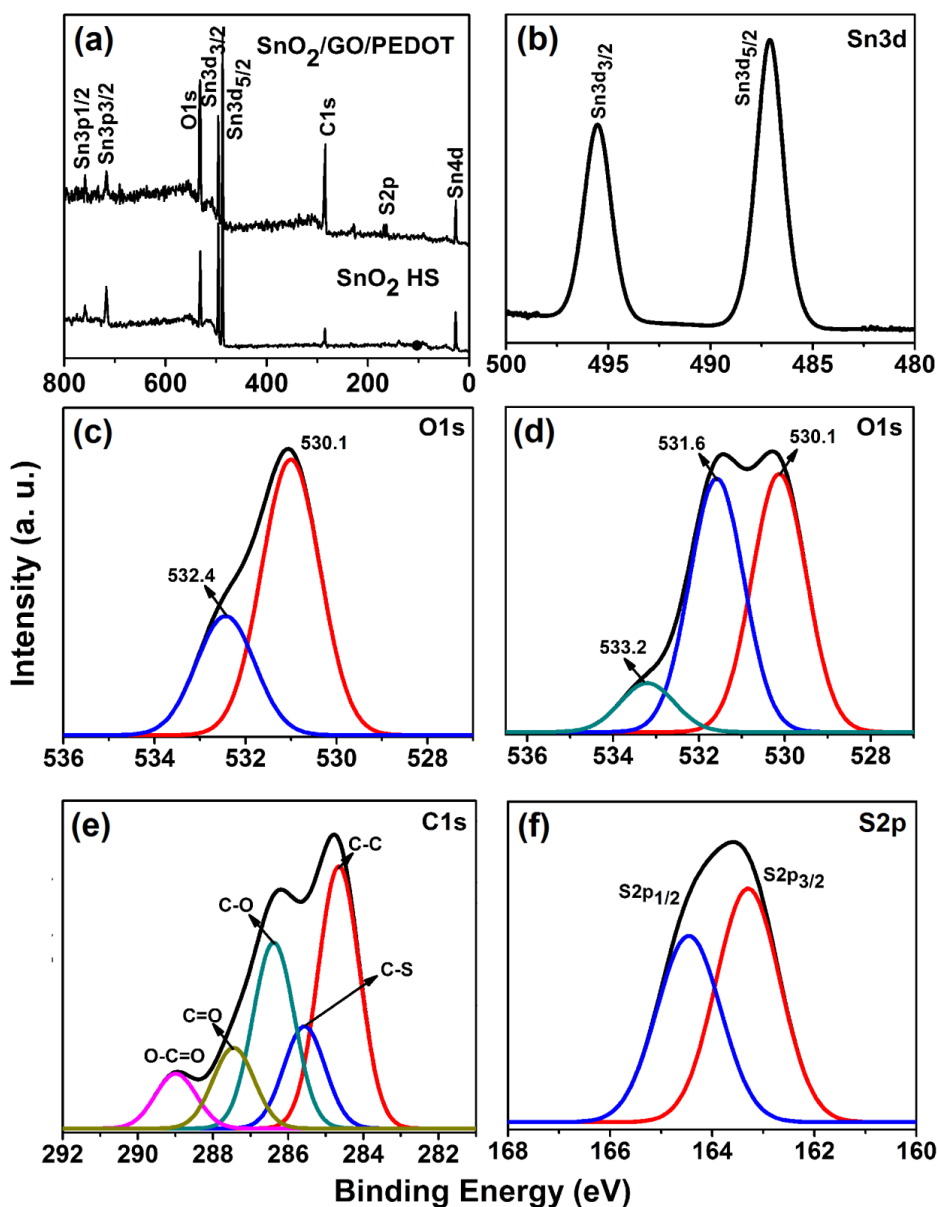


Figure 5.9. XPS survey spectra of (a) SnO₂ HS /GO/PEDOT and SnO₂ HS and deconvoluted core level spectra of (b) Sn3d and (c) O1s from SnO₂ HS and (d) O1s, (e) C1s and (f) S2p from SnO₂ HS/GO/PEDOT hybrid. SnO₂ HS used herein was obtained from hydrothermal treatment at 160 °C for 12 h of a solution with 1:3 molar ratio of SnCl₂.2H₂O to MPA and 100 mg of CTAB, followed by calcination at 500 °C for 3 h.

Thermogravimetric analysis (TGA) was carried out to measure the amount of carbon present in SnO₂ HS/GO and SnO₂ HS/GO/PEDOT hybrids (Figure 5.10). TGA was carried out in the temperature range of 30 - 900 °C. Figure 5.10a shows a

total weight loss of around 35% which corresponds to the carbon content in SnO₂ HS/GO hybrid. The derivative plot of SnO₂ HS/GO hybrid shows peaks at around 286 °C and 660 °C temperatures and these correspond to the surface functional groups of graphene oxide and carbon from the aromatic benzene rings. Figure 5.10b exhibits a total 52% weight loss between 150 - 750 °C temperature range. The weight loss is due to the carbon present in the surface functional groups and benzene rings of GO and in the ethylenedioxythiophene rings of PEDOT in the ternary hybrid.

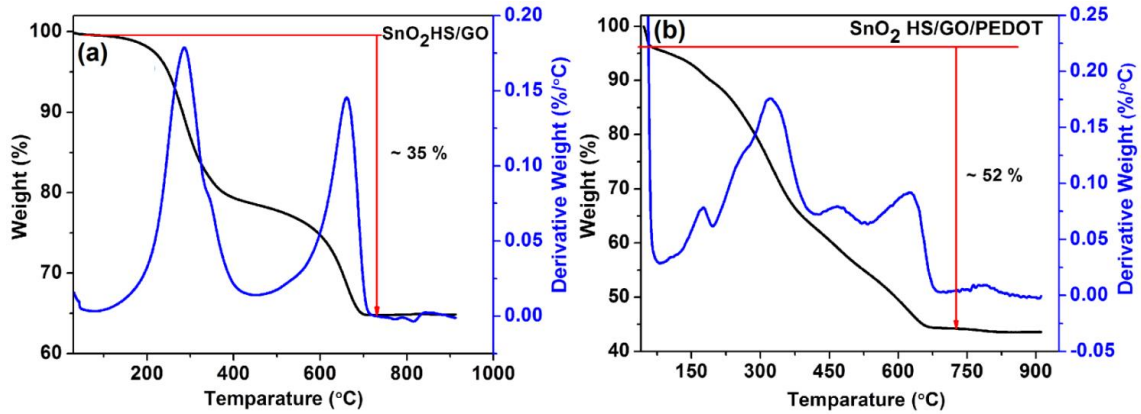


Figure 5.10. TGA plots of (a) SnO₂ HS/GO and (b) SnO₂ HS/GO/PEDOT hybrid. SnO₂ HS used herein were obtained from hydrothermal treatment at 160 °C for 12 h of a solution with 1:3 molar ratio of SnCl₂.2H₂O to MPA and 100 mg of CTAB, followed by calcination at 500 °C for 3 h.

5.4.3. Electrical conduction response

The Nyquist plots of SnO₂ HS, SnO₂ HS/GO and SnO₂ HS/GO/PEDOT recorded over a frequency range of 10⁻² - 10⁵ Hz and an ac amplitude of 10 mV and a dc potential of 0 V are shown in Figure 5.11. Equations used for calculating R_e and R_i are given below.

$$1/(R_h - R_s) = 1/R_e + 1/R_i \quad (5.1)$$

$$3(R_i - R_s) = R_i + R_e \quad (5.2)$$

R_s is the solution resistance, which can be obtained from the impedance curve for the electrolyte with the two bare electrodes. R_h is the high frequency real axis intercept minus R_s . R_l is the low frequency limiting real impedance. R_e and R_i are the electronic and internal ion-diffusional resistances of the electrodes and R_e could be obtained by solving equations 5.1 and 5.2. The electronic resistances of SnO₂ HS, SnO₂ HS/GO and SnO₂ HS/GO/PEDOT were 1311, 3.05 and 0.8 Ω . The impedance to electron movement is significantly decreased, by more than 400 times in SnO₂ HS/GO and by 1600 times in the SnO₂ HS/GO/PEDOT compared to SnO₂ HS, thus implying that electron transport in the ternary hybrid is facile which is advantageous for electrochemical cycling.

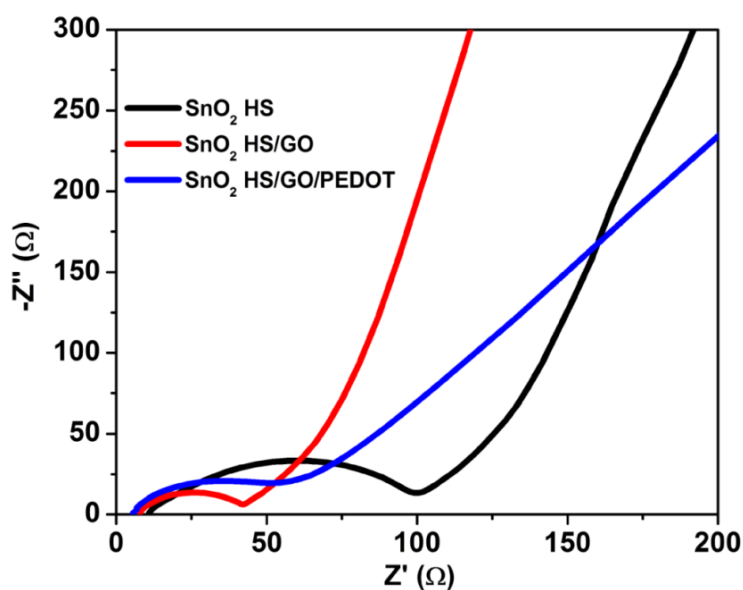
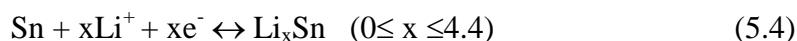
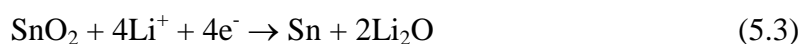


Figure 5.11. Nyquist plots for the SnO₂ HS, SnO₂ HS/GO and SnO₂HS/GO/PEDOT hybrid for the as-assembled cells.

5.5. Electrochemical response

The electrochemical performances of SnO₂ HS, SnO₂ HS/GO and SnO₂ HS/GO/PEDOT hybrids were investigated using lithium metal as counter and reference electrodes. The cyclic voltammograms (CV) of SnO₂ HS, SnO₂ HS/GO and SnO₂ HS/GO/PEDOT hybrid were measured in the voltage range of 0 to 2.5 V at a scan rate 0.1 mV s⁻¹. The CV curves of SnO₂ HS for the first 3 consecutive cycles are shown in Figure 5.12a. The CV curves of SnO₂ HS are consistent with previous reports on SnO₂ HS[8,19]. The electrochemical interaction between lithium and SnO₂ includes two steps given by the reactions:



During the first cathodic scan, the reduction peak at 1.3 V corresponds to the reduction of the electrolyte and formation of a solid electrolyte interface (SEI) layer on the surface of SnO₂ HS electrode and this is followed by another peak at 0.83 V which is assigned to the reduction of SnO₂ to Li₂O and Sn (equation 5.3). The broad peak in the range of 0.5 to 0 V is attributed to an alloying reaction involving the formation of Li_xSn from Sn (equation 5.4). In the first anodic scan, oxidation peaks are observed at 0.56 and 1.25 V and these correspond to the de-alloying reaction of Li_xSn to Sn and partial oxidation of Sn to SnO₂, respectively[13,25]. In the subsequent cycles, the reduction peaks observed between 0.5 to 0 V and the oxidation peak observed at ~0.5 V are reversible. The SnO₂ HS/GO hybrid also shows similar cyclic voltammograms (Figure 5.12b) except that the SnO₂ HS show fast decline in peaks whereas the CV curves of SnO₂ HS/GO hybrid exhibit lesser

decline in peak currents. Figure 5.12c shows the cyclic voltammograms of SnO₂ HS/GO/PEDOT hybrid for the first 4 cycles. The CV curves of SnO₂ HS/GO/PEDOT showed broad redox curves and the conversion and alloying peaks are not distinctive because of the presence of more amount of carbon from GO and PEDOT. Pristine GO or PEDOT did not show any redox peaks in this potential range. The SnO₂ HS/GO/PEDOT hybrid shows a broad peak at 1 V corresponding to reduction of SnO₂ to Sn during the first cathodic scan. The broad peaks in the range of 0.5 to 0 V are attributed to the alloying reaction of Sn to Li_xSn during the cathodic scan. In the anodic sweep, the peaks between 0.3 to 1 V arise from the de-alloying reaction to yield Sn. The CV curves of the SnO₂ HS/GO/PEDOT hybrid show an increase in current with cycling upto 3 cycles and remain steady thereafter. This is an indirect evidence indicating that the SnO₂ HS/GO/PEDOT hybrid is capable of exhibiting a more stable cycling performance compared to SnO₂ HS and SnO₂ HS/GO hybrid.

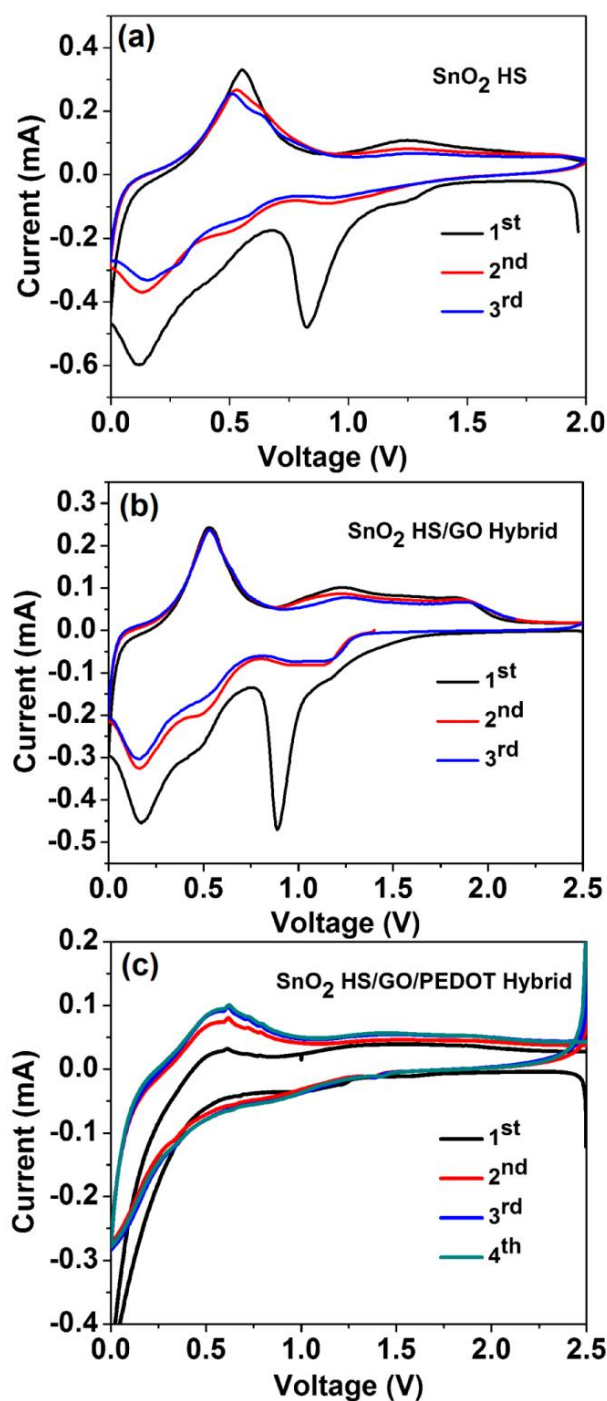


Figure 5.12. Cyclic voltammetry curves of (a) SnO₂ HS (b) SnO₂ HS/GO (c) SnO₂ HS/GO/PEDOT hybrid collected at the scan rate of 0.1 mV s⁻¹ in the voltage window of 0 - 2.5 V with Li metal as anode. SnO₂ HS used herein was obtained from hydrothermal treatment at 160 °C for 12 h of a solution with 1:3 molar ratio of SnCl₂.2H₂O to MPA and 100 mg of CTAB, followed by calcination at 500 °C for 3 h.

The typical charge-discharge curves of SnO₂ HS at a constant current density of 100 mA g⁻¹ from 2 to 0.01 V are shown in Figure 5.13a. The first discharge plateau at ~1 V corresponds to the reduction of SnO₂ to Sn along with formation of SEI and the voltage range between 0.7 to 0.01 V is ascribed to the alloying reaction of Sn to Li_xSn. During the first charge the plateaus at around 0.5 and 1.25 V correspond to the de-alloying and partial oxidation of Sn to SnO₂ reaction, respectively. The redox potentials in the charge-discharge curves match well with the potentials in the CV curves. From the charge-discharge curves, the discharge and charge capacities of SnO₂ HS were deduced to be 1912 and 990 mAh g⁻¹ respectively with a Coulombic efficiency of 51.8%. From equations 5.3 and 5.4 the maximum theoretical capacity in the first discharge is calculated to be 1493 mAh g⁻¹. During the first discharge, at low voltages the electrolyte undergoes decomposition and SEI is formed on the surface of the electrode. This contributes to extra capacity during the first discharge. During the first charge a maximum theoretical specific capacity of 792 mAh g⁻¹ is expected. But the large lithium storage capacity can be in all likelihood linked to the microstructure of the hollow spheres wherein the porous shells allow the innards of the sphere to be electrolyte accessible and another reason could be the partial oxidation of Sn to SnO₂[8]. The SnO₂ HS exhibit a gradual fade in capacity with increase in cycle number. After 30 cycles the SnO₂ HS retain a reversible capacity of 398.4 mAh g⁻¹ with a Coulombic efficiency of 96% (0.01 to 2 V, Figure 5.13b). The V_{OC} of the cell was 3 V at the start, and the cell was discharged to 0.01 V, prior to measuring the capacity *versus* cycling response over a potential window confined to 0.01 to 1 V. Notably, when charge-discharge characteristics of SnO₂ HS were measured in the voltage range of 0.01 to 1 V at a constant current density of 100 mA

g^{-1} , a stable cycle performance was achieved for 30 cycles (Figure 5.13b). The reversible capacity decreased from 585 (for 6th cycle) to 497 mAh g^{-1} (for 30th cycle). The increased cycling stability when cycled between voltage window of 0.01-1 V is due to the inhibition of the surface reaction between Sn and Li_2O which occurs at higher voltages and minimization of SEI formation on Sn[16]. By comparison, the SnO_2 solid microspheres exhibit an initial reversible capacity of 716 mAh g^{-1} and after 30 cycles the capacity faded to 141 mAh g^{-1} (Figure 5.5). The very high capacity of SnO_2 HS compared to solid spheres is mainly because of porous open structure of SnO_2 HS which allows for greater ion uptake during electrochemical cycling. The improved cycling performance of HS compared to solid spheres is ascribed to the relative ease with which the HS can accommodate volume expansion upon lithium insertion and extraction. Hollow SnO_2 spheres provide enough space to buffer the volume change during charging-discharging phenomena and are cyclable compared to solid SnO_2 spheres.

To further improve the electrochemical performance of SnO_2 HS, SnO_2 HS/GO and SnO_2 HS/GO/PEDOT hybrids were synthesized. The SnO_2 /GO hybrid shows little improvement in cycling stability. It shows an initial reversible capacity of 980 mAh g^{-1} and it retained a capacity of 434 mAh g^{-1} after 30 cycles (Figure 5.13c). Comparatively, the SnO_2 HS/GO/PEDOT hybrid measured in the voltage range of 0.01 - 2.5 V at 100 mA g^{-1} current density (Figure 5.13d, Charge-discharge curves) exhibited excellent cycling stability. Initially the hybrid showed discharge and charge capacities of 1654 and 717.5 mAh g^{-1} respectively with a Coulombic efficiency of 43.4% (Figure 5.13e). The irreversible capacity loss is unavoidable for most of the metal oxides and composites with carbonaceous moieties[21,22,26]. The

large irreversible capacity loss was mainly because of irreversible conversion reaction of SnO₂ to Sn and SEI formation. For the preparation of SnO₂ HS/GO/PEDOT hybrid, we used GO which has a large number of oxygen containing functional groups, and this was also validated by XPS analyses in Figure 5.9. The oxygenated surface functional groups from GO and the oxygens on PEDOT can irreversibly trap some of the lithium ions during the first discharge cycle which can also contribute to excess capacity during first discharge. As a consequence, the first discharge capacity of the hybrid is much higher than the theoretical value. The observed high charge capacity (717 mAh g⁻¹) of the hybrid is mainly from SnO₂ and the contribution of GO/PEDOT hybrid is not significant. A GO/PEDOT hybrid was also prepared using the same method as SnO₂ HS/GO/PEDOT but without adding SnO₂ HS. When the electrochemical behavior of the GO/PEDOT hybrid was measured between the same voltage range (0.01 - 2.5 V) and at the same current density (100 mA g⁻¹), it showed a capacity of ~ 50 mAh g⁻¹ for the measured 50 cycles (Figure 5.14). Immediately after the first 2 cycles the Coulombic efficiency of SnO₂ HS/GO/PEDOT hybrid for the 3rd cycle reached to 96.5% and it gradually increased with cycles. After 150 cycles the SnO₂ HS/GO/PEDOT hybrid shows a reversible capacity of 608.4 mAh g⁻¹ with a Coulombic efficiency more than 99%. The electrode material retained a capacity of ~ 85% of its initial value. The observed cycling stability is much better and comparable to some of the earlier reports on SnO₂/GO hybrids[17,20-22]. The higher reversible capacity of the SnO₂ HS/GO/PEDOT hybrid also suggests the full utilization of all the SnO₂ crystallites, as GO and PEDOT can effectively inhibit SnO₂ HS from aggregating during charge-discharge cycling.

The SnO₂ HS/GO/PEDOT hybrid also showed superior rate capability compared to SnO₂ HS and SnO₂ HS/GO hybrid. Figure 5.13f shows the rate capabilities of SnO₂ HS, SnO₂ HS/GO hybrid and SnO₂ HS/GO/PEDOT hybrid measured at different current densities. While the capacity of SnO₂ HS decreased rapidly with increasing current density, the SnO₂/GO hybrid showed a more robust response. The SnO₂ HS/GO/PEDOT hybrid delivers a reversible capacity, as high as 381 mAh g⁻¹ even at high current density of 2000 mA h g⁻¹. A capacity of 636 mAh g⁻¹ was retained after 25 cycles at a current density of 100 mA g⁻¹. The better rate capability can be attributed to the porous structure of SnO₂ HS and the enhanced electronic and ionic conductivity of the electrode induced by GO and PEDOT. Further, the GO nanosheets can also alleviate the mechanical stress caused by the severe volume change during lithium insertion and extraction, and inhibits the detachment of the electroactive material from the electrode. Besides, the buffer layer also prevents the aggregation of tin nanoparticles. PEDOT, by the virtue of its mechanical stability enhances the capacity retention of the SnO₂ HS/GO/PEDOT hybrid by enveloping SnO₂ embedded in GO nanosheets, thus imparting high mechanical integrity to the overall hybrid. PEDOT also prevents the direct contact of SnO₂ crystallites with the electrolyte and thus any side chemical reactions of the electrolyte with the oxide are avoided.

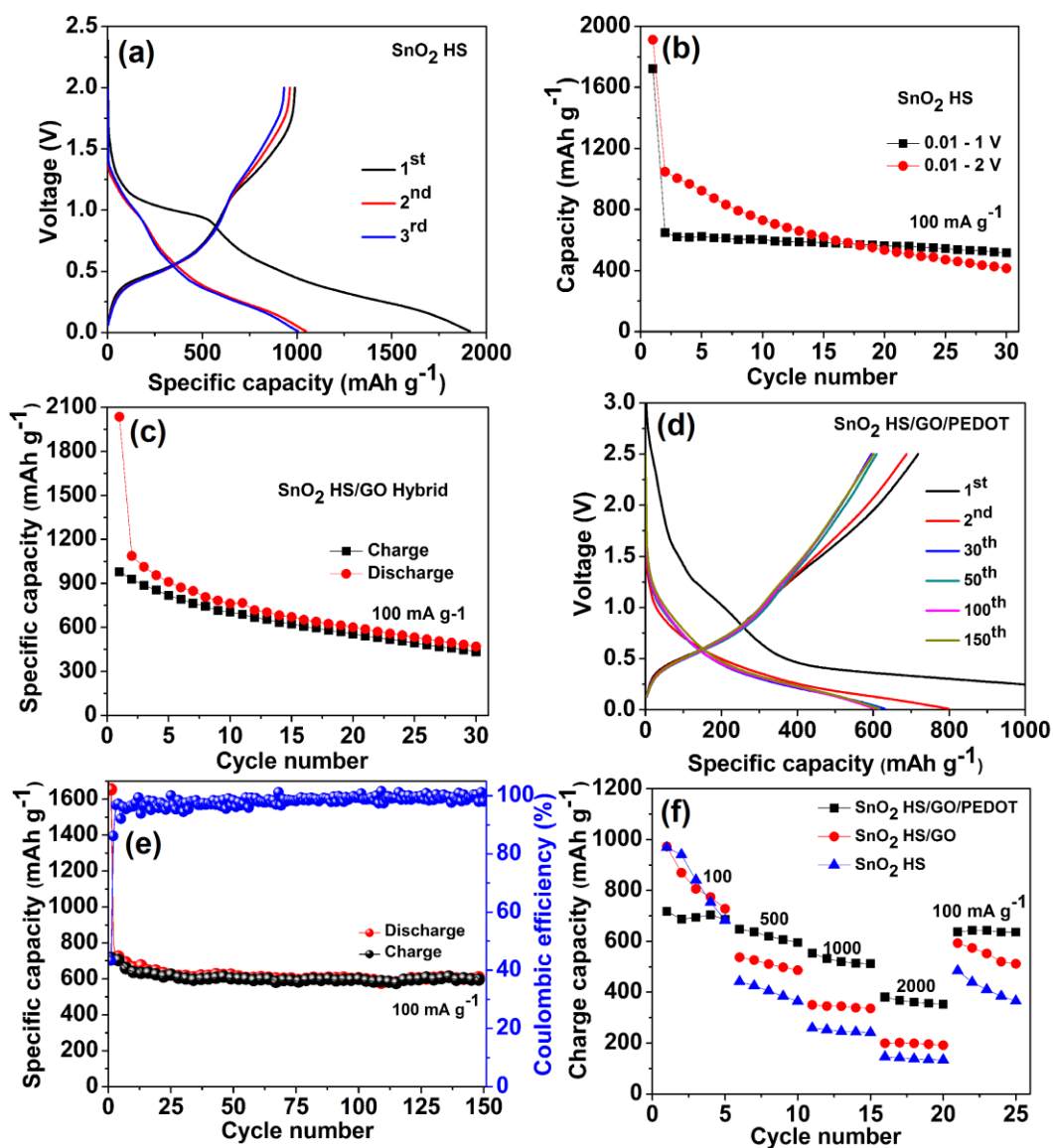


Figure 5.13. Typical charge-discharge curves of SnO₂ HS obtained at a current density of 100 mA g⁻¹ in the voltage window of 0.01 - 2 V, (b) cycling performance of SnO₂ HS recorded in different potential ranges, (c) cyclability of SnO₂ HS/GO/PEDOT hybrid obtained in the voltage range of 0.01 - 2.5 V at 100 mA g⁻¹ and (d) rate capability of SnO₂ HS, SnO₂ HS/GO and SnO₂/GO/PEDOT hybrid.

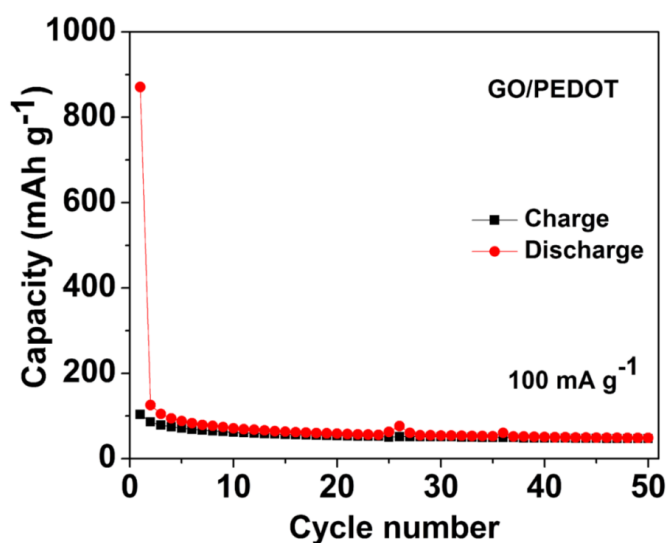


Figure 5.14. Cyclability of the GO/PEDOT hybrid, at 100 mA g^{-1} current density in the voltage range of 0.01-2.5 V.

5.6. Summary

SnO_2 HS were prepared by a hydrothermal method by employing MPA as the structure directing agent, CTAB as the surfactant that inhibited HS from agglomeration and water as the solvent critical to the formation of empty cores in the HS. Optimized SnO_2 HS with outer diameters in the range of 140-150 nm and inner hollow core dimensions of about 100 nm were synthesized. The roles of MPA, CTAB and the solvent were deduced by performing detailed morphological studies. The temperature induced structural evolution of SnO_2 HS from SnO_2 solid spheres was explained using an inward-out Ostwald ripening mechanism. Hybrids of SnO_2 HS with GO and PEDOT were synthesized with the objective of increasing electronic conductivity of the active electrode whilst simultaneously preserving the structural integrity of HS, thereby leading to a more robust material capable of exhibiting an electrochemical cycling response better than that of pristine SnO_2 HS. While the optimized SnO_2 HS displayed a reversible Li^+ storage capacity of 400 mA h g^{-1} attained at a current density of 100 mA g^{-1} at the end of 30 cycles, the SnO_2

HS/GO/PEDOT hybrid delivered a reversible capacity of 608 mA h g^{-1} at the same current density after 150 cycles. The immobilization of SnO_2 HS on GO and further coating by a continuous layer of amorphous PEDOT was affirmed by elemental mapping and XPS. The key roles of GO nanosheets as the electron conducting matrix for SnO_2 HS and PEDOT as the polymer envelope which buffers the severe volume changes that occur during cycling and inhibits electrode disintegration and rapid capacity fading, thus amplifying reversible capacity, rate capability and cycling stability are demonstrated. This route of integrating conductive GO nanosheets and electrochemically stable PEDOT is extendable to a wide range of metal oxides HS which can be useful for developing high quality LIB anodes.

References

1. I. A. Courtney, J. R. Dahn, *J. Electrochem. Soc.*, 144 (1997) 2045-2052.
2. Y. Wang, F. Su, J. Y. Lee, X. S. Zhao, *Chem. Mater.*, 18 (2006) 1347-1353.
3. C. Kim, M. Noh, M. Choi, J. Cho, B. Park, *Chem. Mater.*, 17 (2005) 3297-3301.
4. K. Kravchyk, L. Protesescu, M. I. Bodnarchuk, F. Krumeich, M. Yarema, M. Walter, C. Guntlin, M. V. Kovalenko, *J. Am. Chem. Soc.*, 135 (2013) 4199-4202.
5. Z. Wang, L. Zhou, X. W. Lou, *Adv. Mater.*, 24 (2012) 1903-1911.
6. J. S. Chen, L. A. Archer, X. W. Lou, *J. Mater. Chem.*, 21 (2011) 9912-9924.
7. Y. J. Hong, M. Y. Son, Y. C. Kang, *Adv. Mater.*, 25 (2013) 2279-2283.
8. X. W. Lou, Y. Wang, C. Yuan, J. Y. Lee, L. A. Archer, *Adv. Mater.*, 18 (2006) 2325-2329.
9. Y. Wang, J. Y. Lee, H. C. Zeng, *Chem. Mater.*, 17 (2005) 3899-3903.
10. J. Wang, N. Du, H. Zhang, J. Yu, D. Yang, *J. Phys. Chem. C*, 115 (2011) 11302-11305.
11. J. Liu, Y. Li, X. Huang, R. Ding, Y. Hu, J. Jianga, L. Liao, *J. Mater. Chem.*, 19 (2009) 1859-1864.
12. M. S. Park, G. X. Wang, Y. M. Kang, D. Wexler, S. X. Dou, H. K. Liu, *Angew. Chem. Int. Ed.*, 46 (2007) 750-753.

13. X. Wang, Z. Li, Q. Li, C. Wang, A. Chen, Z. Zhang, R. Fan, L. Yin, *Cryst Eng Comm.*, 15 (2013) 3696-3704.
14. J. Fan, T. Wang, C. Yu, B. Tu, Z. Jiang, D. Zhao, *Adv. Mater.*, 16 (2004) 1432-1436.
15. G. Zhou, D. W. Wang, L. Li, N. Li, F. Li, H. M. Cheng, *Nanoscale*, 5 (2013) 1576-1582.
16. J. M. Haag, G. Pattanaik, M. F. Durstock, *Adv. Mater.*, 25 (2013) 3238-3243.
17. S. M. Paek, E. Yoo, I. Honma, *Nano Lett.*, 9 (2009) 72-75.
18. L. Wang, D. Wang, Z. Dong, F. Zhang, J. Jin, *Nano Lett.* 13 (2013) 1711-1716.
19. X. W. Lou, C. M. Li, L. A. Archer, *Adv. Mater.*, 21 (2009) 2536-2539.
20. Y. Li, X. Lv, J. Lu, J. Li, *J. Phys. Chem. C.*, 114 (2010) 21770-21774.
21. S. K. Park, S. H. Yu, N. Pinna, S. Woo, B. Jang, Y. H. Chung, Y. H. Cho, Y. E. Sung, Y. Piao, *J. Mater. Chem.*, 22 (2012) 2520-2525.
22. R. Liang, H. Cao, D. Qian, J. Zhangc, M. Qu, *J. Mater. Chem.*, 21 (2011) 17654-17657.
23. Y. K. Han, M. Y. Chang, W. Y. Huang, H. Y. Pan, K. S. Ho, T. H. Hsieh, S. Y. Pan, *J. Electrochem. Soc.*, 158 (2011) K88-K93.
24. S. K. M. Jonsson, J. Birgeron, X. Crispin, G. Greczynski, W. Osikowicz, A. W. Denier van der Gonc, W. R. Salaneck, M. Fahlman, *Synthetic Metals*, 139 (2003) 1-10.
25. Y. Zhao, J. Li, N. Wang, C. Wu, G. Dong, L. Guan, *J. Phys. Chem. C*, 116 (2012) 18612-18617.
26. S. J. R. Prabakar, Y. H. Hwang, E. G. Bae, S. Shim, D. Kim, M. S. Lah, K. S. Sohn, M. Pyo, *Adv. Mater.*, 25 (2013) 3307-3312.

Chapter 6

Size Control of SnO₂ Hollow Spheres and How Size Governs Li-ion Storage Behavior

6.1. Abstract

In this chapter, a template-free, one-pot hydrothermal approach was used for preparing SnO₂ HS with controlled hollow sphere size by using organic additives as structure directing agents. The role of the proportion of the organic moiety, namely, acetylacetonate (AcAc) and the thermal conditions which steer the growth of SnO₂ HS with an optimum size for efficient electrochemical energy storage performance was followed by XRD, FE-SEM and HRTEM. By tuning the processing parameters, SnO₂ HS with a narrow size distribution and good structural integrity were prepared. The optimization of SnO₂ HS (size and empty core dimensions) was accomplished by evaluating the Li ion storage performance of various electrodes. In addition, the SnO₂ HS were also found to be luminescent, indicating a dual function capability, as the blue light emitting property can be of use in applications which require both energy storage and emission.

6.2. Introduction

In the previous chapter, SnO₂ HS were prepared, and this was followed by the preparation of a hybrid capable of high Li-ion storage performance. Taking this further, in this chapter, how by varying processing parameters, a good control over the size of the hollow spheres can be achieved and how the size affects Li-ion storage is described.

6.3. Experimental

6.3.1. Synthesis of SnO₂ HS and nanostructures

Hollow spheres of SnO₂ were prepared by a one-step hydrothermal synthesis route using water as solvent. Typically, 1 mL of acetylacetone (AcAc, Aldrich, 98%) was taken in a 100 mL beaker and to this solution 3.324 mmol of SnCl₂·2H₂O (Merck, 98%) was added and stirred for 5 min. To the resulting clear solution, 40 mL of ultrapure water and 1.1 g of 3-mercaptopropionic acid (MPA, Alfa Aesar, 98%) was added and stirred for 30 min. To the resulting solution, 100 mg of cetyltrimethylammoniumbromide (CTAB, Alfa Aesar, 98%) surfactant followed by 10 ml of ultrapure water were added and stirred for 1 h. The resulting solution was transferred to a 80 mL Teflon lined stainless steel autoclave. After heating at 160 °C for 13 h in an oven, the resulting pale yellow color precipitate was filtered and washed with water and dried at 80 °C for 6 h. Similarly, three more precursor solutions with 2.5 mL, 5 mL and 10 mL of AcAc were also prepared while maintaining all other concentrations constant. These solutions were also subjected to the 160 °C for 13 h heat treatment in an autoclave and the three products obtained were analyzed and compared with the one obtained using 1 mL AcAc. The effect of temperature on the morphology of the samples obtained from the solution prepared with 5 mL of AcAc while keeping other concentrations same was studied by heating this solution at two more temperatures of 140 and 180 °C. Solution with precursors 3.3 mmol SnCl₂·2H₂O, 5 mL of AcAc and 100 mg CTAB but without any MPA and yet another precursor the solution with 3.3mmol SnCl₂·H₂O, 1.1 g of MPA and 5 mL of AcAc without adding any CTAB were also prepared. These two solutions (without MPA and without CTAB respectively) were subjected to the 160 °C, 13 h

heat treatment in an autoclave to also obtain SnO₂ products.

6.4. Results and discussion

6.4.1. Structural aspects

Powder XRD patterns of SnO₂ samples prepared from precursor solutions containing 1, 2.5, 5 and 10 mL of AcAc are shown in Figure 6.1a. The XRD pattern of the sample prepared from a solution containing 1 mL of AcAc matches well with the standard diffraction pattern of SnO₂ with a tetragonal crystal structure however extraneous peaks from SnS (impurity) were also observed (JCPDF # 75-2115). The diffraction peaks corresponding to SnO₂ prepared from solutions with 2.5, 5 and 10 mL of AcAc are assigned to the tetragonal crystal structure of SnO₂ with space group P4₂/mnm(136) (JCPDF # 77-0447). In these three samples, no characteristic peaks corresponding to impurities such as SnS or SnS₂ were observed thus confirming that pure phase SnO₂ was formed successfully from solutions with higher proportion of AcAc. Further, a systematic increase in FWHM of the main diffraction peaks of SnO₂ was observed as a function of increasing AcAc content. After annealing, the sample prepared from a solution encompassing 5 mL AcAc at 500 °C for 3 h air, the XRD pattern of the resulting sample was compared with that of the as-prepared sample. The as-prepared sample showed broader peaks compared to the annealed sample thus illustrating that annealing increases the crystallite size of SnO₂. The diffraction patterns of the as-prepared sample (solution prepared from 5 mL AcAc autoclaved at 160 °C for 13 h) were down shifted compared to the annealed sample by $2\theta = 0.1^\circ$. This is clearly visible from the enlarged view of the high intensity peak plotted for the as-prepared and annealed samples (Figure 6.1b). Oxygen deficiency in the as-prepared sample leading to slightly sub-stoichiometric

SnO_{2-x} could be one reason for this downshift.

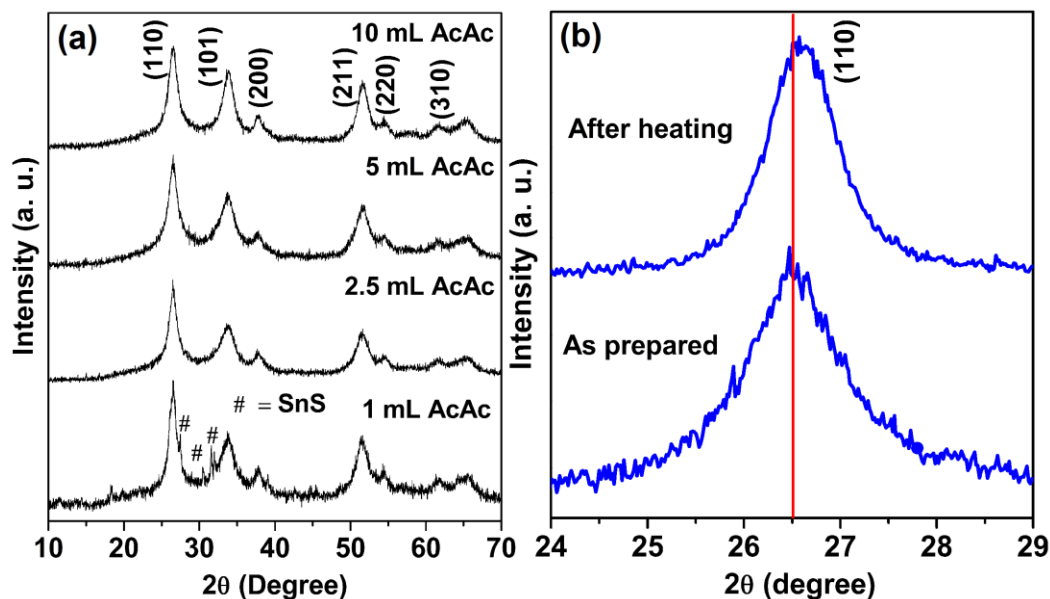


Figure 6.1. Powder XRD patterns of SnO_2 samples synthesized from precursor solutions containing 1, 2.5, 5 and 10 mL of AcAc. Each solution also contained 3.324 mmol of $\text{SnCl}_2 \cdot 2\text{H}_2\text{O}$, 1.1 g of MPA, 100 mg of CTAB and each solution was heated hydrothermally for 13 h at 160 °C, (b) enlarged view of as-prepared and annealed SnO_2 HS of high intensity peak.

6.4.2. Optical characteristics

To confirm oxygen deficiency in the as-prepared SnO_2 HS (prepared from a solution with 5 mL AcAc and 160 °C hydrothermal treatment for 13 h) the UV-Visible spectra of as-prepared SnO_2 HS and annealed SnO_2 HS (500 °C for 3 h) were recorded (Figure 6.2a) in diffuse reflectance mode and converted to absorbance. The optical band gaps for the two samples were calculated from their absorption edges. The optical transitions in crystalline SnO_2 are direct[1]. The as-prepared and annealed samples of SnO_2 HS show band gaps of 3.2 and 3.44 eV, respectively. The annealed SnO_2 HS shows a band gap close to that of bulk (commercial) SnO_2 ($E_g = 3.6$ eV). The lowering of band gap in the as-prepared HS could be due to the presence of a oxygen vacancies to form sub-stoichiometric SnO_{2-x} .

x HS, and upon annealing, stoichiometric SnO₂ was obtained.

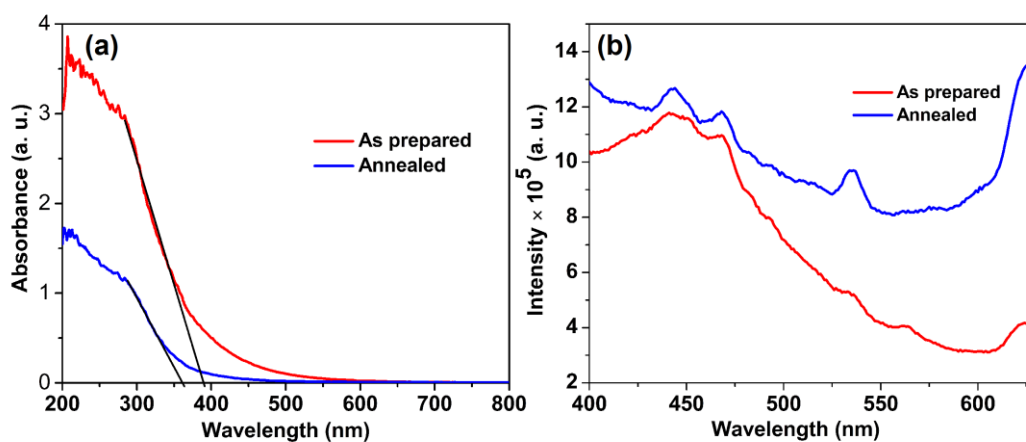


Figure 6.2. (a) UV-vis absorbance spectra of as-prepared and annealed (at 500 °C for 3 h) SnO₂ HS and (b) room temperature PL spectra of as-prepared and annealed (at 500 °C for 3 h) SnO₂ HS. The SnO₂ HS were prepared from a solution with 3.324 mmol of SnCl₂·2H₂O, 5 mL AcAc, 1.1 g of MPA, 100 mg of CTAB and the solution was heated hydrothermally for 13 h at 160 °C.

Figure 6.2b shows the comparative room temperature photoluminescence spectra of as-prepared (prepared from a solution with 5 mL AcAc and 160 °C hydrothermal treatment for 13 h) and annealed SnO₂ HS, recorded at an excitation wavelength of 325 nm. The emission was measured in the wavelength range of 400 to 630 nm. Both as-prepared and annealed SnO₂ HS samples show three peaks at 443, 468 and 535 nm. The broad peak centered at 443 nm was observed earlier for a SnO₂ nanoblades array by Her et al.,[2] and the peak at 468 nm was also observed for SnO₂ nano flowers by Wang et al.,[3] Since the position of these emission maxima are lower than the respective band gaps of the SnO₂, these emission cannot be attributed to the direct recombination of conduction band electrons in the Sn4p band and the holes in the O2p valence band. Therefore, these bands can be assigned to oxygen-related defects introduced during hydrothermal growth. The interactions

between oxygen vacancies and the interfacial tin vacancies lead to the formation of a significant number of trapped states, which form a series of metastable energy levels within the band gap and result in an emission in the low energy region. Apart from these three peaks, the as prepared SnO₂ HS shows two more weak peaks centered at 562 and 622 nm. The origin of these two peaks might be correlated to a greater defect concentration compared to the annealed SnO_{2-x} HS.

6.4.3. Electron microscopy analyses

Morphological studies of the samples prepared with various amounts of AcAc have been performed using FE-SEM and the images are shown in Figure 6.3. The FE-SEM image of the sample prepared from a solution with 1 mL of AcAc shows (Figure 6.3a) aggregated spherical particles of SnO₂. When the amount of AcAc was increased to 2.5 and 5 mL, the FE-SEM images of both the samples show spherical particles of SnO₂ are in the range of 250 - 400 and 450 - 750 nm dimensions, respectively, (Figure 6.3b and c). Some broken spheres with cavities are visible in the images of both samples, further demonstrating the hollow nature of the products. The FE-SEM images after incorporating 10 mL of AcAc shows the formation of aggregated SnO₂ hollow spheres with a wide distribution in size (Figure 6.3d).

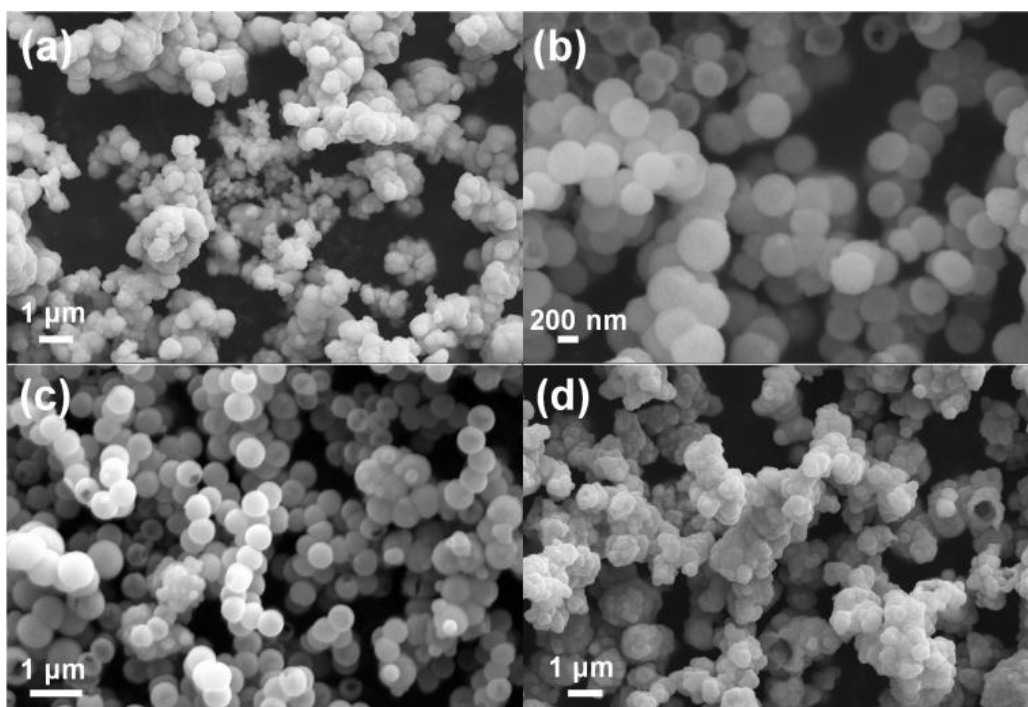


Figure 6.3. FE-SEM images of SnO₂ samples synthesized from precursor solutions containing (a) 1, (b) 2.5, (c) 5 and (d) 10 mL of AcAc. Each solution also contained 3.324 mmol of SnCl₂·2H₂O, 1.1 g of MPA, 100 mg of CTAB and each solution was heated hydrothermally for 13 h at 160 °C.

In order to confirm the hollow nature and the size of the spheres, HRTEM was performed on SnO₂ HS prepared from solutions containing 2.5 and 5 mL of AcAc. The HRTEM image (Figure 6.4a) of SnO₂ HS prepared from a solution with 2.5 mL AcAc, shows a sharp contrast (dark/bright) between the boundary and the center of the spheres, thus confirming their hollow nature. The size of these SnO₂ HS is in the range of 200-300 nm and the shell thickness of each hollow sphere is ~50 nm. Distinct lattice fringes are observed in the Figure 6.4b of the hollow sphere which show that each sphere is composed of small crystallites of about ~ 8 nm dimensions and the fringe separation of 0.33 nm matches very well with the (110) plane of the tetragonal crystal structure of SnO₂. The TEM image of sample prepared from a solution with 5 mL of AcAc (Figure 6.4c) shows the hollow nanostructure of SnO₂

with an outer diameter in the range of 350-400 nm and the shell thickness is approximately 60 nm. Figure 6.4d shows that each hollow sphere is constituted by SnO₂ crystallites of ~7 nm dimensions and the inter-fringe distance of 0.33 nm confirms the tetragonal crystal structure of SnO₂ HS. The HRTEM results concur with the XRD findings.

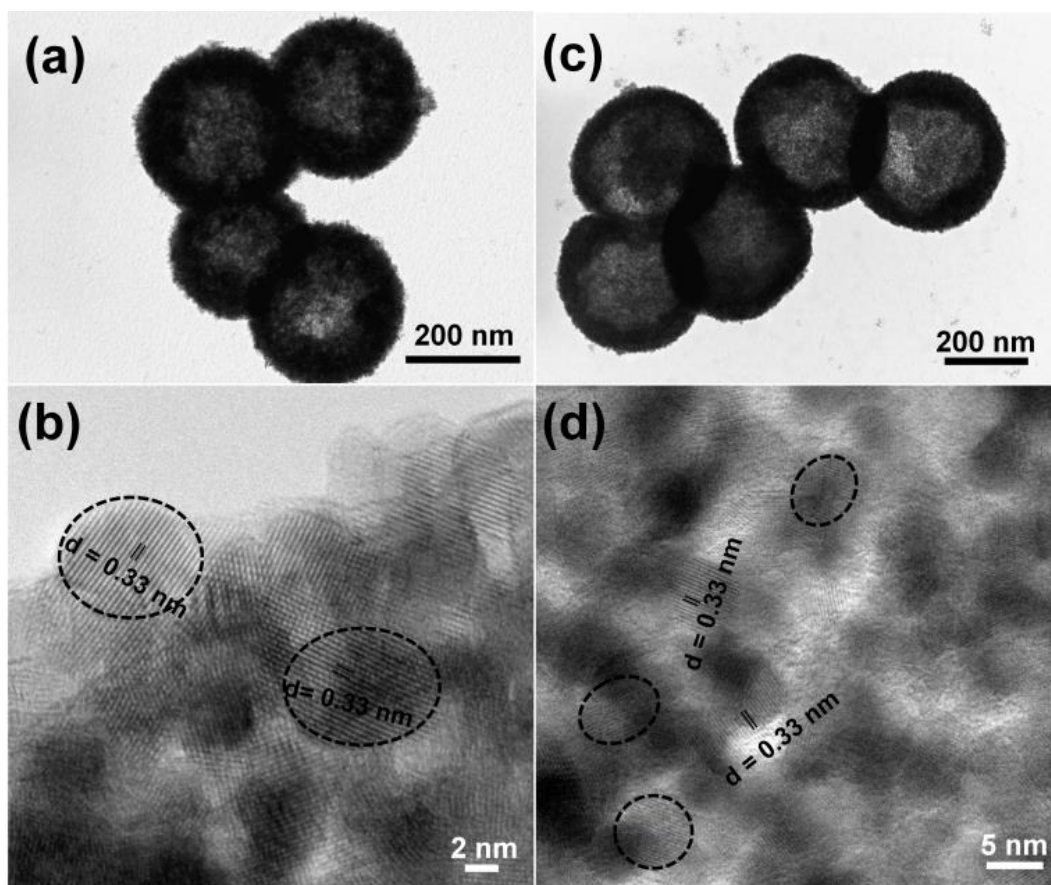


Figure 6.4. TEM images of SnO₂ HS obtained from solutions containing (a) 2.5 mL of AcAc, (b) corresponding lattice scale image, (c) 5 mL of AcAc and (d) corresponding lattice scale image. Each solution also contained 3.324 mmol of SnCl₂·2H₂O, 1.1 g of MPA, 100 mg of CTAB and was heated hydrothermally for 13 h at 160 °C.

6.4.4. Growth mechanism

To explain the SnO₂ HS formation mechanism, time dependent experiments were performed by hydrothermally heating the precursor solution containing 3.3 mmol of

$\text{SnCl}_2 \cdot 2\text{H}_2\text{O}$, 5 mL of AcAc, 1.1 g of MPA and 100 mg CTAB for intervals of 1, 4, 10, 13 and 24 h at a constant temperature of 160 °C. XRD patterns and TEM images were collected at the end of each interval and these are shown in Figure 6.5 and 6.6. The XRD pattern of sample obtained after heating for 1 h shows an amorphous nature whereas after heating for 4, 10, 13 and 24 h, each of the ensuing samples shows diffraction peaks corresponding to the tetragonal crystal structure of SnO_2 (JCPDF # 77-0447) and no other impurity peaks were observed.

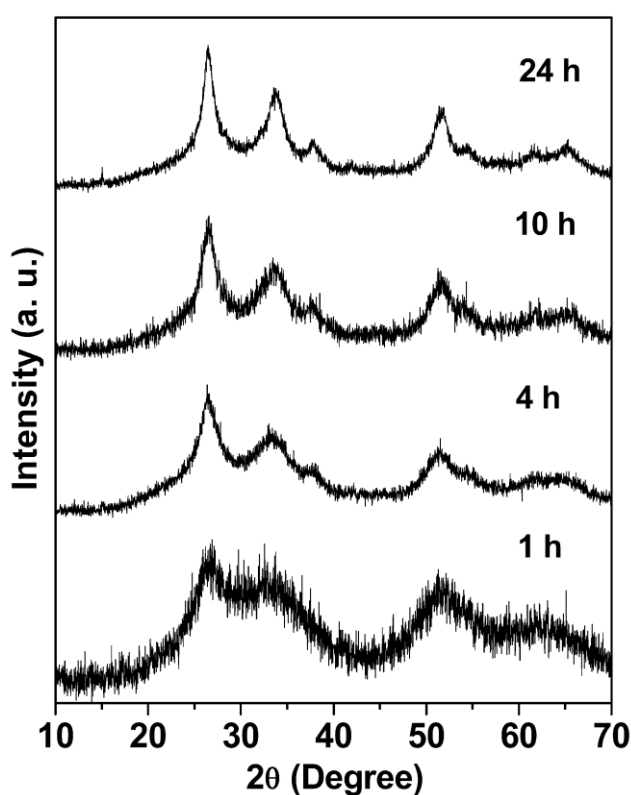


Figure 6.5. Powder XRD patterns of the samples obtained after hydrothermally heating the precursor solution containing 3.3 mmol of $\text{SnCl}_2 \cdot 2\text{H}_2\text{O}$, 5 mL of AcAc, 1.1 g of MPA and 100 mg CTAB for intervals of 1, 4, 10, and 24 h at a constant temperature of 160 °C.

The TEM images of the products obtained at the initial stage i.e., after 1 h heat treatment shows (Figure 6.6a) solid spheres with solid cores and smooth exterior surfaces which are almost amorphous (inferred from XRD pattern) and the average

diameter is about 330 nm. After prolonging the duration to 4 h, the TEM image of the product shows spherical particles (Figure 6.6b). Since XRD revealed SnO₂ to be crystalline, at this point, some of the spheres tend to undergo aggregation, to acquire crystalline structures, which are thermodynamically more stable. The dark contrast in the spheres indicates that the spheres are not hollow at this juncture and spheres continue to retain their solid cores. Upon increasing the heating duration to 10 h, the morphology of the product undergoes a dramatic transformation, in terms of sphere core content. The corresponding image shows loosely packed discrete spheres, with a non-uniform size distribution, and there are empty spaces clearly seen in the cores of the spheres (Figure 6.6c). Figure 6.6d shows the image of a single sphere (10 h), the periphery of the sphere is rough and pores can be detected (encircled by dashed lines), which indicates that evacuation starts at this stage and the size of the SnO₂ hollow spheres is in the range of 80 to 400 nm. As heating is continued, the core of the sphere dissolves and re-deposits on the outer surface of the shell which results in an increase in sphere size. Further, when the heating duration was increased to 13 h, the structure consolidates, as hollow spheres of SnO₂ with solid shells were obtained (Figure 6.6e), the shell thickness is almost uniform and the outer diameters of the spheres are also similar, indicating that this heating duration is optimum for producing mono-dispersed SnO₂ HS. The average sphere size is about 350 nm. After heating for 24 h, the product morphology continues to comprise (Figure 6.6f) of spherical HS but the diameter of the spheres increases to about 750 nm with a shell thickness of ~100 nm. The increase in sphere size is consistent with an increasing degree of crystallinity which causes grain coarsening. When the solution is heated for 24 h, the HS undergo self-expansion, but not at the expense of the evacuated

cores, for the HS structure is retained, albeit a few fractured HS, due to the stresses engendered upon HS enlargement. This also complies with the corresponding FE-SEM image (Figure 6.7) wherein sphere size increment along with an increasing proportion of broken hollow spheres were observed.

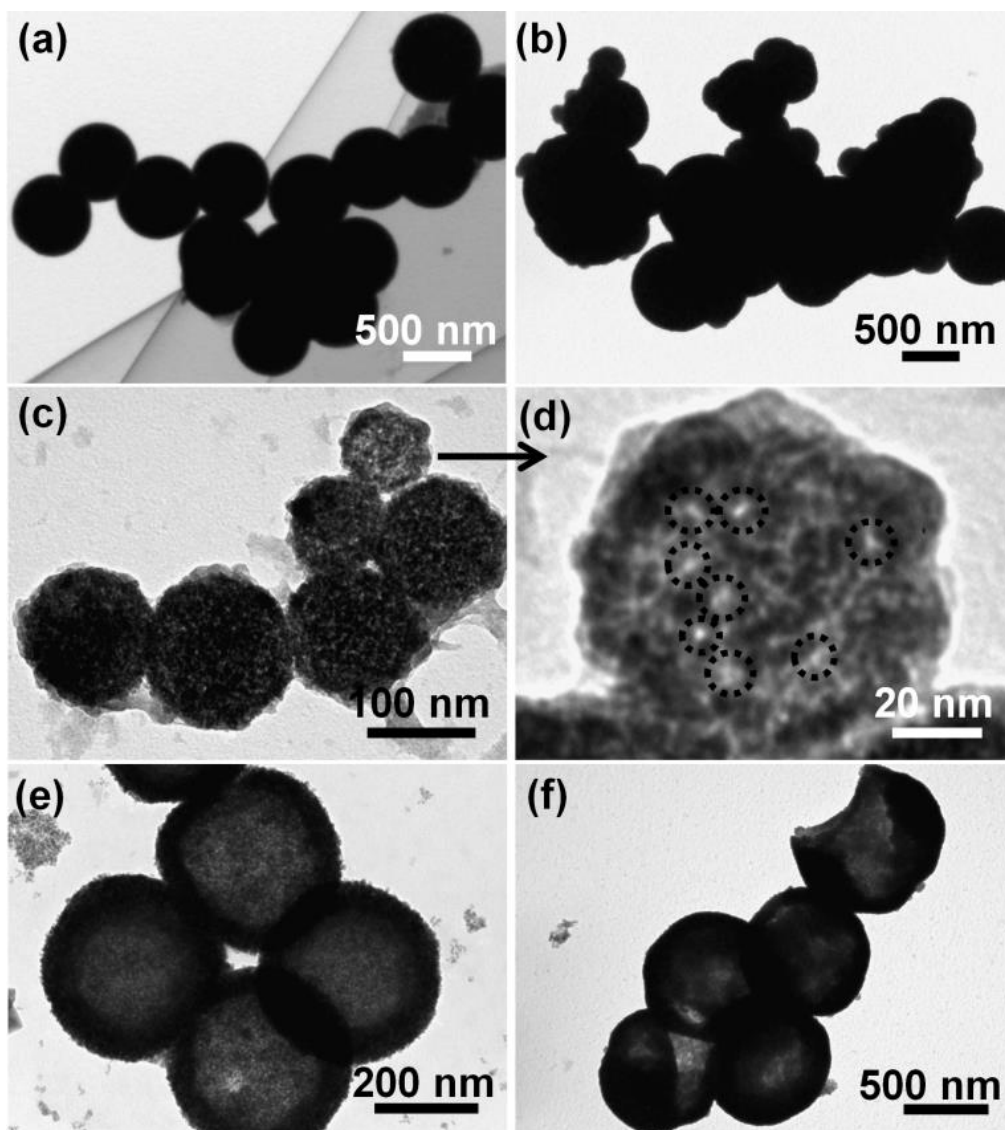


Figure 6.6. TEM images of the samples obtained after hydrothermally heating the precursor solution containing 3.3 mmol of $\text{SnCl}_2 \cdot 2\text{H}_2\text{O}$, 5 mL of AcAc, 1.1 g of MPA and 100 mg CTAB for intervals of (a) 1, (b) 4, (c, d) 10, (e) 13 and (f) 24 h at a constant temperature of 160 °C.

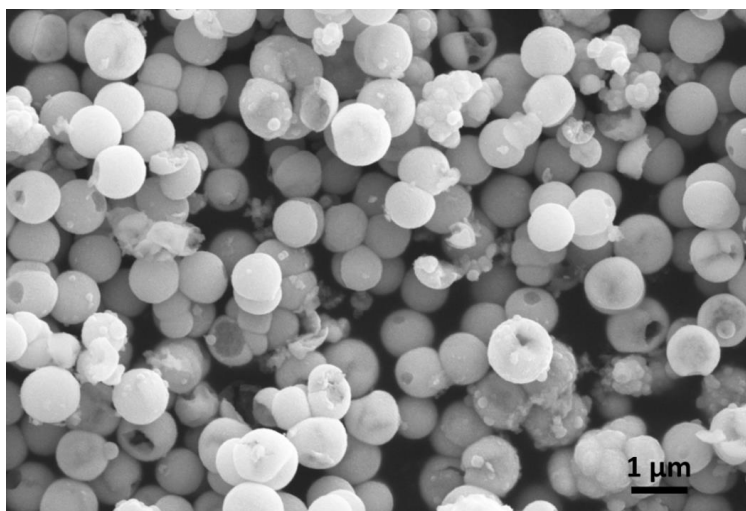
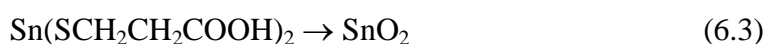
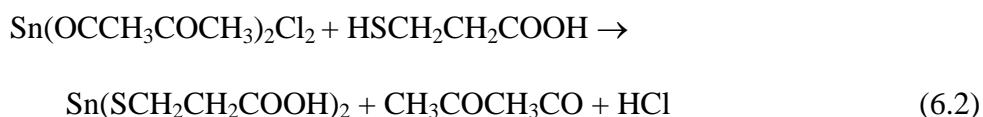
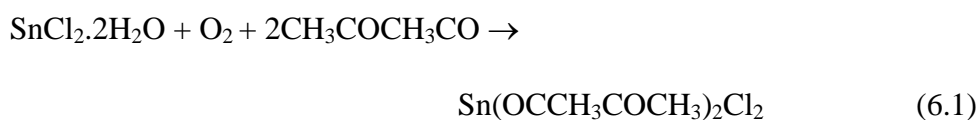


Figure 6.7. FE-SEM image of SnO₂ HS after 24 h hydrothermal heat treatment.

Initially, when SnCl₂ precursor was added to AcAc and stirred for 5 min, it forms a clear solution of Sn(AcAc)₂Cl₂ complex[4] and when the solution was continuously stirred for 1 h, a colloidal suspension was obtained. Further addition of 40 mL water and 1 mL of MPA, and stirring resulted in the formation of a clear solution owing to a stronger complexing ability of MPA[5] compared to AcAc, whereby AcAc moieties around Sn are completely replaced by MPA to result in a clear sol. The Sn(AcAc)₂Cl₂ is thus transformed to a Sn(MPA) complex. Subsequent addition of CTAB, followed by hydrothermal heat treatment causes the decomposition of the Sn(MPA) complex and SnO₂ is formed. All the above steps have been shown below through equations.



On the basis of XRD and TEM observations of the samples subjected to the time

dependent study, we propose an inward out Ostwald ripening mechanism for the formation of SnO₂ hollow spheres. Initially after heating hydrothermally for 1 h, solid (amorphous) spheres of SnO₂ with dimensions of about 330 nm were formed and they remain spheres with solid cores, even after a 4 h hydrothermal heating treatment. When the heating duration was prolonged to 10 h, porous spherical nanostructures comprising of ultra-fine particles which are loosely packed in the interior and tightly packed along the outer surface were formed. When the heating duration was raised to 13 h, the outer surface of sphere which is in direct contact with the solution grows due to Ostwald ripening. Because of a very high interfacial energy of loosely packed small crystallites in the interior of the spheres, and in order to minimize the total energy of the system, the interior particles dissolve and redeposit on the outer surface. As a result, hollow spherical structures are formed. Further when the heating duration was increased to 24 h, more and more interior part of the spheres dissolve and recrystallize on the outer surface and the spheres expand and after 24 h, the size of the hollow sphere is around 750 nm. Furthermore, owing to the large size of the HS at this point, many of them break open due to mechanical stress generated by sphere expansion.

The roles of synthetic parameters like effect of temperature, key roles of MPA, CTAB and AcAc for the formation of SnO₂ hollow spheres was analysed systematically. The effect of temperature for the formation of SnO₂ HS was studied by examining samples prepared from solutions with 3.3 mmol of SnCl₂.2H₂O, 5 mL of AcAc, 1.1 g MPA and 100 mg CTAB, followed by hydrothermal heating at 140 and 180 °C for 13 h. The FE-SEM image of the sample prepared at 140 °C shows a mono-disperse solid spheres of the size of about 500 nm. The solid core of the solid

sphere was also confirmed with the TEM image which is shown in the inset of Figure 6.8a. The FE-SEM image of the SnO₂ synthesized at 180 °C (for 13 h) shows hollow spheres of SnO₂ with outer diameter ~ 800 nm (Figure 6.8b). It can also be seen from FE-SEM most of the HS were broken at this higher temperature. It is evident that the hydrothermal treatment at 160 °C for 13 h leads to SnO₂ HS with optimum dimensions and structural integrity. The roles of CTAB and MPA in the formation of SnO₂ hollow spheres were determined by preparing the SnO₂ with the solution containing 3.3 mmol of SnCl₂.2H₂O, 5 ml of AcAc and MPA (no CTAB) as well as the solution with 3.3 mmol of SnCl₂.2H₂O, 5 ml of AcAc and CTAB (no MPA). In both the cases, the solution was heated at 160 °C for 13 h. The FE-SEM image of SnO₂ prepared from a solution with no CTAB shows (Figure 6.8c) aggregated spheres with thick shells whereas the micrograph of SnO₂ obtained from the solution with no MPA reveals (Figure 6.8d) the formation of flaky particles of irregular shapes and sizes.

From FE-SEM analyses, we found that from the group of the three reagents: MPA, CTAB and AcAc, when any two or any one of the three was used for preparing the Sn salt precursor solution and then, SnO₂ by 13 h hydrothermal heating at 160 °C, mono-disperse non-aggregated SnO₂ HS were not formed. Only when the three reagents were incorporated in the Sn salt solution, discrete SnO₂ HS were obtained. Since from all MPA based solutions (with CTAB or AcAc or without them), spherical structures were obtained, it was concluded that MPA is the structure directing agent. Further, from the hard and soft acid-base concept, the alkylcarboxylate in MPA can serve as a hard base, and will have a strong affinity for acidic Sn⁴⁺ species. The MPA molecules can easily form a monolayer around Sn⁴⁺

species in a manner similar to the way they attach to TiO_2 [6] and therefore this binding might be steering the growth of spherical shapes. Scheme 6.1 shows the formation of SnO_2 HS, by use of the three reagents. During hydrothermal heating, the Sn^{4+} species is capped by MPA, decomposes to form primary particles of SnO_2 (amorphous) which can aggregate to form bigger spherical particles at the end of 1 h heating. This stage is very critical for the formation of SnO_2 HS. Oxygen from the MPA caps the Sn^{4+} in SnO_2 , and CTAB, being a cationic surfactant will have a propensity to associate with oxygens on SnO_2 and prevents the aggregation of particles. The organic moiety MPA and the surfactant CTAB possibly induce recrystallization on the surface of SnO_2 sphere and the inner particles of the spheres remain largely unaffected. Further, when the heating duration was increased to 10 h, the outer particles coarsen and the inner particles dissolve, due to their high interfacial energy. After 13 h, mono-disperse hollow spheres with well-defined shells were formed. The action of AcAc is not very clear, for when SnO_2 was prepared from a CTAB/MPA/ Sn^{2+} solution, (devoid of AcAc), while SnO_2 HS were obtained, but SnS phase was also detected, and the latter was found to be non-existent when AcAc (2.5, 5 and 10 mL) was also added to the CTAB/MPA/ Sn^{2+} solution. Microstructural analyses clearly shows that MPA is responsible for the formation of spherical shapes, CTAB assists in maintaining the HS as discrete entities with distinct grain boundaries and AcAc ensures a pure phase (only SnO_2).

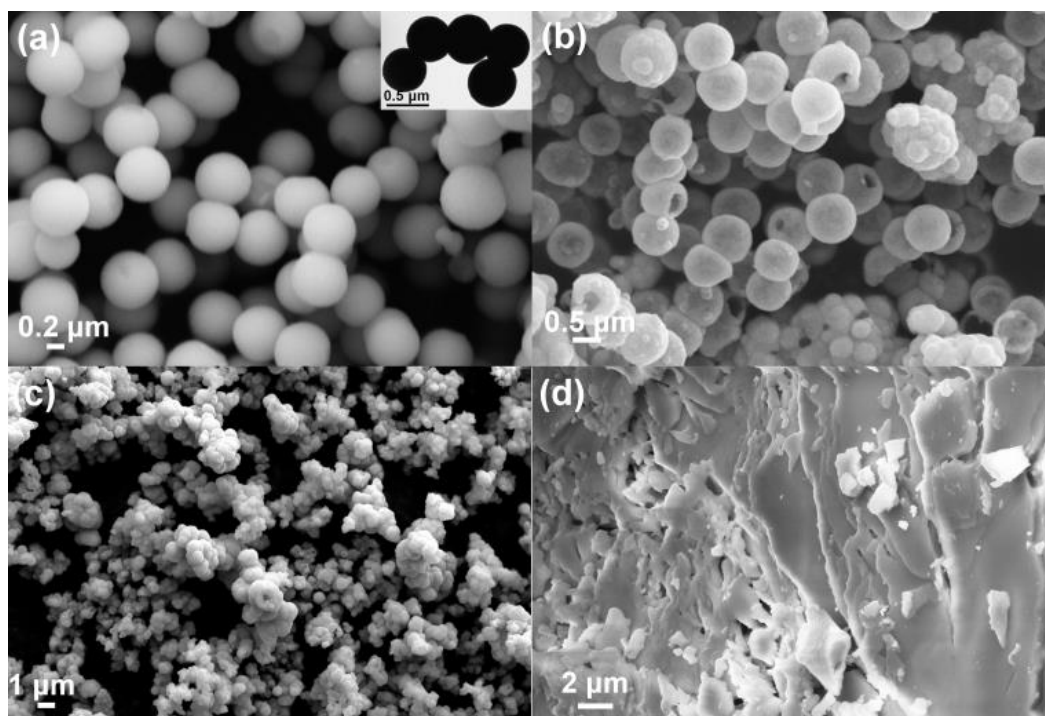
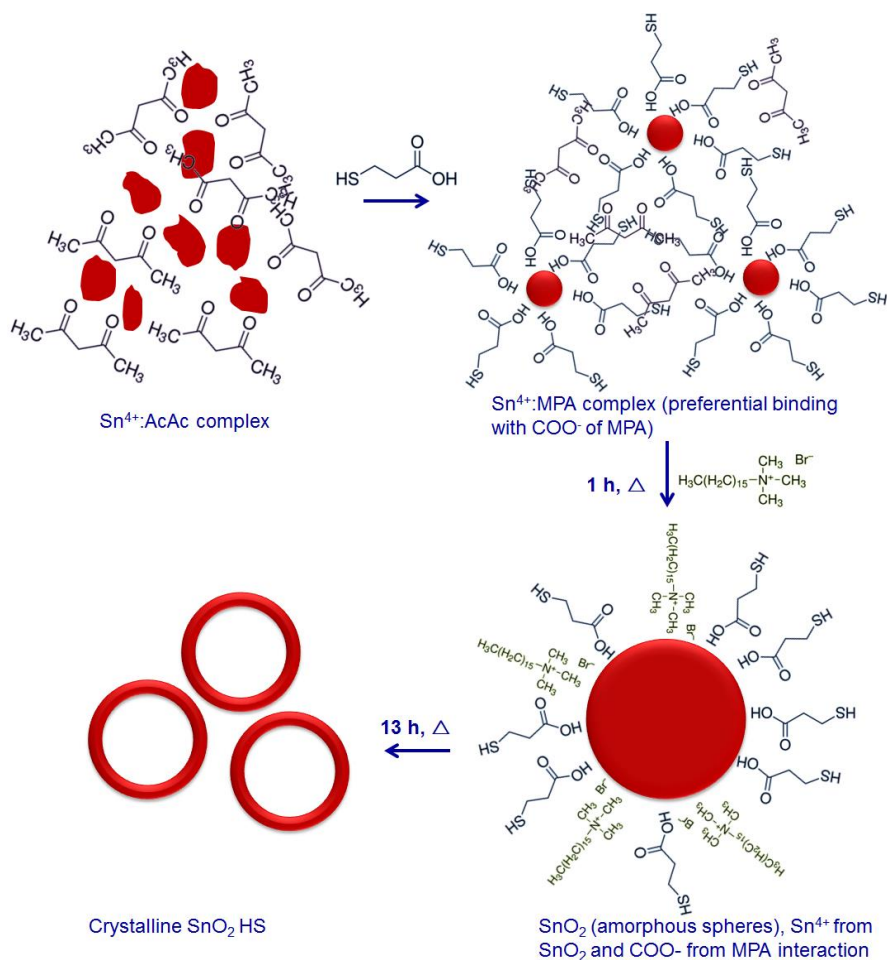


Figure 6.8. FE-SEM images of SnO₂ powders obtained after hydrothermal heating at (a) 140 and (b) 180 °C for 13 h. The solutions contained 3.3 mmol of SnCl₂·2H₂O, 5 mL of AcAc, 1.1 g of MPA and 100 mg of CTAB. (c) SnO₂ prepared from a solution containing 3.3 mmol of SnCl₂·2H₂O, 5 ml of AcAc and 1.1 g of MPA (no CTAB) and (d) SnO₂ prepared from a solution containing 3.3 mmol of SnCl₂·2H₂O, 5 ml of AcAc and 100 mg of CTAB (no MPA). In (c) and (d) the samples were heated at 160 °C for 13 h (under hydrothermal conditions).



Scheme 6.1.: Formation of discrete SnO₂ HS from a solution containing Sn²⁺ salt, MPA, AcAc and CTAB.

6.4.5. Surface area determination

The Brunauer-Emmet-Teller (BET) specific surface area and pore size distributions of the 200, 350 and 750 nm SnO₂ HS were determined by nitrogen adsorption-desorption isotherm measurements and these plots are shown in Figure 6.9a, b and c, respectively. From Figure 6.9, the BET surface areas for the 200, 350 and 750 nm SnO₂ HS were determined as 72.3, 86.6 and 41.3 m² g⁻¹. The hysteresis loops and pore size distribution curves which are shown in the insets of Figure 6.9 imply a typical mesoporous nature for all the three 200, 350 and 750 nm SnO₂ HS. The average sizes of the mesopores calculated from the insets of Figure 9 were: 5

nm for the 200 nm HS (Figure 6.9a), 4.5 nm for the 350 nm HS (Figure 6.9b) and 5.7 nm for the 750 nm HS (Figure 6.9c). The very high specific surface area and the mesoporosity of HS indicates that a very high capacity can be expected for these three materials, when used as Li-ion battery anodes.

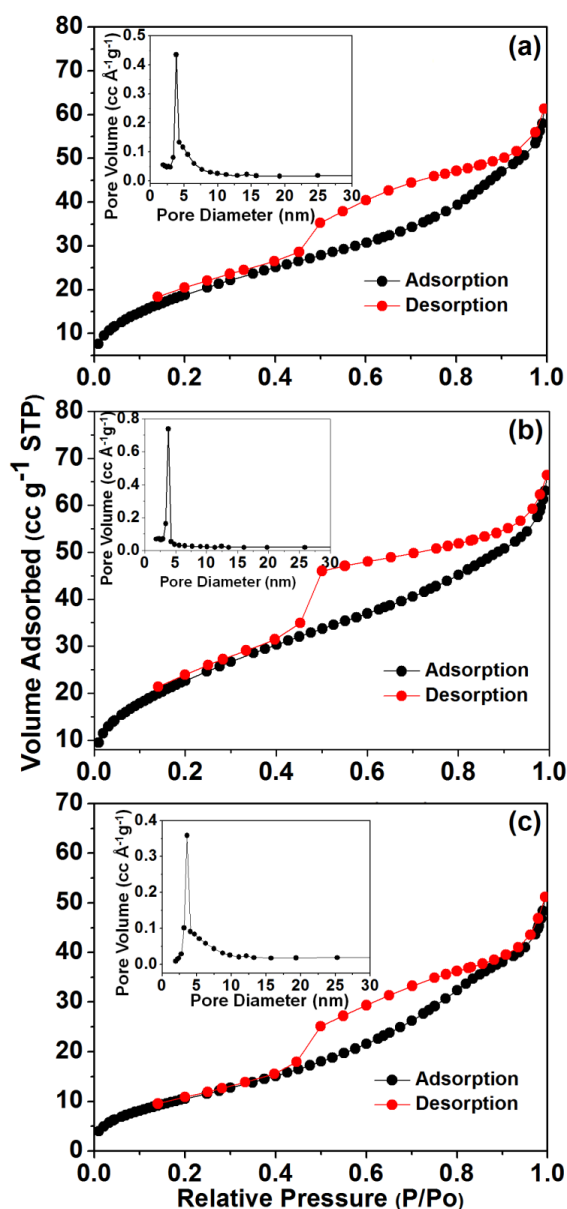


Figure 6.9. N₂ adsorption-desorption isotherm curves at 77 K for (a) 200 (b) 350 and (c) 750 nm SnO₂ HS obtained by BET analysis, and the curves in the insets depict the corresponding pore-size distribution based on the BJH method during desorption.

6.5. Electrochemical Li storage behaviour

The lithium storage properties of SnO₂ HS as anodes for Li-ion batteries was evaluated using a two electrode cell, where SnO₂ HS served as the working electrode and Li metal as reference and counter electrodes. The effects of the SnO₂ HS size on the electrochemical performance are compared. Figure 6.10a shows the cyclability comparison of 200, 350 and 750 nm SnO₂ HS measured in the voltage range of 0.01-2 V at a constant current density of 100 mA g⁻¹. The three samples; 200, 350 and 750 nm SnO₂ HS exhibit initial reversible capacities of 1055, 854.5 and 970 mAh g⁻¹, respectively. The capacities of all the three electrodes fade gradually with cycling. Among the three samples, the 200 nm size SnO₂ HS showed a good cyclability as it retained a capacity of 540 mAh g⁻¹ after 50 cycles whereas the 350 and 750 nm SnO₂ HS retained capacities of 350 and 200 mAh g⁻¹ at the end of 50 cycles. The typical charge-discharge profiles for the SnO₂ HS of size around 200 nm for the initial three cycles are shown in Figure 6.10b. From the charge-discharge profiles it can be seen that the initial discharge and charge specific capacities are 2242.4 and 1055 mAh g⁻¹, respectively with a Coulombic efficiency of around 47%. There are three possible reasons that contribute the large irreversible capacity loss during the first discharge cycle. These are: (i) the decomposition of electrolyte and the formation of SEI layer on the surface of electrode, (ii) the irreversible conversion reaction of SnO₂ to Sn and Li₂O and, (iii) from the interfacial storage of excess lithium ions between Sn nanoparticles and Li₂O[7]. The SEI layer formation and alloying/dealloying potentials were measured by recording CV plots. Figure 6.10c shows the CV curves for the SnO₂ HS (of 200 nm in size) electrodes performed at a scan rate of 0.1 mV s⁻¹ during the first five cycles. The CV curves are

consistent with the literature confirming the following electrochemical reaction pathway. During the first cathodic scan three reduction peaks were observed. An irreversible peak observed at 1.3 V corresponds to SEI layer formation and a broad peak at ~ 1 V is ascribed to the conversion reaction of SnO_2 to Sn and Li_2O . The third prominent peak in the voltage range 0.6 to 0 V corresponds to $\text{Li}_{4.4}\text{Sn}$ alloy formation reaction. Similarly during the first anodic scan two distinct peaks were observed. The peak between 0.3 to 0.8 V is due to $\text{Li}_{4.4}\text{Sn}$ to Sn dealloying reaction and a broad peak at ~ 1.2 V is attributed to the partial oxidation reaction of Sn to SnO on the surface of the electrode. The alloying/dealloying reaction redox peaks decline slowly as a function of increasing number of cycles whereas the SnO_2/Sn conversion peak decays rapidly. This suggests that the alloying/dealloying process is highly reversible. The electrochemical storage mechanism can be written as follows:

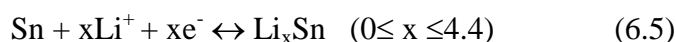
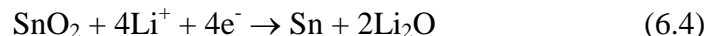


Figure 6.10d shows the rate capabilities of SnO_2 HS of three different sizes, measured at different current densities. Among all the three samples, the 200 nm SnO_2 HS exhibited an excellent rate capability. Even at a very high current density of 2000 mA g^{-1} , the electrode showed a capacity of 422 mAh g^{-1} whereas at the same current density, the 350 and 750 nm SnO_2 HS showed capacities of 368 and 233 mAh g^{-1} respectively. At the end of 30 cycles and at a current density 100 mA g^{-1} , the 200 nm SnO_2 HS retained a capacity of 656 mAh g^{-1} and notably this was achieved after several charge-discharge cycles at various current densities. The very high capacity and good rate capability of the 200 nm SnO_2 HS is due to very high surface area and optimum mesopore size. As the sphere size of SnO_2 HS decreases,

we observed superior electrochemical performance, as small sized particles can tolerate the volume expansion more easily than large particles.

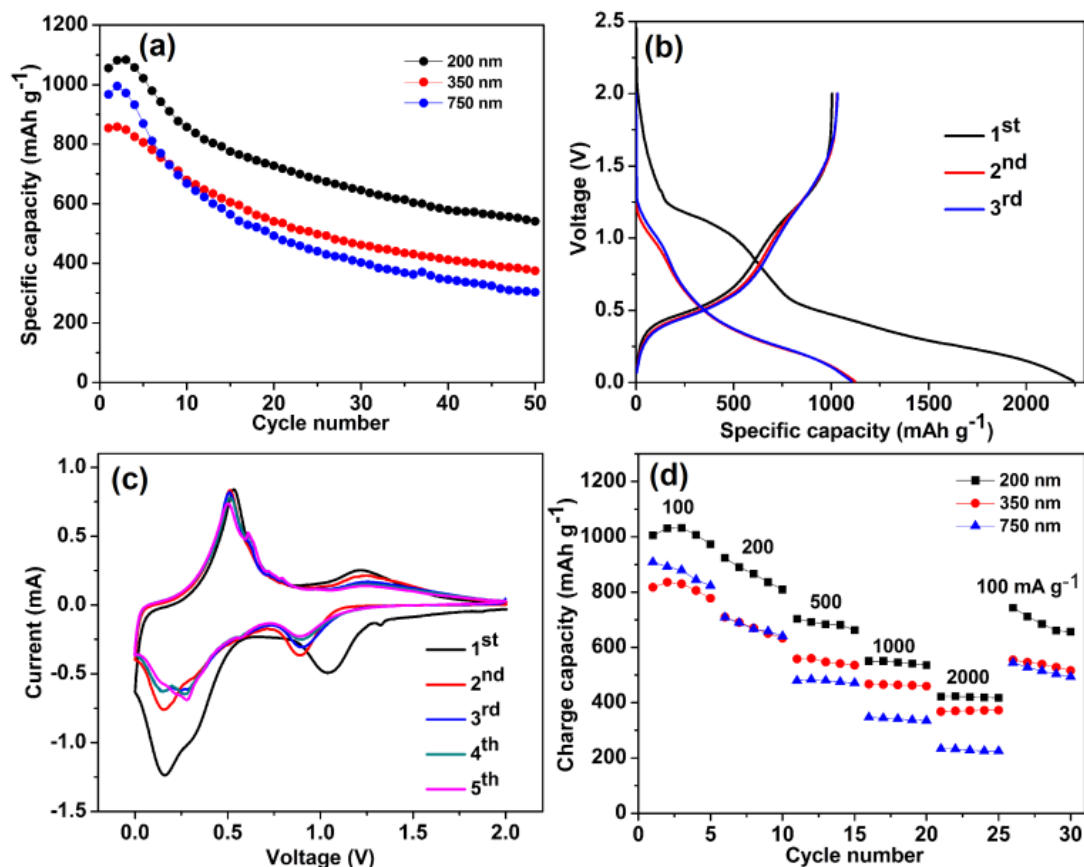


Figure 6.10. (a) Cycling performance of SnO₂ HS of 200, 350 and 750 nm dimensions at a current density of 100 mA g⁻¹, (b) discharge-charge curves for the first three cycles, (c) cyclic voltammograms recorded at a scan rate of 0.1 mV s⁻¹ versus Li/Li⁺, for the first five cycles for 200 nm SnO₂ HS and (d) the rate performance of SnO₂ HS of 200, 350 and 750 nm.

The as-fabricated cell shows a V_{OC} of ~ 3 V, and the cell was discharged to 0.01 V, prior to measuring the capacity *versus* cycling response over a potential window confined to 0.01 to 1 V. Noticeably, the charge-discharge characteristics of 200 nm size SnO₂ HS recorded at a current density of 100 mA g⁻¹, a stable cycle performance was achieved for 50 cycles (Figure 6.11a). The reversible capacity decreased from 637.3 mAh g⁻¹ (for 5th cycle) to 513 mAh g⁻¹ (for 50th cycle). The

increased cycling stability when cycled within a voltage window of 0.01–1 V is due to the prevention of the surface reaction between Sn and Li_2O which occurs at higher voltages and also due to the minimization of SEI formation on Sn. The increased cycling stability was further validated by measuring EIS. Figure 6.11b shows the comparison of the EIS plots of 200 nm SnO_2 HS measured after 50 charge-discharge cycles performed between 0.01-1V and 0.01-2 V. The Nyquist plots show one semicircle followed by an inclined straight line; the latter is ascribed to the low frequency region. The semicircle is assigned to a parallel combination of charge transfer resistance (R_{CT}) and electrical double layer capacitance (C_{dl}), and the straight line originates from the diffusion of charged species through the bulk of the electrode material. From the Nyquist plots it can be observed that after 50 cycles the R_{CT} for the charge-discharge cycles measured in the voltage range 0.01-1 V is much lesser than the R_{CT} obtained between 0.01-2 V, indicating that when the upper cut of voltage is restricted to 1 V the charge transfer process between electrode and electrolyte is more facile than at 2 V. This could be due to minimization of surface reaction of Sn and Li_2O and the side reactions between electrode and electrolyte.

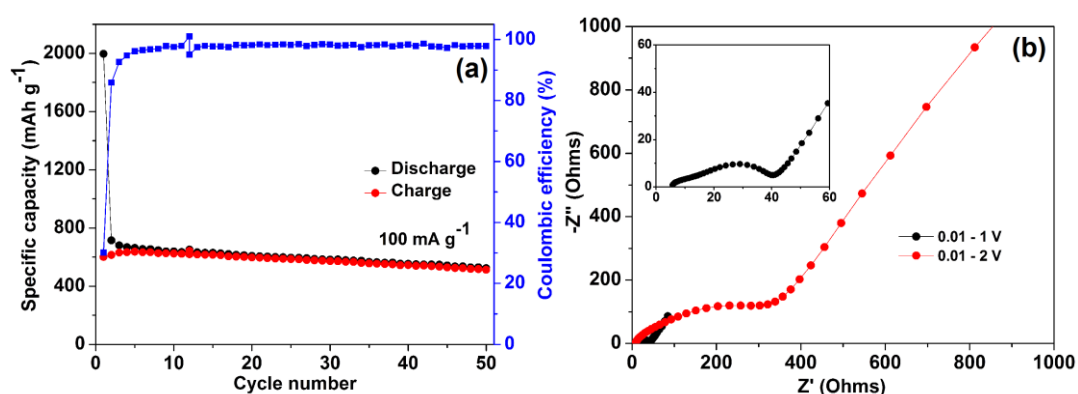


Figure 6.11. (a) Cycling performance and Coulombic efficiency of 200 nm size SnO_2 HS at 100 mA g^{-1} current density between 0.01-1 V versus Li and (b) Nyquist plots after 50 cycles of 200 nm SnO_2 HS over two different potential ranges.

6.6. Summary

A simple hydrothermal method was employed for preparing SnO₂ HS, with the aid of organic moieties as structure directing agents. The content of AcAc in the Sn precursor dispersion was found to have a direct impact on the structure of the final SnO₂ product. Uniform SnO₂ HS with overall diameters of 200 and 350 nm comprising of empty cores surrounded by solid shells of 50 to 60 nm dimensions were successfully prepared from solutions with 2.5/5.0 mL of AcAc. A heating time dependent analyses delineated a stepwise transformation of solid spheres (1 h) to agglomerated spheres (4 h) to porous spheres (10 h) to optimized HS (13 h) terminating with broken blown-up HS (24 h). A temperature dependent reaction progress showed conversion from solid spheres (140 °C) to HS (160 °C) to chipped off-huge spheres (180 °C). The roles of MPA as the sphere forming agent and CTAB as the surfactant which inhibits clumping of SnO₂ HS were also deduced. On the basis of morphological analyses, a growth mechanism for the formation of optimized SnO₂ HS was expounded. The ability of the optimized SnO₂ HS (2.5 or 5.0 mL of AcAc, 160 °C, 13 h) to function as anodes in lithium ion batteries was determined from their electrochemical characteristics. The 200 nm SnO₂ HS delivered a reversible capacity of 540 mAh g⁻¹ at a current density of 100 mA g⁻¹ after 50 repetitive cycles and it showed good rate capability as well. The SnO₂ HS were also found to be strongly fluorescent, thereby suggesting their potential for energy harvesting applications in addition to electrochemical energy storage.

References

1. S. Luo, J. Fan, W. Liu, M. Zhang, Z. Song, C. Lin, X. Wu, P. K. Chu, *Nanotechnology*, 17 (2006) 1695-1699.
2. Y. C. Her, J. Y. Wu, Y. R. Lin, S. Y. Tsai, *Appl. Phys. Lett.*, 89 (2006) 043115-3.
3. Y. Wang, M. Guo, M. Zhang, X. Wang, *Scripta Materialia*, 61 (2009) 234-236.
4. V. Briois, S. Belin, M. Z. Chalaca, R. H. A. Santos, C. V. Santilli, S. H. Pulcinelli, *Chem. Mater.*, 16 (2004) 3885-3894.
5. Y. Cui, G. Wang, D. Pan, *J. Mater. Chem.*, 22 (2012) 12471-12473.
6. I. Robel, V. Subramanian, M. Kuno, P. V. Kamat, *J. Am. Chem. Soc.*, 128 (2006) 2385-2393.
7. Y. F. Zhukovskii, E. A. Kotomin, P. Balaya, J. Maier, *Solid State Sci.*, 10 (2008) 491-495.

Chapter 7

Electrochemical Performance of SnS₂- Nanosheets and Nanoflowers Grown by Precursor Modification

7.1. Abstract

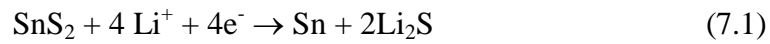
In this chapter, a one-pot solvothermal route is presented for preparing tin disulfide (SnS₂) nanosheets and nanoflowers. Mercapto propionic acid was used as an organic additive. Urea, steers the growth of SnS₂ nanosheets and thiourea (TU) orchestrates the formation hierarchical SnS₂ nanoflowers. We followed the growth mechanism by powder XRD, FE-SEM and HRTEM studies. By tuning the processing parameters, SnS₂ nanosheets and flowers with a narrow size distribution and good structural integrity were prepared. The comparison of Li-ion storage performance of SnS₂ nanosheets and flowers electrodes as anodes were studied. In addition, the SnS₂ nanosheets and flowers were also found to be luminescent and the two architectures showed a significant difference in their luminescent properties.

7.2. Introduction

In the last two chapters, SnO₂ hollow spheres based electrodes were prepared and analyzed in detail. Taking this further, yet another Sn based material suitable as an anode in LiBs is tin sulfide (SnS₂). SnS₂ has a hexagonal layered CdI₂ crystal structure with space group P3ml and lattice constants $a = b = 5.3645$ nm and $c = 5.5898$ nm. In the crystal structure octahedral coordinated Sn atoms are sandwiched between two layers of sulfur atoms hexagonal close packed through strong Sn-S covalent bonds to form triple layers. The adjacent triple layers of SnS₂ are attached via weak van der waals interactions[1-4]. During charge/discharge, lithium ions can easily undergo insertion/deinsertion between these layers which are stacked together

through van der Waals gap. Thus, the layered material can minimize the volume change during the charge/discharge process and facilitate the transport of lithium ions[4-6].

The main drawback of Sn based anodes is the huge stress generation due to large volume expansion and contraction (~ 300%) during alloy/dealloy reaction which causes the pulverization of the electrode material and this results in a rapid capacity decline[2-6]. This can be deduced from the basic electrochemical reactions of SnS₂ with lithium, which are expressed in the following two step reactions.



During the initial discharge process, SnS₂ reacts with Li⁺ and converts to active Sn and Li₂S, where the metallic Sn is embedded within the inert matrix of Li₂S. During the subsequent step, metallic Sn further reacts with Li⁺ to form the Li_{4.4}Sn alloy, which can be reversibly convert into Sn and Li⁺ during charge (dealloy). The second step leads a huge volume expansion about 300%. At the same time, it is stipulated that Li₂S behaves as buffering domain during during Li-Sn alloy/dealloy, thereby reducing the volume variation and the capacity fading by maintaining electrode integrity[7]. It also provides an ion-conducting medium for Li-ion migration and helps to keep the electrochemically formed nano-Sn metal particles apart and prevents their agglomeration[7]. But during the long term cycling the buffer effect of Li₂S is limited, due to huge volume variation and Sn particle aggregation, which ensue in rapid capacity fade with further cycling[7]. Various strategies have been employed to minimize this volume variation. One among them is to control the morphology of the compound, by forming nano or porous nanostructures. So far,

various nanostructure morphologies such as nanorods, nanobelts, nanosheets and 3D nanoflowers have been reported[8-21]. The main advantages of porous nanostructured materials are large surface area and large pore sizes which can easily accommodate the volume expansion. Further, short diffusion path lengths and large contact area between electrode and electrolyte can increase the specific capacity as well as rate capability. Among the various nanostructured morphologies, the 3D hierarchical structure formed by self-assembly of nanostructures offers a larger surface area and greater porosity and is ideal for minimizing the pulverization of electrode. For example Jana et al., reported an ionothermal synthesis method wherein by heating at 180 °C and 240 °C, hierarchical flower-like assemblies composed of 2D nanosheets of SnS₂ were obtained[2]. The nanostructure showed an average discharge capacity of 458 mAh g⁻¹ after 50 cycles. Liu et al., reported 3D flowerlike SnS₂ architectures by solvothermal approach and this material retained a capacity of 502 mAh g⁻¹ at the end of 50 cycles, at 200 mA g⁻¹ current density[12]. Zai et al., produced 3D hierarchical SnS₂ microspheres by biomolecule-assisted hydrothermal method and this unique material retained a capacity of 570.3 mAh g⁻¹ after 100 cycles, at 1 C rate[20].

In view of the aforesaid developments, we employed a simple and one-pot solvothermal route to synthesize SnS₂ nanosheets and hierarchical 3D flowers by using ethanol as the solvent. For the generation of SnS₂ nanosheets, we found that urea plays a significant role and when urea was replaced by thiourea (TU), 3D architectures of flower like shapes of SnS₂ obtained. The role of the solvent and the proportion of the urea or TU control the growth of SnS₂ nanosheets and flowers,

respectively. Both the nanostructures are compared with electrochemical performance.

7.3. Experimental

A simple one pot solvothermal method was employed to synthesize SnS₂ nanosheets and nanoflowers by adding absolute ethanol as a solvent. In a typical synthesis, 50 mL of absolute ethanol was taken in a 100 mL beaker and to that 10.4 mmol of mercapto propionic acid (MPA) was added and stirred for 5 min. To that solution, 2.73 mmol of SnCl₂.2H₂O was directly added and stirred for 30 min at room temperature and a clear solution was formed. Subsequently, various amounts (1.7, 10, 20 and 30 mmol) of urea in 10 mL of absolute ethanol were added. In each case, the solution was stirred for about 2 h and the resultant transparent solution was transferred into a 100 mL Teflon lined autoclave and heated in an electric oven at 180 °C for 12 h. After the completion of reaction, the autoclave was cooled naturally to room temperature and the resultant yellow precipitate was filtered and washed with milli-Q water and dried in a vacuum oven at 60 °C for 6 h. Similarly, SnS₂ nanoflowers were prepared by taking various amounts of TU (1.3, 7.9, 15.8 and 23.6 mmol) instead of urea and by maintaining all remaining parameters same.

7.4. Results and Discussion

7.4.1. Powder X-ray diffraction patterns

The amount of urea as well as TU was optimized for the preparation of monodisperse nanosheets and nanoflowers of SnS₂. This was done after analyzing the XRD and FE-SEM data. Figure 7.1 shows XRD patterns of the SnS₂ nanosheets synthesized from a precursor solution containing 1.7, 10, 20 and 30 mmol of urea and in each case, the solution was heated hydrothermally at 180 °C for 12 h. Most of

the diffraction peaks of the material synthesized with 1.7 mmol urea are assigned to the tetragonal rutile crystal structure of SnO₂. A small peak at $2\theta = 15^\circ$ corresponds to SnS₂. The diffraction patterns of the compounds synthesized with 10, 20 and 30 mmol of urea can be readily indexed to the hexagonal crystal structure of SnS₂ with the space group P3m1(164) (JCPDF # 89-2358). The observable change when the amount of urea increased from 10 to 30 mmol, was the decrease in the relative intensity of the (011) plane whereas the intensity of the peak from the (100) plane increased. Another significant change observed with 30 mmol of urea was that the diffraction peak due to (001) plane vanished and a new peak was seen at $2\theta = 18^\circ$. This indicated that the sample synthesized from a solution with 30 mmol of urea shows poor crystallinity and structural defects. Similarly, the XRD patterns of the compounds prepared from solutions containing 1.3, 7.9, 15.8 and 23.6 mmol of TU are shown in Figure 7.1b, respectively. All the peaks in the XRD pattern of the sample prepared from a solution with 1.3 mmol TU were indexed with the tetragonal rutile SnO₂ phase with a space group P4₂/mnm (JCPDF # 72-1147). The XRD pattern of the sample prepared from a solution with 7.9 mmol of TU indicates an amorphous structure of SnS₂ whereas the XRD patterns of samples synthesized from a solution with 15.8 and 23.6 mmol of TU were readily indexed with the hexagonal crystal structure of SnS₂. No other characteristic impurity peaks such as SnO₂, SnO and SnS were observed.

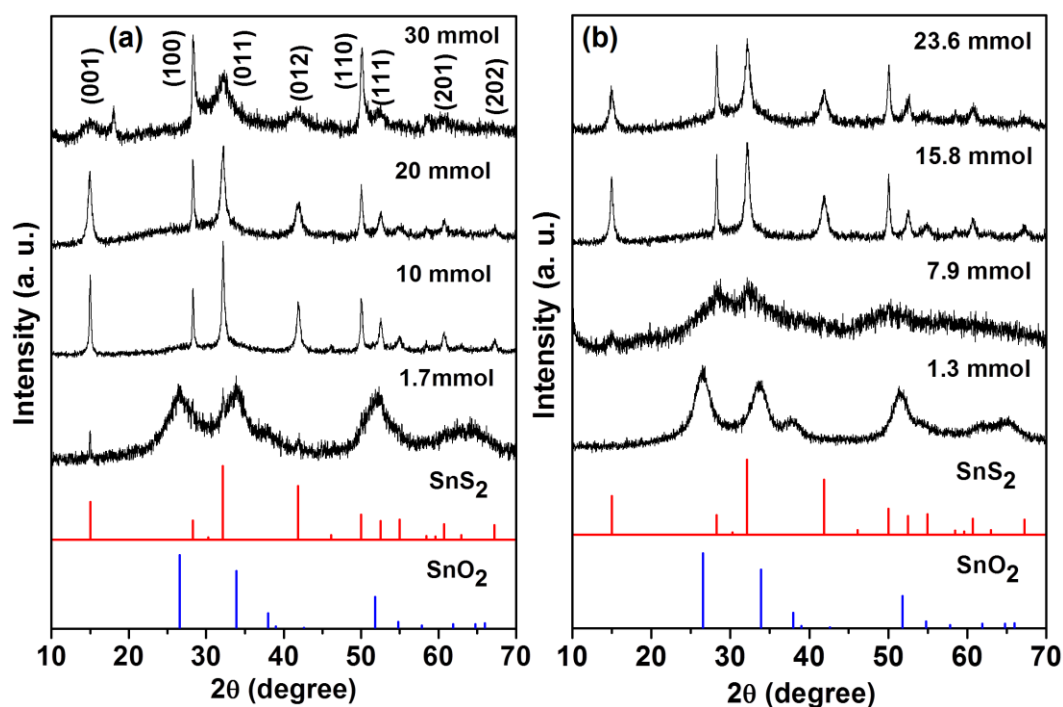


Figure 7.1. XRD patterns of samples prepared at various amounts of urea and TU with fixed amount of $\text{SnCl}_2 \cdot 2\text{H}_2\text{O}$ and MPA at 180°C under solvothermal conditions.

7.4.2. Morphology studies

Figure 7.2 shows the FE-SEM images of the samples synthesized by adding 1.7, 10, 20 and 30 mmol of urea to the precursor solutions and after heating hydrothermally at 180°C for 12 h, in each case to yield SnS_2 nanosheets. Initially, the FE-SEM image of the sample prepared from a solution with 1.7 mmol urea shows aggregated spherical SnO_2 particles (Figure 7.2a). The morphology of the sample prepared from a solution with 10 mmol of urea shows non-uniform spherical flower like hierarchical nanostructures composed of nanosheets mixed with sheet like particles indicating a mixed morphology (Figure 7.2b). When 20 mmol of urea was used in precursor solution, the morphology of the sample shows sheet like nanostructures (Figure 7.2c); it can also be seen that the surfaces of nanosheets are very smooth and no particles were observed. At this point, monodisperse nanosheets

of SnS₂ were obtained. Further, when the amount of urea was increased to 30 mmol in the precursor solution, the nanosheet morphology did not change (Figure 7.2d) but the XRD pattern (Figure 7.1a) showed that the sample is more amorphous. Similarly, the optimization of TU for the formation of SnS₂ nanoflowers was carried out by synthesizing samples from solutions with 1.3, 7.9, 15.8 and 23.6 mmol of TU (180 °C, 12 h, under solvothermal conditions). The FE-SEM image of the sample prepared from a solution with 1.3 mmol of TU shows inhomogeneous SnO₂ spherical particles (Figure 7.3a). For the sample prepared from a solution with 7.9 mmol of TU, the FE-SEM image shows a mixed morphology of both spherical particles as well as nanoflowers (Figure 7.3b). The morphology of the sample prepared from a solution with 15.8 mmol of TU shows 3D flower like hierarchical nanostructures which are composed of SnS₂ nanosheets (Figure 7.3c). Further, when the amount of TU was increased to 23.6 mmol, the flower like morphology remains unchanged (Figure 7.3d). Based on both XRD and FE-SEM results, we fixed 20 and 15.8 mmol of urea and TU as the optimum content for preparation of monodisperse SnS₂ nanosheets and flowers, respectively.

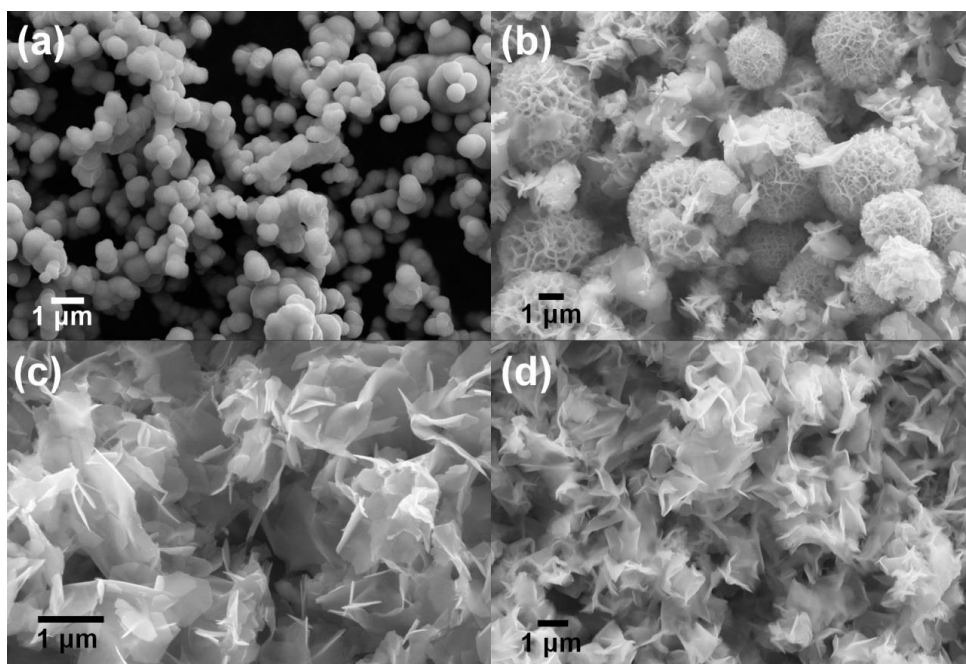


Figure 7.2. FE-SEM images of samples obtained at (a) 1.7 (b) 10 (c) 20, and (d) 30 mmol of urea with a fixed amount of $\text{SnCl}_2 \cdot 2\text{H}_2\text{O}$ and MPA at 180 °C under solvothermal conditions.

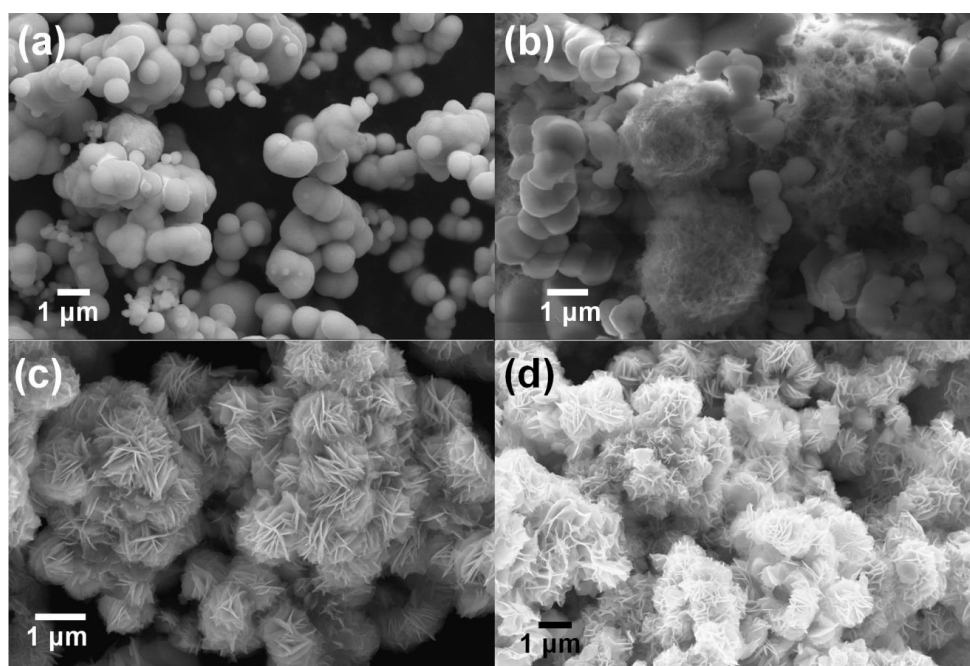


Figure 7.3. SEM images of samples obtained at (a) 1.3 (b) 7.9 (c) 15.8, and (d) 23.6 mmol of TU with a fixed amount of $\text{SnCl}_2 \cdot 2\text{H}_2\text{O}$ and MPA at 180 °C under solvothermal conditions.

The optimized SnS₂ nanosheets and nanoflowers and their crystal structures were further confirmed by HRTEM. Figure 7.4a shows the TEM image of the sample prepared from a solution with 20 mmol of urea, and it showed the wrinkled sheet like morphology. The lateral size of the SnS₂ nanosheets is about 1 μm. The HRTEM image of a SnS₂ nanosheet demonstrates that the nanosheet is composed of randomly oriented nanocrystallites, their dimensions lie between 3-4 nm. The lattice fringes from the sample shows a 0.28 nm inter planar spacing corresponding to the (011) plane of the hexagonal crystal structure of SnS₂ (Figure 7.4b). The HRTEM image of the sample prepared with 15.8 mmol TU is displayed in Figure 7.4c. The image confirms the 3D nanoflower morphology of SnS₂ with an average diameter of about 1.5 μm. From the lattice fringes, the deduced 0.32 nm inter planar spacing corresponds to the (100) plane of the hexagonal crystal structure of SnS₂ (Figure 7.4d).

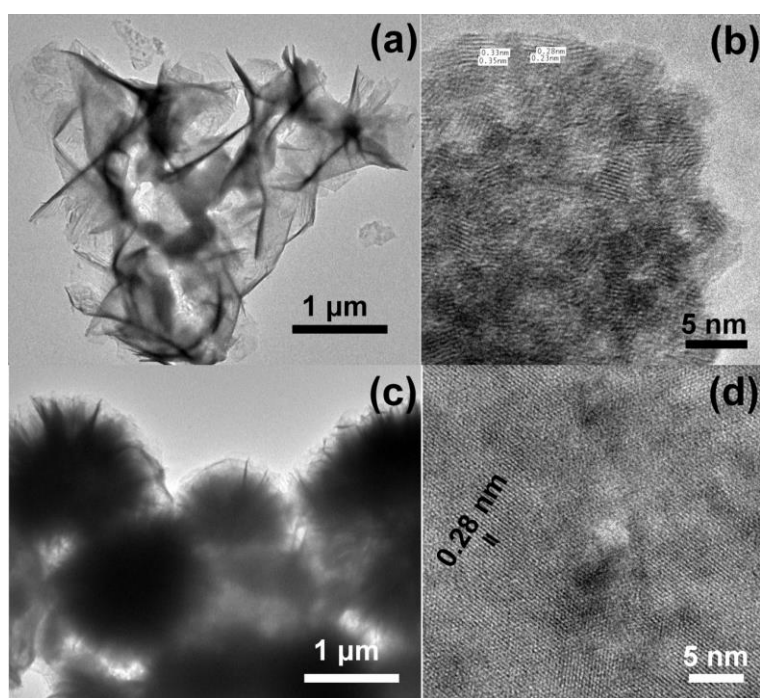


Figure 7.4. (a) TEM, (b) HRTEM lattice fringes- images of SnS₂ nanosheets, (c) TEM, and (d) HRTEM lattice fringes - images of SnS₂ nanoflowers.

7.4.3. Growth mechanism

A time dependent experiment was carried to understand the SnS₂ nanosheets and nanoflowers formation mechanism. Prior to this study, the amount of urea (for nanosheets) and TU (for nanoflowers) was fixed at 20 and 15.8 mmol, respectively, and the precursor solution was heated hydrothermally at 180 °C for 1, 6, 12 and 24 h duration. The samples obtained after each heating time span, were characterized by using XRD and FE-SEM. Figure 7.5a shows the XRD patterns of the samples obtained after 1, 6, 12 and 24 h hydrothermal heat treatment by adding 20 mmol of urea to the precursor solution in each case for the formation of SnS₂ nanosheets. The XRD pattern of the sample after 1 h, shows the tetragonal rutile crystal structure of SnO₂ and no peaks from SnS₂ were observed. After heating for 6, 12 and 24 h, the XRD patterns of the obtained samples show the hexagonal crystal structure of SnS₂ and no diffraction peaks from other impurities such as SnS, SnO₂ and SnO were observed, which indicates the transformation of SnO₂ nanoparticles to SnS₂ nanosheets. Figure 7.6 shows the FE-SEM images of the samples obtained after 1, 6, 12 and 24 h hydrothermal heat treatment, by adding 20 mmol of urea to the precursor solution. The morphology of the sample after 1 h heating shows irregular spherical particles of SnO₂. When the heating duration was increased to 6 h, the FE-SEM image shows mixed morphology of both spherical as well as sheet like particles of SnS₂. Due to the anisotropic crystal structure of SnS₂, the spherical particles of SnO₂ that become flat. They grow anisotropically to form SnS₂ nanosheets like structure. Further, when the heating duration was increased to 12 h, monodisperse sheet like structures were observed. When the heating duration was further increased to 24 h, the morphology of the sample did not change.

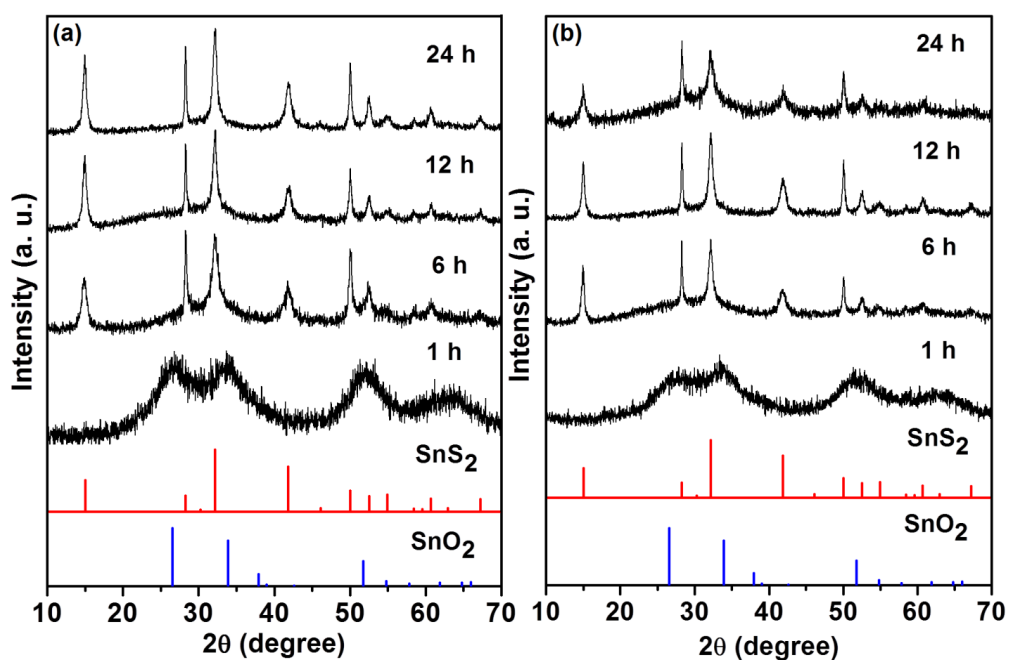


Figure 7.5. XRD patterns of (a) SnS₂ nanosheets (b) SnS₂ nanoflowers at different heating durations with fixed amounts of SnS₂, 2H₂O and MPA.

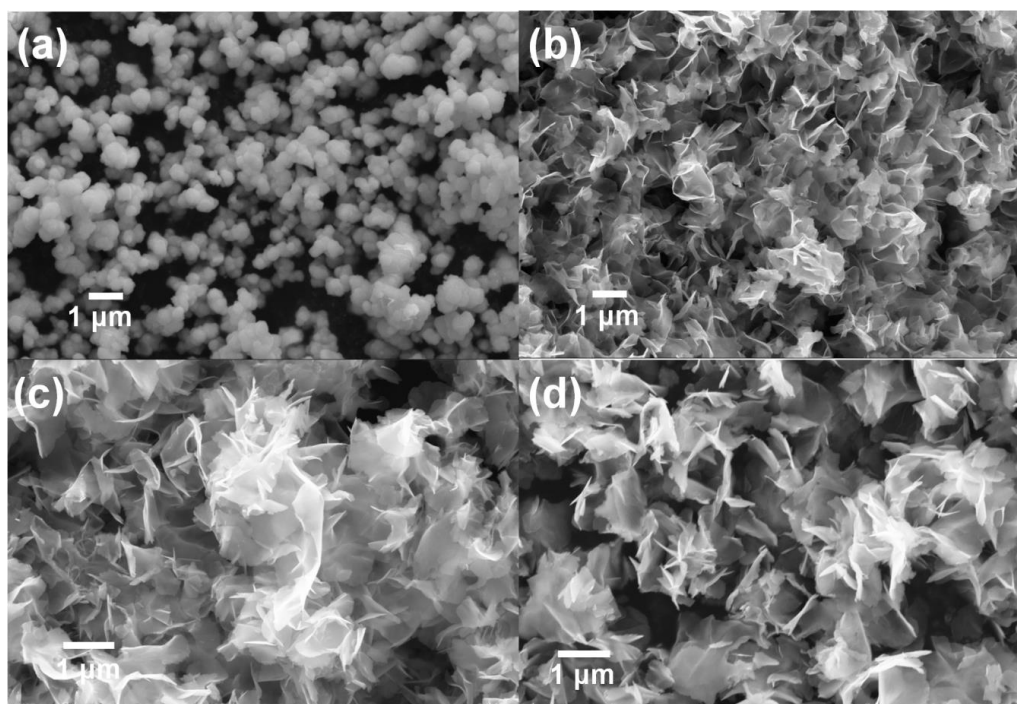


Figure 7.6. FE-SEM images of samples obtained after (a) 1 (b) 6 (c) 12 (d) 24 h solvothermal heat treatment with fixed amounts of SnCl₂·2H₂O, MPA and urea at 180 °C.

The XRD patterns of the samples obtained after 1, 6, 12 and 24 h hydrothermal heat treatment by adding 15.8 mmol of TU to the precursor solution, for the formation of SnS₂ nanoflowers, is shown in Figure 7.5b. The XRD patterns of the sample prepared by heating for 1 h shows the tetragonal rutile SnO₂ phase and when the heating duration was increased to 6, 12 and 24 h, pure hexagonal SnS₂ phase was observed, and the XRD pattern did not show any peaks from impurities such as SnO₂, SnS etc. The FE-SEM images for the samples acquired after 1, 6, 12 and 24 h hydrothermal heat treatment by adding 15.8 mmol of TU to the precursor solution to form SnS₂ nanoflowers, are shown in Figure 7.7. Initially, when the sample was heated for 1 h, random and aggregated spherical particles were observed. After 6 h hydrothermal treatment, the FE-SEM image shows both spherical particles and flower like structures. When the heating duration was increased to 12 h, only flower like architectures were observed and further, when the duration was increased to 24 h the nanoflower morphology did not change. The 12 h heating duration was therefore fixed as the optimized duration to form the SnS₂ nanosheets and flowers.

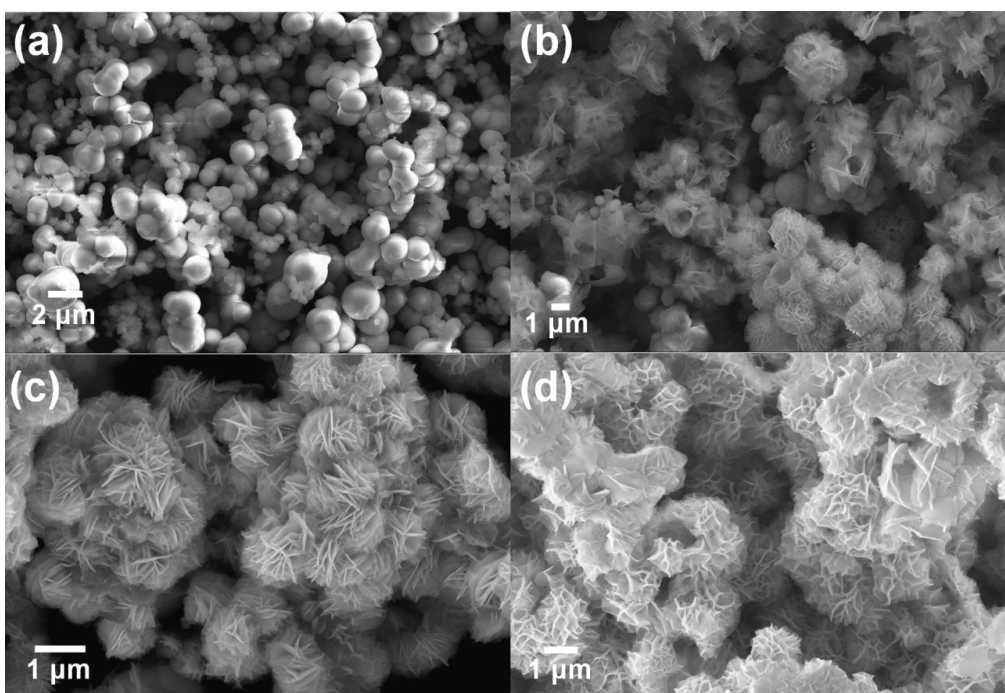
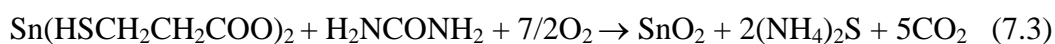


Figure 7.7. FE-SEM images of samples obtained after (a) 1 (b) 6 (c) 12 (d) 24 h solvothermal heat treatment with fixed amounts of $\text{SnCl}_2 \cdot 2\text{H}_2\text{O}$, MPA and TU at $180\text{ }^\circ\text{C}$.

Based on the observations from XRD, the following reaction mechanism was proposed for SnS_2 nanosheets formation.



When the same reaction conditions were applied, and only urea was replaced with TU, SnS_2 nanoflowers were obtained.

In the case of SnS_2 nanosheets, initially, after 1 h heat treatment Sn^{4+} precursors hydrolyze to form irregular shaped primary particles of SnO_2 , and they tend to aggregate (Figure 7.6a). After heating for 6 h, the *in-situ* generated sulfur precursor reacts with SnO_2 to form SnS_2 nanosheets along with nanoparticles. The semi-crystalline SnO_2 , due it's very high interfacial energy aggregate to form a sheet like

nanostructure (secondary particles). Further, after 12 h, monodisperse SnS₂ sheet like nanostructures were obtained, formed via an Ostwald ripening mechanism. The nanosheets that were formed at the initial stage act as building blocks for the nanoparticles to undergo nucleation and further growth of sheet like nanostructures.

When TU was used, initially after 1 h in autoclave, SnO₂ spheres of 0.5 to 2 μm dimensions were obtained. After 6 h of heat treatment, a mixture of rotund shaped SnS₂ micro-particles as well as nano sized particles were obtained. When the duration was further increased to 12 h, monodisperse 3D spherical flower like nanostructures with an average size of 2 μm were obtained. The flower is composed of many petals with smooth surfaces. Ostwald ripening is possibly responsible for the conversion of SnS₂ spheres to flowers with increased dimensions. The formation of the 3D hierarchical flower like shapes is in all likelihood caused by the different types of interactions that can exist between the primary nanoparticles. They include: attraction between the crystal facets, Coulombic and dipolar interactions and hydrogen bonds. Self-assembly via these interactions, leads to the formation of the flower like structures. Upon further heating to 24 h, they tend to disintegrate, due to the mechanical stresses generated in these structures. It must also be noted that in both cases, be it urea or TU: (a) composition, (b) crystal structure, and (c) morphology undergo dramatic changes. In the case of urea, SnO₂ particles with indefinite shapes and a tetragonal structure change to SnS₂ nanosheets with a hexagonal structure. In TU, SnO₂ spheres with a tetragonal structure transform to SnS₂ nanoflowers with a hexagonal structure. It is evident, that the difference in the (a) electrostatic interactions (due to C=O *versus* C=S) and (b) the sulfur content

produced in-situ during the reaction (greater in the case of TU), are responsible for the two different morphologies attained for SnS₂.

The roles of synthetic parameters like effect of urea and TU content and solvent for the formation of SnS₂ nanosheets and flowers were analyzed systematically. Samples were prepared from a solution containing 10.4 mmol of MPA and 2.73 mmol of SnCl₂.2H₂O in 60 mL of absolute ethanol without adding any urea or TU and heated for 12 h at 180 °C under solvothermal conditions. The role of the solvent i.e., ethanol for the evolution of SnS₂ nanosheets or nanoflowers was determined by examining the structure of the product obtained by processing a solution with 10.4 mmol of MPA, 2.73 mmol of SnCl₂.2H₂O and 15.8 mmol TU in 60 mL of water at 180 °C for 12 h. The XRD pattern of the product obtained from a solution with no urea/TU shows mixed phase, tetragonal rutile SnO₂ phase, and hexagonal SnS₂ phase (PCPDF # 23-0677) (Figure 7.8). The XRD pattern of sample obtained from the aqueous solution exhibits mixed phase; hexagonal SnS₂ and orthorhombic phase of SnS (PCPRF # 75-0925) (Figure 7.8). The morphology of the product obtained from a solution with no urea shows solid spherical spheres with an average diameter of about 1.2 μm (Figure 7.9a). The sample synthesized using water as solvent shows hexagonal stacked up plate like structures (Figure 7.9b). The observed results indicate urea/thiourea and solvent (ethanol) play critical roles in leading to the formation of single phase of SnS₂. After adding Sn precursor to the solvent it will hydrolyze to form SnO₂ spherical particles and hydrochloric acid (HCl) is obtained as a by-product. At this stage, HCl accumulate the SnO₂ particles and prevent their reaction with sulfur precursor. Now, hydrolysis of urea produces OH⁻ ions into the

solution, and would completely neutralize the released acid and allow the reaction to complete to form pure SnS₂ phase.

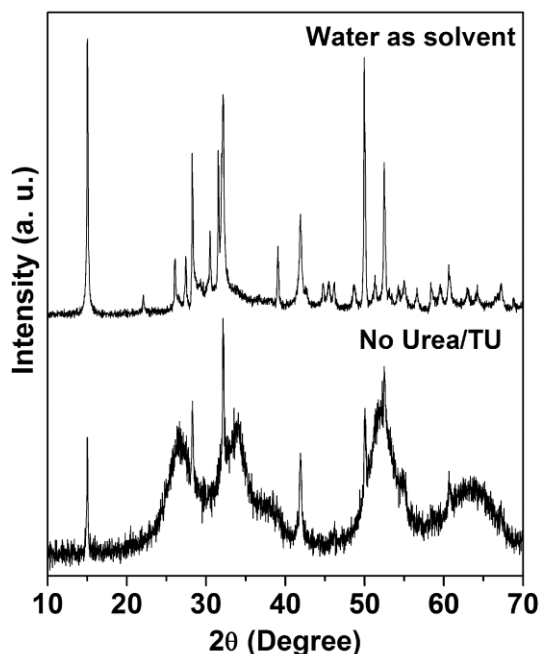


Figure 7.8. XRD patterns of samples obtained from a solution with water as the solvent (with TU) and with no urea/TU (with ethanol as solvent); in both cases the amounts of SnCl₂·2H₂O and MPA (1:3 mol ratio) were same. Samples prepared by heating at 180 °C for 12 h in an autoclave.

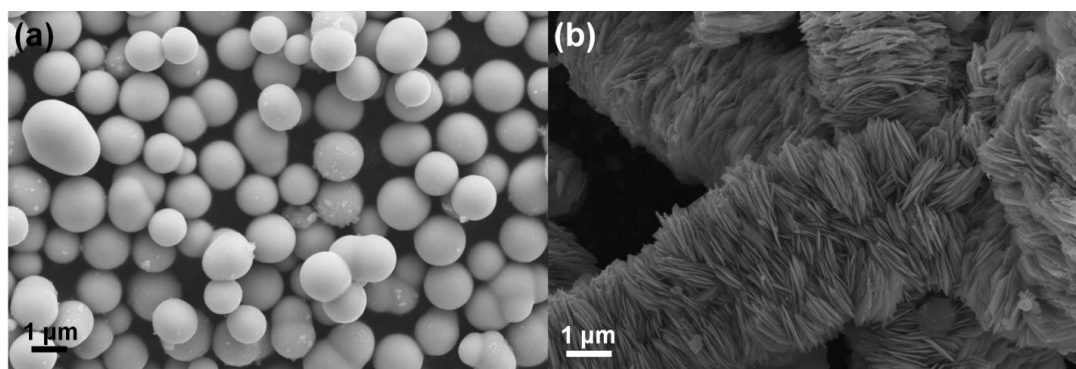


Figure 7.9. SEM images of samples prepared with (a) no urea/TU (with ethanol as solvent) and (b) water as the solvent (with TU) by maintaining SnCl₂·2H₂O, MPA in the same proportions. Samples were heated at 180 °C for 12 h in an autoclave.

Figure 7.10 shows the Raman spectra of SnS₂ nanosheets and nanoflowers at room temperature between the wavenumber range of 100 to 1000 cm⁻¹. The Raman

spectra for both the samples shows a strong peak at 312 cm^{-1} corresponding to the A_{1g} mode, according to group theory analysis. There is a broad peak between 450 to 650 cm^{-1} , which is attributed to second order effects in the SnS_2 phase. These results comply with the hexagonal crystal structure of SnS_2 .

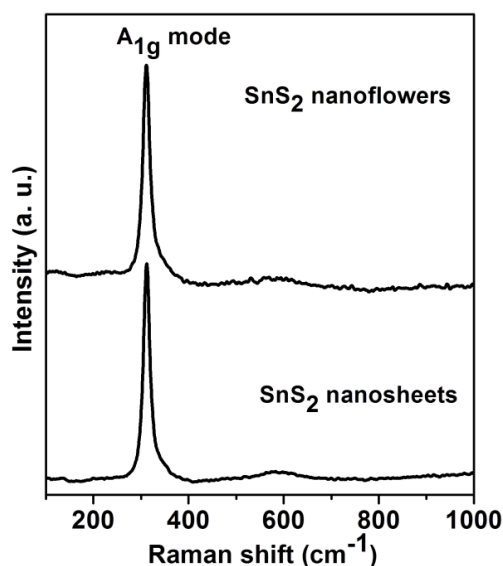


Figure 7.10. Raman spectra of SnS_2 nanosheets and nanoflowers

7.4.4. Optical properties

The optical properties for SnS_2 nanosheets and nanoflowers were measured using the UV-Visible diffuse reflectance mode and later converted into absorbance in the wavelength range of 200 to 800 nm. The optical band gaps for the SnS_2 nanosheets and flowers were calculated from their absorption edges which are shown in Figure 7.11a and b, respectively. The optical transitions in crystalline SnO_2 are estimated be direct. From the absorption spectra, the band gaps of SnS_2 nanosheets and nanoflowers were calculated to be 2.25 and 2.19 eV, respectively.

The comparative room temperature photoluminescence spectra of SnS_2 nanosheets and nanoflowers, recorded at an excitation wavelength of 350 nm are shown in Figure 7.11c and 11d, respectively. The emissions were measured in the

wavelength range of 375 to 600 nm. The emission spectrum of SnS₂ nanosheets shows multiple peaks in the wavelength range of 375 to 600 nm whereas SnS₂ nanoflowers exhibit a single broad peak in the 400 to 550 nm wavelength range with a full width half maximum (FWHM) of about 100 nm. From the PL spectra, it appears as if crystal structure defects or sulfur vacancies are more in the sheets compared to flowers.

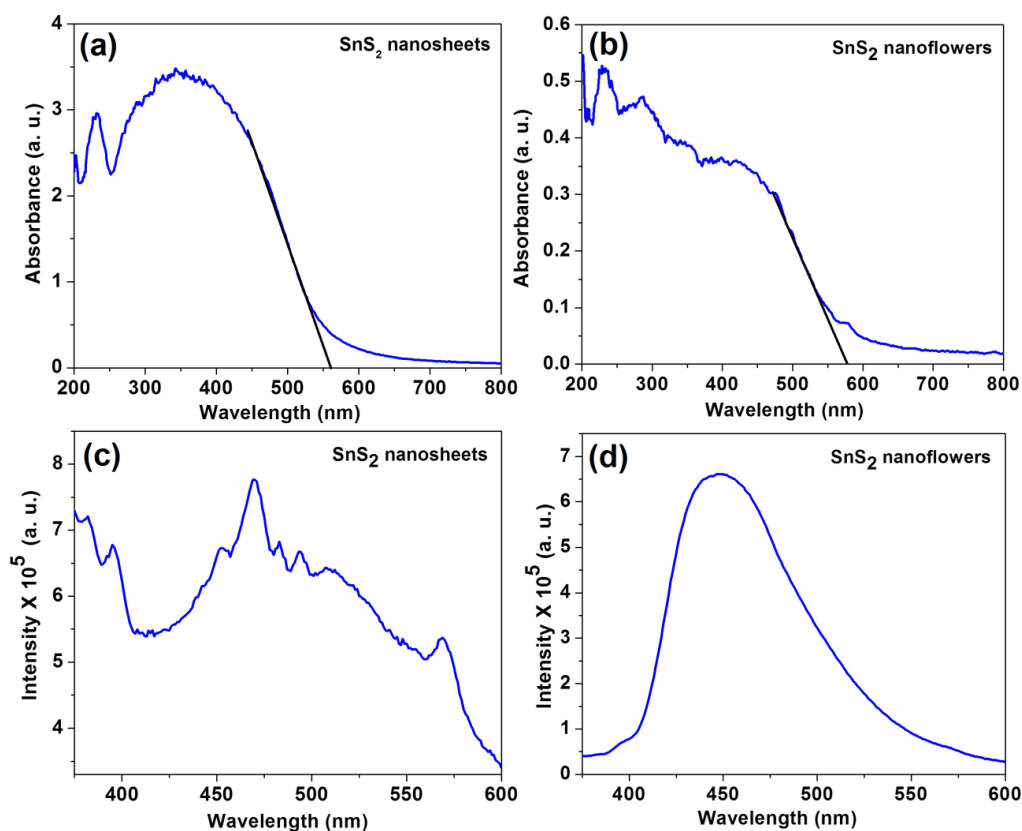


Figure 7.11. UV-Vis spectra of (a) SnS₂ nanosheets (b) nanoflowers; fluorescence spectra of (c) SnS₂ nanosheets and (d) SnS₂ nanoflowers.

7.5. Electrochemical property

7.5.1. Li-ion storage for half cell

The lithium storage properties of these SnS₂ nanosheets and nanoflowers as potential anodes for Li-ion batteries were evaluated using a two electrode cell, where in the SnS₂ nanosheets and nanoflowers serve as working electrode and Li

metal served as reference and counter electrode. Figure 7.12a and b show the cyclic voltammograms of SnS₂ nanosheets and nanoflowers, respectively, for the first cycle measured between 0.01 to 3 V at a scan rate 0.01 mV s⁻¹. The CV curve shows three major reduction peaks during the first cathodic scan. The peaks at ~1.7 and 1.5 V are ascribed to Li-ion insertion into the layered SnS₂ and the peak at about 1.2 V corresponds to the decomposition of lithiated SnS₂ to Sn and Li₂S. The peak at ~ 1.2 V can also be associated to the decomposition of electrolyte and formation of solid electrolyte interphase (SEI) layer on the surface of the electrode. A broad peak is also seen at around 0.2 V which is due to the alloying reaction of Sn to Li_{4.4}Sn. Similarly, during the anodic scan, the main peak at around 0.5 V corresponds to the dealloying reaction of Li_{4.4}Sn to Sn. The SnS₂ nanoflowers shows a peak at ~ 1.9 V which is ascribed to the partial decomposition of Li₂S to form SnS and a peak at ~ 2.4 V is assigned to the transformation of remaining Li₂S to polysulfides. The CV curves for subsequent cycles which were measured for next four cycles for both SnS₂ nanosheets and nanoflowers between 0.01 to 2 V at a scan rate 0.1 mV s⁻¹, are shown in the insets of Figure 7.12a and b, respectively. The alloy/dealloy peaks remained intact with cycling whereas the peak related to decomposition of Li₂S at ~ 1.9 V for SnS₂ nanoflowers vanished gradually.

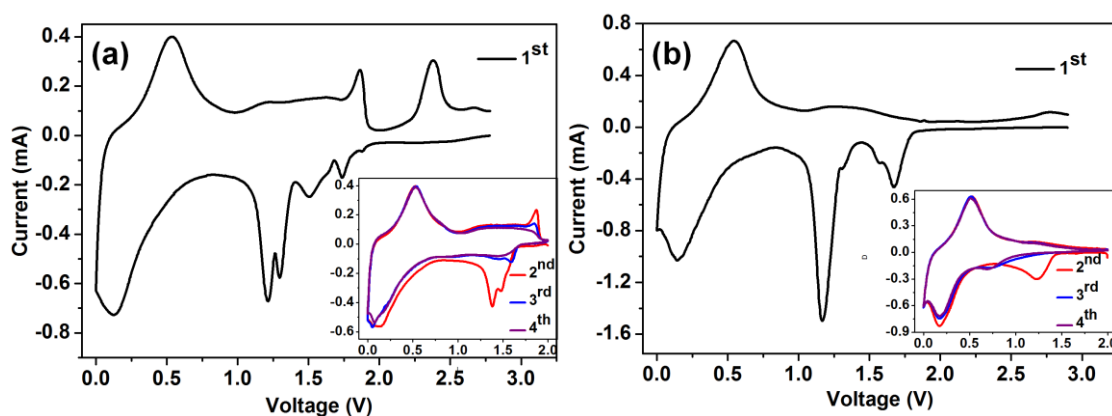


Figure 7.12. Cyclic voltammograms of (a) SnS₂ nanosheets (b) SnS₂ nanoflowers for the first cycle at a scan rate of 0.01 mV s⁻¹ between the voltage range of 0.01-3 V *versus* Li/Li⁺. Inset shows the subsequent cycles at a scan rate of 0.1 mV s⁻¹.

The electrochemical charge-discharge characteristics of SnS₂ nanosheets and flowers were measured between 0.01-1.5 V, at a constant current density of 100 mA g⁻¹. The charge-discharge voltage plateaus (Figure 7.13a and b) observed for both the samples were consistent with the CV curves. Figure 7.13c shows the cyclability comparison for SnS₂ nanosheets and nanoflowers, at 100 mA g⁻¹ current density, for 100 cycles. SnS₂ nanosheets show initial discharge and charge capacities of 2057.2 and 825.6 mAh g⁻¹, respectively with ~ 40% coulombic efficiency. The SnS₂ nanoflowers exhibited initial discharge and charge capacities of 2169.4 and 851 mAh g⁻¹, respectively, with a Coulombic efficiency of 39.2%. Based on the alloy/dealloying reactions, the maximum theoretical capacity for SnS₂ is expected to be 650 mAh g⁻¹. However, the conversion reaction of SnS₂ to Sn and Li₂S is partially reversible for the first few cycles. If SnS₂ undergoes a complete conversion mechanism, the maximum theoretical capacity is anticipated to be 1250 mAh g⁻¹. But the observed irreversible capacity loss during the first cycle needs to be accounted for. The possible reasons could be: (i) Li insertion during first discharge without undergoing any phase decomposition, (ii) decomposition of electrolyte and

SEI layer formation and (iii) irreversible conversion reaction of SnS_2 to Sn and Li_2S . Compared to SnS_2 nanosheets, the nanoflowers exhibited better capacity retention. After 100 cycles, the SnS_2 nanoflowers retained a capacity of 542 mAh g^{-1} with almost 98.6% Coulombic efficiency. Comparatively, the SnS_2 nanosheets after 100 cycles, retained a reversible capacity of 436.5 mAh g^{-1} with a Coulombic efficiency of $\sim 97\%$.

To further investigate the influence of nanostructure on the electrochemical performance, the capacity was monitored over cycling at various current densities ranging from 100 to 3000 mA g^{-1} and then reverted to 100 mA g^{-1} . As shown in Figure 7.13d, the discharge capacity decreases with increasing current density for the two electrodes. SnS_2 nanoflowers exhibit a charge capacity of 798.1 mAh g^{-1} , after 5 cycles at 100 mA g^{-1} . As the current density increases, the reversible capacities are 733.6 , 668.6 , 612.1 , 525.2 and 466.1 mAh g^{-1} at 200 , 500 , 1000 , 2000 and 3000 mA g^{-1} current densities, respectively. When the current density was reverted to 100 mA g^{-1} , after 65 cycles, the capacity recovers to 666.8 mAh g^{-1} , which indicates excellent capacity retention $\sim 78.3\%$. In comparison, the SnS_2 nanosheets suffer from a severe decay in capacity from 733.9 to 196 mAh g^{-1} when the current density was increases from 200 to 3000 mA g^{-1} . The SnS_2 nanoflowers electrode exhibits much better rate capability than nanosheets and the observed cycling stability and rate capabilities were much better than some earlier reports on SnS_2 (without any carbon coating).

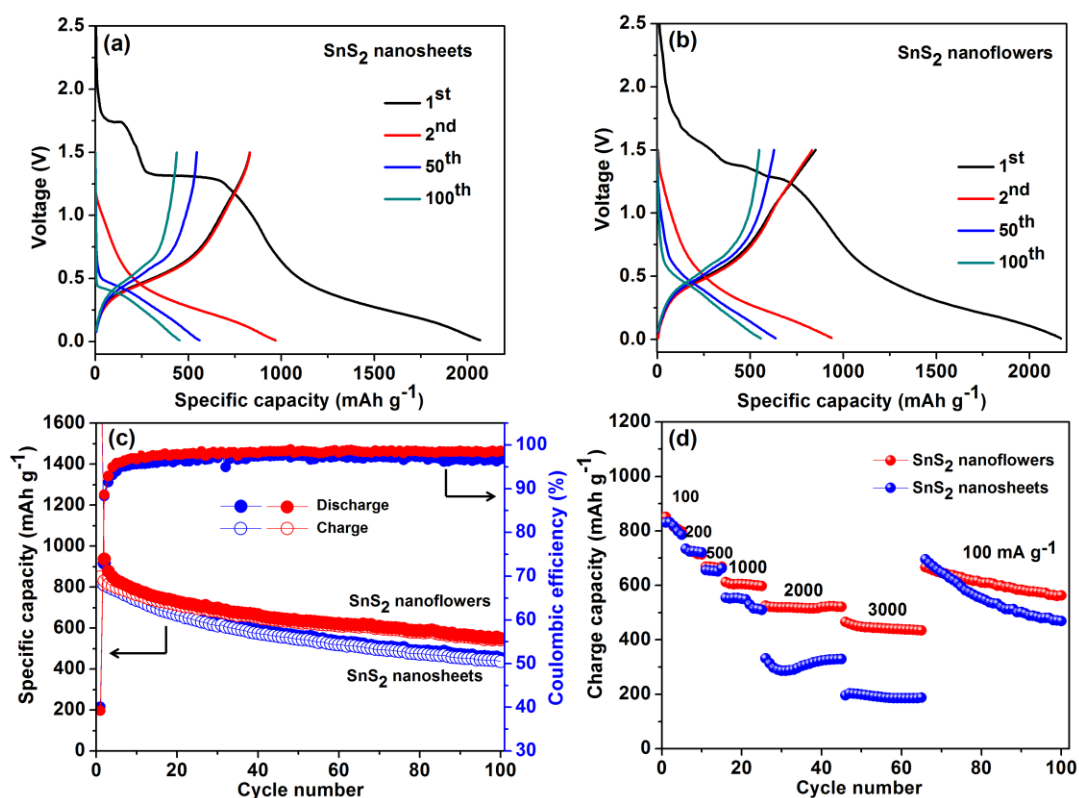


Figure 7.13. Charge-discharge curves of (a) SnS₂ nanosheets, (b) nanoflowers and (c) cyclability for 100 cycles at current density of 100 mA g⁻¹ between 0.01 to 1.5 V *versus* Li/Li⁺ and (d) rate capability of both SnS₂ nanosheets and nanoflowers.

7.5.2. Full cell demonstration

A full cell was fabricated using SnS₂ nanoflowers as anode and LiFePO₄ (gifted from ARCI) as cathode with weight ratio of 1:3, respectively. The LiFePO₄ cathode was prepared by flame spray pyrolysis and gifted to us by ARCI). The electrochemical response was measured between the voltage ranges of 2 to 3.5 V at a 0.2 C-rate. Figure 7.14 shows the typical charge-discharge profiles for the first five cycles. The initial cycle shows a reversible capacity of 131.5 mAh g⁻¹ with a 75.6% Coulombic efficiency. The irreversible capacity loss is mainly because of pseudo-reversible reaction of SnS₂ to Sn. The full cell shows a gradual fade in capacity, and after 20 cycles a capacity of 85 mAh g⁻¹ was retained.

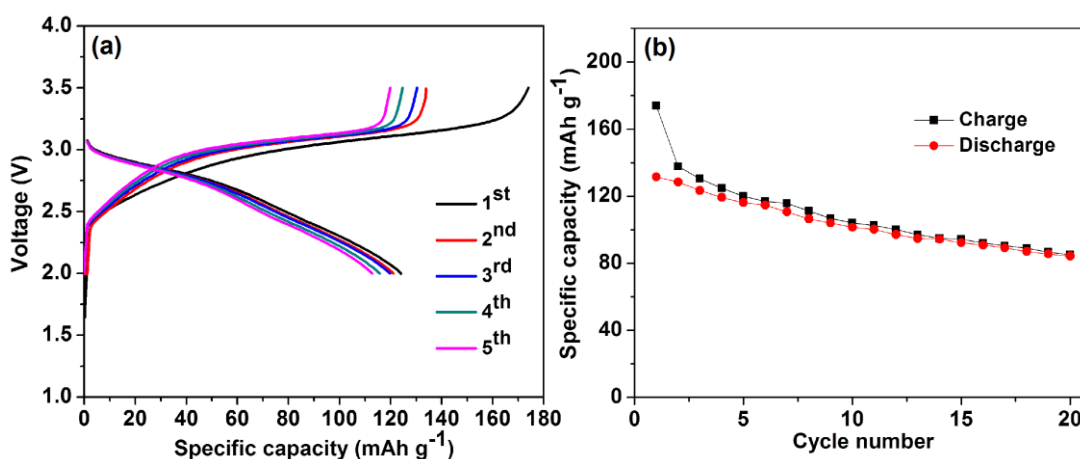


Figure 7.14. (a) Charge-discharge curves (b) cyclability measured at a 0.2C-rate, of a full cell fabricated with SnS₂ nanosheets anode and LiFePO₄ cathode.

To understand the reason for better cyclability and the excellent rate capability of SnS₂ nanoflowers relative to SnS₂ nanosheets, EIS measurements were carried out after 50 cycles, and the Nyquist plots were recorded at 100 mA g⁻¹ current density. Figure 7.15 shows the comparison of the EIS plots of SnS₂ nanoflowers and nanosheets after 50 cycles. The Nyquist plots obtained for the two electrodes consist of one semicircle at high/medium frequency and an inclined line at low frequency region. In general, the semicircle is attributed to the summation of the contact, the solid-electrolyte interface resistance, and the charge-transfer resistance; while the inclined line at a ~45° angle with respect to the real axis corresponds to the lithium-diffusion process within the electrodes. From the Nyquist plots, it can be seen that after 50 cycles, the SnS₂ nanoflowers show very less charge transfer resistance when compared to SnS₂ nanosheets, which is probably the reason for good cycling stability and rate capability.

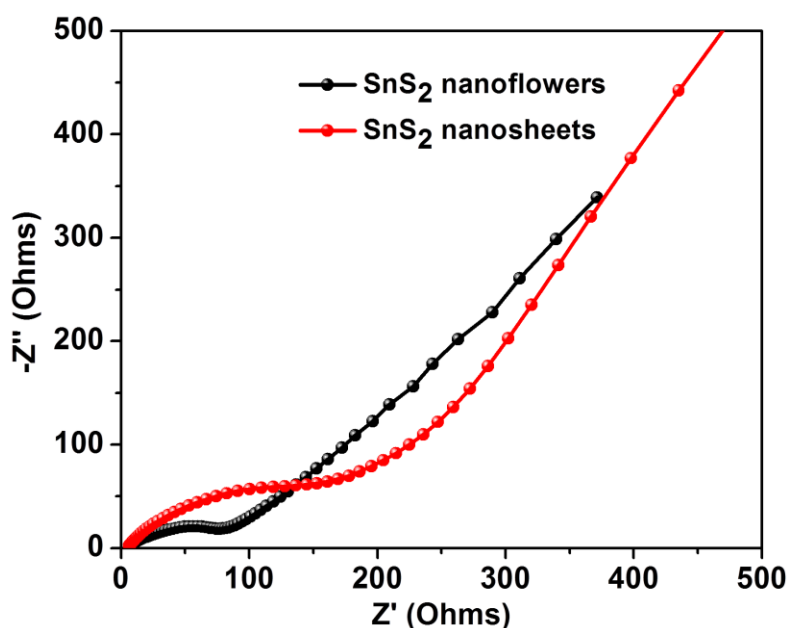


Figure 7.15. Nyquist plots of SnS₂ nanosheets and nanoflowers, after 50 cycles at 100 mA g⁻¹ current density.

7.6. Summary

A novel, simple and one-pot solvothermal route was developed to synthesize the SnS₂ nanosheets and nanoflowers by using ethanol as the solvent. For the generation of SnS₂ nanosheets, urea plays a significant role whereas with TU, a 3D architecture of SnS₂ nanoflowers was obtained. The role of the solvent and the proportion of urea and TU which steer the growth of SnS₂ nanosheets and nanoflowers, respectively, with mono disperse morphologies for efficient electrochemical energy storage performance, has been explained by XRD and electron microscopy studies. By tuning the processing parameters, SnS₂ nanosheets and nanoflowers with a narrow size distribution and good structural integrity were prepared. SnS₂ nanosheets and nanoflowers exhibited excellent electrochemical capacity retention of 436.5 and 542 mAh g⁻¹, respectively, after 100 cycles at a current density of 100 mA g⁻¹. Compared to SnS₂ nanosheets, the 3D hierarchical nanoflowers like structure showed superior rate capability at 3000 mA g⁻¹: 466.1 (for nanoflowers) and 196 (for nanosheets)

mAh g⁻¹. In addition, the SnS₂ nanosheets and nanoflowers also exhibited luminescent properties, with a broad emission in the visible region. These results on SnS₂ architectures indicate the promise they have for energy storage and possibly energy harvesting applications as well.

References

1. A. Ibarz, E. Ruiz, S. Alvarez, *Chem. Mater.*, 10 (1998) 3422-3428.
2. M. K. Jana, H. B. Rajendra, A. J. Bhattacharyya, K. Biswas, *Cryst Eng Comm*, 16 (2014) 3994-4000.
3. K. Chang, Z. Wang, G. Huang, H. Li, W. Chen, J. Y. Lee, *J. Power Sources*, 201 (2012) 259-266.
4. M. He, L. X. Yuan, Y. H. Huang, *RSC Adv.*, 3 (2013) 3374-3383.
5. J. G. Lee, D. Son, C. Kim, B. Park, *J. Power Sources*, 172 (2007) 908-912.
6. T. Brousse, R. Retouxf, L. Herterich, D. M. Schleich, *J. Electrochem. Soc.*, 145 (1998) 1-4.
7. M. V. Reddy, G. V. Subba Rao, B. V. R. Chowdari, *Chem. Rev.*, 113 (2013) 5364-5457.
8. S. Liu, X. Yin, Q. Hao, M. Zhang, L. Li, L. Chen, Q. Li, Y. Wang, T. Wang, *Materials Letters*, 64 (2010) 2350-2353.
9. P. Wu, N. Du, H. Zhang, J. Liu, L. Chang, L. Wang, D. Yang, J. Z. Jiang, *Nanoscale*, 4 (2012) 4002-4006.
10. J. Lu, C. Nan, L. Li, Q. Peng, Y. Li, *Nano Res.*, 6 (2013) 55-64.
11. H. Mukaibo, A. Yoshizawa, T. Momma, T. Osakaa, *J Power Sources*, 119-121 (2003) 60-63.
12. S. Liu, X. Yin, L. Chen, Q. Li, T. Wang, *Solid State Sciences*, 12 (2010) 712-718.
13. C. Zhai, N. Du and H. Z. D. Yang, *Chem. Commun.*, 47 (2011) 1270-1272.
14. J. Wang, J. Liu, H. bo Xu, S. Ji, J. Wang, Y. Zhou, P. Hodgson, Y. Li, *J. Mater. Chem. A*, 1 (2013) 1117-1122.
15. J. Ma, D. Lei, L. Mei, X. Duan, Q. Li, T. Wang, W. Zheng, *Cryst Eng Comm.*, 14 (2012) 832-836.

16. J. W. Seo, J. T. Jang, S. W. Park, C. Kim, B. Park, J. Cheon, *Adv. Mater.*, 20 (2008) 4269-4273.
17. H. Zhong, G. Yang, H. Song, Q. Liao, H. Cui, P. Shen, C. X. Wang, *J. Phys. Chem. C*, 116 (2012) 9319-9326.
18. T. J. Kim, C. Kim, D. Son, M. Choi, B. Park, *J. Power Sources*, 167 (2007) 529-535.
19. J. Ma, D. Lei, X. Duan, Q. Li, T. Wang, A. Cao, Y. Maod, W. Zheng, *RSC Adv.*, 2 (2012) 3615-3617.
20. J. Zai, K. Wang, Y. Su, X. Qian, J. Chen, *J. Power Sources*, 196 (2011) 3650-3654.
21. J. Zai, X. Qian, K. Wang, C. Yu, L. Tao, Y. Xiao, J. Chen, *Cryst Eng Comm*, 14 (2012) 1364-1375.

Chapter 8

Summary and Conclusions

The design and development of new anodes, as alternates to graphite, which can offer a very high charge storage capacity, durable cycle life and safe use is desirable for large scale applications. In this regard, nanostructured materials and nanotechnology offer great promise because of the unusual properties endowed by confining their dimensions and the combination of bulk and surface properties to their overall behavior. However, solution-based synthesis approaches and the associated processing play a critical role in controlling the particle composition, size, morphology, and the overall electrochemical properties and performances. To this end, the present thesis mainly dealt with synthesis of molybdenum and tin based oxides and sulfide nanostructured materials and their composites as anodes, structure and property correlation and their characterization. The observations and conclusions drawn from the work done are summarized in this chapter.

Mo based oxides as anodes have been widely explored due to their very high theoretical specific capacity (840 mAh g^{-1}), easy to process and low cost. The large volume variations in MoO_2 during charge/discharge due to structural reorganization and nanoparticles aggregation decrease its' cycling stability. A carbon nanostructure that can improve the cycling stability of metal oxide such as MoO_2 is multi walled carbon nanotubes (MWCNTs). Since MWCNTs are bestowed with one-dimensional tubular structures, high electrical and thermal conductivities, and large surface areas, they are ideal for combining with MoO_2 . Moreover, the synergy between the functions of the two materials, high capacity of MoO_2 and good electronic conductivity and large surface area of MWCNTs can be exploited in the

MoO₂/MWCNT hybrid to yield high performance anodes in Li-ion batteries. A MoO₂/MWCNT hybrid composed of spherical floral nanostructures of MoO₂, interlinked with curved MWCNTs was synthesized by a hydrothermal route. It was found that the formation of MoO₂ flower-like shapes is dictated by the surfactant, AOT. The unique nanoscale architecture of the MoO₂/MWCNT hybrid is responsible for a large reversible electrochemical lithium storage capacity of 1025.2 mAh g⁻¹ achieved at a current density of 100 mA g⁻¹, after 160 cycles, in comparison to a much lower value of 220 mAh g⁻¹ (after 20 cycles) obtained for neat MoO₂. The inherent electron conducting nature of MWCNTs enabled efficient electron transfer and transport in the MoO₂/MWCNT hybrid by the virtue of the direct interconnects formed between MoO₂ flowers and MWCNTs. The unusual topology of the MoO₂/MWCNT hybrid, the high rate capability (as it showed a capacity of 408 mAh g⁻¹, at a high current density of 1000 mA g⁻¹) and the excellent cyclability demonstrated its' utilitarian value as a high performance anode in LIBs. Our simple single step approach for fabricating a MoO₂/MWCNT hybrid showed that this strategy can be applied to other oxides as well to yield unique architectures for LIB anodes. The use of carbon nanostructures to ameliorate metal oxides' Li⁺ storage performance can be extended to other anode oxides.

Another carbon nanostructure which can increase the operation cycling lifetime of MoO₂ based anode is Graphene. It has been proved that Graphene layers prevent both volume changes and aggregation of metal oxide nanoparticles during charge/discharge processes as the oxide nanoparticles are sandwiched between the sheets and therefore cannot agglomerate. Furthermore, the attachment of metal oxide or any other inorganic moiety on Graphene effectively inhibits the restacking of

Graphene layers. By using this concept, herein, a MoO₂/Graphene composite was synthesized by a hydrothermal route, involving the *in-situ* reduction of a Mo salt precursor and embedding of MoO₂ nanoparticles on Graphene sheets in a single step. Electron microscopy, XPS and *ex-situ* XRD analyses confirmed the homogeneous distribution of metal oxide nanoparticles in a 2D network of Graphene sheets. The Graphene layers prevented the aggregation of MoO₂ nanoparticles thus reducing volume expansion during cycling and the MoO₂ nanoparticles due to their confinement to Graphene layers inhibited the layers from stacking. Such a concerted interplay between the two moieties, effectively manifested in a remarkably high lithium ion storage capacity, rate capability and cycling performance relative to the neat oxide or carbon nanostructure based composites prepared by other methods. Further the nanoscale current images showed a significantly amplified current carrying capability for the composite, induced by Graphene and electrochemical impedance spectroscopy revealed a lower resistance to charge transfer and transport for the MoO₂/Graphene composite in comparison to neat MoO₂, which are responsible for enhanced capacity and better endurance. Our results pave way for fabricating electrodes based on Graphene/metal oxide composites, for realizing significant improvements in Li-ion storage performance in batteries.

Other anodes such as tin based oxides and sulfides have been widely studied; they can offer a very high specific capacity through alloy/dealloy mechanism. Usually, pure tin electrodes can undergo pulverization very rapidly during Li insertion/extraction. On the other hand, in SnX₂ (X = O and S) materials via formation of Li₂X up on discharge, can absorb some of the volume expansion, and as a result, the cycling stability can be improved. However, even in SnX₂, prolonged

cycling leads to pulverization of the electrodes and capacity fade. These problems can be suppressed to some extent by designing nanostructures such as hollow spheres, nanowires etc. Composites of SnX_2 with carbonaceous materials such as graphene oxide (GO), carbon nanotubes (CNTs) and conducting polymers can be prepared. SnO_2 hollow spheres (HS) were prepared by a hydrothermal method by employing mercaptopropionic acid (MPA) as the structure directing agent, CTAB as the surfactant that inhibited HS from agglomeration and water as the solvent critical to the formation of empty cores in the HS. Optimized SnO_2 HS with outer diameters in the range of 140-150 nm and inner hollow core dimensions of about 100 nm were synthesized. The roles of MPA, CTAB and the solvent were deduced by performing detailed morphological studies. The temperature induced structural evolution of SnO_2 HS from SnO_2 solid spheres was explained using an inward-out Ostwald ripening mechanism. Hybrids of SnO_2 HS with GO and poly(3,4-ethylenedioxythiophene) or PEDOT were synthesized with the objective of increasing electronic conductivity of the active electrode whilst simultaneously preserving the structural integrity of HS, thereby leading to a more robust material capable of exhibiting an electrochemical cycling response better than that of pristine SnO_2 HS. While the optimized SnO_2 HS displayed a reversible Li^+ storage capacity of 400 mA h g^{-1} , attained at a current density of 100 mA g^{-1} , at the end of 30 cycles, the SnO_2 HS/GO/PEDOT hybrid delivered a reversible capacity of 608 mA h g^{-1} at the same current density after 150 cycles. The immobilization of SnO_2 HS on GO and further coating by a continuous layer of amorphous PEDOT was affirmed by elemental mapping and XPS. The key roles of GO nanosheets as the electron conducting matrix for SnO_2 HS and PEDOT as the polymer envelope which

buffered the severe volume changes that occurred during cycling and inhibited electrode disintegration and rapid capacity fading, thus amplifying reversible capacity, rate capability and cycling stability were demonstrated. This route of integrating conductive GO nanosheets and electrochemically stable PEDOT is extendable to a wide range of metal oxides HS which can be useful for developing high quality LIB anodes.

The template free synthesis of the SnO₂ hollow spheres with controlled size was also demonstrated for high Li-ion storage response. The work on SnO₂ HS was extended by using a simple hydrothermal method for preparing SnO₂ HS, with the aid of organic moieties as structure directing agents. The content of acetylacetone (AcAc) in the Sn precursor dispersion was found to have a direct impact on the structure of the final SnO₂ product. Uniform SnO₂ HS with overall diameters of 200 and 350 nm comprising of empty cores surrounded by solid shells of 50 to 60 nm dimensions were successfully prepared from solutions with 2.5/5.0 mL of AcAc. A heating time dependent analysis delineated a stepwise transformation of solid spheres (1 h) to agglomerated spheres (4 h) to porous spheres (10 h) to optimized HS (13 h) terminating with broken blown-up HS (24 h). A temperature dependent reaction progress showed conversion from solid spheres (140 °C) to HS (160 °C) to chipped off-huge spheres (180 °C). The roles of MPA as the sphere forming agent and CTAB as the surfactant which inhibits the coalescence of SnO₂ HS were also deduced. On the basis of morphological analyses, a growth mechanism for the formation of optimized SnO₂ HS was expounded. The ability of the optimized SnO₂ HS (2.5 or 5.0 mL of AcAc, 160 °C, 13 h) to function as anodes in LIBs was determined from their electrochemical characteristics. The 200 nm SnO₂ HS

delivered a reversible capacity of 540 mAh g⁻¹, at a current density of 100 mA g⁻¹, after 50 repetitive cycles, and it showed good rate capability as well. The SnO₂ HS were also found to be strongly fluorescent, thereby suggesting their potential for energy harvesting applications in addition to energy storage.

In addition to MoO₂ and SnO₂, SnS₂ based nanostructured electrodes were also employed as anodes in LiBs. A novel, simple and one-pot solvothermal route was developed to synthesize SnS₂ nanosheets and nanoflowers by using ethanol as solvent. SnS₂ nanosheets were formed by using urea in the precursor solution, whereas with thiourea (TU), a 3D architecture of SnS₂ nanoflowers was obtained. The role of the solvent and the proportion of urea and TU which steer the growth of SnS₂ nanosheets and nanoflowers, respectively, for efficient electrochemical energy storage performance, was elucidated by XRD and electron microscopy studies. SnS₂ nanosheets and nanoflowers exhibited excellent Li⁺ storage capacity retention of 436.5 and 542 mAh g⁻¹, respectively, after 100 cycles at a current density of 100 mA g⁻¹. Compared to SnS₂ nanosheets, the SnS₂ 3D nanoflowers showed a high rate capability at 3000 mA g⁻¹. It was 466.1 (for nanoflowers) and 196 (for nanosheets) mAh g⁻¹. A full cell was also demonstrated with SnS₂ nanoflowers as anode. In addition, the SnS₂ nanosheets and nanoflowers also exhibited luminescent properties.

In future, the focus would be on minimizing the irreversible capacity loss or improving the Coulombic efficiency of Sn-based anodes by coating with metal oxides and robust conducting polymer coatings. The cathode (e.g. LiFePO₄) cathode and anode (e.g. SnS₂ nanoflowers) proportions can be optimized to enable the rendering of full cells with high Coulombic efficiency and improved cycling

stability. The synthetic methods developed herein can be further extended to the synthesis of few layered MoS₂ nanosheets and their Li-ion storage response and mechanism can be studied.

Li-ion battery technology has emerged as one of the most promising solutions for energy storage today, primarily due to a growing demand for both stationary and mobile power. In this thesis, novel transition metal oxide composites and electroactive materials with monodisperse nanostructured morphologies were developed, their electrochemical performance and structural characteristics were studied in detail, and their potential for use as anodes in LIBs was unambiguously demonstrated. We observed that cycling stabilities improved significantly in composites, by use of a carbon nanostructure or a conducting polymer, or by simply controlling the monodisperse quality of the pristine electroactive material, indicating the power of wet chemistry routes in steering the formation of high performance composites. All the three components: the anode, the cathode and the electrolyte, play pivotal roles in controlling the LIB performance and therefore, the future prospects for LIBs include development of new, low cost, scalable and non-toxic materials for anode, electrolyte and cathodes, capable of delivering high energy density while not posing any safety threat to the user. Further, the commercialization of LIBs based on electrodes of novel composites or unique active material nanostructures, requires a deeper understanding of the manufacturing aspects of the battery design. Today, research in LIBs, is poised at a very advanced stage, and therefore, it is possible that in future, LIBs, apart from being used in portable electronic devices, will be used in transportation sector as well. The impetus to extend the LIB technology to such challenging applications stems from the fact that

LIBs can be designed as green, environment friendly, sustainable sources of power. The carbon based fillers used for forming composites in this thesis were environmentally benign and cost-effective. The work presented in this thesis provides a good understanding of Li-ion storage mechanisms in a few composites and in some nanostructures of the electroactive anode material and thus this elaborate study will be useful for development of new composites or materials for stable electrochemical energy storage.

Publications

1. List of Publications included in this thesis

- 1) Akkisetty Bhaskar, M. Deepa, T.N. Rao, U.V. Varadaraju, Enhanced Nanoscale Conduction Capability of a MoO₂/Graphene Composite for High Performance Anodes in Lithium Ion Batteries, *J. Power Sources*, 216 (2012) 169-178.
- 2) Akkisetty Bhaskar, M. Deepa, T.N. Rao, MoO₂/Multiwalled Carbon Nanotubes (MWCNT) Hybrid for Use as a Li-Ion Battery Anode, *ACS Appl. Mater. Interfaces*, 5 (2013) 2555-2566.
- 3) Akkisetty Bhaskar, M. Deepa, M. Ramakrishna, T.N. Rao, Poly(3,4 ethylenedioxythiophene) Sheath Over a SnO₂ Hollow Spheres/Graphene Oxide Hybrid for a Durable Anode in Li-Ion Batteries, *J. Phys. Chem. C*, 118 (2014) 7296-7306.
- 4) Akkisetty Bhaskar, M. Deepa, T. N. Rao, Size-Controlled SnO₂ Hollow Spheres via Template Free Approach as Anodes for Lithium Ion Batteries, *Nanoscale*, 6 (2014) 10762-10771.

2. Publication not included in this thesis

- 1) Akkisetty Bhaskar, M. Deepa, T.N. Rao, U.V. Varadaraju, In-situ Carbon Coated Li₂MnSiO₄/C Composites as Cathodes for Enhanced Performance Li-ion Batteries, *J. Electrochem. Soc.*, 159 (2012) A1-A7.

3. Contributions to academic conferences and proceedings

- 1) Akkisetty Bhaskar, Malepurath Deepa, Tata Narasinga Rao, U. V. Varadaraju, Lithium Niobium Oxyfluoride LiNbO₂F as Anode Material for Lithium Ion Battery, 6th Asian Conference on Electrochemical Power Sources (ACEPS)-2010, January 5th - 8th, CECRI, Chennai (Poster Presentation)
- 2) Akkisetty Bhaskar, Malepurath Deepa, Tata Narasinga Rao, U. V. Varadaraju, Spinel LiMn₂O₄ Nanorods/Poly(3,4-ethylenedioxythiophene) Composite with Enhanced Performance Characteristics for Li-Ion Batteries, International conference on nanoscience and technology (CONSAT)-2012, ARCI, Hyderabad (Poster Presentation)
- 3) Akkisetty Bhaskar, Malepurath Deepa, Tata Narasinga Rao, A MoO₂/multiwalled Carbon Nanotubes Composite with Flower like Nanostructures for Li-ion Battery

Anodes, 7th International Conference on Materials for Advanced Technologies (ICMAT)-2013, June 30 to July 5, Singapore (Oral Presentation)

4) Akkisetty Bhaskar, Malepurath. Deepa, Tata Narasinga Rao, Simple and Large Scale Synthesis of SnS_x Nano-Belts, Flowers and Sheets for Li-Ion Battery Anode Applications, The 17th International Meeting on Li-Ion Battery (IMLB)-2014, June 10-14, Como, Italy. (Poster Presentation)